UNIVERSIDAD DE EXTREMADURA

TESIS DOCTORAL

Fabricación mediante Moldeo Robotizado y Optimización Mecánica de Andamiajes Vitrocerámicos Bioactivos para Ingeniería de Tejidos

Siamak Eqtesadi

**Departamento de Ingeniería Mecánica,
Energética y de los Materiales**

Conformidad de los Directores

Fdo: Pedro Miranda González   Fdo: Antonia Pajares Vicente

2015

GRUPO ESPECIALIZADO DE MATERIALES

UNIVERSIDAD DE EXTREMADURA

Este trabajo se enmarca en el contexto de la línea de investigación ***Desarrollo de materiales para aplicaciones biomédicas*** desarrollada en el Grupo Especializado de Cerámicos de la Universidad de Extremadura

Dª. Antonia Pajares Vicente, Catedrática de Universidad y **D. Pedro Miranda González**, Profesor Titular de Universidad, pertenecientes al Área de Ciencia de los Materiales e Ingeniería Metalúrgica del Departamento de Ingeniería Mecánica, Energética y de los Materiales de la Universidad de Extremadura

INFORMAN

que la presente memoria **"Fabricación mediante Moldeo Robotizado y Optimización Mecánica de Andamiajes Vitrocerámicos Bioactivos"** para Ingeniería de Tejidos" ha sido realizada por **D. Siamak Eqtesdai** en los laboratorios del área de Ciencia de los Materiales e Ingeniería Metalúrgica (Universidad de Extremadura), bajo nuestra dirección.

Y para que conste, en cumplimiento de la legislación vigente, firmamos el presente, en Badajoz a 9 de junio de 2015.

Fdo: F. Antonia Pajares Vicente   Fdo: Pedro Miranda González.

TRIBUNAL

Dr. Martin Trunec
Full Professor
Institute of Materials Science and Engineering
Brno University of Technology

Dra. Leena Marita Hupa
Associate Professor
Department of Inorganic Chemistry
Åbo Akademi University

Dra. Nuria Vilaboa Díaz
Investigadora
Instituto de Investigaciones Sanitarias
Hospital Universitario La Paz

Dr. Ángel Luis Ortiz Seco
Titular de Universidad
Departamento de Ingeniería Mecánica,
Energética y de los Materiales
Universidad de Extremadura

Dr. Óscar Borrero López
Titular de Universidad
Departamento de Ingeniería Mecánica,
Energética y de los Materiales
Universidad de Extremadura

Dedications

I dedicate this thesis to my beloved wife, Azadeh, who offered me unconditional love, support and encouragement throughout the years. I will always appreciate her for helping me throughout my life.

Acknowledgments

I would like to express my special appreciation and thanks to my supervisors Dr. Pedro Miranda González and Dra. Antonia Pajares Vicente for their invaluable guidance and support during these past four years.

A special thanks to Dr. Fidel Hugo Perera Martínez for his patience to assist me with this project.

I would also like to acknowledge and thank all the members of our laboratory for their friendship and assistance during my career in Badajoz.

Table of Contents

List of Figures

List of Tables

Abstract

A new type of approach is being developed to address the problems associated with the repair of bone-related lesions. The idea is to stimulate the natural cellular processes of bone regeneration beyond their normal capabilities, to allow them to operate even in defects larger than the critical size, thus avoiding the need of resorting to conventional, permanent, implants. The need to develop this new type of approach lies in the limitations associated with the two alternatives currently available to surgeons and orthopaedic physicians: grafts (autologous or heterologous) and prostheses.

Although there have been undeniable improvements in both types of clinical options, they both suffer from important drawbacks. In the case of autografts, the limited amount of material and the fact that they involve secondary surgical sites, impose serious restrictions on the size of the defects to be repaired by this means. Thanks to the creation of Bone Banks, allografts are not so restricted in terms of the amount of tissue that can be replaced, but they have other associated problems: risk of immunogenic response and disease transmission from donor, and low cell survival during cryopreservation of the tissues. All these drawbacks lead to a much lower success ratio for allografts compared to autografts [1].

With respect to artificial prostheses, although some synthetic biocompatible materials are widely used in medical and dental applications, their long-term effectiveness as implants needs improvement. Today's implants have a variety of shortcomings related to their fixation and, unlike natural bone, cannot self-repair or adapt to the changing physiological conditions [2]. Also, many implants fail, causing damage to the surrounding tissues, because of a mismatch in physical properties between bone and implant.

This has motivated significant effort towards improving implant performance through the design of artificial bone-like materials, with similar mechanical properties and able to interact with the tissues, so that they can actively induce bone regeneration. A strategy to achieve this type of interaction with surrounding tissue and to stimulate cell penetration and growth is to use porous matrices of osteophilic materials.

Among the materials most commonly used to fabricate those porous substrates, biodegradable polymers—such as polylactic acid (PLA), polyglycolic acid (PGA),

polycaprolactone (PCL), chitosan, etc.—stand out. However, their low elastic moduli and the fast degradation of their mechanical properties limit their application to non-load-bearing regions of the skeleton. There are also bioresorbable bone substitutes fabricated from inorganic materials with compositions similar to apatite, the mineral component of bone, which can be slowly dissolved by osteoclasts and transformed into live bone [3]. Different calcium phosphates (hydroxyapatite, tricalcium phosphate, etc.) and some bioactive glasses (bioglasses) belong to this group of materials.

Bioactive glasses are attracting an increasing attention for the fabrication of bone tissue engineering scaffolds, due to their high bioactivity [4-6]. Among them, 45S5 bioglass (45 % SiO_2, 24.5 % CaO, 24.5% Na_2O y 6 % P_2O_5) is probably the most thoroughly studied and most widely used in clinical applications, as bone graft substitute [7-9], being highly bioactive and both osteoinductive and osteoconductive, [10-13]. However, despite the fact that after more than 40 years of research no other calcium phosphate or bioactive glass composition has surpassed 45S5 bioglass biological performance, its commercial success is somewhat limited and calcium phosphates remain market leaders as bone substitute materials [9]. The main reason for this limited success lays in the need to sinter the material at temperatures higher than crystallization temperature to achieve a significant densification and mechanical integrity [9][14-16]. Another bioactive glass that has aroused great interest is 13-93 bioglass (53 % SiO_2, 20 % CaO, 6 % Na_2O, 4 % P_2O_5, 12 % K_2O, 5 % MgO). Although the higher silica content in 13-93 bioglass, compared to 45S5 bioglass, reduces its degradation and conversion rates, easier processing characteristics and promising compressive strengths make this bioactive glass an interesting alternative for the fabrication of bone scaffolds in load-bearing applications.

The main drawback of these bioactive glasses, especially when they are porous, is their low fracture strength, which, together with their intrinsic brittleness, again limits their use to low–load applications (e.g. cranial implants). One of the reasons for the low mechanical resistance of bioglass scaffolds lies in the fact that their porosity must be interconnected and with a certain interconnection size, to allow vascularization, cell penetration and nutrient diffusion into the scaffold. In conventional porous scaffold fabrication methods—such as solvent casting in combination with particulate leaching, fibre meshing, gas foaming, melt molding, freeze drying, etc.—it is difficult to precisely control pore size, geometry, and spatial distribution, and therefore to achieve the

required degree of interconnectivity it is necessary to produce very high porosities [17-18].

In other to overcome these obstacles and produce 45S5 and 13-93 bioglass scaffolds with improved mechanical properties, three different strategies have been used in this study:

(i) Optimizing the pore architecture. Rapid Prototyping or Solid Freeform Fabrication (SFF) techniques allow achieving a high degree of interconnectivity with relatively low porosities, which improves significantly the mechanical properties of the scaffolds. In this study 45S5 and 1393 bioglass scaffolds have been fabricated by robocasting, an additive manufacturing technique that provides a much greater level of control over pore architecture and more regular strut morphologies than in conventional techniques. Developing an ink appropriate for robocasting requires careful tailoring of the viscoelastic properties of the colloidal suspension through precise control of its composition. That is why, despite the great potential of this technique for tissue engineering applications, robocasting inks were not developed for 45S5 bioglass and only through extremely complex recipes for 13-93 bioglass [19]. Here, a new approach has been adopted to prepare the concentrated suspensions required by robocasting from 45S5 and 13-93 bioglass powders.

(ii) Improving the intrinsic properties of the struts. Since rod microporosity reduces the intrinsic strength of the rods—the micropores act as starting flaws for cracking—defect free struts are desirable. In this study, the microstructure of the rods has been tailored by controlling the sintering parameters. Besides, in the case of 13-93 bioglass scaffolds, the influence of powder milling environment on the microporosity in the scaffold rods and on the mechanical performance of the scaffolds has also been investigated.

(iii) Incorporating a polymeric phase. According to previous studies performed in calcium phosphate scaffolds fabricated by robocasting, polymer infiltration increases both strength and toughness of the ceramic structure [20-21]. In this study, besides quantifying the strengthening and toughening achieved in 45S5 and 13-93 bioglass scaffolds upon polymer-melt infiltration with ε-polycaprolactone (PCL) and poly-lactic acid (PLA), the correlation between the flaw population and the mechanical improvement associated to polymer infiltration has been analyzed.

To quantify the mechanical enhancement reached through these approaches, the mechanical performance of the materials developed in this study has been evaluated under compressive and, in some cases, under bending stresses. Also, the effect of the immersion in simulated body fluid in the bioactivity and compressive strength of selected bare 45S5 and 13-93 bioglass scaffolds has been analyzed. The results obtained in this study have been compared to results from the literature and with natural bone properties.

Resumen

En la actualidad se tiende a un nuevo enfoque en el tratamiento de los problemas asociados a la reparación de las lesiones óseas. No se trata ya tanto de "reparar" en el sentido clásico del término, sino de "estimular" los procesos celulares naturales de autoregeneración ósea, para permitir su extensión a defectos de tamaño superior al crítico, de forma que no sean necesarios los tratamientos quirúrgicos sustitutorios. La necesidad de este nuevo enfoque radica en las limitaciones de las dos alternativas actualmente existentes en la práctica clínica: injertos (autólogos o heterólogos) y prótesis.

Aunque es innegable que se han producido avances en estas dos opciones clínicas, ambas presentan aún importantes limitaciones. En el caso del homoinjerto, la disponibilidad limitada de material, y la necesidad de producir una nueva lesión al sujeto, son serios inconvenientes que limitan la extensión de las lesiones susceptibles de reparación por este procedimiento. Los aloinjertos, gracias al desarrollo de los Bancos de Huesos, superan estas limitaciones pero llevan asociados inconvenientes también importantes: posibilidad del rechazo, baja supervivencia celular y riesgo de transmisión de enfermedades víricas del donante. Todo esto hace que las tasas de éxito de este tipo de intervenciones disminuyan notablemente con respecto a los homoinjertos [1].

En cuanto a las prótesis artificiales, si bien algunos materiales biocompatibles han sido ampliamente utilizados con cierto grado de éxito, su efectividad a largo plazo es limitada. Los implantes comúnmente empleados hoy en día presentan una serie de problemas relacionados con su capacidad de fijación y, al contrario que el hueso natural, no tienen la capacidad de autorepararse o adaptarse a las condiciones fisiológicas cambiantes del organismo [2]. Muchos implantes fallan, provocando daño a los tejidos circundantes, debido fundamentalmente a que las propiedades físicas del material difieren considerablemente de las del tejido óseo.

Por todo ello, existe en la actualidad un gran interés en las investigaciones orientadas a mejorar las prestaciones de los implantes, mediante el diseño de materiales artificiales que se asemejen al hueso no sólo en sus propiedades mecánicas sino también en su capacidad de interacción con los tejidos, de manera que induzcan activamente la regeneración ósea. Una manera de conseguir esta interacción con el tejido circundante y

estimular la penetración y el crecimiento celular es utilizar materiales osteofílicos en forma de matriz porosa.

Entre los materiales más utilizados para fabricar estos sustratos porosos (también denominados andamiajes) cabe destacar los polímeros biodegradables como los ácidos poliláctico (PLA) y poliglicólico (PGA), la policaprolactona (PCL), etc. El bajo módulo elástico y la rápida degradación de las propiedades mecánicas de este tipo de sustratos orgánicos limitan su aplicación a regiones del esqueleto donde el hueso no está sometido a fuertes tensiones. También existen sustitutos óseos bioabsorbibles fabricados a partir de materiales inorgánicos de composición próxima a la apatita del hueso natural, que pueden ser disueltos lentamente por los osteoclastos y transformados en hueso vivo. En este grupo de materiales se encuentran diferentes fosfatos cálcicos (hidroxiapatita, fosfato tricálcico, etc.), el sulfato cálcico y ciertos vidrios bioactivos, comúnmente denominados biovidrios.

Los biovidrios se consideran materiales óptimos para la fabricación de andamiajes para ingeniería de tejido óseo por su excelente bioactividad, capacidad osteoconductora y controlable biodegradabilidad [4-6]. Entre todos ellos, el biovidrio 45S5 (Bioglass ®, 45 % SiO_2, 24.5 % CaO, 24.5% Na_2O y 6 % P_2O_5) es el más estudiado y más ampliamente utilizado en aplicaciones biomédicas [7-9], siendo considerado un material de referencia en cuanto a bioactividad y capacidad osteoconductora [10-13]. Sin embargo, a pesar de que durante los últimos 40 años ningún otro fosfato cálcico o biovidrio haya superado la respuesta biológica del biovidrio 45S5 su uso comercial es limitado y los fosfatos cálcicos lideran el mercado de materiales para ingeniería de tejido óseo [9]. Ello es debido a que para obtener un material con densidad y propiedades mecánicas suficientes es necesario sinterizarlo a temperaturas superiores a la de cristalización, lo que reduce su bioactividad [9][14-16]. Otro vidrio de sílice bioactivo que ha suscitado gran interés es el denominado 13–93 que, con una composición modificada respecto al 45S5 (53 % SiO_2, 20 % CaO, 6 % Na_2O, 4 % P_2O_5, 12 % K_2O, 5 % MgO), presenta un comportamiento de flujo viscoso más sencillo y menos tendencia a desvitrificar que éste, aunque a costa de un menor grado de bioactividad asociado a su mayor contenido en sílice.

El principal inconveniente de los materiales vitrocerámicos bioactivos, especialmente cuando se fabrican en forma de estructuras porosas mediante métodos convencionales, es su escasa resistencia a la fractura que, de nuevo, relega su aplicación a regiones de baja carga (por ejemplo, implantes craneales). Uno de los motivos de la escasa

resistencia mecánica de los andamiajes biocerámicos estriba en que la porosidad debe ser interconectada y con un tamaño de interconexión mínimo, para permitir la penetración celular, así como la vascularización y difusión de nutrientes hacia el interior [17-18]. Los métodos tradicionales para la fabricación de sustratos porosos (solvent casting con filtrado de partículas, replicación de esponjas, espumado, freeze-drying, etc.) no permiten controlar de forma precisa la geometría, tamaño y distribución espacial de los poros y, por tanto, para lograr ese grado de interconectividad es necesario producir porosidades muy elevadas.

Para superar estos inconvenientes y desarrollar andamiajes de biovidrio 45S5 y 13-93 con propiedades mecánicas mejoradas, en este trabajo se han seguido tres estrategias:

(i) Optimización de la arquitectura de poros. Las técnicas de prototipado rápido o conformado libre (rapid prototyping o Solid Freeform Fabrication) permiten obtener altos grados de interconectividad incluso con porosidades reducidas, lo que mejora significativamente las propiedades mecánicas de los andamiajes [19]. En este trabajo, se han fabricado andamiajes de biovidrio 45S5 y 13-93 mediante moldeo robotizado, una técnica de fabricación aditiva que proporciona un mayor control de la arquitectura de poros y regularidad en la morfología de las paredes de los poros que las técnicas convencionales. El desarrollo de las tintas para moldeo robotizado requiere adaptar las propiedades viscoelásticas de las suspensiones coloidales mediante el control riguroso de su composición. Por ello, a pesar del gran potencial de esta técnica para fabricación de andamiajes para ingeniería de tejido óseo, no se han desarrollado tintas de biovidrio 45S5 y las que existen de biovidrio 13-93 son extremadamente complejas. En este trabajo, se ha abordado un nuevo enfoque para fabricar tintas para moldeo robtizado a partir de polvos de biovidrio 45S5 y 13-93.

(ii) Mejora de las propiedades intrínsecas de las barras que componen los andamiajes. Dado que la microporosidad reduce la resistencia intrínseca de las barras—los microporos actúan como defectos precursores de la fractura—se prefiere que las barras estén libres de defecto. En este estudio, la microestructura de las barras se ha variado mediante la modificación de los parámetros de sinterización. Además, en el caso de los andamiajes de biovidrio 13-93, se ha analizado la influencia del medio de molienda de los polvos de partida en la microposidad de las barras y en la respuesta mecánica de los andamiajes.

(iii) Incorporación de una fase polimérica. De acuerdo con estudios previos en andamiajes de fosfatos cálcicos fabricados mediante moldeo robotizado, la infiltración con polímero mejora tanto la resistencia como la tenacidad de la estructura cerámica [20-21]. En este estudio, además de cuantificar el aumento de resistencia y tenacidad de andamiajes de biovidrio 45S5 y 19-93 tras ser infiltrado con ε-policaprolactona (PCL) y ácido poliláctico (PLA), se ha analizado la influencia de la población de defectos en la mejora de las prestaciones mecánicas asociada a la infiltración.

Para cuantificar la mejora que se obtiene en las propiedades mecánicas al aplicar las estrategias descritas, se ha determinado la respuesta mecánica de los materiales fabricados bajo tensiones de compresión y, en algunos casos, bajo tensiones de tracción. También se ha analizado el efecto de la inmersión en fluido corporal simulado en la bioactividad y en la resistencia a compresión de determinados andamiajes de biovidrio 45S5 y 13-93. Los resultados obtenidos en este trabajo se han comparado con otros resultados tomados de la literatura y con las propiedades del hueso.

Outline

The manuscript of the present work has been organized as follows:

In chapter 1, an introduction to bioactive glass scaffolds for bone tissue engineering is performed. After a brief account of bone structure and its properties, bioactive glasses and their interaction with surrounding tissues are described, with especial emphasis in the 45S5 and 13-93 compositions.Then the processes for bioglass powders synthesis and for the fabrication/forming of scaffolds including conventional and additive manufacturing methods are briefly reviewed. Especial attention is given to robocasting as the fabrication method selected for this study. The importance of debinding and sintering post-assembly heat treatments is discussed next. And finally, polymer infiltration is proposed as an alternative to improve mechanical performance of bioceramic and bioglass scaffolds for bone regeneration.

Chapter 2 deals with the description of the materials and methods used in this study, including the processes for the fabrication of porous 45S5 and 13-93 bioglass-derived robocast structures and their impregnation with PCL and PLA biodegradable polymers. Besides, the microstructural and mechanical characterization and *in vitro* testing procedures used in this work are described.

Chapter 3 is devoted to the presentation and analysis of the results obtained in the present work. This chapter is divided in three sections. The first two present and analyze the results obtained for each of the two bioglasses studied, 45S5 and 13-93, respectively. Results related to the optimization of the robocasting inks and subsequent sintering step; as well as the microstructural, mechanical and *in vitro* characterization of the bare porous scaffolds; and the microstructural and mechanical characterization of the corresponding polymer-infiltrated structures, are presented for each bioglass. Subsequently, the implications of all these results for biomedical and other engineering applications are analyzed in a final section.

The manuscript ends with a brief summary of the main conclusions derived from this study.

Chapter 1

Introduction: Bioactive glass scaffolds for bone regeneration

1.1   Bone structure and properties

Bone is an open cell composite material composed of inorganic calcium phosphate in the chemical arrangement termed calcium hydroxylapatite, or simply hydroxyapatite (HA), organic molecules such as collagen (an elastic protein which improves fracture resistance) and water (10-20%). The theoretical composition of stochiometric HA is: $Ca_{10}(PO4)_6(OH)_2$ with a corresponding Ca/ P ratio of 1.67 [9]. HA gives bones their rigidity and it comprises 60-70% of its dry mass. Bone is formed by the hardening of the aforementioned composite around entrapped osteoblast cells, which then become osteocytes. Bone comprises two different types of tissue: the outer shell of a given bone is dense and is referred to as *compact* or *cortical* bone, while the inner core is comprised of a porous cellular structure called *cancellous* or *trabecular* bone, as shown in Figure 1.1.
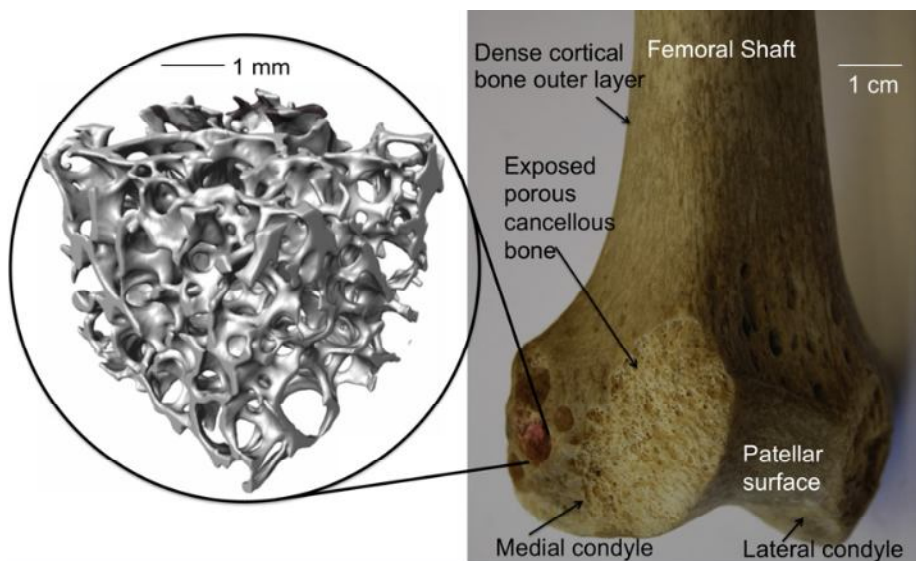
Figure 1.1. The structure of bone [9].

Cortical bone is highly dense (5-10 % porosity) [22-23], wet apparent density of 1.99 g.cm^{-3} [24]) and contains cylindrically organized osteons, also known as Haversian system, with dimensions ranging between 10 to 500 μm. Osteons contain a central

Haversian canal which hosts the blood vessels that keep the tissue alive, running in parallel to the long axis of the bone. These blood vessels are interconnected with vessels on the surface of the bone through perforating canals.

Contrary to cortical bone, cancellous bone is highly porous (typically 75-90 % [22-23], wet apparent density of 0.05-1.0 $g.cm^{-3}$ [25]), consisting of an interconnected network of trabeculae of about 50-300 μm in diameter. The porosity of cancellous bone is the total volume that is not occupied by bone tissue and is usually filled with marrow. The change from compact to cancellous bone is usually clear and takes place over a small distance in which intermediate porosities are found.

Bone is a living material that is continuously regenerated throughout human life. Every year, approximately 10 % of bone mass is renewed in response to the stresses applied to bone itself. The process of bone regeneration involves two types of cells. Osteoclasts that resorbs bone tissue and osteoblasts that synthesize bone. Osteoclasts are produced in the marrow. If osteoclasts are too active, bone demineralizes too quickly, and some serious diseases such as osteoporosis may occur [26]. Demineralization can also occur around stiff bioinert implants. Materials used for orthopedic prostheses have to bear high cyclic loads and are basically selected for their mechanical resistance. Because of the complexity of bone structure, finding a material with a good match to the mechanical properties of is difficult. While polymers exhibit elastic moduli relatively close to bone values, their low strength limits the number of potential applications [27]. Therefore, as a results of the search for strong enough materials, the elastic modulus of inert ceramics or metals used for current orthopedic implants is much higher (at least by an order of magnitude) than that of bone—the mechanical properties of the bone are shown in Table 1-1) [28].

Table 1-1. Summary of the mechanical properties of human bone [28] .

Material property	Trabecular bone	Cortical bone
Compressiv e strength (MPa)	2-12	100-150
Tensile strength (MPa)	1-5	50–151
Compressive modulus (GPa)	0.12–1.1	11.5–17
Young's modulus (GPa)	0.1-5	10-20
Fracture toughness (MPa·m$^{1/2}$)	0.1-0.8	2–12
Porosity (%)	50-90	5-10

This huge mismatch can cause demineralization of surrounding bone. Since the stress imposed by motion and loading is carried by the stiffest component of the system, the bone around the implant becomes subject to load levels substantially lower than in normal conditions. This phenomenon, called stress-shielding, or stress protection, stops bone remodeling [29-31]. Indeed, bone continuously regenerates itself, if sufficiently loaded by cyclic stresses. However, when osteoblast are shielded from normal stress levels by the presence of a stiffer material in contact with bone, their regeneration activity does not occur, and bone weakens at the interface. Therefore, achievinga good match between mechanical properties is a sought after feature for biomaterial for bone replacement or regeneration. Another important property is the ability to form a stable interface between the material and the host tissue. This ability is what makes a material to be called bioactive in the field of orthopedic applications. Among the list of bioactive materials for bone replacement, bioceramic materials such as various calcium phosphates, glass and glass-ceramic compositions can be highlighted. Usually, these materials are used in the form of porous structures, called *scaffolds*, in order to facilitate colonization by cells and tissue ingrowths.

1.2 Bioactive glasses

Since the present work deals precisely with bioactive glass-derived compositions, in this section a brief introduction and review of the state of the art regarding this important group of biomaterials for bone replacement and regeneration is performed.

1.2.1 A brief introduction to glasses

A glass is an amorphous solid material. This means that they do not possess a crystalline structure, instead their atomic structure is similar to that of a liquid, where order exist only over a very short-range (first neighbors) [32-33]. A glass is formed when a liquid is super cooled: in absence of enough sites of nucleation and without enough time to organize themselves, the atoms retain the disordered configuration they had in liquid form. Another typical feature of glasses is that they exhibit over a temperature range, a time dependent transformation called glass transition. The transition comprises, upon cooling, of a smooth increase in the viscosity of a material by several orders of magnitude without any pronounced change in material structure. The consequence of this dramatic increase is a glass (a super-cooled liquid) exhibiting solid-like mechanical properties on the timescale of practical observation. The temperature around which this dramatic transformation takes place is called glass-transition temperature, T_g, and is always lower than the melting temperature, T_m, of the crystalline state of the material, if one exists.

Most glasses are silica-based. In a crystalline silica or quartz, SiO_4 tetrahedrons are organized in a well-defined network. In amorphous silica, SiO_4 tetrahedrons are still linked together, but the angle between them is not constant. The resulting structure is not organized [34], (see Figure 1.2), and it is usually called a random network, and was first hypothesized by Zachariasen in 1932 [35].
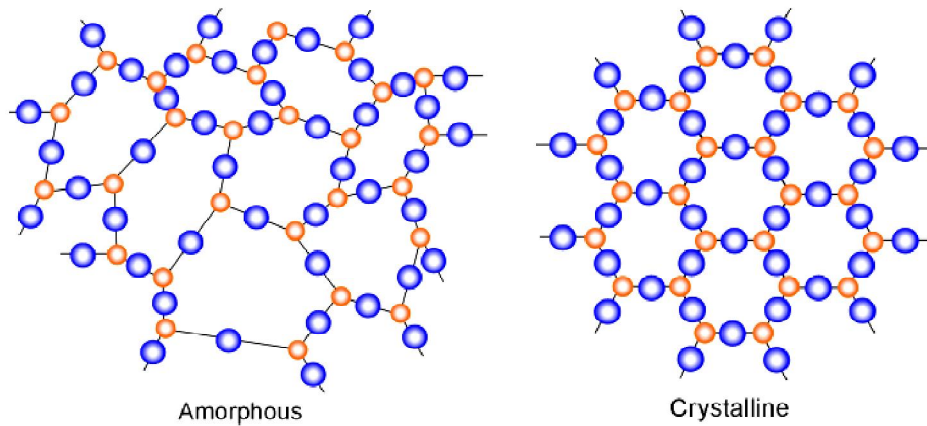
Figure 1.2. Two dimensional models of an amorphous and a crystalline form of silica [34] .

Since glass structure is mostly kept together by SiO_4 tetrahedrons, SiO_2 is called a glass former. Other oxides can be used as glass formers, such as Na_2O, B_2O_3 or P_2O_5. Alkaline and alkaline-earth oxides are added to glass as glass modifiers, which interrupt the network created by the glass former. In pure silica glass (Figure 1.2), all the SiO_4 tetrahedra are linked together, with every *O* atom is linked to a *Si* atom. These *O* atoms are called bridging oxygens (*BO*). When a network-modifier is added to a glass composition, cations interrupt the silica network, and some *O* atoms are no longer linked to Si atoms (Figure 1.3). These O atoms are called non-bridging oxygens (*NBO*) [36].
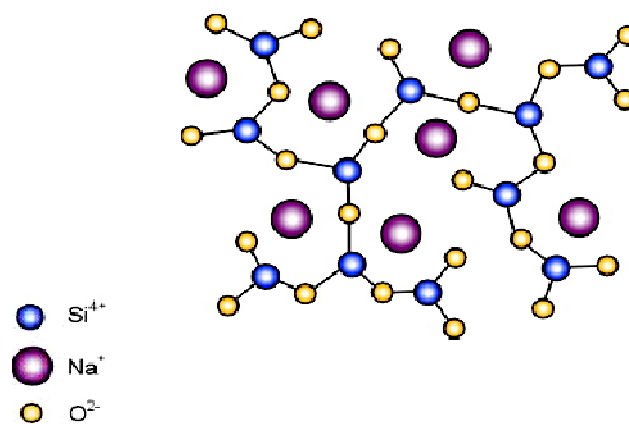
Figure 1.3. The structure of glass after adding Na2O as a network modifier [36] .

1.2.2   Bioglasses

A bioactive glass or bioglass is a type of glass with potential applications as a medical implant material. Bioglasses are designed to be resorbable and slowly replaced by bone in a biological environment. It is obviously a primary requirement for a bioactive glass that it should contain no toxic elements in its composition so that upon dissolution only metabolizable or at least easily excretable substances are released [37]. Apart from this critical requirement, bioactivity is controlled by chemical release kinetics at the surface of bioglass. Too rapid dissolution rates lead to excess concentration of ions, and tissue/implant integration is difficult because of the ever retreating material surface. On the other hand, too slow rates of dissolution make the ionic concentration too low to stimulate cellular proliferation and differentiation.

Bioactive glasses are typically classified in two classes. Class A refers to bioglasses which exhibit both osteoinductive (induce bone formation in locations outside the skeleton, i.e. in heterotopic sites) and osteoconductive (induce growth of adjacent bone along the surface of the material, in orthotopic sites) properties [8][38][39]. Osteoinduction implies the recruitment of immature cells and the stimulation of these cells to develop into preosteoblasts. On the other hand, in class B bioactivity only osteoconduction occurs, which requires only extracellular responses, due to slower interfacial reaction. Table 1-2 summarizes some characteristics of A and B classes of bioactivity [40][41][42].

Table 1-2. *Classification of bioglasses according to bioactivity* [40].

Class A	Class B
Osteoinductive and Osteoconductive	Only osteoconductive
Rapid bonding to bone	Slow bonding to bone
Enhanced bone proliferation	No enhancement of bone profileration
Bonding to soft connective tissues	No bonding to soft connective tissues

The first bioactive glass composition was developed by Hench in the late 1960s and named 45S5 glass or bioglass [9]. Since then, the term bioglass has been extended to refer to all bioactive compositions. 45S5 bioglass after development of 45S5 bioglass, a large series of bioglasses has been developed based on the SiO_2- CaO- Na_2O- P_2O_5 quaternary system. Three key compositional features of these glasses distinguish them from traditional Na_2O-CaO- SiO_2 glasses: (1) less than 60 mol.% SiO_2, (2) high-Na_2O and high-CaO content, and (3) high-CaO/P_2O_5 ratio. These compositional features made the surface highly reactive when exposed to aqueous medium [28].

The chemical composition is indeed one of the key factors affecting the rate of bonding of bioactive glasses. The most rapid rates of bonding for bioactive glasses composed of SiO_2, CaO, Na_2O and P_2O_5 are obtained with SiO_2 contents of 45-52 wt.%. In this compositional range, a bonding both to soft and hard connective tissue occurs within 5-10 days. Bioactive glasses or glass ceramics containing 52-60 % SiO_2 require a longer time to form a bond with bones, and do not bond to soft tissues. Glass compositions with more than 60 % SiO_2 do not bond either to bone or to soft tissues, and elicit formation of a non-adherent fibrous interfacial capsule.

The level of the bioactivity of a bioglass, the bioactivity index (I_B), is defined as the inverse of the time, $t_{0.5}$, required for more than 50 % of the interface to be bonded to bone:

$$I_B = 100/t_{0.5} \quad (days^{-1}) \qquad\qquad (1.1)$$

The compositional dependence of bone bonding and soft-tissue bonding for the Na_2O- CaO- P_2O_5- SiO_2 glasses (at constant 6 wt.% of P_2O_5) is presented in Figure 1.4.
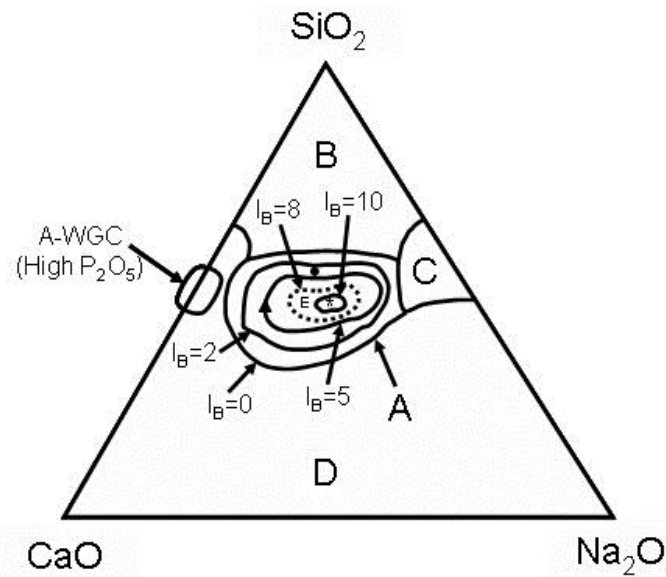
Figure 1.4. Different bioactive regions in the CaO-SiO$_2$-Na$_2$O system. All glasses have 6 wt.% P$_2$O$_5$. Region E is a region of Class A bioactivity where bioactive glasses bond to both bone and soft tissues and are gene activating [43].

Glasses in different regions in this phase diagram exhibit different behaviors nupon implantation. Silicate glasses within region *A* form a bond with bone. Silica glasses within region B (such as bottle, window or slide glasses of microscope) behave as nearly inert materials and elicit a fibrous capsule at the implant-tissue interface. Glasses within region C are resorbable and disappear within less than 1 day of implantation. Glasses within region D are not technically realistic and have not been tested as implants. Therefore, the line delimiting region A is termed as the bioactive-bone bonding boundary. As the composition gets closer to the center of region *A* bioactivity increases. The collagenous constituent of soft tissues can strongly adhere to the bioactive silica glasses which lie within the compositional range marked as region *E* within region *A*. Therefore, the dotted line delimiting region E in Figure 1.3, corresponding to $I_B = 8$, marks the limit dividing bioglasses in the aforementioned classes A and B [43].

1.2.2.1   45S5 bioglass composition

The chemical composition of 45S5 bioglass is 45 wt.% SiO_2, 24.5 wt.% CaO, 24.5 wt.% Na_2O and 6 wt.% P_2O_5. The name "45S5" refers to the glass composition: 45S indicates the 45 wt.% silica content, and the final 5 indicates the Ca/P molar ratio of this glass composition [38][44].

45S5 bioglass like other bioactive silica based glasses presents an open structure which enables the accommodation of alkali cations. These network modifiers (Na^+, K^+) disrupt the continuity of the glassy network by breaking the Si–O–Si bonds, which leads to the formation of non-bridging oxygen groups (Si–O–NBO) [45]. This is key to the bioactive process, because the concentration of Si–O–NBO groups controls the dissolution rate of the silica in aqueous environments through the formation of silanol (Si–O–H) groups at the glass surface [46]. Besides, the presence of Na_2O or other alkali cations in the glass composition generally increases the solution pH at the implant-tissue interface and thereby enhances the precipitation and crystallization of HA [47]. On the other hand, the presence of Ca^{2+} and P^{5+} ions is essential since they are the two main elements presented in HA composition. Besides, Ca^{2+} also acts as a network modifier and increases the rate of dissolution of 45S5 bioglass. Consequently, the combination of high Na_2O and CaO content and high CaO/P_2O_5 ratio makes the surface of this glass highly reactive [48].

45S5 bioglass is the most widely studied bioactive glass: it exhibits high bioactivity ($I_B = 10$) and easily bonds to both hard and soft tissues [8], thus belonging to Class A bioglasess [4][43].

1.2.2.2   13-93 bioglass composition

The chemical composition of 45S5 bioglass is 53 wt % SiO_2, 6 wt % Na_2O, 12 wt % K_2O; 5 wt % MgO, 20 wt % , CaO, and 4 wt % P_2O_5 has a silicate-based composition..

Glass with the 13–93 composition are prepared by melting a mixture of the appropriate quantities of analytical grade Na_2CO_3 K_2CO_3, $MgCO_3$, $CaCO_3$, SiO_2, and $NaH_2PO_4.2H_2O$ in a platinum crucible at 1300 °C and quenching between cold stainless steel plates. The glass are crushed in a hardened steel mortar and pestle and classified using stainless steel sieves to provide glass particles [49].

1.3   Bioglass/tissue interfacial interaction

Generally, the interfacial reaction of class A bioactive glasses upon insertion in the body is described to occur in 12 stages. Stages 1-5 occur on the material upon interaction with surrounding aqueous media and can be reproduced *in vitro* by immersion in a *Simulated Body Fluid* (SBF). The first five stages happen rapidly on the surface of most bioactive glasses because of fast ion exchange of alkali ions with hydrogen ions from body fluid. Figure 1.5 illustrates these initial stages, which are also briefly described below:
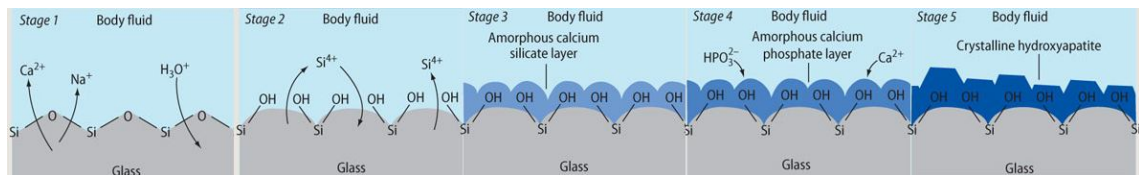
Figure 1.5. The schematic illustration of interfacial reaction between bioglass and simulated body fluid (SBF) resulting in HA formation [50].

Stage 1: A rapid exchange of cations present in the bioglass (Ca^{2+}, Na^+, K^+) with H^+ or H_3O^+ from solution occurs:

$$Si\text{-}O\text{-}Na + H^+ + OH^+ \rightarrow Si\text{-}OH + Na^+ \ (solution) + OH$$
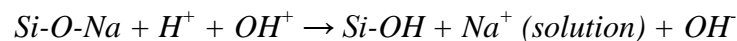
The weak ionic bonding, especially of the alkali ions gives rise to a very rapid ion exchange. Eventually the pH of solution increases as a result of H^+ consumption in the solution [51]. Stage 1 is usually controlled by diffusion and exhibits a $t^{-1/2}$ dependence on time.

Stage 2: The pH increase (i.e. the increased the concentration of hydroxyl groups) leads to attack of the silica glass network producing additional silanol formation and controlled interfacial dissolution [9]:

$$2(Si\text{-}O\text{-}Si) + 2(OH) \rightarrow Si\text{-}OH + OH\text{-}Si$$
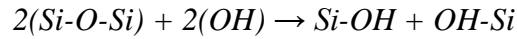
This stage is usually controlled by interfacial reactions and exhibits linear time dependence.

Stage 3: *SiOH* repolymerizes and forms a *Si-O* network. The resulting amorphous silica gel is depleted in alkaline earth cations.

$$2(Si\text{-}OH) + 2(OH\text{-}Si) \rightarrow \text{-}Si\text{-}O\text{-}Si\text{-}O\text{-}Si\text{-}O\text{-}Si\text{-}O\text{-} + 2H_2O$$
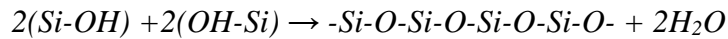
This process is again controlled by interfacial reactions and exhibits linear time dependence.

Stage 4: Ca^{+2} and PO_4^{-} ions from the media migrate to the surface of the silica gel layer and form a $CaO\text{-}P_2O_5$-rich amorphous film on top of it.

Stage 5: Finally apatite (HA) crystals nucleate and grow from the amorphous calcium phosphate layer [6] Incorporation of OH^- and CO_3^{-2} or F^- anions from solution can simultaneously occur giving the typical compositional variances observed in natural apatites (hydroxyl, carbonate, and fluor-apatite). The HA layer nucleates as extremely small 100-600 Å platelets and therefore has a very large surface area [52]. It has been shown that new HA will form not only directly on the surface of silica gel, but also on the surfaces or interfaces of growing apatite crystals [53].

but stages 6-12 happen on tissue side of interface [54] The surface reactions lead to the biochemical adsorption of growth factors (stage 6) and the synchronized sequence of cellular events (stages 7-12) that result in rapid formation of new bone. Generally, the rapid attachment, proliferation and differentiation of osteoblast progenitor cells are the critical steps of new bone formation [55].

Summarizing, the five stages are: (1) silanol groups formation, (2) network dissolution, (3), silica-gel polymerization, and (4) chemisorptions and (5)

crystallization of apatitic layer. After apatite formation has occurred the process of bonding to bone tissue can start. This process comprises seven stages that are briefly described below [40]:

Stage 6:   Adsorption and desorption of biological growth factors in HA layer to activate differentiation of stem cells (this stage will continue throughout the process).

Stage 7:   Action of macrophages to remove debris from the site, allowing cells to occupy the space.

Stage 8:   Attachment of stem cells on the bioactive surface.

Stage 9:   Differentiation of stem cells into bone forming cells, osteoblasts.

Stage 10: Generation of extracellular matrix by osteoblasts to form bone.

Stage 11: Crystallization of inorganic calcium phosphate matrix to enclose bone cells in a living structure.

Stage 12:   Bone growth.

1.3.1   In vitro evaluation of bioactivity of 45S5 and 13-93 bioglasses

Immersing biomaterials in simulated body fluid (SBF)—with ion concentrations nearly equal to those of human blood plasma— is a useful method for simulating *in vivo* conditions in order to evaluate their biological properties. These type of *in vitro* studies were done for the first time 20 years ago by Kokubo [56-57]. In comparison with *in vivo* studies, *in vitro* tests are faster, cheaper and rise lower safety and ethical concerns [58-59]. The bone-bonding ability of a material is often evaluated by examining the ability of apatite to form on its surface upon immersion in a SBF. However, the validity of this method for evaluating bone-bonding capacity is still a subject of debate [60].

In vitro responses of bioactive glass scaffolds are dependent primarily on the glass composition and the architecture of the scaffolds. Here we briefly review existing

evidences of *in vitro* apatite formation ability for the two bioglass compositions of interest.

Figure 1.6 shows the XRD spectra of 45S5 bioglass scaffolds sintered at 1000 °C for 1 h and then immersed in SBF for up to 4 weeks, as well as the XRD patterns of as-received glass and the as-sintered scaffolds. Before immersion in SBF, the sample sintered at 1000 °C for 1 h exhibits sharp diffraction peaks, most of which were identified as corresponding to the majority $Na_2Ca_2Si_3O_9$ phase [61] (see section 1.7.2.1). The crystallinity of the sintered scaffolds decreased with immersion time, confirming that 45S5 bioglass-based glass–ceramic scaffolds decompose into an amorphous calcium phosphate upon immersion in SBF. After immersion in SBF for just 3 days, diffraction peaks of the HA phase are already apparent and after soaking in SBF for 28 days immersion the material was mainly composed of an amorphous phase and crystalline apatite [62].
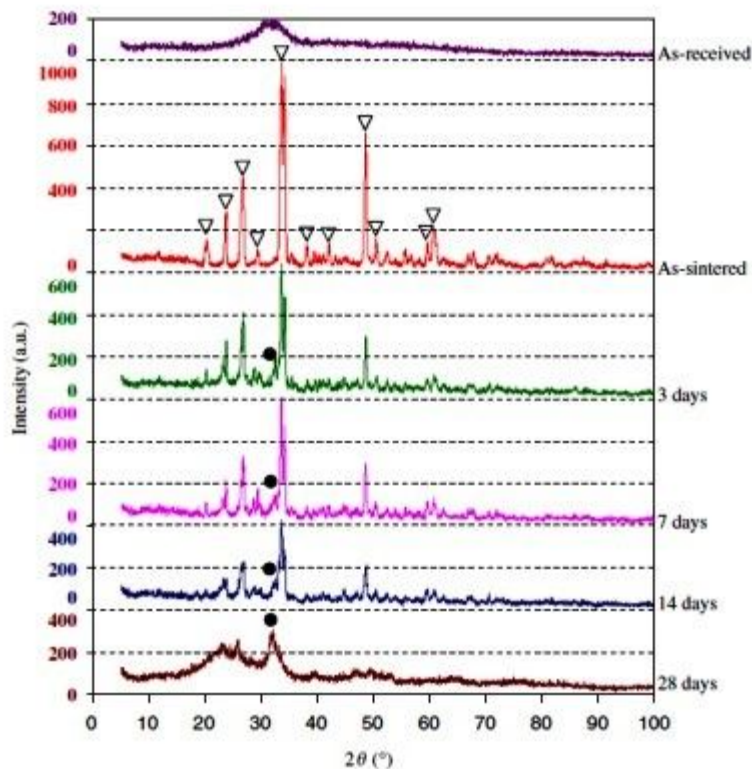
Figure 1.6. XRD spectra of 45S5 bioglass-based scaffolds sintered at 1000 °C for 1 h, and immersed in SBF for 3, 7, 14, and 28 days. The major peaks of $Na_2Ca_2Si_3O_9$ phase and hydroxyapatite are marked by (∇) and ($\bullet$), respectively [62].

13-93 bioglass scaffolds also exhibit apatite formation in SBF. Figure 1.7 shows the XRD patterns for as-sintered 13-93 glass and for the material after immersion in SBF. The sintered 13-93 scaffolds preserve the state after sintering (XRD pattern in Figure 1.7d). This XRD pattern is typical of an amorphous glass. After immersion in SBF for 7 days, peaks corresponding to those for a standard HA were superposed to the broad amorphous band centered at $2\theta = 30$. The peaks appeared in the sample soaked in SBF occurred at approximately the same 2θ values like those. The broad aspect of these peaks was quite similar to those observed in human trabecular bone, and indicates the presence of nanometric crystals [63-64].
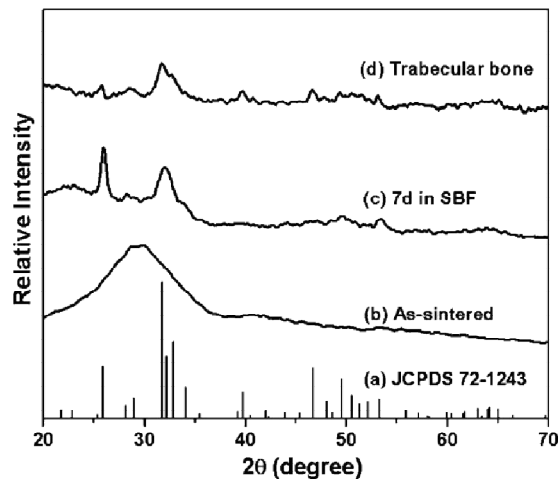
Figure 1.7. X-ray diffraction patterns of: (a) reference hydroxyapatite; (b) porous 13–93 glass scaffold in the as-sintered condition; (c) sintered 13–93 glass scaffold after immersion in a simulated body fluid for 7 days; and (d) human trabecular bone [63].

Figure 1.8 shows SEM images of the fine particulate apatite layer formed on the surface of a 13–93 bioglass scaffold after immersion in an SBF for 7 days. High-resolution SEM images (Figure 1.7c) shows that the surface is covered with a porous network of nanometer-sized, needle-like apatite crystals. Similar formations can also be observed in 45S5 bioglass after immersion in SBF.
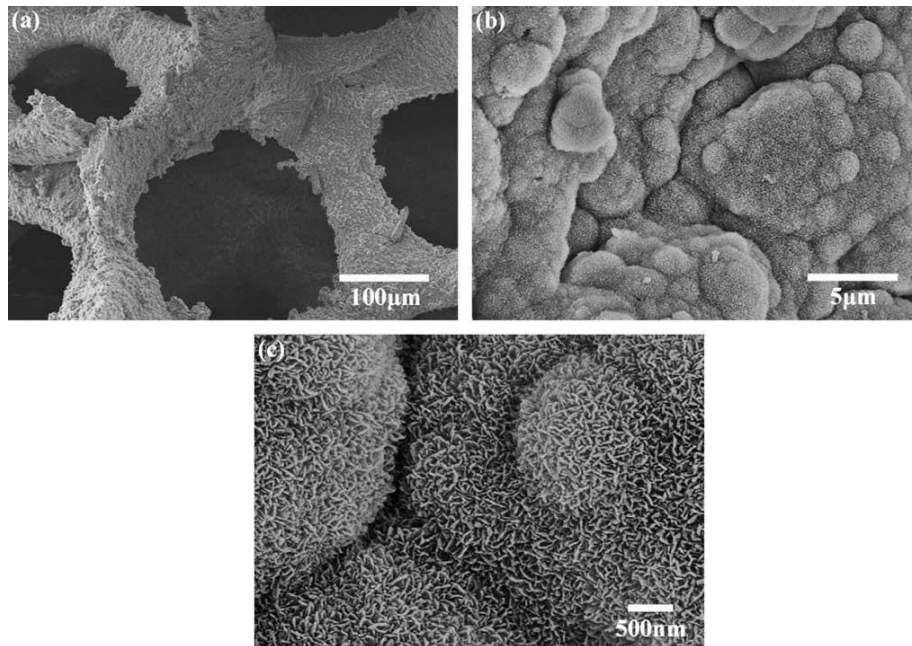
Figure 1.8. SEM images of the surface of the 13–93 glass scaffold after immersion for 7 days in SBF: (a) lower magnification image; and (b, c) higher magnification image showing fine needle-like hydroxyapatite crystals [63].

1.4 Synthesis of bioglass powder

In this section, we review the most common routes for synthesizing bioactive glass compositions. Since, as will be discussed later, most fabrication methods of porous scaffolds require the use of material in powder form as feedstock, we will describe the processes leading to the production of such bioglasses in powder form.

1.4.1 Melt derived bioglass

Mixing and melting the starting materials is the traditionally, method for manufacturing most kinds of glasses and glass ceramics. For example, since 45S5 bioglass has a melting point around $T_m = 1450$ °C, temperatures higher than this value are required for its production.

The glass formation process starts by mixing different kinds of oxides and carbonates at high temperature in a crucible. This process, when performed in oxidating atmosphere as is usual removes carbon in the form of CO_2 and CO. After a

homogeneous melt is produced, the material is quenched in water. The cooling rate should be high enough that crystals do not have time to form. As a result of this rapid cooling, relatively large glass particles called *frits* can be formed. When finer powder is required, frits are grounded by dry or wet milling processes, usually followed by sieving.

When preparing bioactive glass compositions the process has some specific features. Due to the high purity required for optimal bioactivity platinum crucibles have to be used, which considerably increases production costs [65-66]. Even so care need to be taken since due to the high temperatures involved the components (especially alkaline ions) tend to dissolve in the platinum crucible during melting. Care should be taken also during grinding and sieving processes that expose the powder to potential contaminants which can have a negative effect on bioactivity.

1.4.2   Sol-gel derived bioglass

Another method for manufacturing bioglasses is sol-gel. The sol-gel process involves the transition of a system from a liquid (sol) into a solid (gel) phase, followed by the removal of the initial solvent. The chemistry involved in the process is based on inorganic polymerization reactions of metal alkoxides [67-70]. This procedure was developed for processing of oxide materials more than 50 years ago. Since then, this technique has been extensively used not only for the production of oxide materials, but also of non-oxides such as nitrides and carbides [71-72].

Bioglass powders prepared by sol-gel have higher surface area than melt-derived glasses because of the porous 3D network of the precursor gel which is completely interpenetrated by liquid. This high surface area makes the material even more bioactive. The chemical composition and stabilization temperature are the main synthesis conditions that define the final size of the powder, and the network connectivity, textural properties and conformational structure of the glass. By changing the processing conditions, very wide ranges of porosities and compositions can be obtained [38][66][73]. Despite the aforementioned advantages, the low yield of sol-gel processes and the relatively high cost of starting alkoxydes may be the reason why this type of bioglass powders, although extensively used in research, are not yet commercial available.

1.5   Scaffold fabrication

As mentioned before, bioactive materials are usually employed in the form of porous scaffolds in order to facilitate colonization by cells and eventually produce the regeneration of the damaged tissue. In this section, the main requirements for a successful bone tissue engineering scaffold and the most common scaffold fabrication methods are reviewed. Especial attention is given to reviewing the fabrication of 45S5 and 13-93 bioglass scaffolds by either conventional fabrication or additive manufacturing techniques.

1.5.1   Requirements for bone tissue engineering scaffolds

Scaffolds are basically a supporting structure, but ideally should also provide the chemical, mechanical, and biological environment to facilitate tissue regeneration [74-75]. Scaffolds for tissue engineering should fulfill the following requirements:

1) Biocompatibility: The most basic feature of any scaffold used for tissue engineering is that it must be biocompatible. After implantation, the scaffold or tissue engineered construct must elicit a negligible immune reaction in order to prevent it from causing a severe inflammatory response that might impede healing or cause rejection by the body [76-77].

2) Osteoconductivity: The scaffold material should able to serve as a template for bone formation by encouraging cells to colonize its surface, to proliferate and to produce new bone [78].

3) Biodegradability: The scaffold material should be able to degrade over time *in vivo* to allow cells to produce their own extracellular matrix [75][79].

4) Scaffold architecture: The architecture of scaffolds used for tissue engineering is another critical issue if cells have to penetrate the structure to produce tssue ingrowth. In this sense, pore architecture becomes paramount. The amount of porosity and, especially, the pore size of the supporting three-dimensional structure have been shown to affect the regeneration of specific tissues aided by synthetic

materials. optimum pore size is around 5 μm for neovascularization, 5–15 μm for fiberblast ingrowth, close to 20 μm for the ingrowth of hepatocytes, 20–125 μm for the regeneration of adult mammalian skin, 40–100 μm for osteoid ingrowth [78] and 100–350 μm for regeneration of bone [80]. Fibrovascular tissues appear to require pores sizes greater than 500 μm for rapid vascularization and for the survival of transplanted cells [81]. An ideal bone tissue scaffold should also possess a well interconnected porous structure, i.e., it should be highly permeable   This is required to ensure cellular penetration and adequate diffusion of nutrients to cells within the construct, and   the excretion of waste products resulting from cells activity and scaffold degradation out of the scaffold [80-82].

5) Mechanical integrity: The scaffold should have the mechanical performance needed to ensure it maintains mechanical integrity during surgical implantation and to replace bone function during most of the healing process. This is a especially harsh requirement in the reconstruction of hard, load-bearing tissues. The mechanical stability of the implant/tissue system depends on factors such as the materials' strength, modulus, toughness, and the rates of absorption at the material interface and chemical degradation [83]. It is worth mentioning that, higher scaffold porosity results in diminished mechanical properties, thereby setting an upper functional limit for pore size and porosity. Also, a balance must be reached between the rate of remodeling and rate of degradation of the scaffold material to ensure the mechanical integrity. The need to keep mechanical integrity is indeed the major hurdle in the design of tissue engineering scaffolds, since mechanically strong materials are usually bioinert, while degradable materials tend to be mechanically weak.

6) Manufacturability: Finally, the scaffold material should by easily manufactured into practical products. To make a particular scaffold or tissue engineered construct become clinically and commercially viable, the manufacturing process should be flexible and cost effective [84-85].

1.5.2   Conventional scaffold fabrication techniques

Conventional techniques can build scaffolds with interconnected porous structures. However, they are incapable of precisely controlling pore size, pore geometry, pore interconnectivity, and spatial distribution of pores. The following subsections review a few of the most significant methods within this family.

1.5.2.1   Gas foaming

This method was originally developed for fabrication of polymeric scaffolds. In this method molded biodegradable polymers are pressurized at high pressures with gas-foaming agents, such as CO_2 and nitrogen [86], water [87], or fluoroform [88], until the polymers are saturated. The removal of the high pressure results in nucleation and growth of gas bubbles with sizes ranging between 100 and 500 μm in the polymer. This technique has the advantage of being an organic solvent-free process and the main weakness is that the process may yield a structure with largely unconnected pores and a non-porous external surface [89].
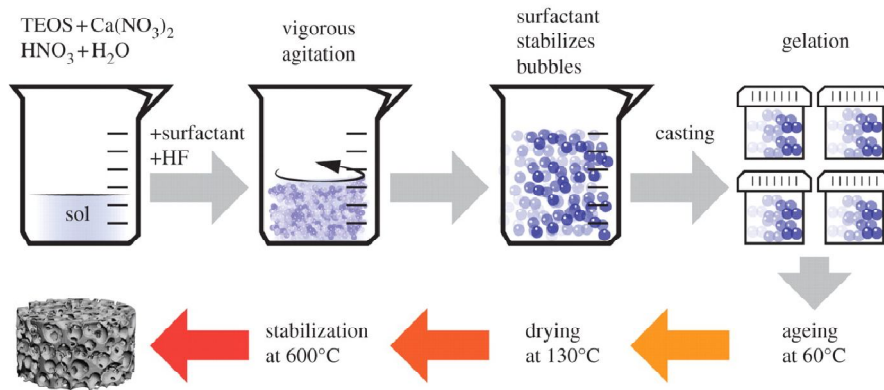
Figure 1.9. Schematic of the sol–gel foaming process [90].

Bioactive glass scaffolds have been prepared by an analogous method (the schematic is shown in Figure 1.9), which typically involves the foaming of a sol with the aid of a surfactant, followed by condensation and gelation reactions, as described for the glasses

designated 58S and 70S30C [90-91]. The gel is then subjected to aging processes to strengthen it, drying to remove the liquid byproduct, and sintering to form porous, three-dimensional scaffolds. These scaffolds consist of both interconnected macropores (10–500 μm) resulting from the foaming process (Figure 1.10), and mesopores (2–50 nm) that are inherent to the sol–gel process [70][92-94].
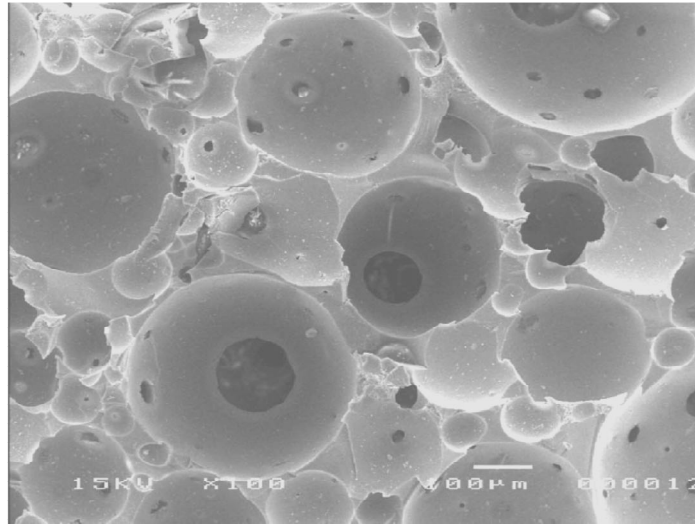
Figure 1.10. SEM micrograph of a typical pore network within a 58S bioactive foam glass scaffold [91].

This porous structure is considered to be beneficial for stimulating the response of cells to the scaffold. These macro-porous glasses have shown favorable results in both *in vitro* and *in vivo* tests for bone regeneration [95-96]. However, although sol–gel foaming scaffolds show appropriate biological properties, they have low strength (0.3–2.3 MPa) due to their large volumetric porosities and consequently they are suitable for substituting defects in low-load sites only [94].

1.5.2.2 Freeze drying

A schematic of this method for the fabrication of polymeric porous scaffold is shown in Figure 1.11. A polymer solution is cooled down to a specific temperature at which all materials are in a frozen state and the solvent forms ice crystals, forcing the

polymer molecules to aggregate into the interstitial spaces. In the second phase, the solvent is removed by applying a pressure lower than the equilibrium vapor pressure of the frozen solvent. When the solvent is completely sublimated, a scaffold with an interconnected porous microstructure remains [97]. The porosity of the scaffolds depends on the concentration of the polymer solution; pore size distribution and morphology is affected by the freezing temperatures and cooling rate. Apart from fabricating porous scaffolds, this technique is also used to dry biological samples to protect their bioactivities [98].
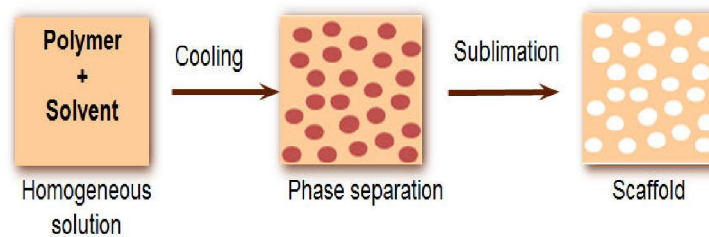
Figure 1.11. Schematic of fabrication of polymeric scaffold by freeze drying [97].

Similarly, for the production of porous glass and ceramic scaffolds, the freeze casting route involves rapid freezing of colloidally-stable suspension of particles in a nonporous mold, and sublimation of the frozen solvent under cold temperatures in a vacuum. After drying, the porous constructs are sintered to remove the fine pores between the particles in the walls of the macropores, which results in an improvement in the mechanical strength. Directional freezing of the suspensions leads to growth of the ice in a preferred direction, resulting in the formation of porous scaffolds with an oriented microstructure. The technique has been used to produce porous scaffolds of Alumina, Zirconia, CaP, HAp, HAp/ TCP [99- 106].

A benefit of the oriented microstructure is higher scaffold strength —e.g. up to four times higher in the case of Hydroxyapatite scaffolds—in the direction of orientation, compared to the strength of a scaffold with a randomly oriented microstructure [107-108]. These strengths allow their consideration for load-bearing applications. However, most oriented scaffolds prepared from aqueous suspensions typically have a lamellar microstructure with a pore width in the range of 10–40 μm, which is considered to be too small to support tissue ingrowths.

Both 45S5 and 13–93 glass scaffolds have been prepared using freeze drying technique[109][110]. In addition to the higher strength of these scaffolds achieved due to oriented columnar structure, these bioactive glass scaffolds have also shown the ability to support cell proliferation and differentiation *in vitro* as well as tissue infiltration *in vivo* [110-111]. Nonetheless, it is worth mentioning that while textured microstructures enhance strength along determined orientations, they simultaneously weaken the material in other directions, which seriously limits their application in regions subject to multiaxial loading.

1.5.2.3   Foam replication technique

The foam or sponge replication technique is a process originally developed for the manufacture of ceramic foams in 1963 [112] and has been extensively used to fabricate scaffolds. The process is shown schematically in Figure 1.12 [113].
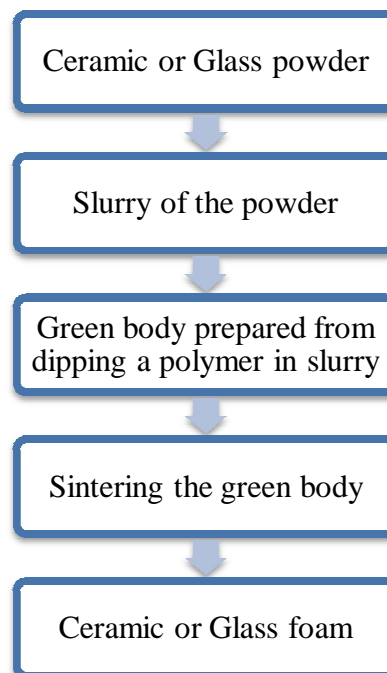
Figure 1.12. The flowchart of traditional foam replication method [113].

According to the process flowchart, the green body is prepared by immersing a synthetic or natural foam template in a ceramic or glass slurry which subsequently

infiltrates the structure producing a homogeneous coating of particles on the surface of the polymer substrate. After drying the coated foam, the polymer template and any organic binders used to prepare the slurry are burned out through careful heat treatment, typically between 300 and 600 °C, and the ceramic or glass struts are densified by sintering at appropriate temperature. For most bioglasses the sintering temperature is around 600–1000 °C, depending on the composition and particle size of the glass [113].

The main advantage of this method is the production of highly (40–95 %) porous glass/ceramic scaffolds with open and interconnected porosity that resembles that of cancellous bone. The external shape and the microstructure of the scaffold replicate those of the porous polymer (generally polyurethane) foams serving as templates. Therefore, different pore sizes and geometries can be achieved by using appropriate polyurethane foams, as shown in Figure 1.13. Additionally, the foam replication technique does not involve the use of toxic chemicals and is rapid and cost effective. The weakest point of foam replication technique is that the strength of the initial green body and of the final scaffold is low. Therefore, handling of the green body is difficult and the strength of the final scaffold is typically in the range reported for cancellous bone, which limits its use to the repair of non load-bearing bones. This method has been used for fabricating scaffold from a wide variety of ceramic materials including HAp [114-115], TCP [116-117] and silicate, borosilicate, and borate bioactive glasses [118- 121], including 45S5 [62] [122] and 13-93 bioglass [63].
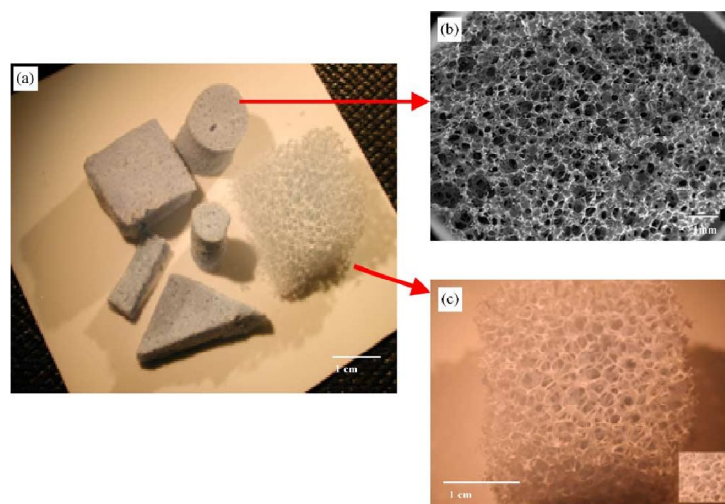
Figure 1.13. Optical microphotographs of (a) HA scaffolds of different shapes; (b) and (c) macroporous structures of HA scaffolds fabricated using polymer sponge methods [114].

Figure 1.14a shows that the microstructure of the polyurethane foam is obviously similar to that of a sample of dry human trabecular bone (Figure 1.14b).

The microstructure of a fractured cross-section of the 13–93 glass scaffold (Figure 1.14c and d) consisted of a dense network of glass and interconnected cellular pores.
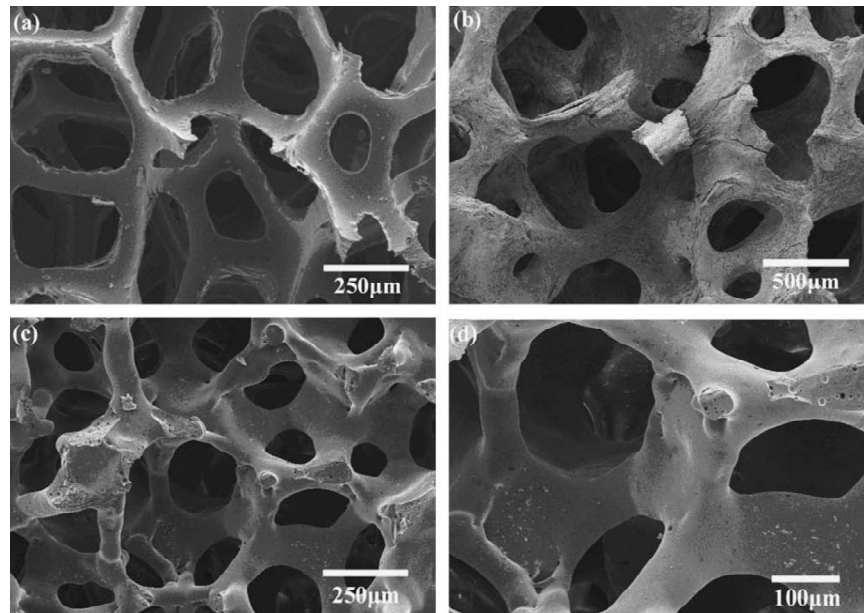
Figure 1.14. Microstructures of: (a) polyurethane foam (b) dry human trabecular bone; and (c, d) 13–93 glass scaffolds fabricated by polymer foam replication [63].

1.5.3   Additive manufacturing methods

As an alternative to conventional scaffold fabrication methods, additive manufacturing (AM), also referred to as rapid prototyping (RP) or solid freeform fabrication (SFF) or 3D printing (3DP), techniques have received significant attention in the field of tissue engineering [123]. Additive manufacturing technologies are a common name for a number of advanced fabrication techniques that can be used to produce objects layer-by-layer from a computer aided design (CAD) model, without using traditional tools such as dies or molds [124]. These techniques can be used also to build scaffolds whose porous structure follows a predesigned architecture modeled on a

computer. In that way, the scaffold architecture can be controlled and optimized to achieve the desired mechanical response, and accelerate the bone regeneration process [125]. Moreover, by using data from medical scans (magnetic resonance imaging, tomography techniques, etc.) to create the CAD model, it is possible to produce customized scaffold that fit the patient's lesion.

Additive manufacturing was used for the first time in the early 1980s to fabricate automotive engine parts and small telecommunication industry components. However, it took until the 1990s before rapid prototyping techniques were adapted into the medical and biomedical fields [126]. Over the past two decades more than 20 additive manufacturing techniques have been developed and commercialized. Basically, these methods can be classified into three basic types: liquid based, solid-based and powder-based rapid prototyping systems [127].

In the following sections a few additive methods which have been used in the preparation of tissue engineering scaffolds from bioactive glasses are reviewed and their typical features, characteristics and processing limitations with regard to tissue engineering are highlighted.

1.5.3.1   Stereolithography

Stereolithography (SLA or SL) is an additive manufacturing technology that produces the parts by curing a photo-reactive resin with a UV laser or another similar power source.

The scheme and fabrication process of 3D scaffolds in SLA are shown in Figure 1.15. The CAD-file describes the geometry and size of the parts to be built. For this, the STL file format was developed. The STL file lists the coordination of triangles that together make up the surface of the designed 3D structure. This designed structure is virtually sliced into layers of the thickness that is used in the layer-by-layer fabrication process (usually in the range of 25-100 μm). These data are then uploaded to the SLA apparatus and the structure is fabricated [128] . After an UV laser produces the photo-polymerisation of the first layer, the platform is moved away from the surface and the built layer is recoated with liquid resin to repeat the process. After draining and washing-off excess resin, the green structure is obtained.
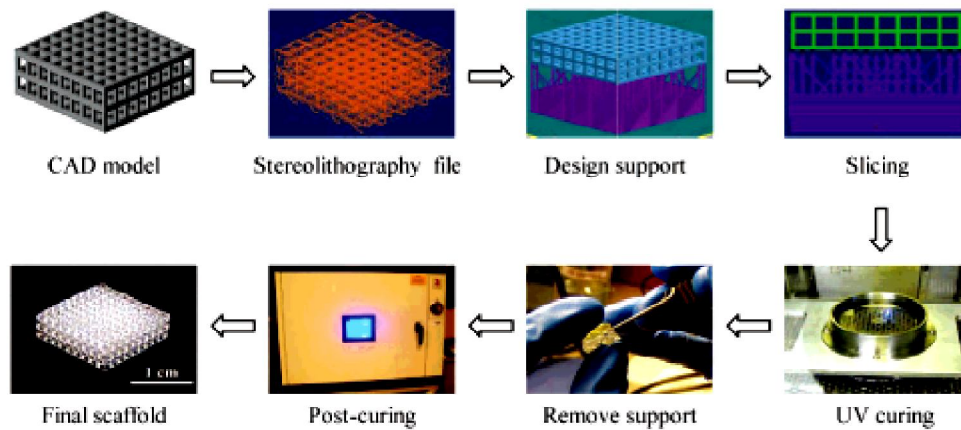
Figure 1.15. Schematic of the CAD model preprocessing and stereolithography fabrication of 3D scaffolds [129].

The green structure is obtained after draining and removing excess resin. In order to improve mechanical properties of the structures a post-curing with ultraviolet light is often done [129]. The stereolithography is one of the most powerful and versatile fabrication methods among all SFF techniques. It has the highest fabrication accuracy and an increasing number of materials that can be processed with. When printing ceramic or glasses the photo-curable resin has to be eliminated and a sintering treatment has to be used to consolidate the part. The main advantages of SLA technique are its high reproducibility and high resolution (down to 200 nm when two-photon polymerization is used), which enable the fabrication of parts with very small features [130].

In the biomedical field, SLA has been used to fabricate moulds for the preparation of heart valves, ear-shaped implants, aortas and hearing aids [130-133]. The main limitation of this technique is the scant number of available resins exhibiting appropriate biocompatibility and biodegradability. Most of the resins used for SLA are conventional epoxy resins, thermoplastic elastomers, and poly (ethylene glycol) (PEG)-based hydrogels. The aforementioned polymers have limited application in bone tissue engineering are lacking either biodegradability or sufficient mechanical strength. Alternatives such as is poly (propylene fumarate) (PPF) and diethyl fumarate (DEF) have been developed to overcome these limitations. Figure 1.16a and b show prototypes

fabricated by SLA using PPF and poly(ethylene glycol)/poly(D,L-lactide)(MA-PDLLA-PEG-PDLLAMA) based resins [128-129][134].
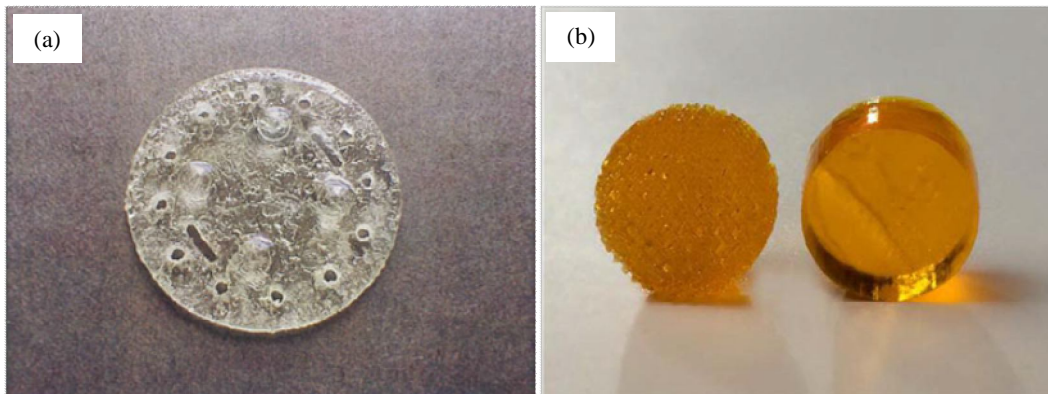
Figure 1.16. Photographs of (a) PPF/DEF and (b) MA-PDLLA-PEG-PDLLAMA prototype parts fabricated by SLA [147][153].

The implantation of devices prepared by SLA has only been reported in a few cases. Degradable cross-linked structures prepared by SLA using poly(trimethylene carbonate-co-ε-caprolactone) resins caused no adverse effects after a 1 month of implantation period under the dorsal skin of rats [134-135]. Also, non-resorbable polyacrylate and hydroxyapatite composite parts have been fabricated and implanted into the femurs of rats for time periods of up to 8 weeks [136].

45S5 bioglass has been hired recently in a lithography-based AM technique called Digital Light Processing (DLP). By using DLP cellular structures such as those shown in Figure 1.17 were produced from a 45S5 bioglass slurry (43% of solid loading) containing an acrylate-based monomer, an organic solvent (polypropylene glycol), a light absorber and a photo initiator [137]. These structures have a porosity around 50 % and showed a compressive strength of 0.33 MPa, which is even lower than the strength of porous 45S5 bioglass structures made by the foam replica method with much higher volumetric porosities [62].
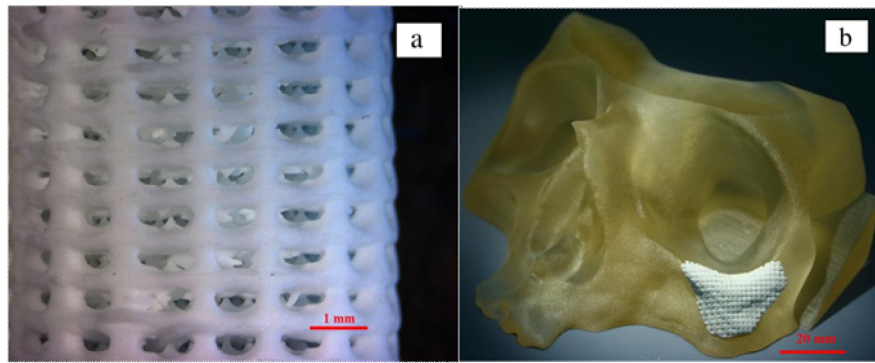
Figure 1.17. 45S5 bioglass parts fabricated by lithography-based DLP after sintering: (a) cylindrical cellular structure and (b) customized bone implant [137].

1.5.3.2 Selective Laser sintering

Selective Laser Sintering (SLS) is one of the most widely used rapid prototyping processes that have appeared in the last two decades [138]. SLS is an AM process that allows generating complex 3D parts by consolidating successive layers of powder material by sintering selected areas using the thermal energy supplied by a focused laser beam. [139-142]. Consolidation mechanisms involved in SLS can be solid state sintering, liquid phase sintering, partial melting, full melting or chemically induced binding [143-144].After one layer of powder is selectively sintered, a new layer of powder is spread on top to repeat the process. The preprocessing of the part model is similar in all other aspects to that described for SLA (Figure 1.15).

Figure 1.18 shows a schematic example of an SLS system. Existing commercial SLS systems differ in the way the powder is deposited (roller or scraper), the atmosphere (Ar or N_2) or the type of laser they use [145].
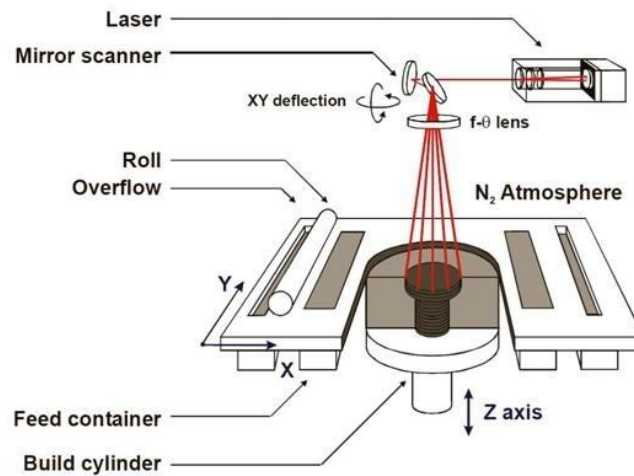
Figure 1.18. Basic layout of a selective laser sintering system [145].

SLS has the potential for building the parts in a wide range of materials, including polymers, metals and various types of composites. Theoretically, SLS can be applied for fabrication of the structures from any materials in powder form but practically because of limitations on laser sources, reaching full consolidation is not always attainable, especially in the case of ceramics. Nevertheless, a wide range of biocompatible and biodegradable materials has been processed by SLS for fabrication of tissue engineering scaffolds [146-147]. Among the polymers, Polycaprolactone (PCL) and polyvinyl alcoholha (PVA) have been used widely in SLS technique. Both polymers are biodegradable polymers with potential applications for bone and cartilage repair [79][148]. Other non-biodegradable polymers such as polyetheretherketone (PEEK) [149] and polyamide [150], have also been used for building TE scaffolds. Figure 1.19 shows examples of a PCL scaffold fabricated using SLS [79].
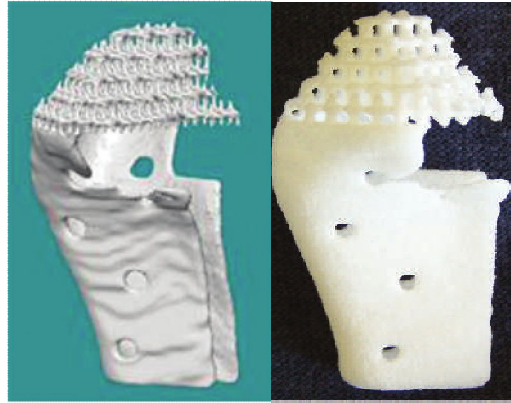
Figure 1.19. Examples of (a) design and (b) PCL scaffolds directly fabricated using SLS [79].

SLS has also been used for fabrication of biocomposites such as poly ether etherketone/hydroxyapatite, poly caprolactone / hydroxyapatite, poly (vinylalcohol) /hydroxyapatite and poly caprolactone /tricalcium phosphate (PCL/TCP) composites [151- 154].

More recently, porous scaffolds of pure β-TCP have been successfully fabricated by SLS with a good level of densification and restricted grain growth due to the rapid sintering and cooling produced by the laser [155], as shown in Figure 1.20, the scaffold exhibit tailored porosity of around 46 % with a high level of interconnectivity and good mechanical properties [156].
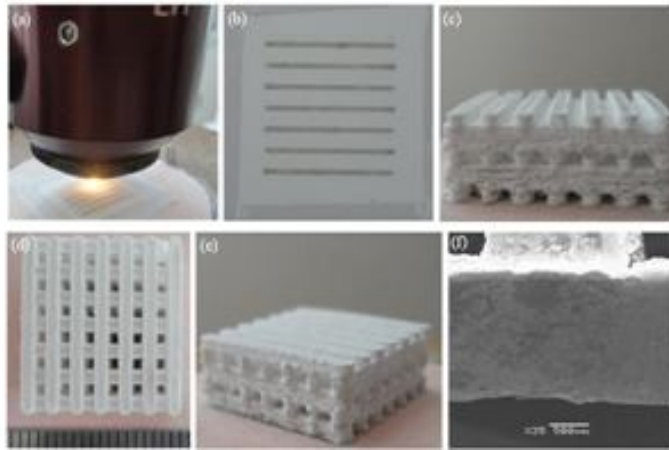
Figure 1.20. (a) In situ optical image of the SLS process on a β-TCP powder bed and optical images of (b) a sintered layer, and (c)–(e) of the final porous β-TCP scaffolds. (f) SEM micrograph of a single sintered line [156].

Glasses and glass-ceramics are easier to produce by SLS technique than fully crystalline ceramic due to the lower temperatures involved and the presence of a liquid or easy flowing phase. Indeed, SLS has been used to produce parts with suitable biological and mechanical properties for use in bone replacement applications from apatite-mullite glass-ceramic [157]. and apatite–wollastonite (A–W) glass–ceramics [158].

Among the bioglasses, 13-93 composition has been used more frequently in SLS technique. In one work cylindrical 13-93 scaffolds fabricated by SLS (Figure 1.21) show a compressive strength varying from 41 MPa for a part with ~ 60 % porosity to 157 MPa for a part with no designed porosity [159].
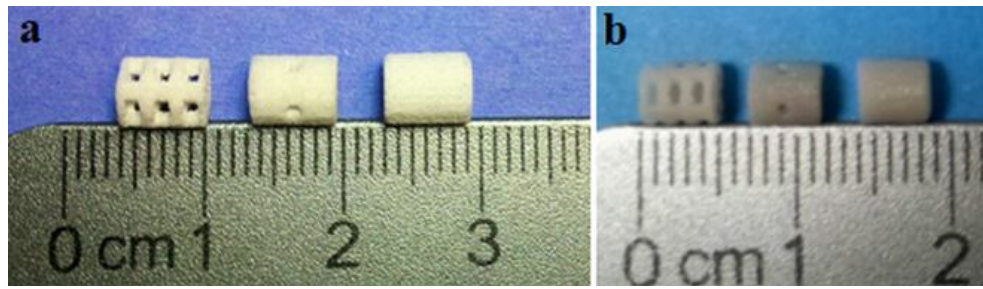
Figure 1.21. (a) green and(b) sintered 13-93 bioglass parts fabricated by SLS [159].

In the other study, sintered 13-93 bioglass scaffolds with cubic pores (Figure 1.22) of sizes ranging from 300 to 800 μm and 50% apparent porosity exhibited an average compressive strength of 20.4 MPa, which is appropriate for non-load bearing applications [160].
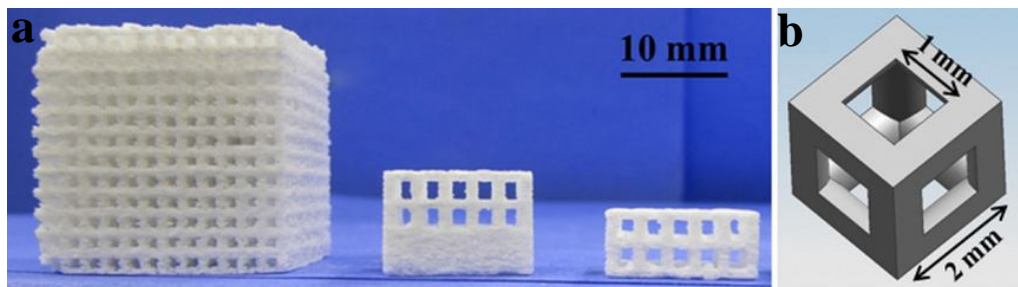
Figure 1.22. (a) SLS-fabricated 13-93 cubic porous parts with different pore size (b) repeatable cubic unit in the CAD model [160].

There are few works reported regarding hiring 45S5 bioglass in SLS technique [161] which might be due to difficulties in sintering 45S5 bioglass that will be later discussed.

1.5.3.3   Direct ink writing

Direct ink writing is a term that describes different fabrication methods that employ a computer-controlled translation stage, which moves an ink-deposition nozzle, to create materials with controlled architecture and composition [162].

Direct ink writing techniques are mainly divided into:

1- Filament-based methods such as robocasting [163-167], fused deposition [168][169], and freeze extrusion [170][19].

2- Droplet-based approaches such as ink-jet printing [171-172] and hot-melt printing [173].

Regardless whether the ink is deposited as a continuous filament or individual drops, a careful control of ink composition, rheological behavior, and printing parameters, enables the fabrication of 3D structures layer-by-layer.

Among all the techniques belonging to this family, since it is the technique selected for the execution of this study,   robocasting is highlighted and reviewed in greater detail in the following separate section.

1.6   Robocasting

Robocasting is unique among the SFF techniques because it allows one to build scaffolds using water-based inks (highly concentrated suspension of desired materials for fabrication of the scaffolds) with minimal organic content (< 1 wt.%) capable of fully supporting their own weight during assembly [174]. Thus, a 3D mesh of interpenetrating rods is built layer-wise by extrusion of the inks through the deposition nozzle. The schematic of robocasting system is illustrated in Figure 1.23 and the different stages of the process are described in detail in the following sections.
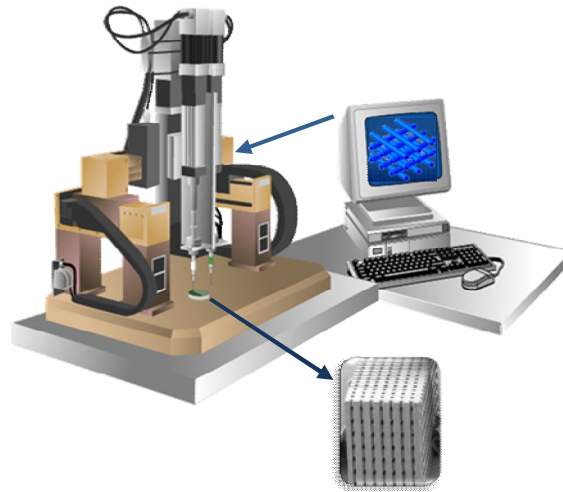
Figure 1.23. The schematic illustration of the robocasting fabrication technique.

Colloidal gels are excellent candidate materials for direct ink writing of complex 3D structures. The inks must have two important criteria. First, they must exhibit a well-controlled viscoelastic response, so they flow through the deposition nozzle and then set immediately to facilitate shape retention of the deposited features even as they span gaps in the underlying layers. Second, they must contain a high colloid volume fraction to minimize drying-induced shrinkage after assembly is complete, so the particle network is able to resist compressive stresses arising from capillary tension [175- 177].

1.6.1 Ink preparation

Colloidal gels are excellent candidate materials for direct ink writing of complex 3D structures. The inks must meet two important criteria. First, they must exhibit a well-controlled viscoelastic response, so they flow through the deposition nozzle and then set immediately after, in order to facilitate shape retention of the deposited features even as they span gaps in the underlying layers. Second, they must contain a high colloid volume fraction to minimize drying-induced shrinkage after the assembly is complete, so that the particle network is able to resist compressive stresses arising from capillary tension [175-177]. A high solid loading also produces a higher green density, which facilitates densification of the part during the subsequent sintering treatment.

1.6.1.1   Powder dispersion in the suspension

Ink preparation starts with making a highly concentrated and stably dispersed suspension of the starting powder. So there is a necessity to understand inter particle forces in order to control the rheology of concentrated suspensions. The main hurdle for dispersing particles in any solution is attractive Van der Waals forces between powder particles which are always present and induce agglomeration. To break down these agglomerations, the suspended particles must be separated through establishing repulsive forces. Electrostatic, steric and electrosteric are the three mechanisms for inducing interparticle repulsion. Electrostatic repulsion is due to charged particles attracting free ions from solution to form a dielectric double layer. Each double layer is repelled by another double layer leading to stabilization of the suspension [178-179].

Steric stabilization consists of covering the particles with large, polymeric molecules which prevents the particle from getting close enough, into the range of attractive forces [180].

Polyelectrolytes adsorbed onto particle surfaces can combine the physical steric dispersion mechanism with electrostatic repulsion and produce the electrosteric mechanism [181-182].

For either electrostatic or electrosteric mechanism, the charge on a given particle plays an important role on the adsorption of ion species and charged branches of polyelectrolyte from solution. The charge on a particle in suspension depends on the surrounding environment and its isoelectric point (IEP) which is the pH at which a particular molecule or surface carries no net electrical charge. At every pH there are positive, negative, and neutral sites on the particle surface. However, if the environment is at a pH greater than the particle IEP, then the particle will have more negative sites and the particle surface will be negatively charged. Further increasing the surrounding pH creates even more negative sites and less positive sites and a more negative surface. Conversely, decreasing the pH below the IEP will create a more positive particle surface. The adjustment of pH could be used as a mean for of providing enough charged sites on the surface of the particles to amplify the repulsive forces between particle as well as helping the used polyelectrolytes to be disassociated and adsorbed more easily by the surface of the particles.

The particle size of the powder used for ink preparation is also a critical factor in the dispersion step. A range of particle size between 1 and 10 µm is typically preferable for

making an ink for robocasting. Using bigger particles, results in problems such as clogging during printing step. Using finer particles could also be problematic since they have much higher surface area and consequently have dispersion problems [183]. Figure 1.24 shows the particle size distribution of a 6P53B bioglass powder used for robocasting ink preparation [183].
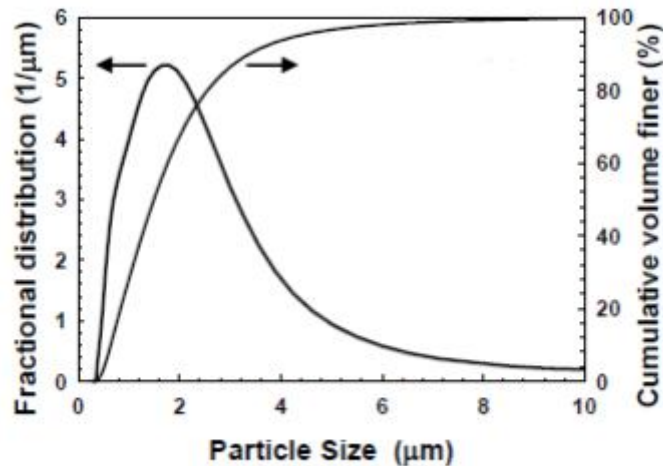
Figure 1.24. Particle size distribution of 6P53B bioglass powder used in the preparation of inks for robocasting [183].

Subsequently, by selecting appropriate starting powder and organic dispersant (typically a polyelectrolyte) and carefully adjusting their concentrations and, if necessary, the pH, a nice suspension with good fluidity should be obtained after this step [184-185].

1.6.1.2   Fluid to gel transition

The second step in ink preparation is inducing fluid-to-gel transition in the system. As shown schematically in Figure 1.25, his gel transition can be done through a pH or temperature change [162], or by modifying the ink composition, generally through the addition of salts or ionic additives [186].

.
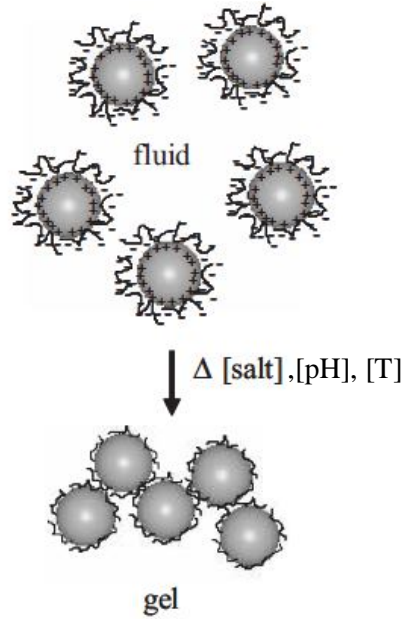
Figure 1.25. Schematic illustration of the fluid-to-gel transition [162].

The rheological behavior of a suspension or ink is non-Newtonian and can be described by the Krieger–Dougherty equation which is as follow [187]:

$$y = k\left(\frac{\emptyset}{\emptyset_{max}} - 1\right)^x \qquad (1.2)$$

Where y is the mechanical property of interest (shear yield stress, τ_y, or elastic shear modulus, G'), k is a constant, $\emptyset$ is the volumetric concentration of particles, $\emptyset_{max}$ is the maximum packing at the gel point—which scales inversely with bond strength [162] and x is the scaling exponent. As the attractive forces between particles strengthen through fluid to gel transition, a dramatic increase in both τ_y and G' is observed [185]. (Figure 1.26) since $\emptyset_{max}$ will decrease. Both mechanical parameters need to increase if the gel is to sustain its own weight when spanning underlying gaps or the weight the subsequently deposited layers without large distortions of its shape.
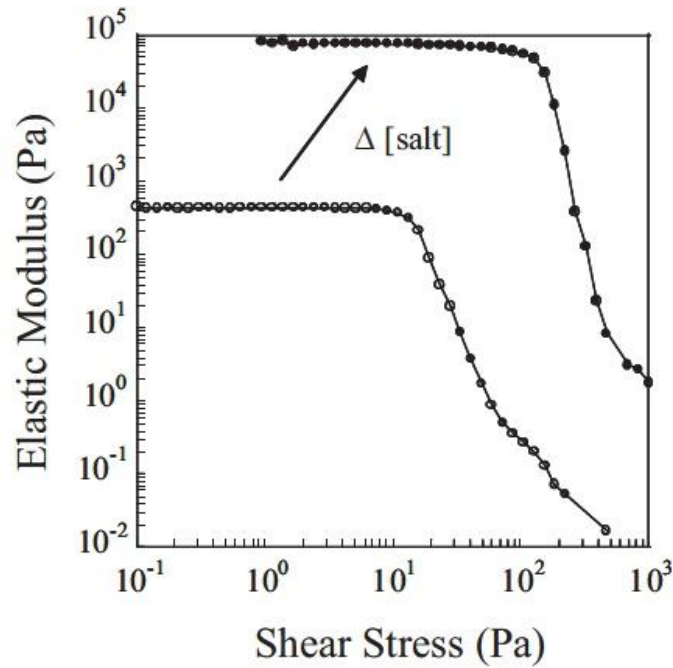
Figure 1.26. Elastic modulus as a function of shear stress for 50 vol.% BaTiO₃ nanoparticle inks with 0.01M (open symbols) and 0.08M (closed symbols) zinc acetate addition [185].

When stressed beyond its yield point (τ_y), interparticle bonds begin to rupture leading to the sharp decrease in G', as observed in Figure 1.26. The colloidal gel then exhibits a shear thinning flow behavior due to the attrition of particle-particle bonds within the gel, as described by the Herschel-Bulkley model constitutive equation [188]:

$$\tau = \tau_y + K(\gamma')^n \qquad (1.3)$$

Where γ' is the shear rate, τ is the shear stress, τ_y is the yield stress, n (< 1) is the shear thinning exponent and K is the viscosity parameter. The yield stress is the shear stress in the absence of shear motion and represents the minimum stress leading to deformation of the static form of the material, which is already mentioned, should be high for the gel to maintain its shape after extrusion. A shear thinning behavior is desired as it means that the ink has a decreased viscosity when subjected to shear strain, which facilitates extrusion through the deposition nozzle.

1.6.2   Ink deposition (printing)

After ink preparation, the ink must be loaded into an appropriate container for deposition. Loading process can be critical since bubbles can be introduced in the ink. Such bubbles are deleterious to the deposition process since they create defects in the deposited structure and may even lead to a premature abort of the deposition. If bubbles are introduced during loading, a method for eliminating them should be devised.

Once the ink is correctly housed in its reservoir, it has to be delivered according to a predefined CAD model CAD design preparation and pretreatment is similar to that described in Section 1.5.3.1 (Figure 1.15). There are two possible forms of ink delivery system for filament-based writing: (1) constant-displacement and (2) constant-pressure extrusion [188]. In both systems, the ink is extruded as a continuous filament through a single or multi-nozzle array. The filament diameter is dependent on the nozzle diameter, ink rheological characteristics and printing speed. Constant pressure approach is less desirable as slight variations in rheological properties induce fluctuations in the volumetric flow rate that will distort the shape of the deposited filaments.

During constant-displacement printing, ink filaments are extruded at a constant volumetric flow rate. In the robocasting system used for this study, this is done by fixing the displacement rate of the plunger in the ink reservoir in order to obtain the volumetric flow rate required to maintain the selected linear printing speed, taking into consideration the internal diameters of the nozzle and the reservoir. The plunger movement generates a pressure gradient, ΔP, at the nozzle which creates a radially varying shear stress, τ_r, on the ink as described by the following equation [189]:

$$\boldsymbol{\tau_r} = \frac{r\Delta P}{2l} \qquad\qquad\qquad (1.4)$$

Where *r* is the radial position within the nozzle and *l* is the length under pressure. As a consequence of this radial variation of the shear stress, the flow velocity profile of the gel-based ink in the cylindrical deposition nozzle shows three different zones: a rigid core moving at a constant velocity surrounded by a less rigid (fluid) shell experiencing laminar flow and a thin slip layer free of colloidal particles at the nozzle wall [175][188].

The ink exits the nozzle as a continuous, rod like filament with a rigid (gel)-core/fluid-shell architecture, which simultaneously promotes shape retention and allows it to fuse with previously patterned features at contact points. Upon deposition, the fluid shell quickly transforms to a gelled state as the attractive particle bonds reform [190].

Consequently, printing speed is another key processing parameter in robocasting, it does not only affect the pressure gradient induced in the nozzle, but also determines the time the ink has to reform the aforementioned bonds as the nozzle moves during assembly. Accordingly, large printing speeds are more likely to produce departures of the deposited lines from their pre-designed paths, especially upon abrupt changes in the printing direction, and may also produce the printing procedure to abort due to overpressure. On the contrary, slow printing speed may facilitate clogging and, obviously, increase the assembly time and thus the cost of producing the intended part. Other printing defects may arise from a non uniform drying of the structure during assembly, especially at low printing speeds. To avoid this problem, the printing step is, whenever possible, carried out in an oil bath [191].

When all the ink properties and printing parameters are properly adjusted very homogenous and reproducible 2D and 3D green assembled structures can be produced, as shown in Figure 1.27 [185].
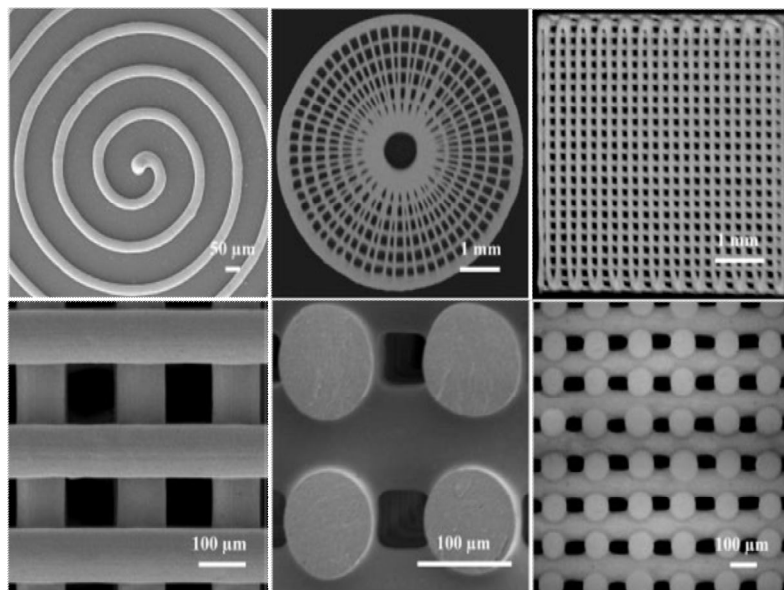
Figure 1.27. Optical and SEM images of 2D and 3D periodic lattices assembled by robocasting [185].

1.7 Post-assembly heat treatments

In most of the fabrication methods discussed in preceding sections, including robocasting , apart from the main solid phase (metals, ceramics, glasses, etc.), there are other organic additives, which are normally polymeric. These are normally unwanted chemicals that have to be removed in posterior heat treatments, usually referred to as debinding treatments. After removal of the organics a sintering step is normally required to consolidate the green part. This last step is critical in e the main densification and strengthening of the part happens during this step. Both types of post-assembly heat treatments are now described in some detail.

1.7.1 Debinding

Depending on the processing method various polymeric additives are added in different concentrations and for different purposes: as dispersants, flocculants, defoamers, binders, lubricant, etc. For instance, the role of the binders—polyvinyl alcohols (PVA), polyacrylate or cellulose are examples of common binders [192-193] is giving the green body strength by gluing together particles at their boundary surfaces. As already mentioned, all these processing chemicals have to be removed at sufficiently high temperatures, during so-called debinding treatments.

The organic additives of the green body must be removed essentially before the main sintering step [194]. The temperatures for de-binding vary between 150 °C and 600 °C, depending on the polymer decomposition temperature. Organic polymers have to be removed completely from the green body because residual carbon can influence the sinter process and the quality of the final product negatively [195], especially in biomedical applications. Organic additives can enhance the mechanical strength of a green body, but its strength will decrease as the binder is removed. Since the pressure build-up from gaseous binder degradation will rise with increasing polymer degradation rates, the speed of decomposition of the polymers should not exceed the transport velocity of the products of pyrolysis [196]. Once the gas pressure exceeds the strength of the compacts, excess pressure of the trapped gaseous pyrolysis products can lead to generation of bubbles and other defects, and eventually to the destruction of the parts

[197]. On the other hand, a slow heating rate increases the post-processing time, which could eventually decrease the attractiveness and cost-effectiveness of the method.

Thus, it is generally understood that the microporosity increases and the strength of the parts decreases as the heating rate augments [198]. For instance, Figure 1.28 shows the increase in the micropore sizes of 13-93 bioglass parts, fabricated by selective laser sintering using 22 wt.% of stearic acid (SA) as binder, with de-binding heating rate [159].
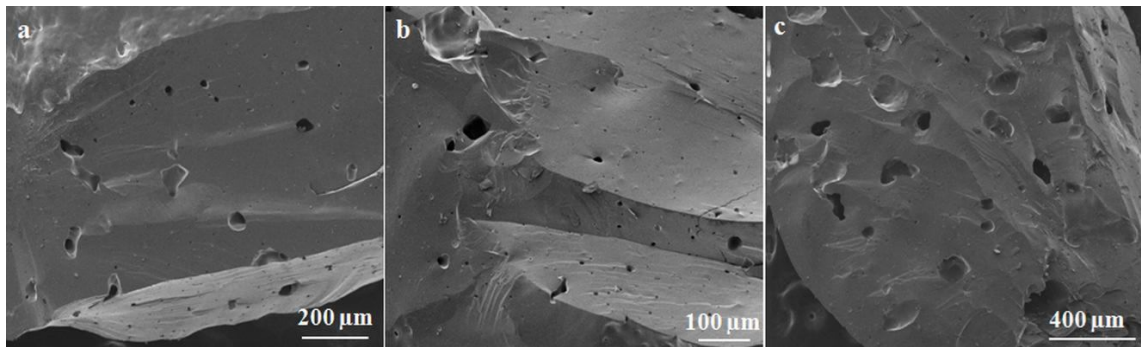
Figure 1.28. Effect of de-binding heating rate on micropore size in13-93 bioglass parts fabricated by SLS: (a-c) 0.1, 1 and 1.5 °C/min [159].

Thermal analysis (e.g. DTA/TGA) is useful for determining the optimal heating rates and soaking times in heat-treating of green parts. Figure 1.29 shows the TGA curve for the decomposition of the13-93 bioactive glass paste containing different organic additives, used in freeze extrusion fabrication. Noticeable changes in the slope of the curve appeared to occur at approximately 80, 240, 320, 350 and 440 °C. The low melting point polymers and residual water are evaporated in the temperature range 80–120 °C and the higher molecular weight polymers are decomposed at higher temperatures [199]. Since each polymer has its own decomposition temperature, it is sometimes necessary to develop a binder burnout schedule with several isothermal holding stages or very slow heating rates [200]. This may result in lengthy debinding treatments that may last even several days [19][170][199].

.
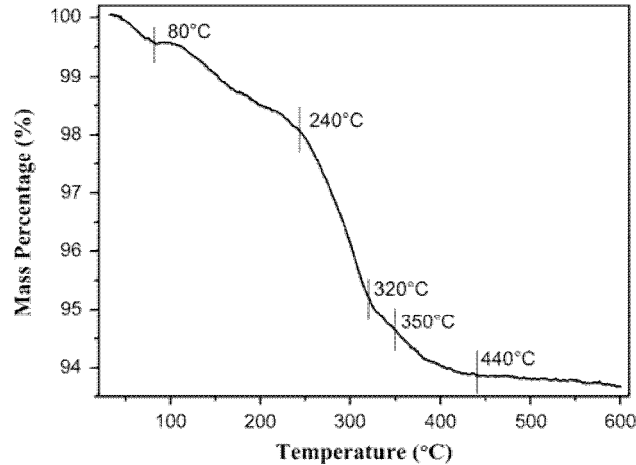
Figure 1.29. Thermogravimetric (TGA) analysis of paste used in freeze extrusion fabrication of 13-93 bioglass parts [199].

1.7.2   Sintering

After binder removal, the green scaffolds should be strengthened and densified by sintering. Sintering is the process of compacting and forming a solid mass of material by heat and/or pressure without melting it to the point of liquefaction. Sintering happens as atoms in the materials diffuse across the boundaries of contacting particles, fusing them together and creating one solid piece. Sintering occurs in two different stages, starting from the formation of necks between particles and followed by elimination of existing pores. The driving force for this densification and the whole sintering process is the reduction of surface free energy. The temperature required to produce sintering depends greatly on the chemical nature of the particles, but for ceramics is typically around half the melting temperature of the material. Since the subject of the current work is devoted to 45S5 and 13-93 bioglasses, in the following section the most important sintering features of these two bioglasses are reviewed.

1.7.2.1   Sintering of 45S5 bioglass

Figure 1.30 shows that there are several structural transformations occurring during the heating of 45S5 bioglass up to melting point [201].

1200°C —	Melting
850°C —	Glass transition 2 (T_{g2}) of the remaining glassy phase
800°C —	Crystallisation of $Na_2Ca_4(PO4)_2SiO_4$ from the phosphate rich phase
610°C —	Crystallisation of $Na_2CaSi_2O_6$ from the silica rich phase
580°C —	Glass-in-glass phase separation (T_s) : Creation of a silica-rich phase and a phophate rich phase
550°C —	Glass transition 1 (T_{g1})
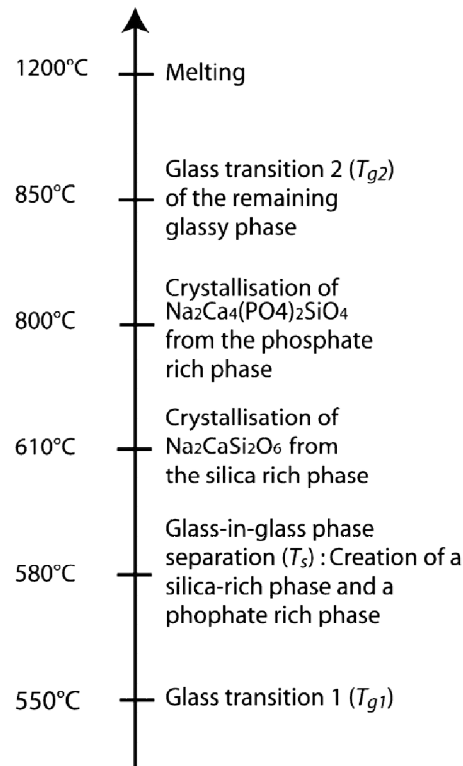
Figure 1.30. Summary of the structural transformations of 45S5 with temperature [201].

The characteristic temperatures such as the glass transition (T_g), the crystallization (T_c) and the melting (T_m) temperatures of 45S5 can be determined from thermal analysis. Figure 1.31 shows a typical TGA–DTA curve obtained for 45S5 bioglass powder.
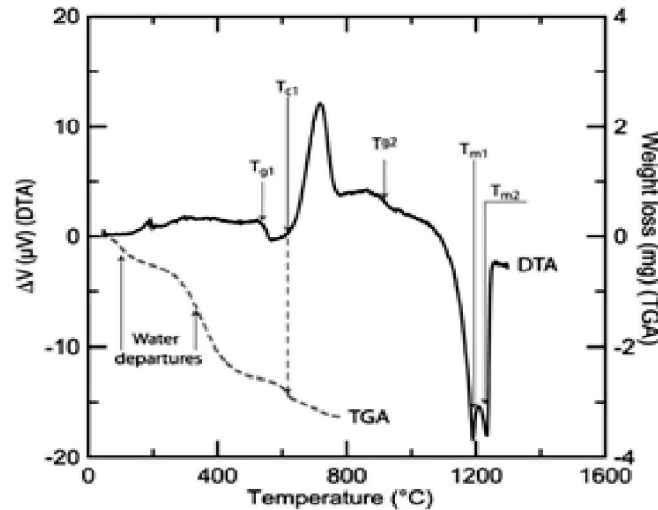
Figure 1.31. TGA–TDA of 45S5 bioglass [201].

DTA shows an endothermic effect at T_{g1} = 550 ºC caused by the first glass transition, followed by an exothermic peak beginning at T_c = 610 ºC attributed to the onset of crystallization. A second small endothermic effect is observed at T_{g2} = 850 ºC which is attributed to second glass transition. Finally, melting takes place in the 1070–1278 ºC range. Two endothermic peaks respectively at T_{m1} = 1192 ºC and T_{m2} = 1235 ºC are attributed to the melting of two different crystalline phases. These characteristic temperatures have been repeatedly reported in the literature [16][202-203]. However, it is worth to mention that the characteristic temperatures (T_g, T_c and T_m) are dependent on the heating rates and particle size of the bioglass. By increasing the heating rate, the onset of glass transition temperature (T_g) and the peak crystallisation temperature (T_c) increase, while the onset melting temperature (T_m) decreases. A shift of the crystallization peaks to lower temperatures has been observed with decreasing particle size [203].

The relative variation of the sample length $(\Delta L/L_0)$ versus temperature during heating up to melting point as measured by dilatometry is also a useful method for studying sintering behavior of 45S5 bioglass (Figure 1.32) [201].
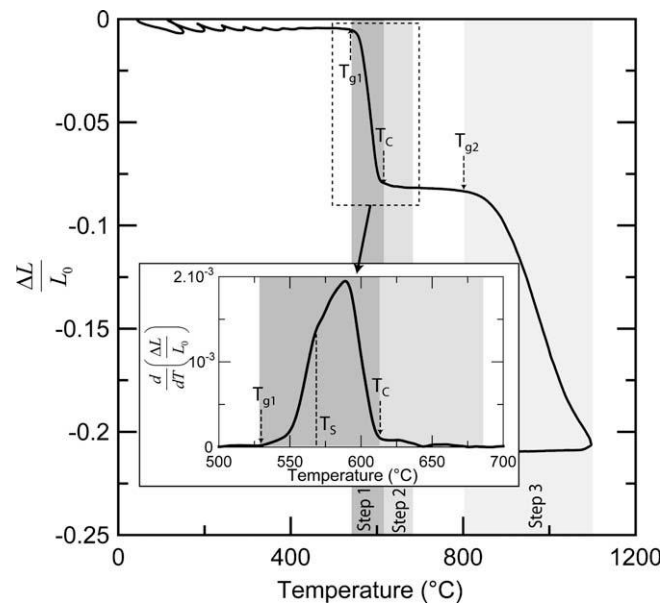
Figure 1.32. Dilatometric curve of 45S5 bioglass powder compact, with its derivative as inset [201].

The sintering process of 45S5 bioglass is composed of three main stages:

1- First densification step ($T_{g1} < T < T_c$).

This densification normally starts around 500 °C and ends at around 600 °C. No sintering occurs below the onset of the glass transition. The glass transition temperature is usually estimated to be at 550 °C. During the glass transition, the glass becomes soft enough to allow sintering by viscous flow. Diffusion of atoms in the viscous glass enable the particles start to bond to each other through sintering necks in order to reduce their surface area. The shrinkage rates which are obtained from the derivative of the dilatometric curve (inset in Figure 1.32), show that the faster shrinkage starts at 550 °C. The shrinkage rate then increases rapidly and steadily up to 570 °C, and then more slowly up to 595 °C, when it starts to decrease. The reduction in shrinkage rate above this temperature is attributed to glass decomposition. Just after the glass transition (T_{g1}), the glass starts suffers a phase separation and this phenomenon could lead to hardening of the surface of the bioglass particles through the formation of silica-rich domains which will dominate viscous flow by progressively increasing the viscosity. Tipically, the total shrinkage produced during this first step is around 12 % [16][204-205]. However, as mentioned

before, T_c depends on the heating rate and the particle size and therefore it is possible to obtain various degrees of densification by changing these parameters. Nonetheless, the level of densification achieved during this step is typically very low which up to date have prevented the fabrication from conventional techniques of amorphous 45S5 bioglass scaffolds with enough mechanical resistance for practical applications. Figure 1.33 shows micrographs obtained from the fracture surface of powder compacts heat treated at 600 ºC, end of the first densification step. The particles begin to soften and fuse together locally, but a lot of intergranular porosity is still present [201].
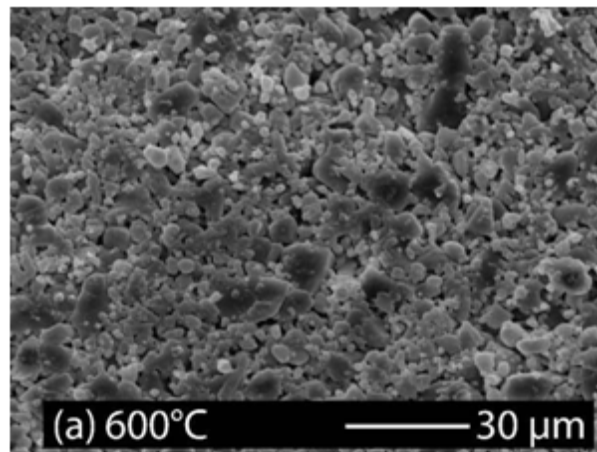
Figure 1.33. Fracture surface of bioglass powder compacts heat treated at 600 ºC [201].

2- Crystallization step ($T_c < T < T_{g2}$).

After the phase separation occurs, phosphate-rich regions are formed that can act as heterogeneous nucleation sites and, consequently, decrease the energy necessary for nucleation of silica-rich crystals. Densification stops immediately once the initial crystalline phase of $Na_2CaSi_2O_6$ forms a continuous and percolating network in the glass [205]. The viscosity becomes too high and viscous flow is stopped at T_c. The plateau part of the dilatometric curve (Figure 1.32) confirms that at the temperature between T_c-T_{g2} there is not any significant change in the samples length. However, crystallization progresses as shown in the X-ray diffractograms for 45S5 bioglass powder of Figure 1.34. Indeed, a secondary phase, $Na_2Ca_4(PO_4)_2Si_2O_4$ crystallizes

also from the remaining phosphate rich glass around 800 ºC [229-230][232][282] and the crystallization is completed at the end of the shrinkage plateau, at temperatures higher than T_{g2} [206]. Nonetheless, the maximal crystallinity attainable in 45S5 composition is about 80 %, so in most sintered materials, the remaining amorphous phase forms a glassy matrix around the crystalline particles [14][16] [207].
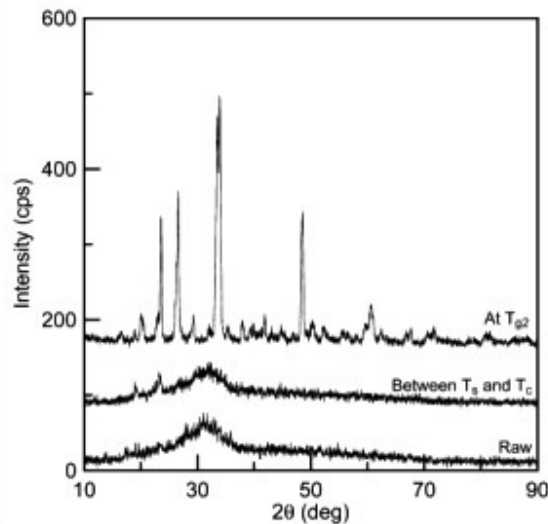
Figure 1.34. XRD patternof 45S5 bioglass powders with different thermal treatments (raw, after the onset of crystallization, and at Tg2) [201].

3- Second densification step ($T > T_{g2}$).

At temperatures above T_{g2}, 45S5 the amorphous matrix surrounding the crystalline phase becomes soft enough to allow again viscous flow sintering [14]. *In situ* heating SEM studies confirm that as happen at T_{g1}, particle soften and become rounder around T_{g2} (Figure 1.35) [15].
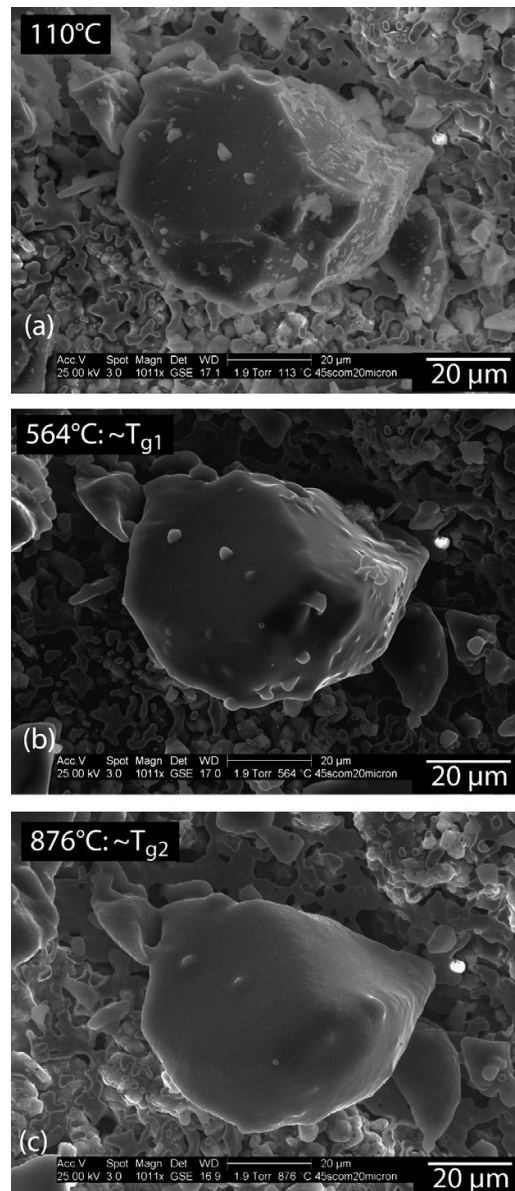
Figure 1.35. SEM micrographs of in situ heating showing the evolution of a 45S5 bioglass grain morphology at (a) 110 ºC, and around (b) T_{g1} = 550 ºC (and (c) Tg2 =850 ºC [15].

Above T_{g2} densification and shrinkage increases steadily with sintering temperature, much more so than with increasing sintering time, as is usually the case (see Figure 1.36) however, sintering at excessively high temperature, at 1100 and 1200 °C for 2 h for example, has been reported to produce segregation of the glassy phase, leaving an inhomogeneous microstructure with bared crystalline particles with virtually no glass matrix around. This has a negative effect in the mechanical

performance of the material and therefore over-sintering at the temperatures close to melting temperatures should be avoided [62][208].
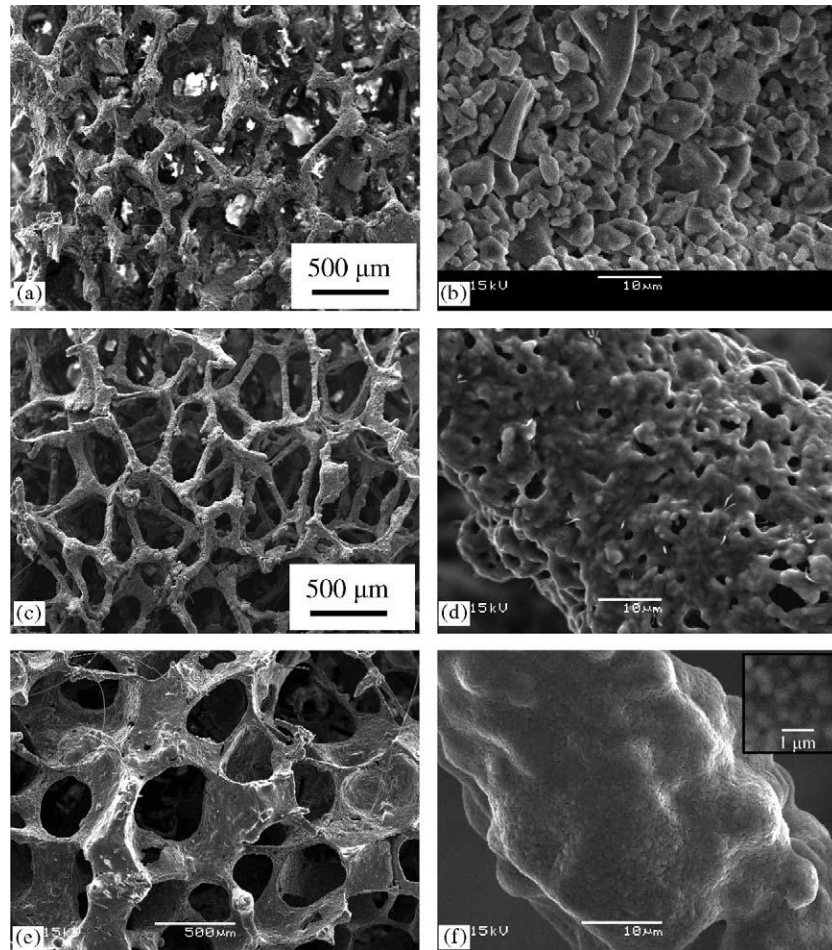
Figure 1.36. Pore structure and strut microstructure of 45S5 bioglass-derived foams sintered at (a)–(b) 900 ºC for 5 h; (c)–(d) 950 ºC for 2 h; and (e)–(f) 1000 ºC for 1 h [62].

Even at the highest sintering temperatures it is not possible to achieve a full densification of 45S5 bioglass by a conventional sintering process. The presence of pores and other micro defects in 45S5 scaffolds generated during sintering/crystallization, are responsible for the mechanical weakness of this material.

Application of simultaneous pressure has been shown to enhance densification and much fewer micropores are present in bulk 45S5 glasses sintered by spark plasma sintering (SPS) technique. The presence of fewer micro voids and

homogeneous microstructure of fine crystalline particles in the glass matrix produced much improved mechanical properties in the SPS-processed 45S5, compared to those treated with the conventional heating process [208]. Unfortunately pressure-assisted sintering is normally not a suitable process for the fabrication of porous scaffolds.

1.7.2.2   Sintering of 13-93 bioglass

In comparison to 45S5 bioglas, 13-93 bioglass is much less problematic in terms of sintering behavior. The DTA thermogram of a 13–93 glass is shown in Figure 1.37. The onset of the glass transition is observed to occur at 606 ºC, followed by two crystallization events, with onset temperatures of 714 ºC and 851 ºC, respectively. This means that 13-93 bioactive glass has a wider window between glass transition (~ 600 ºC) and the onset of crystallization (~ 700 ºC) compared to 45S5 bioglass, and the 13-93 glass remains stable (does not decompose) within this window. This greatly facilitates its full densification by viscous flow sintering, without crystallization occurring, at sintering temperatures selected within this window [49][64].
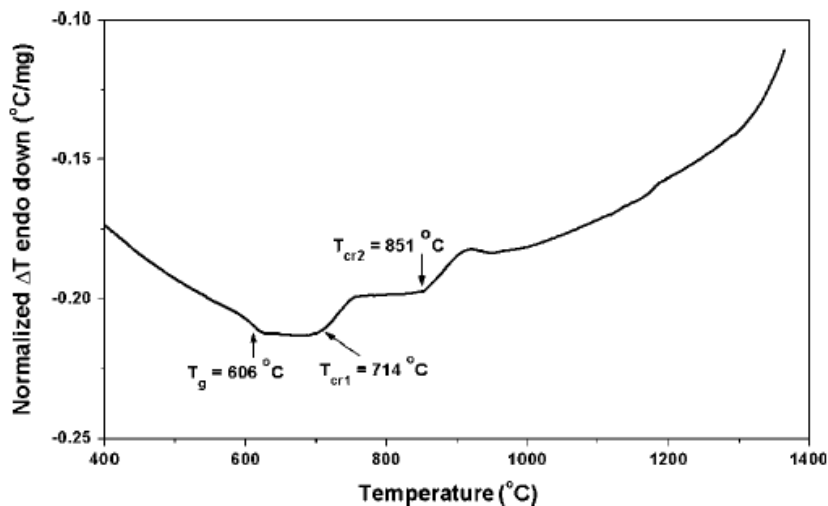
Figure 1.37. Differential thermal analysis plot for 13–93 glass, showing the glass transition and crystallization regions [49].

This latter assertion is confirmed by the XRD pattern of fully-sintered 13-93 bioglass scaffolds, which is similar to that of the starting glass particles [170] (Figure 1.38), and consists of a broad band at $2\theta = 30$, typical of an amorphous glass [63].
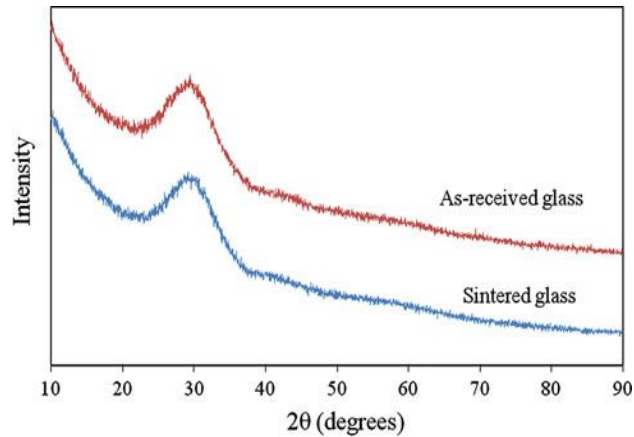
Figure 1.38. X-ray diffraction patterm of as received 13–93 glass particles and sintered scaffold, showing preservation of the amorphous state after sintering [63].

Therefore, 13-93 bioglass can be sintered to full-density, in an amorphous state and at a relatively low temperature (< 710 ℃), something that is impossible to achieve for the 45S5 composition even after sintering at temperatures well above the crystallization temperature. This enables the fabrication of scaffolds with significantly improved mechanical properties, which explains the significant attention that 13-93 bioactive glass is receiving despite its lower bioactivity, as we discussed in preceding sections.

1.8   Reinforcing porous bioactive glass scaffolds by polymer infiltration

In spite of all proven biological properties of bioglasses, the brittleness of these porous structures limits their potential use in load-bearing biomedical applications. The compressive strength of 45S5 scaffolds is normally comparable with that of cancellous bone, but far from cortical bone values [209-210].

And although 13-93 scaffolds have higher compressive strength in comparison to 45S5, the brittleness of this material is still a limiting factor for load bearing applications [211].

One applicable solution for overcoming brittleness of bioceramic and bioglass scaffolds is the addition of a biodegradable polymeric phase to form a biocomposite structure. This hybridization combines the advantages of the organic and inorganic phases, ideally to achieve materials with a better combination of stiffness, strength and toughness.

Indeed, mixing of polymers and ceramics has been shown to be a suitable solution to improve the brittleness of ceramics and the strength of polymers [212-215].

A wide variety of polymers have been used for hybridization with bioactive glass and other bioceramic scaffolds. Polymers are divided generally into two groups of natural and synthetic polymers [216]. Natural polymers, such as collagen, glycos amino glycan, chitosan, starch, hyaluronic acid, alginate and bacterial sourced poly (hydroxyl alkanoates), offer the advantage of flexibility to adapt their shape to desired forms and faster biodegradation [217]. On the other hand synthetic biodegradable polymers such as polylactic acid (PLA) and poly (e-caprolactone) (PCL) exhibit better mechanical properties, with PLA being much stiffer and stronger than PCL but much less ductile. On the other hand, PLA degrades faster than PCL [218-220].

To produce these organic/inorganic hybrids from existing scaffolds, it is necessary to impregnate the three-dimensional structure with the selected polymer, although this might come at the expense of reducing its bioactivity [51]. Polymer melt infiltration is a suitable method to produce such hybridization of bioceramic scaffolds recently used in our group. The advantage of this method is that unlike in most existing reports the infiltration of bioceramic scaffolds with biodegradable polymers is complete, and the polymer fills all the micropores and microcracks on the strut surfaces. This produces significant improvements in terms of strength and toughness over the bare bioceramic structures. Fracture resistance of the composites is improved in bending, compressive and tensile tests [20-21][221]. The strengthening achieved in fully impregnated structures is attributed to two mechanisms: stress shielding and defect healing. The former is produced by the polymer occupying large predesigned macropores, which sustains part of the load thus reducing the stresses on the ceramic rods, whereas the latter is due to the impregnation of the rods micropores, which makes it harder to initiate a crack from these defects.

Besides, the presence of a continuous ductile polymeric phase produces also a significant toughening of the structure that is a considerable increase in strain energy

density and, thus, in energy to failure. The main toughening is crack bridging by polymer fibrils [20][222-225].

Chapter 2

Materials and Methods

2.1 Materials

In this section, the materials used in the preparation of experimental samples are described.

2.1.1 Bioactive glasses

Two bioglass compositions, namely 45S5 and 13-93, were used in the current work for fabrication of 3D robocast scaffolds from commercial sources. Bioactive glass powder with the 45S5 composition—45 % SiO_2, 24.5 % CaO, 24.5 % Na_2O and 6 % P_2O_5 (in wt.%) was supplied by MO-SCI Corporation (USA). The density of the glass, as indicated by the manufacturer, was 2.7 $g \cdot cm^{-3}$. 13-93 bioactive glass frits containing 53 % SiO_2, 20 % CaO, 6 % Na_2O, 12 % K_2O, 5 % MgO and 4 % P_2O_5 (wt.%) were supplied also by MO-SCI Corporation (USA). The density of the glass, as reported by the manufacturer, was 2.65 $g \cdot cm^{-3}$.

2.1.2 Organic additives

In the development and optimization of suitable ink formulations for robocasting, various dispersing agents were tested:

(i)   a sub-group of anionic nature: ammonium polymethacrylate (Darvan C; mol. wt. = 2000; R.T. Vanderbilt Co., Norwalk, CT); poly (methylvinyl ether) (EasySperse; ISP, Wayne, NJ); Targon 1128 (BK Ladenburg GmbH, Ladenburg, Germany);

(ii)   a sub-group of cationic ones: Tetramethylammonium hydroxide (TMAH, Moses Lake Industries, Inc, USA); Polyethyleneimine (PEI, low M_w, ALDRICH, USA); and

(iii)   Carboxymethyl cellulose (CMC, M_w = 35 000 and M_w = 250 000, Lamberti Iberia S.A.U., Castellón, Spain) was also used as the sole processing additive—as indicated by the supplier, a 2 wt.% aqueous solution of this CMC had a viscosity in the range of η = 1–3 $Pa \cdot s$.

2.1.3   Synthetic polymers

Two commercial polymers were used to impregnate the porous robocast scaffolds: PLA in powder form (ICO Polymers, Ecorene NW61-100 PLA powder) and PCL beads (Capa^{TM} 6500, Perstorp, UK). The most relevant physical properties of these two polymers, as provided by the supplier, are summarized in Table 2-1.

Table 2-1. Specifications of commercial PCL and PLA polymers provided by supplier.

Properties	PCL	PLA
Melting point	58-60 ^{o}C	173-178 ^{o}C
Glass transition temperature	-71 to -55 ^{o}C	60-65 ^{o}C
Elastic modulus	0.45 GPa	3.5 GPa
Poisson's ratio	0.47	0.36
Degradation temperature	310 ^{o}C	230 ^{o}C
Density	1.14 g.cm^{-3}	1.25 g.cm^{-3}

2.2   Fabrication of 45S5 and 13-93 bioglass scaffolds by robocasting

As described in section 1.6, the fabrication of the bioglass robocast scaffolds involves several steps that are described in detail in the following sections:

2.2.1   Powder preparation

As described in section 1.6.1.1, particle size of the powder used for ink preparation is a critical factor. Particles between 1 and 10 µm are preferred to facilitate dispersion and avoid clogging [226]. Therefore, the commercial bioglass particles were pre-treated by milling. The as-received 45S5 bioglass powder was milled for 4 h in an attrition mill (Model 01-HD, Union Process, Akron, OH), using high-purity zirconia container and balls (6 mm) as milling media and ethanol as dispersing medium. On the other hand, the as-received 13-93 glass frits were first grinded for 5 min in a centrifugal ball mill (model S100, Retsch GmbH), then sieved through a 200 µm size mesh, and finally refined in the attrition mill for 3 hours using distilled water or anhydrous ethanol 96 % (Panreac, Spain) as solvent, and zirconia balls (6 mm) as the milling media. In both

cases, the resulting slurries were dried at 60 °C and then sieved through 106 and 73 µm stainless steel sieves to eliminate any agglomerates created during the drying step. To make sure that the obtained bioglass particles were in the desired size range (1–10 µm), the particle size distribution of the milled powders was measured using a laser diffraction particle size analyzer (Mastersizer 2000MU, Malvern, UK).

2.2.2   Ink preparation

The aqueous colloidal dispersing ability of the 45S5 bioglass particles was firstly investigated in the presence of the anionic and cationic dispersing agents enumerated in section 2.1.2, aiming at setting the experimental conditions to stabilize the particles in water and obtaining suspensions that could be easily adapted to the robocasting technique.

Zeta potential (ζ) electrical potential at the shear plane between the particle and the liquid [227] measurements as a function of the pH (changed by adding drop by drop appropriate amounts of 0.1 M HCl to the suspension) were performed for the 45S5 bioglass particles dispersed in water in the absence and in the presence of 1 wt.% of each dispersant using a Zeta-potentiometer (Zetasizer Nano ZS, Malvern, UK). At each pH value, an excessive number (100) of measurements was set, and the instrument automatically stopped when a constant zeta-potential value was measured, typically after 20–25 scans.

The preparation of 45S5 colloidal suspensions using different added amounts of each of the abovementioned dispersants ranging from 0.5–2 wt.% was attempted. All mixing procedures were performed in a centrifugal planetary mixer for 20 min (ARE-250, Thinky, Japan).

Alternatively, carboxymethyl cellulose was used as the sole processing additive, to act simultaneously as dispersant and binder/gelling agent. Concentrated inks containing 45 vol.% solids could be prepared with CMC that exhibited a rheological behavior appropriate for robocasting—optimal performance was achieved with a a concentration of 1 wt.% of CMC . The flow properties of all these colloidal gels were evaluated using a rheometer (Bohlin CVO, Malvern, UK). The measuring configuration adopted was a cone and plate (4°, 40 mm, and gap of 150 µm), and flow measurements were conducted at shear rates between 0.2 and 100 s^{-1}.

Since the chemical composition of 13-93 is similar to 45S5, CMC was also used for 13-93 ink preparation with small changes in the amounts of CMC. Two series of 13-93 aqueous inks with 42 vol.% solid loading were made by adding 1.5 wt. % of CMC (relative to powder content) to distilled water and then the 13-93 glass powders, previously milled either in ethanol or water, to the mixture.

2.2.3   Robocasting of 3D bioglass scaffolds

Figure 2.1 shows the robocasting device (A3200, 3D inks, Stillwater, OK, USA) employed to fabricate three-dimensional structures of 45S5 and 13-93 bioglasses from the developed inks. The ink was housed in a syringe and, after removing any trapped air bubbles, extruded through a conical nozzle (inner diameter, $d = 410$ μm) by the computer-controlled robotic system. The position of the nozzle moved following the CAD model designed previously in the control software (Robocad 3.0, 3D inks, Stillwater, OK, USA).
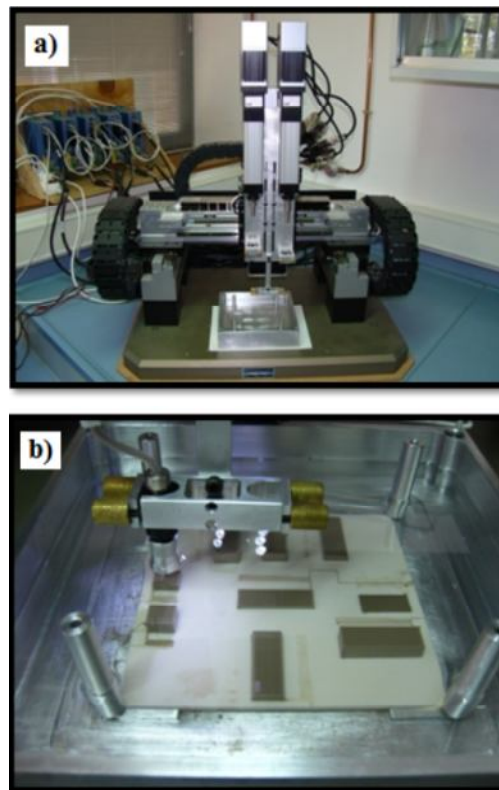
Figure 2.1. Optical images of (a) the robocasting system, (b) 3D structures as-deposited within an oil bath.

The external dimensions of the scaffolds were set at about $13 \times 13 \times 10$ mm, for the specimens used in the optimization of polymer impregnation processes and the fabrication of compression test samples; or at $40 \times 20 \times 12$ mm for the specimens used in the fabrication of bending test samples. The scaffold design consisted of a tetragonal mesh of cylindrical rods with a center-to-center spacing between adjacent parallel rods within a layer of 820 µm and a layer height of 287 µm. The ink flowed through the nozzle at the volumetric flow rate required to maintain a constant deposition speed of 20 mm s^{-1}. To prevent a non-uniform drying of the structure during assembly, the deposition process was carried out within a paraffin oil bath. All the process, including the ink preparation, was carried out at room temperature. After deposition the samples were removed from the bath and dried in ambient conditions for 3 days before thermal processing.

2.2.4   Thermal processing of assembled structures

Thermal de-binding kinetics of robocast bioglass constructs was evaluated using thermo gravimetric analysis, TGA, and differential thermal analysis, DTA, (Setsys Evolution-16 Setaram). Samples of as-received 45S5 bioactive glass powder and of robocast inks prepared from 45S5 and 13-93 glass milled powders, after drying for 1 day at 100 °C, were heated in air at 5 °C min^{-1} up to 1200 °C. Based on these kinetic data, the following thermal treatments were selected for the removal of the polymeric additive and sintering of the as-printed structures.

For 45S5 robocast scaffolds, thermal burn-out of CMC was performed in air at 400 °C for 1h, with a heating rate of 1 °C min^{-1}. After this dwell time, heating continued at a rate of 2 °C min^{-1} up to the sintering temperature. The 45S5 bioglass scaffolds were sintered (in air) for 1 h at different temperatures up to 1200 °C, and then cooled in the furnace at a rate of approximately 10 °C min^{-1}.

For as-printed 13-93 scaffolds CMC burn out was also performed at 400 °C for 1 h but with heating rates varying from 0.2 to 2 °C min^{-1}. Following the binder removal stage, the constructs were sintered in air for 1 h at 670 ℃ and 700 ℃, selection of these temperatures was based on microstructural observations and data from thermo-gravimetric analysis. The heating rate up to sintering temperature was of 1 °C. min^{-1}, and the cooling rate was approximately 4 °C. min^{-1}.

2.3   Polymer melt impregnation of robocast scaffolds

Robocast 45S5 and 13-93 bioglass scaffolds were fully impregnated with either PCL or PLA to develop a co-continuous organic/inorganic dense composite. Infiltration of PCL and PLA was done by immersion of the bioglass-derived scaffolds in a polymer melt, in a process called melt impregnation. 45S5 bioglass structures sintered at 550 °C and 1000 °C, as well as 13-93 bioglass scaffolds from ethanol-milled powder and sintered at 700 °C were used for this task. Melt impregnation was carried out in air by placing the bioglass-derived scaffold in a glass vial full of polymer pellets within a vacuum furnace (EQ-DZF-6020, MTI Corporation, USA). Optimal soaking temperatures and times for infiltration of each polymer were selected by relying on a previous study [20] after small refining adjustments. After complete melting of the polymers at 227 ºC for PLA and 223 ºC for PCL, the samples were kept under a mild for 2 h and then cooled to room temperature. A transversal cut through the center of the impregnated scaffold was made to assess the quality of the impregnation process during the optimization phase.

2.4   Microstructural characterization

The experimental procedures used in the microstructural characterization of the fabricated specimens are described in detail in the following sections:

2.4.1   Density and shrinkage measurements

The density of the scaffolds, ρ_s, was determined from the mass and external dimensions of the structures. The porosity, p, was then calculated as:

$$p = 1 - \rho_{s}/\rho_{th} \qquad\qquad\qquad (2.1)$$

Where $\rho_{th} = 2.7$ g·cm^{-3} and 2.65 g·cm^{-3} are, respectively the theoretical density of bulk 45S5 and 13-93 bioglasses, as provided by the supplier. For more accurate determination of the in-rod open microporosity in 45S5 bioglass-derived samples, the

apparent density, ρ_a, measured at each sintering temperature by He-pycnometry (SPY-D160-E Quantachrome) was used instead of ρ_{th}. Porosity was evaluated both on green and sintered samples.

The linear shrinkage, ΔL, on the samples was calculated at specific temperatures from the variation of their external dimensions as:

$$\Delta L = (L_i - L_f)/ L_i \qquad\qquad (2.2)$$

Where L_i is the initial dimension of the specimen at room temperature and L_f is the dimension after sintering at the selected temperature. Both shrinkage and porosity were evaluated as the average of measurements performed on four different specimens, with standard deviations as error.

2.4.2 X-ray diffraction analysis

X-ray diffractometry (D8 Advance, Bruker, Germany) using CuKα radiation (step width 0.03° 2θ, and count time 4 s per step) was performed on 45S5 and 13-93 bioglass grounded samples—angular intervals 10–65° and 20–70° 2θ, respectively—,after sintering at selected temperatures for identification of the phases present.

X-Ray Photoelectron Spectroscopy (K-Alpha, Thermo Scientific, MA) using AlKα radiation (spot size 0.3 mm, step size 0.1 eV and dwell time 50 ms), was performed on 13-93 grounded samples before and after sintering at optimal temperatures for an accurate compositional analysis.

2.4.3 Scanning Electron Microscopy (SEM)

The microstructure of fabricated specimens was examined using a scanning electron microscopy (SEM, S-3600N, Hitachi, Japan). As-cut and as-fractured cross-sections were used when required. Internal dimensions, such as rod diameter, d, and in-plane and out-of-plane gaps, x and z (Figure 2.2), of scaffolds fabricated at different temperatures were determined as the average of a minimum of 100 direct measurements performed on SEM images. These dimensions were then used to estimate the macroscopic, pre-

designed porosity from geometrical considerations assuming an ideal network of interpenetrating cylinders.
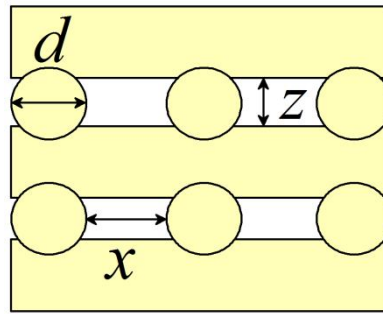
Figure 2.2. Schematic of scaffold's internal dimensions evaluated from SEM micrographs: rod diameter, d, and in-plane and out-of-plane gaps, x and z.

2.5   Mechanical testing

The mechanical response of green and as-sintered scaffolds, as well as structures fully-impregnated with PCL and PLA, was evaluated under compression and bending stresses. For the sake of comparison, the properties of bulk samples of the pure polymers (PCL and PLA) obtained by simple molding were also evaluated under the same conditions.

All tests were performed in air using a universal testing machine (AG-IS 10KN, Shimadzu Corp., Kyoto, Japan), and a constant crosshead speed of 0.6 mm min^{-1}. The force was applied in a direction perpendicular to the printing plane (i.e. orthogonal to the scaffold rods). Prior to mechanical testing, the contact surfaces of each sample were ground to produce smooth parallel surfaces.

In uniaxial compression tests nine parallelepipedic samples of 45S5 scaffolds ($3 \times 3 \times 6$ mm), were tested for each condition (green, sintered and polymer impregnated) and the compressive strength was evaluated as the maximum applied stress. Toughness was estimated as the strain energy density, G_C, from the integral of the nominal stress–strain curves at 20 % strain. Likewise, for 13-93 scaffolds, fifteen parallelepipedic samples ($\sim 3.7 \times 3.7 \times 4.7$ mm), were tested for each condition. In this case, toughness was estimated as the strain energy density, G_C, at 30 % strain.

Mechanical characterization was also done by four-point bending tests. 45S5 and 13-93 bioglass scaffolds were cut to final dimensions around $25 \times 4 \times 2$ mm with rods aligned parallel to the length and width of the sample. Fifteen and nine samples of 13-93 and 45S5 bioglass, respectively, were tested for each condition.

The flexural strength of each structure, σ_f, was calculated from the maximum load applied during the test, F_{max}, using the following equation:

$$\sigma_f = 3 \ (L_2 - L_1) \ F_{max} \ /2wh^2 \qquad (2.3)$$

where $L_1 = 10$ mm and $L_2 = 20$ mm are the distances between the two upper and two lower support cylinders, respectively, w the width of the specimen and h its thickness (Figure 2.3). Toughness of tested specimens was estimated as the strain energy density, G_f, from the integral of the load (F) displacement (x) curve (normalized by the effective volume of the sample) at 0.5 mm stroke. The flexural modulus of each sample was also measured with the aid of an extensometer, using the following equation:

$$G_f = \int_0^{0.5} F. \ dx \qquad (2.4)$$
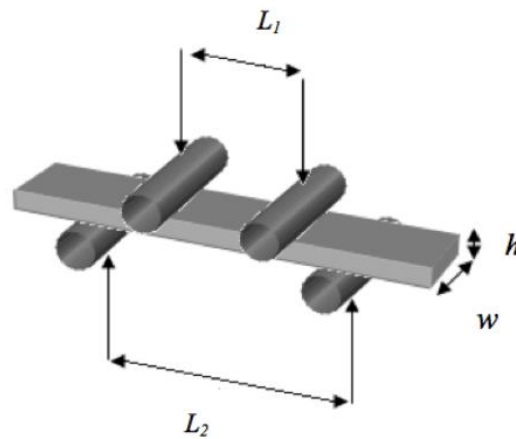
Figure 2.3. The schematic diagram of 4-point bending test.

All magnitudes were expressed as mean with standard deviation as error, with the exception of strength data for 13-93, where the larger number of sample enabled an analysis using Weibull statistics [228]. Weibull's failure probability, P, is given by

$$P = 1 - exp[-(\sigma/\sigma_0)^m] \hspace{3cm} (2.5)$$

where m is the Weibull modulus, which is a measure of sample reliability and σ_0 is the central value of the strength distribution.

The flexural strength of 13-93 individual rods, σ_f, obtained by simple extrusion of both water and ethanol-milled inks through the selected nozzle (410 μm diameter) followed by the same heat treatment as full scaffolds (Section 2.2.4), was also measured in 3-point bending (with L=10 mm separation between rods) in the same universal testing machine and at the same crosshead speed, using 30 samples per material. Bar diameters (d) after sintering for each material were evaluated by optical microscopy as the average of 50 measurements, and then used to evaluate the strength of the bars from the fracture load (F) in the bending tests, using the following equation:

$$\sigma_f = \frac{FL}{\pi d^3} \hspace{3cm} (2.6)$$

2.6 *In vitro* testing

The biological performance of bare bioglass-derived scaffolds was evaluated *in vitro* by immersion in simulated body fluid (SBF), and in the case of 13-93 bioglass samples also by cell culture experiments, as described below:

2.6.1   SBF immersion tests

Simulated body fluid (SBF) solutions were prepared according to Kokubo traditional procedure [229]. Table shows the ionic composition of human blood and simulated body fluid.

It should be noted that preparation of clear SBF with no precipitation due to highly supersaturated solution and with respect to apatite is not easy and needs careful preparation to prevent precipitation.

Table 2-2 The ionic composition of human and simulated body fluid [230].

Species	Human blood plasma/mM	Simulated body fluid/mM
Na^+	142	142
K^+	5	5
Mg^{2+}	1.5	1.5
Ca^{2+}	2.5	25
Cl^-	103	147.8
HCO_3^-	27	4.2
HPO_4^{2-}	1	1
SO_4^{2-}	0.5	0.5
pH	7.2	7.2

45S5 bioglass scaffolds sintered at 550 °C (amorphous) and 1000 °C (highly crystalline glass-ceramic) and 13-93 bioglass sintered scaffolds made from water- and ethanol-milled powder were immersed in polyethylene bottles containing the SBF solution, and kept for up to 8 weeks, without shaking, in an incubator at 37 °C. Weight loss, HA deposition, pH and mechanical properties evolution with immersion time were evaluated for each type of sample. Different samples were used for each immersion time and type of measurement.

When immersed in SBF, conversion of the bioactive glass to an HA-like material was accompanied by a weight loss. The weight loss was defined as $\Delta W/W_0$, where $\Delta W=W_0-W_t$, W_0 is the initial mass of the scaffold, and W_t is the mass at time t. A ratio of 1 g of scaffold to 100 mL of SBF was used in the conversion experiments, and two scaffold samples were used per immersion time. After retrieving them from the containers, the scaffolds were dried at 60 °C for 1day and then weighed. The surface of selected scaffolds was also viewed by SEM to analyze the progress of HA layer deposition.

Evolution of pH was measured on separate samples. After retrieving these scaffolds from SBF solution, the solution was cooled to room temperature, and its pH was measured. Separate samples were used also to evaluate the evolution of their mechanical properties with immersion time by compressive tests (Section 2.5), using a minimum of 9 samples per condition.

2.6.2   Cell culture study

A cell culture study was performed in 13-93 scaffolds to rule out potential cytotoxicity issues. Gibco® culture medium (Thermo Fisher Scientific Inc. MA, USA) was used: DMEM, 1 % hepes, 10 % FCS, 1 % pen-strept, 1 % L-Glut. Scaffolds were sterilized by UV radiation during 12 hours. After that time they were deposited on wells from a 24-wells plate and incubated with Poly-Lysin (0.1 % in PBS) during 4 to 6 hours to enhance cell attachment. Then, 50 000 C2C12 cells were deposited on the scaffolds as a drop in whole medium during 2 to 4 hours. Later, 1 mL of whole medium was added to each well and the plate was incubated at 37 °C in humidity. Cell counting was done at day 1, 4, 8, 11 and 16 of culture. Three scaffolds per biomaterial (water-milled 13-93, ethanol-milled 13-93, and HA as control) were analyzed.

Cells were stained with Hoechst 33342 (10 μg/mL) to label cell nuclei and Propidium Iodine (0.1 %) to label dead cells. Biomaterials were analyzed by confocal microscopy (FluoView 1000, Olympus) using 405 nm and 565 nm laser lines to excite fluorochromes and 440/40 and 610/20 BP filters for fluorescence emission detection. Biomaterials 3D sets were acquired and, using FV10 software (Olympus), a 3D reconstruction from each scaffold was obtained. Image J software (NIH free software) was used to count cell nuclei using Cell counting and 3D Object Counting plugins.

Chapter 3

Results and Discussion

3.1   Robocasting of 45S5 bioglass-derived scaffolds

This section is discussing issues regarding fabrication of 45S5 bioglass scaffolds by robocasting, sintering, *in vitro* study and toughening approaches.

3.1.1   Optimization of robocasting Ink

As described in section 1.6, the fabrication of the bioglass robocast scaffolds involves as a critical step the preparation of a concentrated colloidal suspension or with a very specific rheological behavior, which enables it to be extruded through a narrow nozzle and then retain shape immediately after deposition. Indeed, the main challenge in the robocating of 45S5 bioglass is ink preparation. This section analyzes the difficulties existing for making a suitable robocasting ink from 45S5 bioglass powders in aqueous medium, and how were they overcome.

3.1.1.1   Stabilization of the 45S5 bioglass suspension

The particle size distribution of the as-milled 45S5 bioglass particles (see Section 2.2.1) used in preparing the inks for robocasting are shown in Figure 3.1. The particles had a wide distribution of sizes, with a median diameter of 4.3 μm.
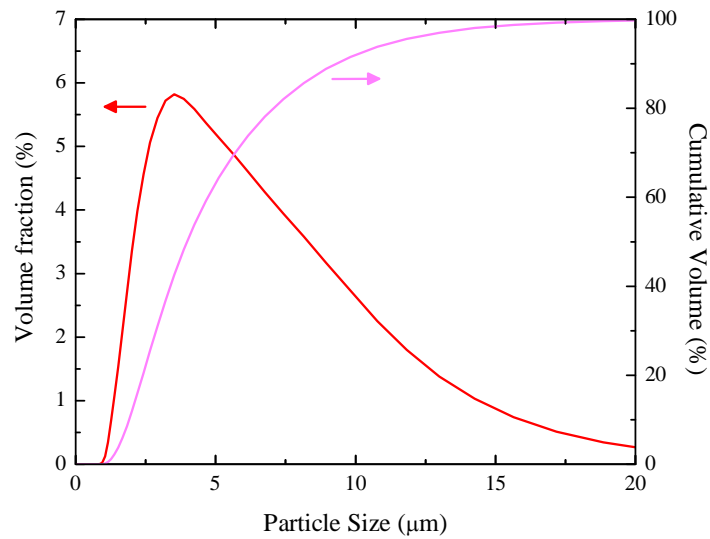
Figure 3.1. The particle size distribution of the as-milled 45S5 bioglass powder.

As the 45S5 bioglass powder was immersed in deionized water, the pH was augmented from 6 to 10 within the first 30 seconds. The fast ionic Na^+/H^+ exchange is responsible for this increase in pH [231].

Figure 3.2 shows that ζ-potential measurements of 45S5 suspensions in the absence and in the presence (at a concentration of 1 wt.% based on the dry mass of the powder) of different dispersants: Darvan C; EasySperse; Targon 1128; PEI and TMAH. PEI and TMAH are cationic dispersants, while the rest of the dispersing agents are anionic.

These ζ-potential *versus* pH profiles could be systematically reproduced in several repeated measurements with standard deviation values smaller than the size of markers used in the plot. These results show that, except in the presence of PEI, there is a common isoelectric point, $pH_{iep} \sim 1.5$, irrespective of the presence or the absence of the other dispersing agents studied. This isoelectric point is close to the values reported for silica [232], suggesting that bioglass particles exhibit a silica type surface.
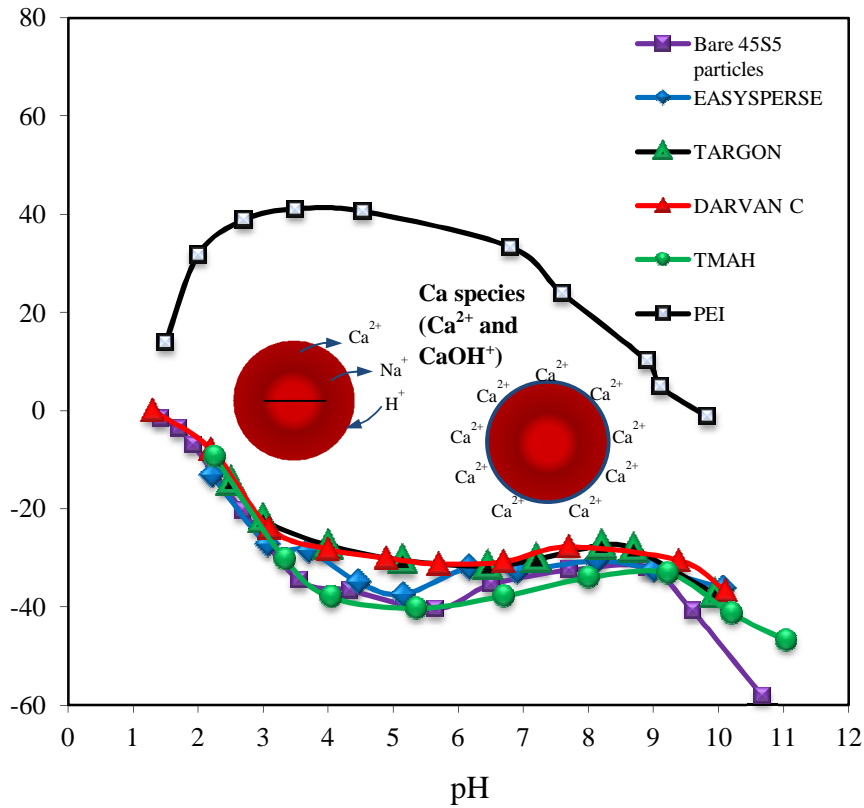
Figure 3.2. Zeta-potential of 45S5 glass particles vs. pH in the absence and in the presence of a fixed added amount (1 wt.%) of the dispersants tested (Darvan C; EasySperse; Targon 1128; PEI and TMAH). Schematic diagrams of the proposed solid/liquid interface events explaining the results for the lower curves are included.

The electrophoretic curve obtained in the presence of the cationic PEI is completely different, showing positive ζ-potential values from the acidic region up to the isoelectric point at about pH_{iep} 10, with a maximum value around +40 mV within the pH range of 3–5. This ζ-potential versus pH curve is similar to that reported elsewhere [233] for SiC particles with a naturally occurring surface oxide (SiO_2) layer. The fact that the curve changes so dramatically from that of the bare powder proves that PEI species are specifically adsorbed at the surface of the 45S5 bioglass particles.

The decreasing ζ-potential values upon shifting pH from the maximum plateau towards the more acidic region can only be attributed to the increase of ionic strength of the medium. On the other hand, the decreasing trend observed in ζ-potential for pH > 4–5 is attributed to a decreasing protonation of PEI—Taking into account the acid dissociation constant, pK_a, values of PEI (4.5 for primary, 6.7 for secondary, and 11.6

for tertiary amine groups) [233-234], PEI is expected to exist in its fully protonated form (PEI–H$^+$) only below pH 5 and to a concomitant increase of negative surface charge density that the specifically adsorbed protonated PEI species tend to neutralize. Interestingly, the presence of the other cationic dispersant (TMAH) did not cause any apparent effect on ζ-potential with the respective curve following a similar profile as those observed in the presence of anionic dispersants. This suggests that TMAH ions are not prone to be specifically adsorbed at the surface of the 45S5 bioglass particles. A similar behaviour has been reported elsewhere for TMAH towards a silica-like (SiC) surface [235]. In any case, the low dissociation degree of cationic additives under the high pH environment created by the bioglass powder in water [233-234] reduces their electrostatic affinity towards the surface, although this does not hinder the specific adsorption of PEI species. Besides, adsorbed PEI is not effective as electrostatic dispersant at the dispersion environment, pH ~10, since this pH coincides with the isoelectric point for this system (Fig. 3.2). As a consequence, cationic additives are questionable candidates as dispersants for the 45S5 bioglass particles.

For all dispersion conditions other than in the presence of PEI, continuous decreases of ζ-potential curves were registered up to pH ~ 5–6 where the trend is reversed and a slight increase is observed up to about pH 8, and then a new sharp decrease is evident within the more alkaline region (Figure 3.2). This evolution means that besides H$^+$ and OH$^-$ ions, cationic species, likely Ca^{2+} and CaOH$^+$ leached from the 45S5 Bioglass, are also playing the role of potential determining ions, as schematized in Fig. 3.2. This hypothesis is supported by the findings of Nardin et al, [236] who reported superior isoelectric point of glass fibres in basic medium, when the measurements were made in Ca(II) solutions in comparison to those performed in the absence of dissolved Ca species. Thermodynamic calculations related to flotation response as a function of solution pH for calcite also suggested the presence of Ca^{2+} as potential-determining ion together with other ions (HCO$_3^-$, CO$_3^-$, H$^+$, and OH$^-$) [237].

Interestingly, the highest absolute ζ-potential values were generally measured for the bare particles. Also, the electrophoretic curves did not shift towards the acidic direction as one would expect if sensitive surface adsorption of negatively charged species was taking place, even in the presence of the anionic polyelectrolytes. This can be understood considering: (i) the expected low dissociation degrees of polyelectrolytes in the lowest pH region; (ii) the electrostatic repulsive interactions between the dissociated

dispersant species and the negatively charged surface of the 45S5 particles in the remaining pH range, which are opposing to adsorption. Therefore, the apparent upwards shift observed for ζ-potential curves in the presence of all additives does not support the hypothesis of extensive surface adsorption of anionic species. However, one cannot completely exclude this possibility because some masking effects might concomitantly occur: (i) an increase of the hydrodynamic hindrance slowing the electrophoretic mobility of the particles; (ii) a consequent shift of the shear plane to larger distances where ζ-potential is smaller. Even though, a significant adsorption of these dispersants at the surface of 45S5 Bioglass particles cannot be expected.

Consequently, the maximum solid loadings achieved by adding different amounts of all these dispersants was low, as shown in Table 3-1. Maximum values—35 vol.% at most, for 2 wt.% Darvan C—were achieved with anionic dispersants, as could be expected. Although being in good accordance with solid loadings reported for 45S5-derived bioglass slurries [63], such low solid volume fractions are not suitable for the preparation of inks for robocasting, since they imply high shrinkages upon drying and sintering and, thus, low dimensional and shape control of the fabricated scaffolds. The main reason behind this might be the increase of the apparent size of dispersed particles with a polyelectrolyte adlayer stretched into the solution due to the repulsive electrostatic interactions among themselves and the negatively charged surface of 45S5 Bioglass, as sketched in Figure 3.3. The thick adlayer increases the effective solids volume fraction and strongly limits the maximum achievable solids loading in the suspensions.

Table 3-1. Maximum solid loadings achieved in aqueous 45S5 bioglass suspensions with different added amounts of the various polyelectrolyte dispersants tested.

Dispersant	Type	Maximum achievable solid loadings (vol.%)			
Dispersant concentration (wt.%)		0.5	1.0	1.5	2.0
Darvan C	Anionic	29.8	31.9	33.8	35.3
EasySperse	Anionic	28.1	29.2	31.5	33.1
Targon 1128	Anionic	22.5	23.7	25.1	27.8
TMAH	Cationic	21.2	22.5	23.8	26.5
PEI	Cationic	19.5	22.2	23.4	26.7

Moreover, even with these insufficiently concentrated suspensions it was not possible to obtain dense pastes/gels with the appropriate rheological behaviour. Reasons for the unsuitability for robocasting of the best systems produced with anionic dispersants include: (i) the leaching of ionic species from the 45S5 Bioglass and the consequent increase of ionic strength of dispersing medium [238] which negatively affects the colloidal stability of the suspension by screening the electrostatic repulsions among the particles—; (ii) the loose attachment of the anionic species at its surface; (iii) the high pH environment created by the dissolution/ionic exchange undergone by the 45S5 Bioglass powder that hinders the dissociation of cationic additives commonly used for inducing the fluid-to-gel transition necessary for robocasting.
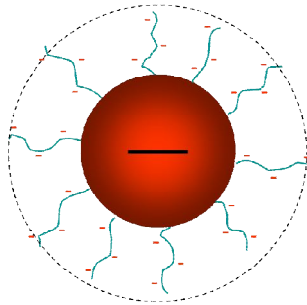
Figure 3.3. Schematic diagram of the adlayer formed around 45S5 bioglass particles by adsorption of fully dissociated anionic polyelectrolyte chains, which stretch into the solution due to the repulsive electrostatic interactions among themselves and the negatively charged surface of the particle. The effective particle size is increased, and this strongly limits the maximum achievable solids loading in the suspensions. surface of the particle. The effective particle size is increased, and this strongly limits the maximum achievable solids loading in the suspensions.

Therefore, it became clear that the traditional approach—where anionic/cationic interactions of species added to the system in different successive steps are used to promote the rheological transition from a fluid-like behaviour (starting suspension) to a paste-like character (robocasting ink)—could not offer successful prospects for robocasting processing of 45S5 bioglass.

Based on all the above considerations, a completely different and simplified approach was adopted: searching for a single additive that could adsorb on the 45S5

bioglass particles and act as both dispersant and binder for robocasting. In this pursue, carboxymethyl cellulose (CMC) was regarded with interest due to its aptitude to play different but complementary roles as processing additive and the fact that CMC molecules possess a less accentuated anionic character, which facilitates adsorption.

Adsorption of CMC on equally charged surface has been reported by Girod *et al.*[239] and attributed to hydrogen bonding between deprotonated carboxylic groups and surface hydroxyl groups [240], an hypothesis also supported by the findings of Hoogendam *et al.* [241] according to whom the oxide surfaces have the possibility to locally adjust their charge, thereby reducing the negative charge and facilitating adsorption. So, despite the electrostatic repulsive interactions, the dissociated CMC chains could be adsorbed in localized surface sites of 45S5 bioglass powder. CMC has also the ability to play different roles (dispersant, binder, thickening/gelation agent enhancing the viscosity of the dispersing solution) depending on its molecular weight, M_W.

Figure 3.4 compares the ζ-potential curves for the bare 45S5 glass particles with those measured in the presence of 2 wt.% of carboxymethyl cellulose additives with two different molecular weights(CMC-35, $M_W = 35\,000$ g mol^{-1}, and CMC-250, $M_W = 250\,000$ g mol^{-1}). All ζ-potential curves show similar features to those already seen in Figure 3.2: common isoelectric point (pH$_{iep}$ ~ 1.5), continuous decrease up to pH ~ 5−6, slight increase up to about pH 8, and then a new sharp decrease in the more alkaline region. Again the highest absolute ζ-potential values were generally measured for the bare particles and the electrophoretic curves did not shift towards the acidic direction as one would expect if sensitive surface adsorption of negatively charged species was taking place. Therefore, adsorption between the dissociated CMC molecules—which are fully dissociated at pH > 5.5 [242] and the negatively charged surface of the 45S5 bioglass particles is not electrostatically driven because both have the same negative polarity.

Consequently, the adsorption is likely to occur through small chain segments, with laces and tails extending to the solution. Under these conditions, the hydrodynamic hindrance might increase and the electrophoretic mobility of the particles is expected to decrease. Furthermore, the shifting of shear plane to larger distances where ζ-potential is smaller would contribute to decrease the absolute value of ζ-potential, as observed in Figure 3.4.

Nonetheless, despite the lack of electrostatic affinity, the CMC additives enabled increasing the solids loading up to 45 vol.% and varying the flow/elastic properties of the colloidal suspensions to values suitable for their use as robocasting inks, as will be discussed in the following section.
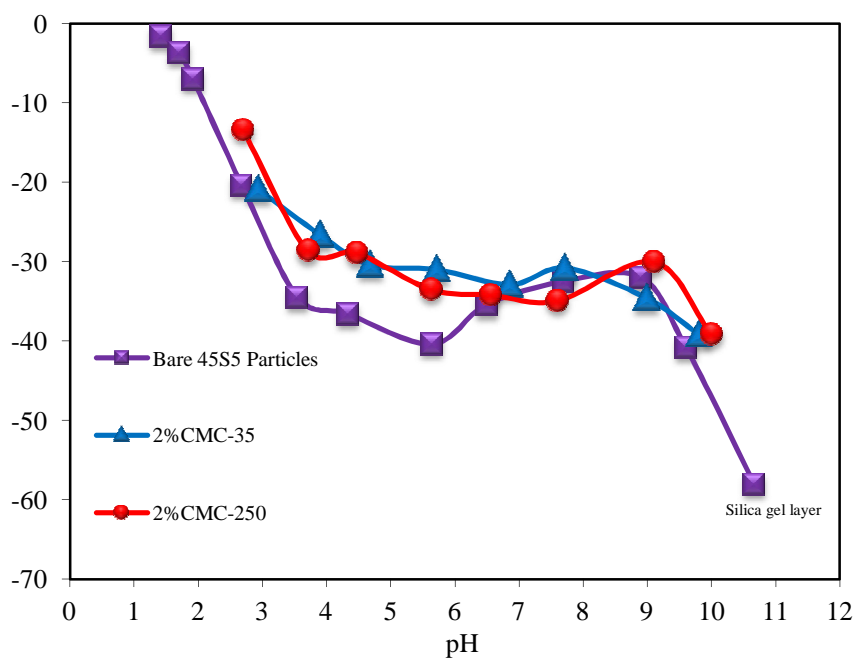
Figure 3.4. Evolution of zeta potential of the 45S5 bioglass particles before and after the incorporation of the indicated CMC additives

3.1.1.1   Rheology of 45S5 bioglass robocasting inks

To prove this finding that CMC is an appropriate single additive for making the robocasting ink, a more detailed rheological study of the stabilized suspensions is essential.

Figure 3.5 shows a plot of the shear elastic (storage) modulus, G', as a function of shear stress, τ, for 45 vol.% suspensions with 0, 1 and 2 wt.% added concentrations of CMC-35 or CMC-250.
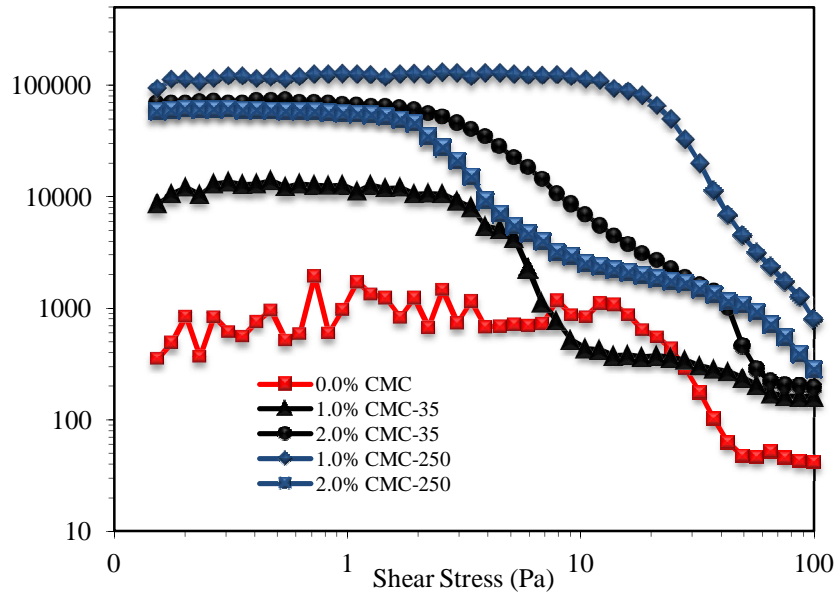
Figure 3.5. Log-log plot of the shear storage modulus, G', as a function of shear stress, τ, for 45 vol.% 45S5 suspensions with indicated amounts of CMC-35 or CMC-250 additives.

An initial plateau (linear viscoelastic region) is observed in these curves and then, at a given shear stress value, the elastic modulus suddenly drops, indicating the disruption of the gel network. The shear stress at which this structural change occurs is known as the yield stress (τ_y). High values of both the initial elastic modulus and yield stress are key factors for a good performance of colloidal inks for direct-write assembly, since they need to retain shape upon deposition and the yield stress, which is also the shear stress in the absence of shear motion, represents the minimum stress leading to deformation of the static form of the material and be capable of rigidly spanning gaps in the underlying layers. The profiles in Figure 3.5 reveal interesting features:

1- In the absence of CMC the G′ values are too low for robocasting and the curve roughness indicates the low consistency and poor flow properties of the suspension. Although being difficult, the possibility of preparing this 'pasty-like' system containing a significantly higher solids loading in comparison to suspensions with the tested anionic dispersants, supports the interpretation given above of an increased adlayer thickness in the presence of this polyelectrolyte (Figure 3.3).

2- In the presence of CMC the ink stiffness increased by 1–2 orders of magnitude, with G′ and yield stress (τ_y) values being strongly dependent on the M_W and the amount of CMC additive.

3- CMC-35 acts as dispersing and gelling agent especially at 1 wt.%, exhibiting G′ ~ 10^4 Pa and τ_y ~ 2–2.5 Pa. This additive is expected to adsorb at the surface of the particles in an airy configuration as sketched in Figure 3.6. The moderate surface coverage at 1 wt.% enables CMC-35 molecules to easily align under flow, while the adlayer thickness and their interpenetration under near rest conditions confers the system some stiffness. The stiffness of the gel network was significantly enhanced to G′ ~ $7 \cdot 10^4$ Pa by increasing the added amount to 2 wt.%, while τ_y remained practically unchanged, although the decrease of G′ with increasing shear stress became slower. Nonetheless, this comes at the expense of a reduction in the freedom of the chain to align along the flow direction, which hinders the deposition process.

4- The higher M_W of CMC-250 confers it a stronger thickening effect and at the lower concentration used (1 wt.%), the relatively low surface coverage is likely enabling adsorption of individual molecules in more than one particle through a bridging flocculation mechanism Figure 3.6. This is the probable reason for the highest values of G′ (~ $12 \cdot 10^5$ Pa) and the longest elastic plateau measured under these conditions, with a τy that is about one order of magnitude larger than in the presence of CMC-35. Increasing the added amount of CMC-250 to 2 wt.% enables a better surface coverage and decreases the probability of a given molecule to be adsorbed in more than one particle, therefore cancelling the bridging flocculation effect. This might explain the observed decreases in G′, by about one half, and of τ_y, by more than one order of magnitude, relatively to the values measured in the presence of 1 wt.% CMC-250. As for the lower M_W CMC, the different interaction modes of CMC-250 molecules with the surface of bioglass particles are sketched in Figure 3.6.
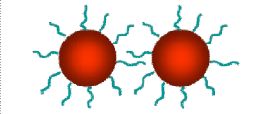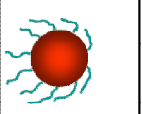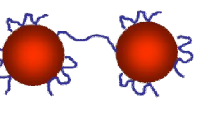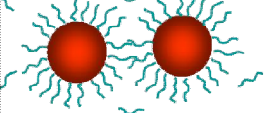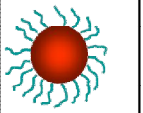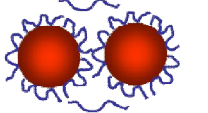
Added amount (wt.%)	CMC-35		CMC-250
	At rest (chain entanglement)	Flowing $\longrightarrow$	Bridging at low surface coverage
1			
2			

Figure 3.6. Schematic diagram of the proposed configurations of CMC molecules around the 45S5 bioglass particles as a function of molecular weight (CMC-35 and CMC-250) and added amount. Explanation is given in the text.

According to these results, high molecular weight CMC-250 was found more appropriate for the preparation of inks for robocasting.

The flow properties of 45 vol.% suspensions prepared using different amounts of this CMC as the sole binding agent are shown in Figure 3.7. Figure 3.7a shows the shear stress versus shear rate curves, and Figure 3.7b the apparent viscosity v*ersus* shear rate curves . All systems exhibit an evolution of shear stress *versus* shear rate that approaches the Bingham plastic behaviour, typical of suspensions containing polymeric binder/thickening agents. The polymer molecules help forming a network structure under rest or near rest conditions, which is then gradually disrupted under the applied shear stress field as the polymeric molecules align along the flow direction.
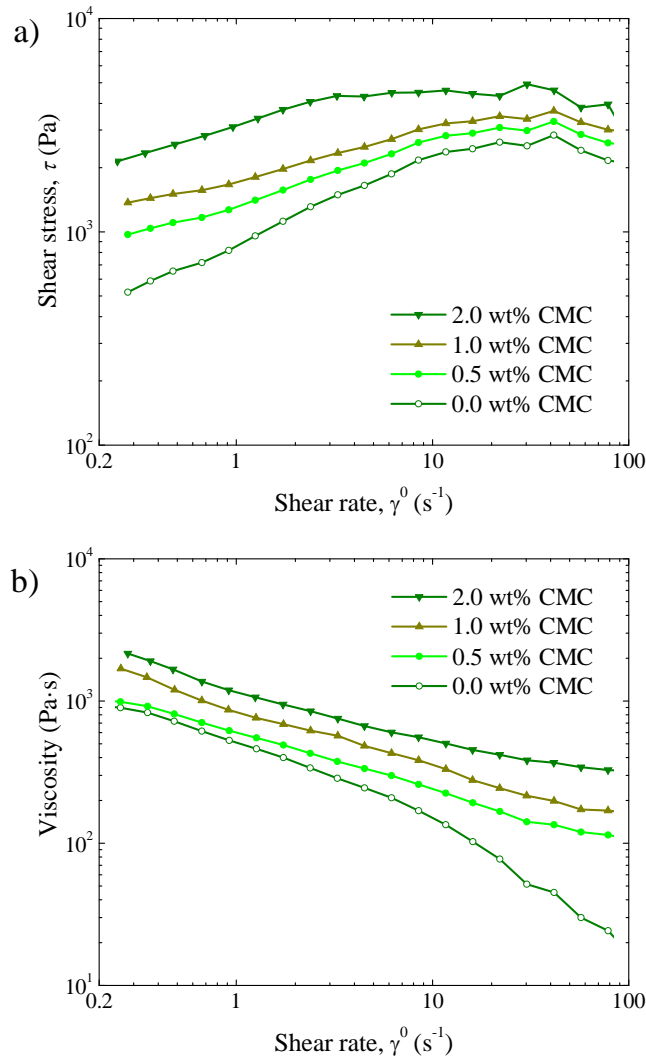
Figure 3.7. Plots of (a) shear stress and (b) apparent viscosity as a function of shear rate for 45 vol.% 45S5 bioglass suspensions with indicated amounts of CMC as binder.

The initial data plotted in Figure 3.7a (up to 3 s^{-1})were fitted with the Herschel-Bulkley model [235], which is described as:

$$\tau = \tau_y + K(\gamma^0)^n \qquad\qquad (3.6)$$

where γ^0 is the shear rate, τ is the shear stress, τ_y is the yield stress, n is the shear thinning exponent and K is the viscosity parameter. The yield stress is the shear stress in the absence of shear motion and represents the minimum stress leading to deformation of the static form of the material. The model parameters were estimated as $n = 0.66 \pm 0.06$ and $K = 580 \pm 50$ Pa·s^n for suspensions containing up to 1 wt.% of CMC and $n = 0.36 \pm 0.03$ and $K = 2600 \pm 200$ Pa·s^n for samples with 2 wt.%.

Figure 3.8 shows the evolution of the estimated yield stress, τ_y, obtained from Figure 3.7 and the average elastic (storage) modulus, G′, obtained from Figure 3.5 at low shear stress of suspensions with added CMC. Modulus values were calculated as the average of the virtually constant G′ data within the 0.1–1 Pa stress range.
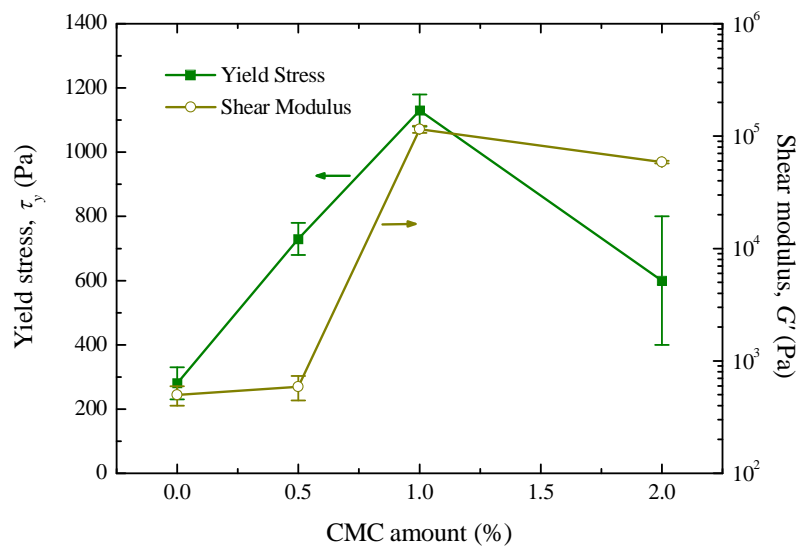
Figure 3.8. The effect of the amounts of CMC on the yield stress, τ_y, and the average elastic modulus at low stress (0.1-1 Pa), G', of 45 vol.% 45S5 bioglass suspensions. G' data were calculated from previous results Error bars represent standard deviations (from fitting in the case of τ_y).

These parameters reflect, respectively, the strength and stiffness of the attractive network structure resulting from interactions between 45S5 bioglass particles, CMC and

water. In the absence of CMC, both the yield stress and the modulus of the suspension are very low. Upon addition of CMC, the yield stress increases linearly with the amount of binder up to a concentration of 1 wt.%, decreasing at 2 wt.%. This thickening effect promoted by CMC might be attributed to chain entanglement of the molecules adsorbed at the surface of the particles and/or to an increased viscosity of the dispersing medium. On the other hand, the elastic modulus increase first very slowly, then dramatically (by 2 orders of magnitude) at 1 wt.% CMC additions, and finally decreases at 2 wt.% CMC concentrations.

The dramatic change in modulus observed for 1 wt.% CMC indicates a fluid-to-gel transition attributed to the occurrence of bridging-flocculation, in which the longer polymeric chains might adsorb at the surface of different neighboring particles (Figure 3.6).

Increasing the amount of CMC-250 further, leads to a higher degree of surface coverage and a denser adsorbed layer, which decreases the probability of one polymeric chain to adsorb in more than one particle, thus hindering bridging-flocculation and reducing both the modulus and the yield stress.

Since high values of yield stress and modulus are desired features for robocasting inks, 1 wt.% was considered as the optimal CMC amount. This concentration yielded maximum network stiffness (> 100 kPa), and yield stress (> 1 kPa) at a relatively low viscosity, which facilitates flowability through the deposition nozzle. Indeed, such suspensions exhibited both very good flowability (unlike suspension with higher CMC concentrations) and excellent shape retention capacity upon deposition, which made them ideal inks for robocasting.

Indeed Figure 3.9 shows three dimensional porous scaffolds made of multiple layers produced by robocasting using this ink. These results demonstrate that it is possible to create well shaped, uniform lattices having rod sizes in the range of 250-410 µm using 45S5 gels with 1 wt.% CMC-250 as a single additive.
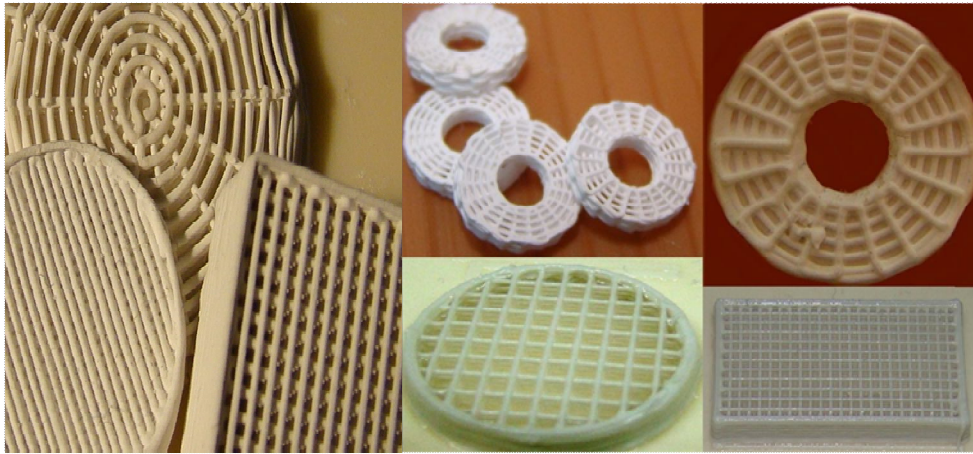
Figure 3.9. 3D porous scaffolds produced by robocasting from a 45S5 bioglass ink with 1 wt.% CMC-250 additive optical image showing different scaffolds geometries with up to 60 layers.

3.1.2   Sintering and microstructural characterization of robocast 45S5 scaffolds

In this section the results of the sintering study performed on 45S5 scaffolds fabricated by robocasting within the temperature range 500-1050 ºC are discussed. The scaffolds used for the study consisted of a tetragonal mesh of cylindrical rods, created using the optimized ink recipe described in the preceding section and the CAD model detailed in section 2.2.3. Figure 3.10 shows SEM micrographs of an as-cut scaffold sintered at 1000 ºC for 1 h. Note the regularity of the structure and the straight geometry of the rods, attesting the quality of the ink used for its fabrication.
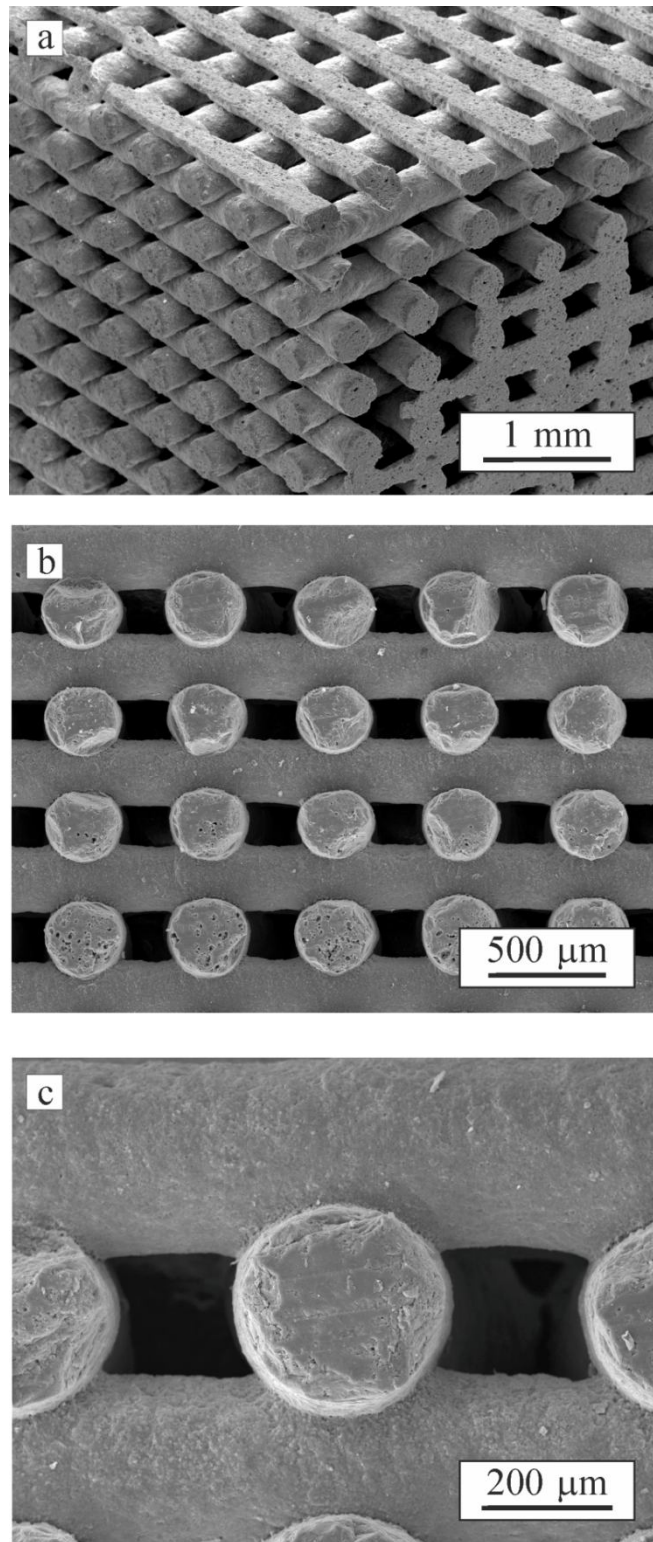
Figure 3.10. SEM micrograph of an as-cut 45S5 bioglass scaffold sintered at 1000 °C.

3.1.2.1   Thermal analysis

Figure 3.11 presents TGA and DTA results of 45S5 bioglass as-received powder and of the as-dried ink. The as-received powder underwent a slight weight loss up to ~ 900 ºC, with the more marked changes in the range of 200–400 ºC (Figure 3.11a). This weight loss is associated to the evaporation of free water and the release of surface –OH groups, a phenomenon reflected as an endothermic effect, especially observed between room temperature and 200 ºC in the DTA plot (Figure 3.11b). After recovering the base line, a second endothermic dip centered at ~560 ºC is observed, which is attributed to the first transition temperature of the glass (T_{g1}). This is followed by an exothermic effect starting around ~ 600 ºC and with a maximum at about 685 ºC (T_{p1}), which is attributed to crystallization, in agreement with previously reported values [14-15][202]. A second exothermic peak centred at ~ 850 °C (T_{p2}), attributed to the formation of a secondary crystalline phase, is followed by a new endothermic valley associated to a second glass transition (T_{g2} ~ 910 °C) of the remaining glass matrix [244]. Melting clearly occurred above 1100 °C, as deduced from the associated endothermic valley.
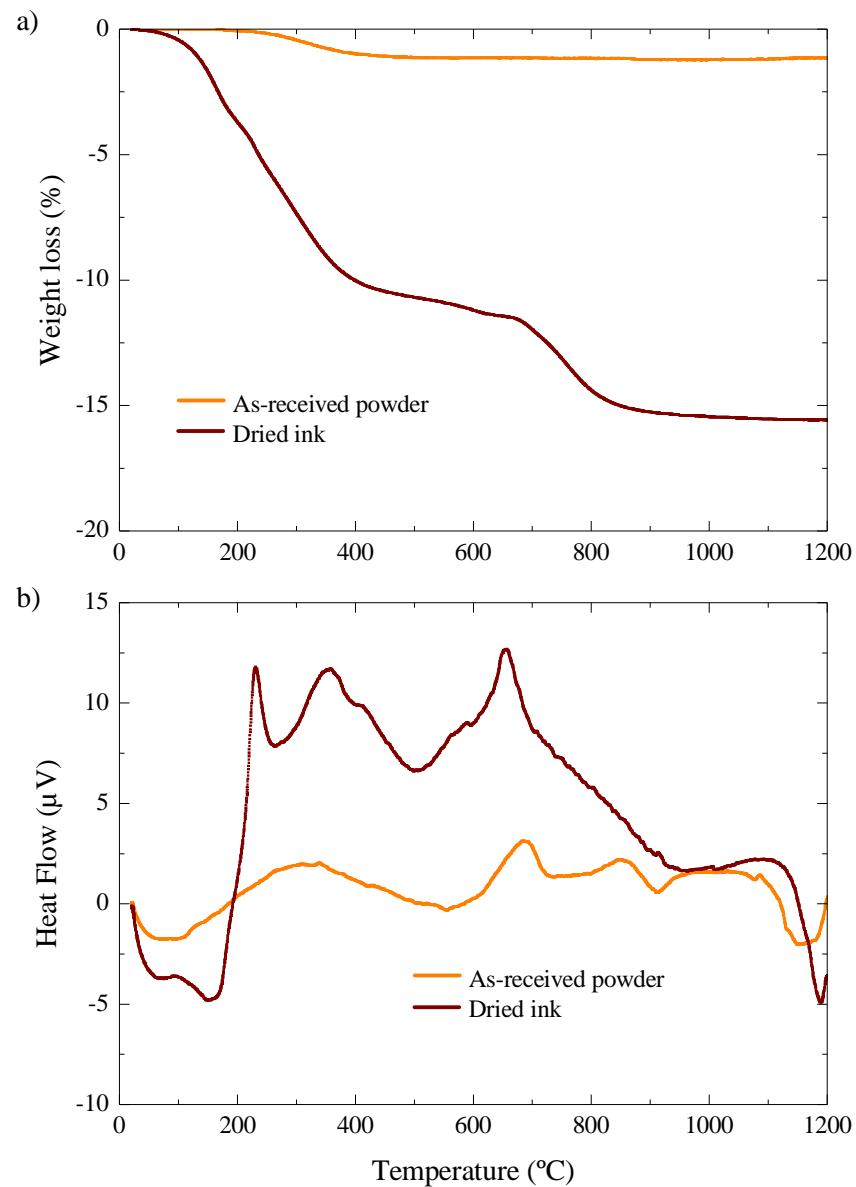
Figure 3.11. Results of the simultaneous (a) thermal gravimetric analysis (TGA, weight loss) and (b) differential thermal analysis (DTA, heat flow) of 45S5 bioglass as-received powder (light color) and as-dried robocasting inks (dark color).

The weight changes (Figure 3.11a) and the corresponding thermal effects (Figure 3.11b) were greatly enhanced in the dried ink, probably as a result of a more extended surface hydration of the powder undergone while in contact with dispersion

media (ball milling and ink preparation), and of the burnout of CMC additive. Indeed, the weight loss centred in the range of 700–800 °C, but extending beyond these limits, is attributed to the burnout of carbonaceous remnants from CMC degradation. This degradation occurred in two successive steps, originating two exothermic peaks at ~225 °C and ~350 °C (Figure 3.11b), as confirmed by a TG/DTA test performed on pure CMC (results are shown in Figure 3.12). This suggested the use of a debinding treatment at 400 °C for 1 h prior to sintering.
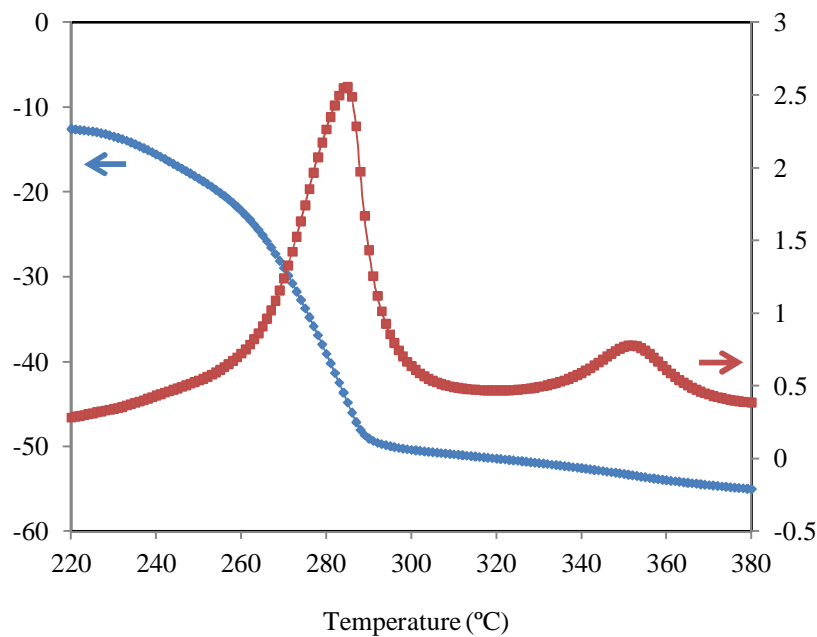
Figure 3.12. Result of TGA/ DTA for CMC-250 powder

Interestingly, the thermal events T_{g1} and T_{p1} occurred in the ink, respectively, at about 60 °C and 30 °C below the corresponding temperatures in the as-received 45S5 bioglass powder, implying a concomitant shift of the intermediate exothermic effect associated to the nucleation step. This shift is attributed to a change in the composition at/near the particles' surface as a result of leaching of modifier cations (Na^+, Ca^{2+}) during wet-milling, and also to the reduction in the particle size [245-246]. Besides, T_{p2} and T_{g2} cannot be distinguished for the dried ink, possibly because they are also shifted to lower values and became overlapped with the peak for first crystallization.

The apparent increase of melting temperature of the ink is also consistent with the leaching of modifier cations into the milling media.

3.1.2.2   XRD analysis

These results obtained from thermal analysis are in good agreement with the XRD results shown in Figure 3.13. The 45S5 bioglass remained amorphous up to above 550 °C but there is evidence of crystallization already at 600°C. The angular location and intensity of the new peaks appearing upon crystallization of 45S5 bioglass closely match the standard JCPDF database 77-2189, confirming that the major crystalline phase is $Na_2CaSi_2O_6$. Minor peaks of a secondary phase, attributed to $Na_2Ca_4(PO_4)_2Si_2O_4$ (JCPDF database 32-1053), were also identified on samples sintered at 1000 °C, all in good accordance with previous reports [14][207-208][247].
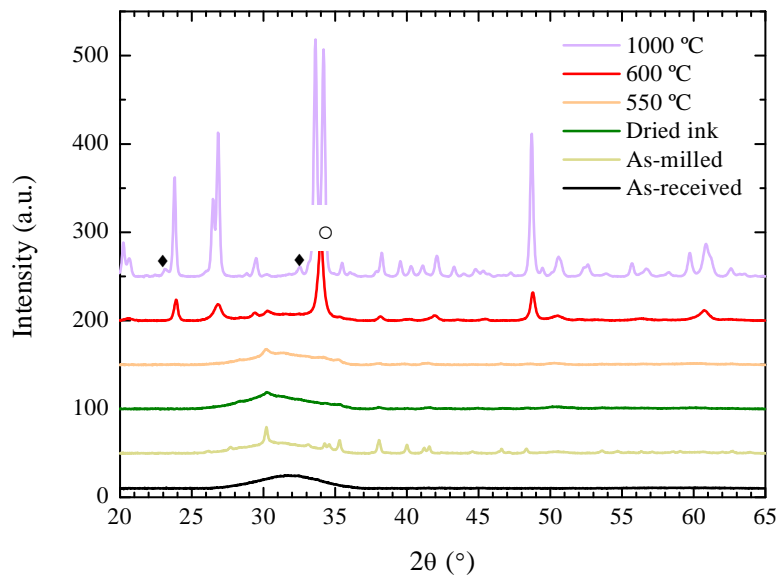
Figure 3.13. X-Ray diffractograms of 45S5 bioglass as-received and as-milled powders, and ground scaffolds sintered at the indicated temperatures. Sodium carbonate (Na₂CO₃, JCPDF database 19-1130) peaks are clearly visible on the as-milled powders, and barely on the sample sintered at 550 °C. Peaks at 600 °C, correspond to Na₂CaSi₂O₆ (JCPDF database 77-2189) crystallized from the glass. At 1000 °C, Na₂CaSi₂O₆ remains the main crystalline phase with some additional peaks, noted by ♦ and ○, corresponding to Na₂Ca₄(PO₄)₂Si₂O₄ (JCPDF database 32-1053) and tetragonal zirconia (ZrO₂, JCPDF database 72-7115), respectively.

There are, however, some peaks already observable at 550 °C and below, which correspond to sodium carbonate (Na2CO3, JCPDF database 19-1130) formed during the milling process in ethanol, with some small contribution of tetragonal zirconia from the milling media and container. The sodium carbonate, deposited onto the surface of the particles during milling, partially dissolves in water during ink preparation, which produces a substantial decrease in the intensities of the peaks corresponding to this extraneous phase. Actually, the peaks more clearly observable in the dried ink or in samples sintered at 550 °C, located at 30.2° and 35.3° 2θ, can also be appreciated even at 1000 °C, and are therefore attributed to the overlapping tetragonal zirconia phase rather than the sodium carbonate. Nonetheless, the presence of even small amounts of sodium carbonate in the XRD results support the explanation for the systematic down shift of thermal events (except melting) in Figure 3.11b based on a changed composition, rich in Na+ cations, at/near the particles' surface.

3.1.2.3   **Geometrical analysis**

In order to investigate the dimensional changes of the fabricated scaffolds versus temperature, the cubic shape scaffold were heated up to 1050 °C. Figure 3.14 shows the evolution of scaffolds' macroscopic linear shrinkage and internal dimensions with the sintering temperature, with standard deviations as error bars. The data at room temperature correspond to as-dried green structures. The structure shrinkage during sintering was essentially isotropic, and the scaffolds kept the designed parallel epipedical shape upon sintering for 1 h up to 1050 °C. Above 1050 °C or for longer sintering times at this temperature, indications of melting/softening of the material became evident to the naked eye:the scaffold specimen deformed under its own weight and the shape was distorted, with some material accumulation at the bottom. For instance when treated at 1200 °C for 1 h the samples completely melted and collapsed with almost no remaining macroporosity. Due to the severe distortions they presented, samples sintered above 1050 °C were not characterized.

According to shrinkage curve obtained from measurements of the scaffolds external dimensions, the shrinkage increases steadily with the raise in temperature, although at a somewhat faster rate around the two glass transition temperatures (500-550 ºC, Tg1, and 800-850 ºC, T_{g2}). This result is in good agreement with previous reports [14-16].

The internal dimensions of the scaffolds (the actual size of rod diameter, in-plane spacing and out-of-plane spacing) show the same trend already seen for the shrinkage.
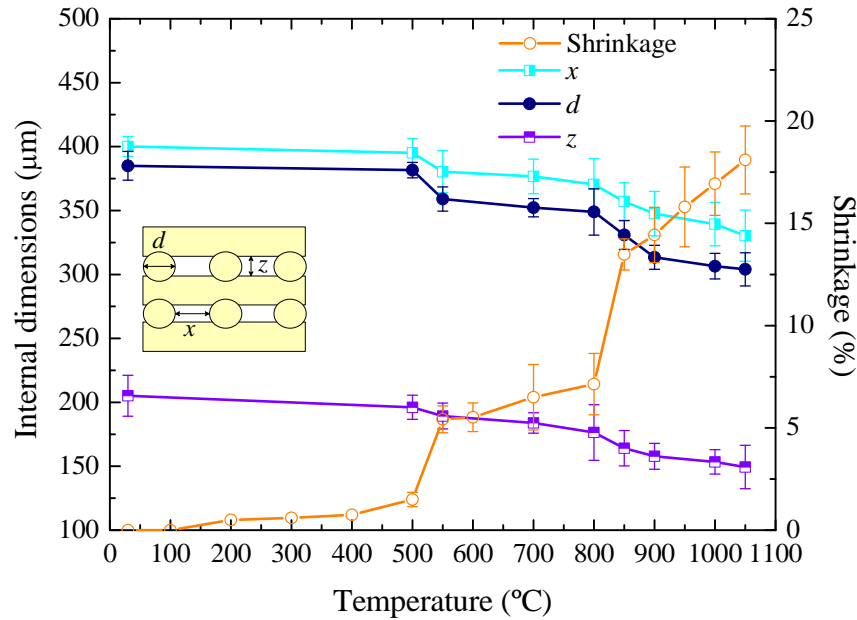
Figure 3.14. The evolution of macroscopic shrinkage and scaffold's internal dimension as a function of sintering temperatures. Data represent mean values with standard deviations as error bars.

Figure 3.15 shows the evolution of total, macro and micro porosity with sintering temperature. The reduction in the different dimensions did not translate into any appreciable change in the pre-designed volumetric macroporosity, which remained constant at around 50 % for all sintering temperatures. Consequently, all the densification produced during sintering, from an as-dried green body porosity of 80 ± 2 % to a minimum of 60 ± 2 % after sintering at 1050 °C, was associated to a reduction of the microporosity within the glass-ceramic rods Meaning that the rods reduced their initial ~ 60 porosity (which roughly agrees with the 45% solid loading of the inks) to around a final 20 % porosity at the highest sintering temperature. Failure to achieve a high densification of the rods even at temperatures so close to the melting point is not an unexpected result, given the poor sintering ability of 45S5 bioglass even

under pressure-assisted sintering [208][248]. Again, the evolution of densification with sintering temperature found in this work (Figure 3.14) is in agreement with the results obtained from shrinkage. There is a steady densification of the scaffolds with increasing sintering temperature, but densification is significantly enhanced around the two glass transition temperatures, and sluggish in-between.
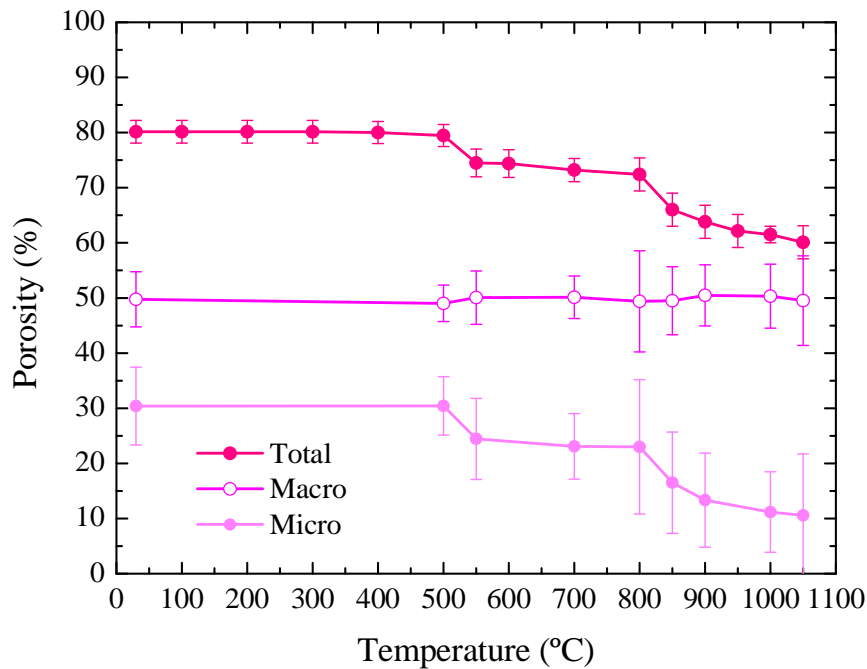
Figure 3.15. The evolution of scaffold porosities as a function of sintering temperatures. Data represents mean values with standard deviations as error bars.

3.1.2.4   SEM microstructural analysis

Figure 3.16 shows SEM micrographs of rod surfaces of scaffold sintered at the indicated temperatures. No sintering occurred up to the glass transition temperature at 550 °C, when the glass softened enough to allow some viscous flow, and even at that temperature the microstructure does not differ all that much from that of green samples (compare top images in Figure 3.16), except for the evidences of inter-particle neck formation (see inset in top-right image of Figure 3.16). At around 600 °C, just after the glass transition, the glass started to crystallize (Figure 3.13), which severely slows down

the densification process by reducing the species diffusivity and increasing the system viscosity. At this point, it is worth mentioning that the maximum percentage of crystallinity achievable in 45S5 bioglass is about 80 % [62], so that even at the highest sintering temperatures the material remains a glass–ceramic. Densification regains pace at around 850 °C, when the residual phosphate-rich glassy phase softens and progresses appreciably with further increasing sintering temperature. Indeed, porosity at the rod surfaces is almost gone at 1000 °C (bottom-left image in Figure 3.16), although there remains a significant level of internal (closed) porosity (Figure 3.10). Up to this sintering temperature, the rod surface microstructure evidences the presence of crystalline grains homogenously embedded in a glass matrix. However, the intergranular glassy phase seemingly disappeared from the surface of the rods upon increasing the sintering temperature to 1050 °C, or the holding time at 1000°C to $\geq$ 2 h and the naked grains became apparent (bottom-right image in Figure 3.16). This inhomogeneous microstructure which consists of bared crystalline particles with virtually no glass matrix reveals an over-sintering process. This over-sintering was accompanied by an apparent increase in surface porosity, while the material's microporosity continued diminishing steadily with the chronothermic increments, as shown in Figure 3.13.

This suggests that the glassy phase—with a very low viscosity so close to the melting temperature—might be draining from the surface towards the interior of the rods and aiding in the reduction of the aforementioned closed porosity.
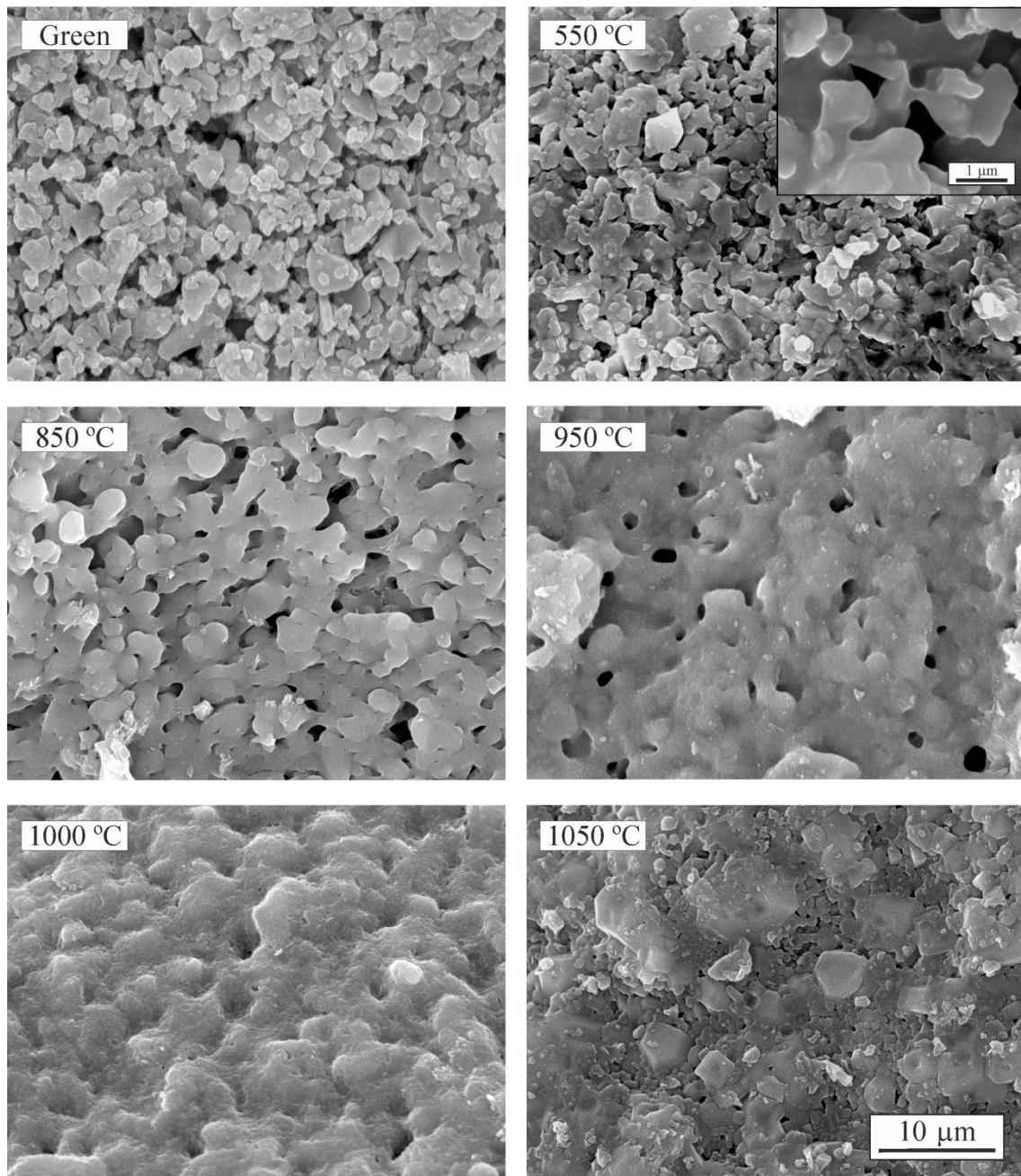
Figure 3.16. SEM micrographs of the rod surfaces of 45S5 bioglass-derived scaffold before and after sintering at the indicated temperatures.

Figure 3.17a and b show the SEM micrographs of a single rod sintered at 550 °C and 1000 °C, respectively. It is obvious from the rod images that not only the rod size decreases at 1000 °C because of the main shrinkage but also the rod surface becomes much smoother showing a glassy feature with less microporosities.
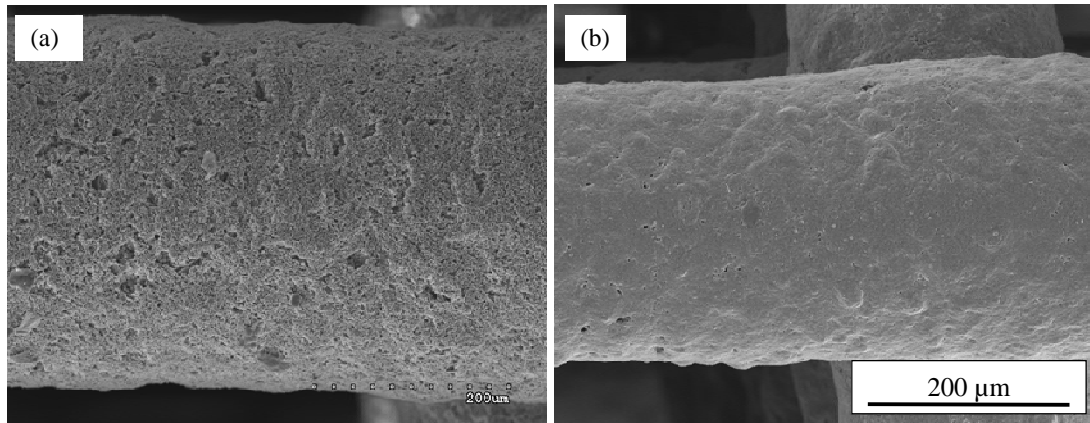
Figure 3.17. SEM micrographs of the 3D 45S5 scaffolds sintered at:(a) 550 °C and (b) 1000 °C.

3.1.3 Mechanical characterization of robocast of 45S5 scaffolds

Figure 3.18 shows representative stress-strain curves of scaffolds as printed and sintered at 550 °C, 800 °C and 1000 °C for 1 h. These samples were tested under uniaxial compression in the direction perpendicular to the deposition plane. The scaffolds show an elastic response almost until the compressive strength of the structure (i.e. the maximum stress) is reached. At this point, the first longitudinal cracks pops-in, breaking the unsupported rod segments close to the joints with adjacent layers, where maximum tensile stresses are located [249-250], and the applied stress drops. As cracking multiplies and propagates all over the scaffold, the stress continues decreasing progressively down to zero with some eventual temporary increases associated to a certain densification of the fractured structure under the applied compression, which is typical on cellular structures [251].
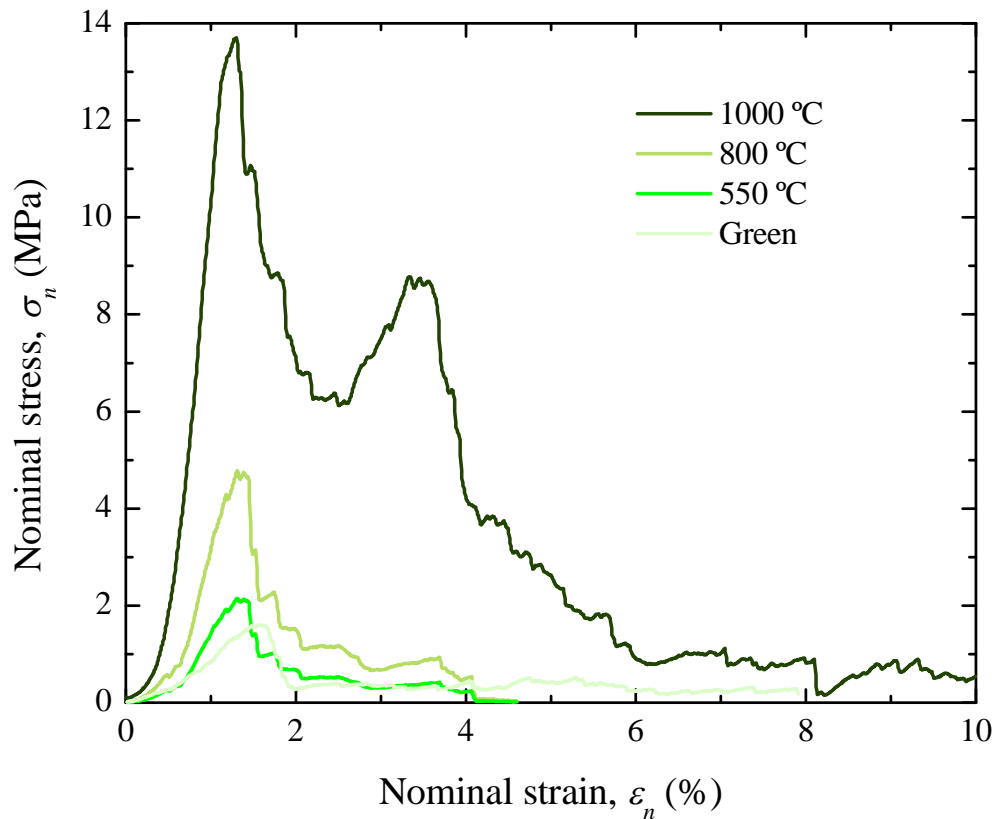
Figure 3.18. Representative compressive stress-strain curves of 45S5 bioglass-derived scaffolds sintered at the indicated temperatures for 1 h.

The evolution of the compressive strength of robocast 45S5 bioglass-derived scaffolds with the sintering temperature is shown in Figure 3.19. It is evident, that strength increases steadily and strongly with sintering temperature, but there is no clear correlation of strength data with rod density or rod diameter, and the different stages observed in the data for the latter (Figure 3.14 and Figure 3.15) are not so clearly observed in Figure 3.19.
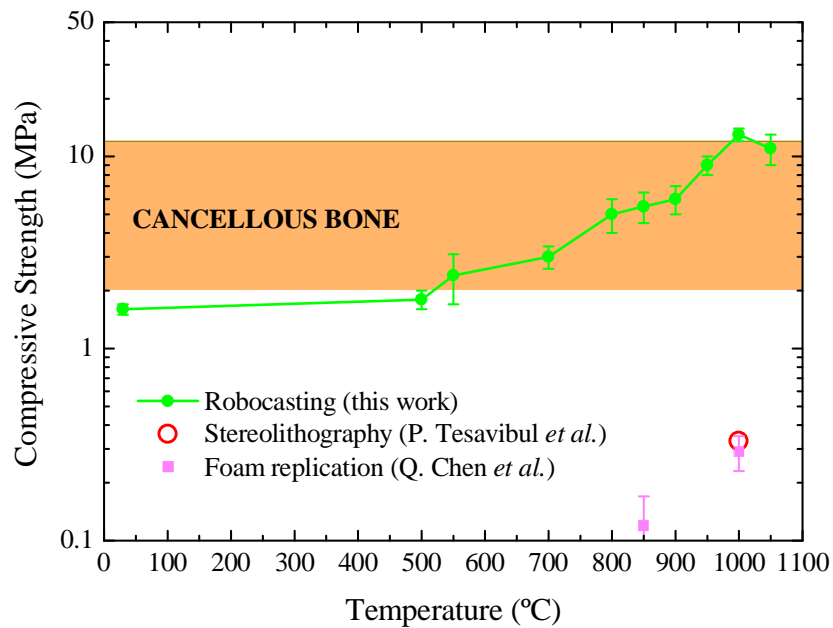
Figure 3.19. Evolution of the compressive strength of 45S5 bioglass-derived scaffolds with sintering temperature. Data represent mean values with standard deviations as error bars. Cancellous bone strength (shaded band) [252][44] and results for scaffolds from other authors [137][253] are included for comparison.

Especially indicative of this lack of complete correlation is the fact that while densification was improved in scaffolds sintered at 1050 °C, there is a statistically significant ($p<0.05$) reduction in strength compared to structures sintered at 1000 °C (from 13 ± 1 MPa to 11 ± 1 MPa). This reduction is attributed to the deleterious change in the starting flaw population at the rod surfaces, where cracking initiates [249-250], upon the aforementioned disappearance of the glass matrix (bottom-right image in Figure 3.16). This result emphasizes that surface defects are to be minimized whenever possible since their negative influence on scaffold strength can counteract and even supersede the positive effect of a reduction in the total porosity of the structure. Thus, surface flaw population effects, and maybe some toughness variations associated to the different microstructural and phase-compositional changes occurring in the material at different sintering temperatures, might be responsible for blurring the correlation between strength data and porosity/shrinkage results. In any case, it is evident from

these results that, at least in terms of mechanical performance, the optimal condition for sintering 45S5 bioglass-derived scaffolds fabricated by robocasting is 1000 °C for 1 h.

On the other hand, as shown in Figure 3.19, when comparing these strength results with existing literature reports [137][253] and cancellous bone properties it becomes evident that scaffolds produced by robocasting exhibit strength values far superior to anything previously reported for 45S5 bioglass-derived scaffolds — under the same sintering conditions, the enhancement is well over one order of magnitude (~ 4000 %). The reason for the enhancement of mechanical resistance over conventional scaffolds fabricated by foam replication [254] should be found on the improved pore architecture and thicker struts provided by robocasting. More surprising is the fact that other solid freeform fabrication methods such as stereolithography (STL) [137], which in principle provide the same advantages, have not been able to duplicate these strength results. Nonetheless, as the authors of the latter report point out, the reason for this may lay in a less than optimal selection of the sintering process. 45S5 bioglass is difficult to sinter, especially into complex scaffold geometries, and great care needs to be taken in selecting the thermal treatment parameters to avoid deleterious cracking during sintering. This must be especially critical in the case of STL, were larger amounts of organic binders (compared to robocasting) have to be burnt out in the process. In any case, all robocast 45S5 bioglass-derived scaffolds sintered between 550 °C and 1000 °C fall within or even surpass the range 2-12 MPa frequently quoted for cancellous bone [255][44]. Consequently, robocasting provides, for the first time, a means to produce mechanically competent bioglass (not just bioglass-derived) scaffolds. Indeed, the robocast scaffolds sintered at 550 °C remain completely amorphous and exhibit a compressive strength that, while barely improved over that of as-dried green structures, lies at the lower end of cancellous bone range and is enough for safe handling during implantation. This could help overcome the main hurdle for the successful application of 45S5 bioglass as a broad-use bone substitute material: the difficulty to produce scaffold with sufficient mechanical integrity without reducing the outstanding bioactivity of amorphous 45S5 particles[9].

At this point it is worth discussing some issues regarding porosity. Although the total porosities reported here (~ 60 % and ~ 80 % for scaffolds sintered at 1000 °C and 550 °C, respectively) are lower than typical values of conventional 45S5 bioglass-derived scaffolds (90-95%) [253], conventional (foam replication) scaffolds with similar

porosities as those reported here will still fall well short of robocast scaffolds in term of strength (as can be easily estimated by extrapolating reported data [253]). Moreover, there is ample evidence that, while such extremely high porosities might be required to attain significant bone ingrowth in the tortuous architectures of conventional scaffolds, porosities such as those reported here are enough to allow bone regeneration in the case of calcium-phosphate robocast structures [256-258]. In any case, robocast scaffold porosities could be easily increased to match reported values by modifying the initial design, for example by increasing rod-spacing within each deposition layer.

3.1.4   Effect of immersion in SBF on robocast 45S5 scaffolds

In this section, results concerning the formation of hydroxyapatite on the surface of bioglass scaffolds during immersion in simulated body fluid (SBF) and its effect on the scaffolds compressive strength are presented. As mentioned before, this *in vitro* study has been done for samples in amorphous (sintered at 550 °C) and crystalline (sintered at 1000 °C) states, since it is expected they have different bioactivity.

3.1.4.1   The *in vitro* bioactivity

Figure 3.20 shows data for pH of the SBF solution and the weight loss of the scaffolds as a function of immersion time for amorphous and crystalline 45S5 scaffolds.

The weight loss and pH data show approximately the same time dependency in the SBF, because the reactions that lead to weight loss of the glass are also the same reactions that control the pH of the solution [259-260]. During immersion in SBF, species such as H^+, H_3O^+ and OH^- from the solution attack the glass scaffold and are exchanged with Na^+ and Ca^{2+} ions from the glass network and as a result silanol group (Si–OH) is formed on the glass surface due to reaction of Si with OH^- ions that act as nucleation sites for HAp formation. Leaching of alkali and alkaline ions form glass to solution leads to the increase of pH and weight loss observed in Figure 3.20. The amorphous glass tends to leach more alkali to the solution, causing a larger weight loss and a higher increase of pH as compare to crystalline glass.
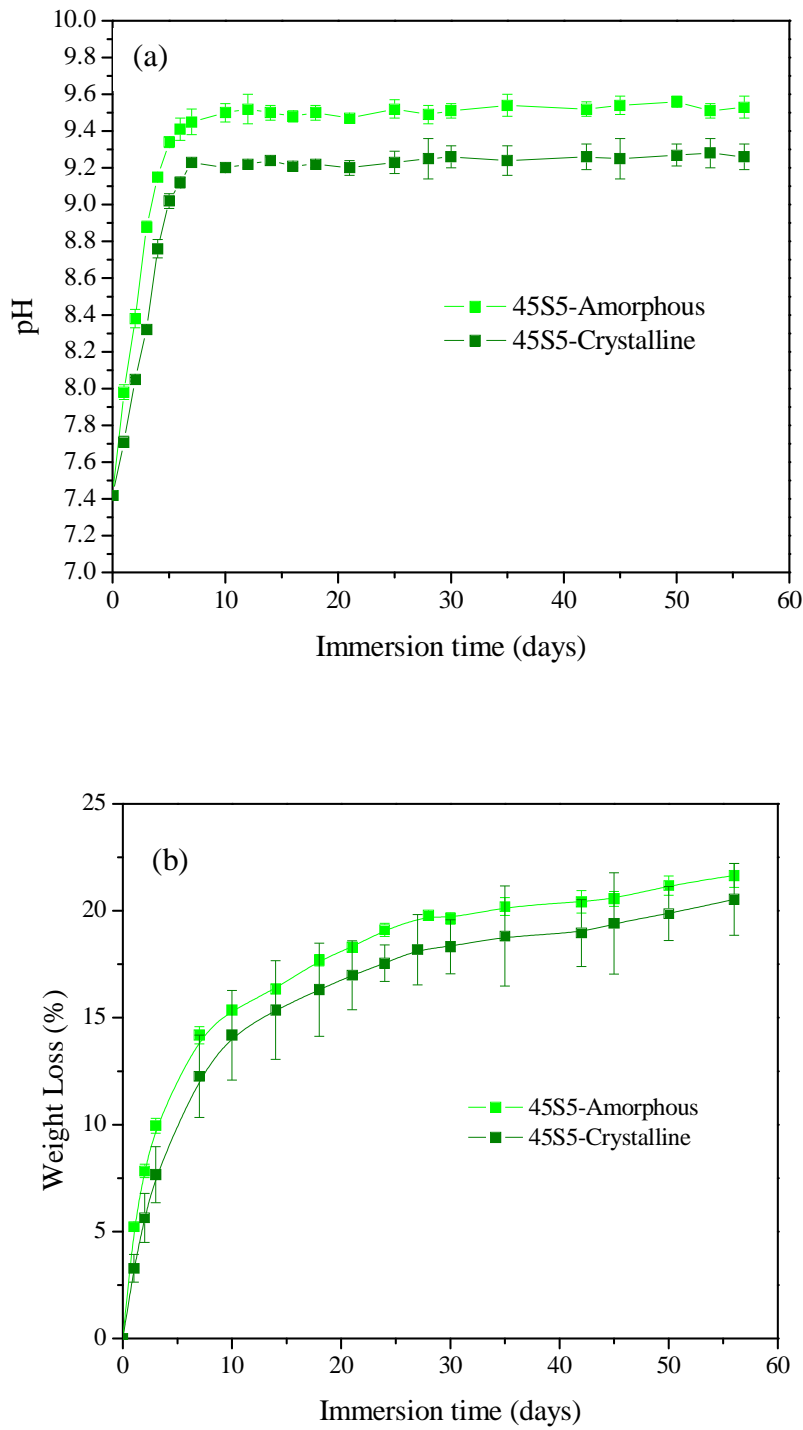
Figure 3.20. (a) pH of SBF solution and (b) weight loss of the scaffolds as a function of immersion time for amorphous and crystalline 45S5 samples.

For both kinds of scaffolds, pH increased rapidly during the first 10 days. Above 10 days, the pH increased more slowly and reached a plateau. The plateaus in pH curves are due to formation of Hydroxyapatite layer on the surface of the samples that consequently makes the surface of bioglass more passive.

There is another term that has a considerable effect on the change of pH and weight loss. Amorphous scaffolds have more microporosities as well as bigger surface area in comparison to crystalline scaffolds. The existence of these two factors seems to provide not only faster degradation kinetics but also a means for enhanced overall conversion factor of the bioactive glass to HAp.

Figure 3.21 and Figure 3.21 show HAp formation during immersion in SBF for different soaking times in amorphous and crystalline 45S5 scaffolds, respectively. It is obvious that the amount of the HAp increases with soaking time. In the amorphous scaffolds the nucleation of HAp occurred just after 1 day of soaking in SBF (Figure 3.21a and the inset photo), while in crystalline 45S5, there is no evidence of HAp formation after 1 day (Figure 3.22a). Nucleation of HAp formation in crystalline 45S5 occurred slightly later than amorphous ones. Figure 3.22b shows the HAp nucleus after 3 days immersion in SBF which was observable after 1 day in the case of amorphous samples. In comparison to the smooth surface of the as sintered 45S5 scaffold (Figure 3.17d), the surface of the scaffold immersed in the SBF is covered with a fine particulate HAp layer. High-resolution SEM image (the inset photo in Figure 3.22a) of the surface showed that the surface consisted of porous network of nanometer-sized, needle-like crystals, characteristic of HA deposited by precipitation from solution [260].

The growth of HAp formed continued up to 7 days of immersion which is in agreement with the results obtained from pH and weight loss measurements (Figure 3.20a, b). The feature of the samples soaked for 14 days and more are similar indicating that the rate of HAp formation is reduced (Figure 3.21 and Figure 3.22d, e, f).
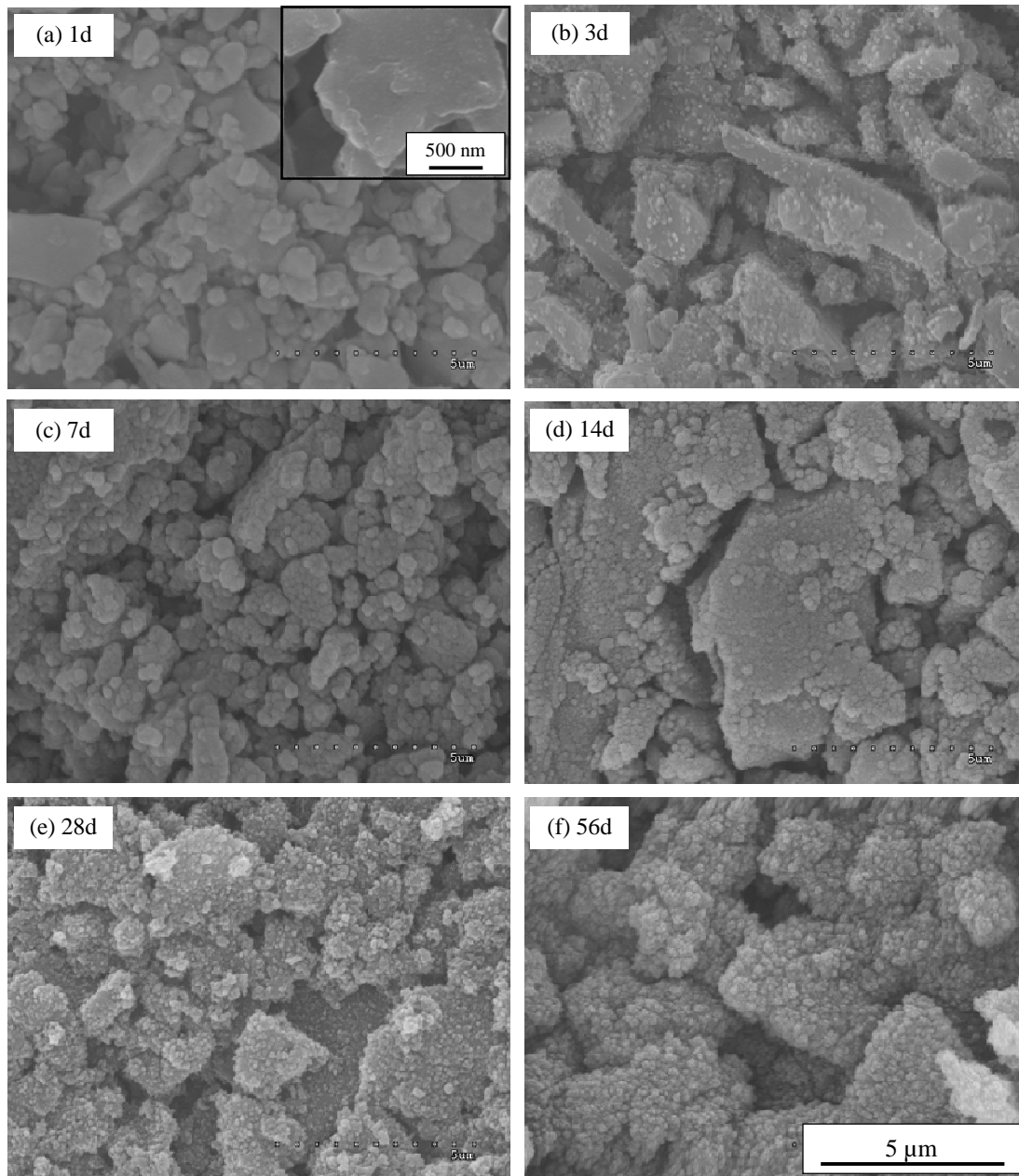
Figure 3.21. SEM micrographs for amorphous 45S5 scaffolds soaked in SBF for 1, 3, 7, 14, 28, and 56 days.
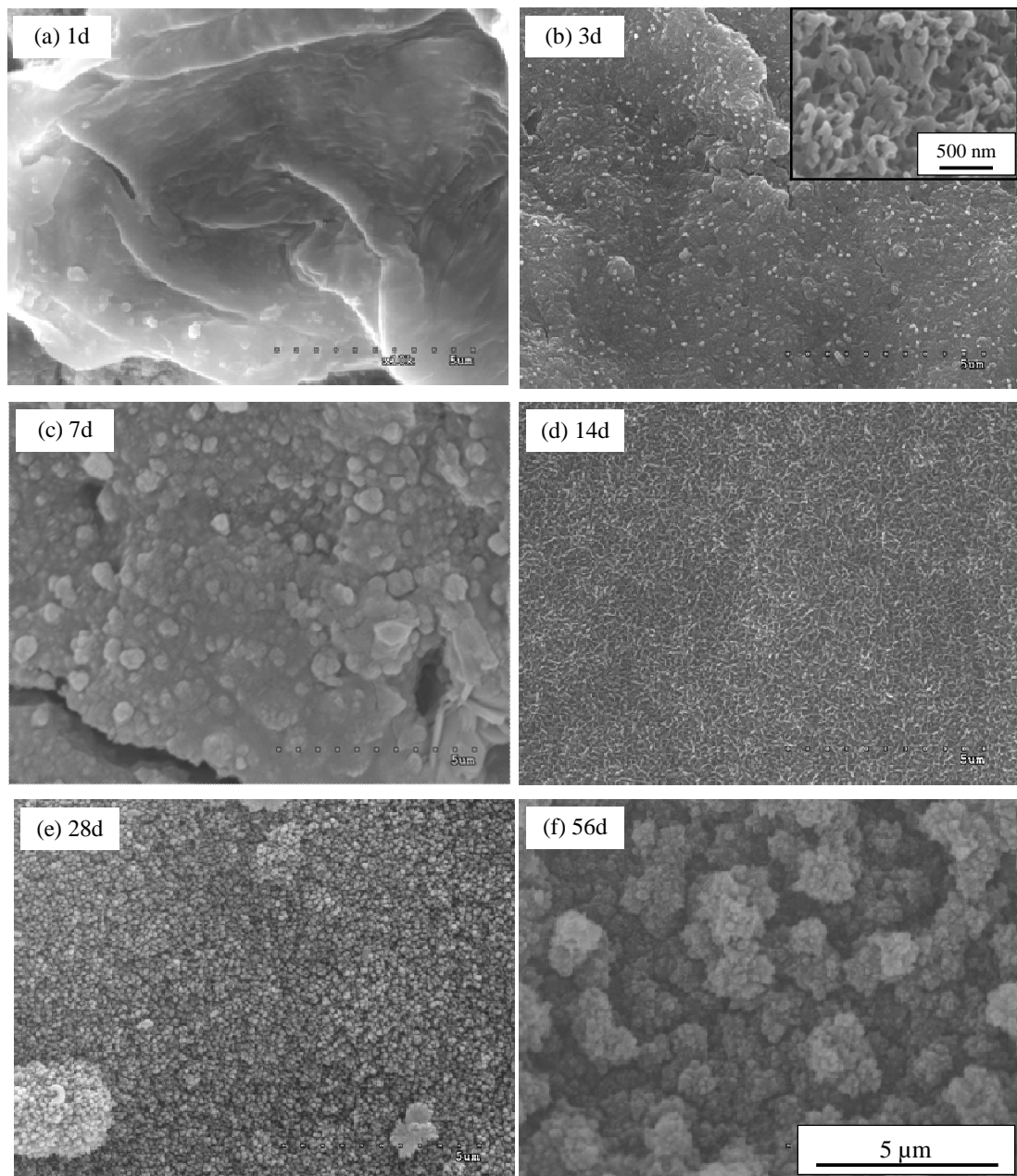
Figure 3.22. SEM micrographs for crystalline 45S5 scaffolds soaked in SBF for 1, 3, 7, 14, 28, and 56 days.

3.1.4.2   Compressive strength of 45S5 scaffolds after immersion in SBF

The evolution of compressive strength of amorphous and crystalline 45S5 scaffolds as a function of immersion time in the SBF is shown in Figure 3.23.
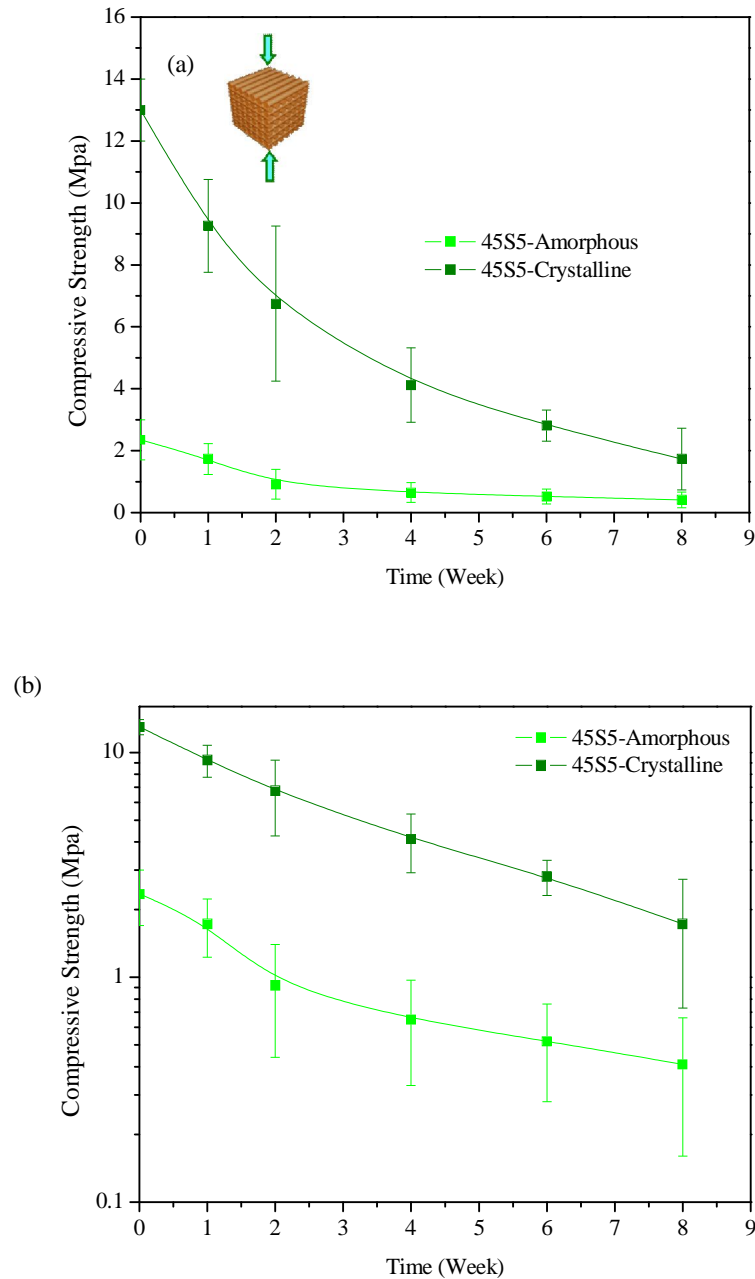
Figure 3.23. Compressive strength of amorphous and crystalline 45S5 scaffolds as a function of immersion time in the SBF with standard deviation as error bars in (a) linear and (b) logarithmic scale.

In both cases, the conversion of the bioglass/ bioceramics to a weak porous HAp-like product resulted in a reduction of compressive strength. In the case of the amorphous scaffolds, the rate of this reduction decreases after two weeks of immersion in SBF (Figure 3.23a, b).

Due to the higher degradation of the amorphous scaffolds during immersion in SBF (see Figure 3.20), the amorphous scaffolds showed also a higher strength loss comparing to crystalline scaffolds. SEM observations of amorphous and crystalline scaffolds after immersion in SBF revealed an interesting finding.

Figure 3.24 shows SEM micrographs of the rod surface of the amorphous and crystalline samples soaked for 3 and 56 days in SBF. In the case of crystalline samples (Figure 3.24a, c), it is evident that the HAp participated layer formed on the surface has been dried and undergoes a volume decrease. This phenomenon consequently develops a tensile stress and the layer may crack or peel in order to relieve the stress. This has been reported earlier for the 45S5 samples after immersion in PBS [261]. According to Figure 3.24a, the surface of the crystalline sample after 3days of immersion shows clearly crack paths distributed thoroughly all around the rod. These cracks became bigger and more prone to detachment from the underneath layer by increasing the immersion time to 8 weeks (Figure 3.24c). On the other hand, there is not any evidence of peeling or crack generation in amorphous samples after 3 days and even after 8 weeks of immersion (Figure 3.24b, d).
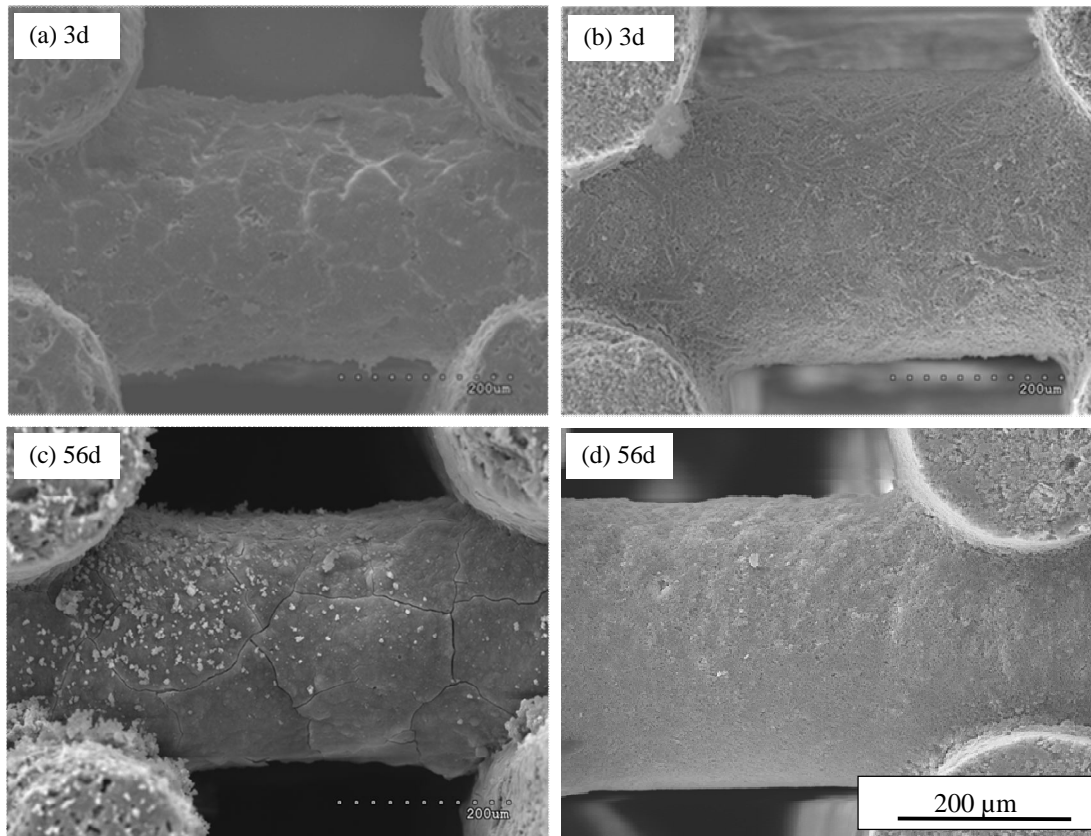
Figure 3.24. The rod surface of the crystalline (a,c) and amorphous (b,d) samples soaked in SBF for 3 and 56 days.

It can be concluded that the mineralized layer is bonded loosely to the crystalline bioactive glass resulting in weaker adhesion and subsequently peeling off to release strain energy. On contrary, the amorphous samples show a higher adhesion capability to the mineralized layer formed on the surface which results in much less visible propagated crack due to peeling.

3.1.5 Polymer-impregnated 45S5 robocast scaffolds

In this section, toughening of 45S5 scaffolds has been investigated through melt impregnation by using PCL and PLA polymers. Since the 45S5 scaffolds sintered at different temperatures, show different percentages of microporosity, it would be interesting to find the relation between defects elimination and associated mechanical improvement. The mechanical characterization has been performed by compression and

bending test. The main attention of this part of the work has been paid to two sintering temperatures 550 °C and 1000 °C.

3.1.5.1   Melt impregnation process for 45S5 scaffolds

During impregnation of 45S5 scaffolds sintered at different temperature with molten PLA, a reaction took place between the 45S5 scaffolds and the polymer which changed the transparent color of molten PLA to dark brown. This color change can be appreciated in Figure 3.25, which shows optical images of molten PLA after soaking for the indicated times at 227 °C, alone and in the presence of 45S5 bioglass scaffolds sintered at 500 °C and 1000 °C.

The reaction started at the regions close to the surface of the sintered scaffolds (Figure 3.25) and gradually expanded to the whole volume of PLA. While at 1 hour the reaction has barely become evident for the sample sintered at 1000 °C (Figure 3.25 f) it is already pronouncedly apparent for samples sintered at lower temperature (Figure 3.25 e). Evidently, the sample sintered at 550 °C, which is amorphous and has a higher surface area, reacts faster with the molten PLA than the crystalline, denser sample sintered at 1000 °C. Increasing the soaking time to 2 hours, while still harmless to pure PLA (Figure 3.25 g), is completely deleterious to PLA around the scaffolds, which now appears a uniform dark brown color, independently of the scaffold's sintering temperature (Figure 3.25 h-i). A similar change in color has been observed upon decomposition of PLA at higher temperatures or substantially longer heating treatments, and therefore, the interaction with the scaffold is considered to accelerate/facilitate decomposition of the polymer at the selected temperature.
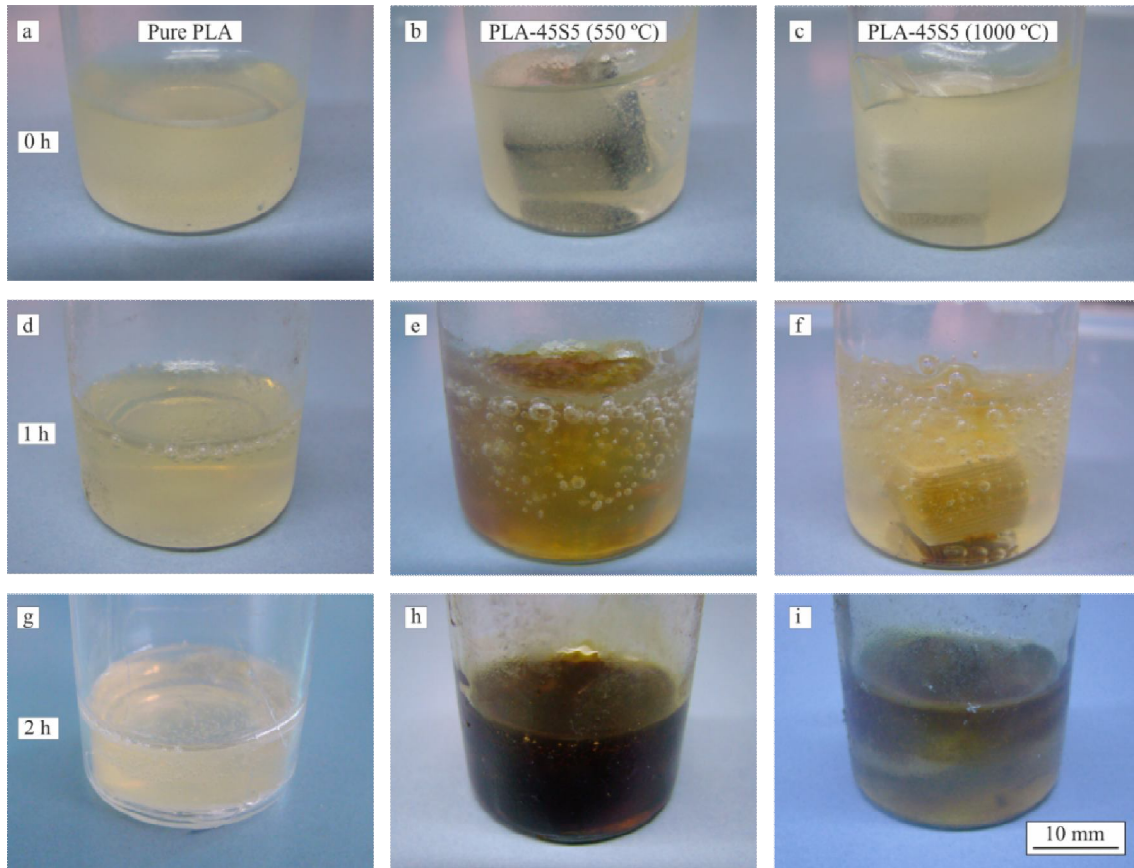
Figure 3.25. Optical images of molten PLA after soaking at indicated times at 227 °C, alone (left) or in the presence of a Bioglass®-derived scaffold sintered at 550°C (center) or 1000 °C (right).

In the case of samples impregnated with PCL, there was not any change in the color of molten PCL up to completion of the impregnation process.

3.1.5.2   Microstructural characterization of polymer impregnated 45S5 scaffolds

SEM micrographs of representatives as-fractured specimens of the 45S5 scaffolds after sintering at 550 °C and subsequently impregnated with PCL and PLA are shown at different magnifications in Figure 3.26.
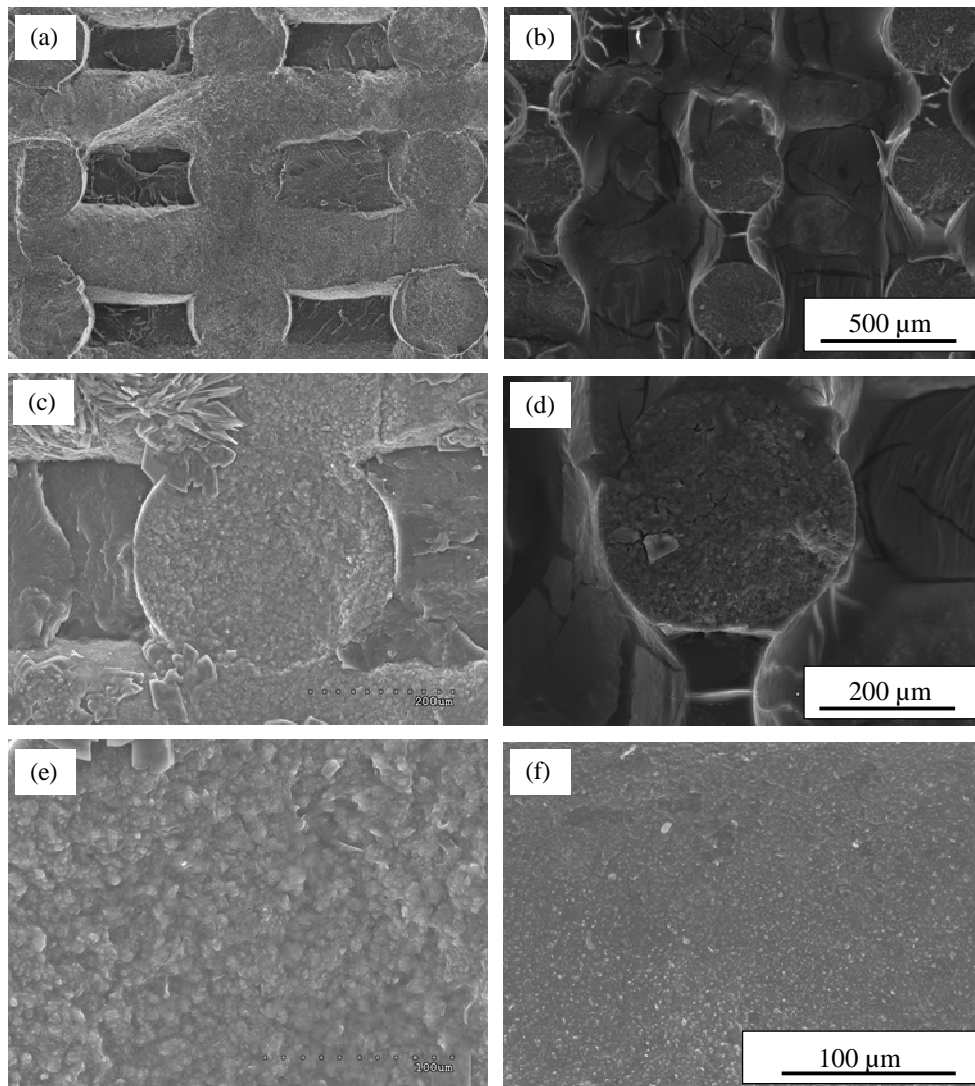
Figure 3.26. SEM micrographs of representative specimens of robocast 45S5 scaffolds sintered at 550 °C and and subsequently impregnated with (a, c, e) PCL and (b, d, f) PLA at different magnifications.

The SEM micrographs of Figure 3.26 confirmed that the selected infiltration conditions were appropriate to completely fill with polymer not only the macroporosities (Figure 3.26a and b), but also the in-rod microporosities (Figure 3.26c, d, e and f).

The micrographs of Figure 3.26 b, d and f proved the deleterious nature of the aforementioned interaction between PLA and 45S5 bioglass. Damage to the polymer is evident in the form of cracks in the PLA filling the macropores (Figure 3.26b) and also

in the polymer within the rods (Figure 3.26 d). There is also evidence of weak adhesion between the rods and the degraded PLA.

3.1.5.3   Mechanical characterization of polymer impregnated 45S5 scaffolds

—   *Compression tests*

Figure 3.27 shows representative uniaxial compressive stress–strain curves for the 45S5 scaffolds sintered at 550 °C and 1000 °C impregnated with PCL and PLA. For comparison the curves for bare-scaffolds (Fig. 3.20) have been included in Figure 3.27.
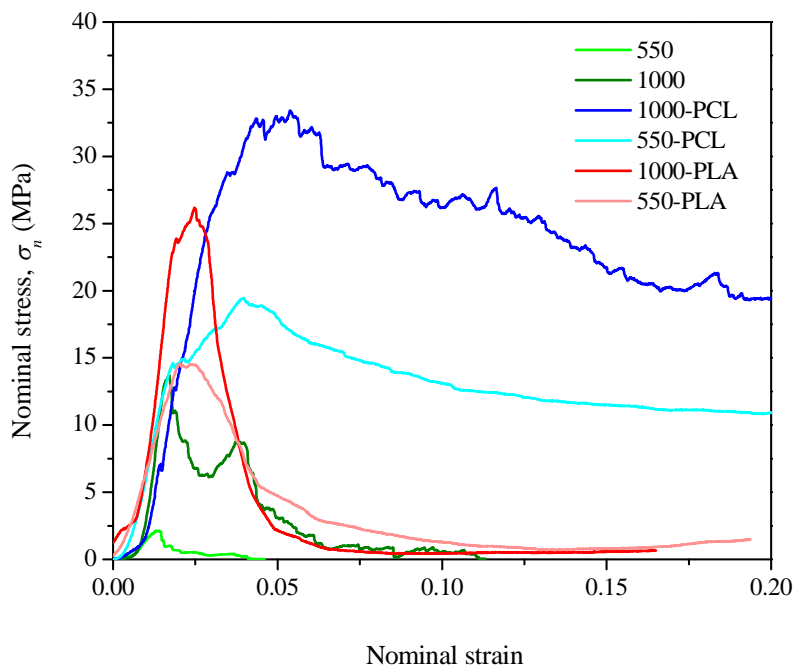
Figure 3.27. Representative nominal stress-strain curves obtained during uniaxial compression tests performed on robocast 45S5 scaffolds along the direction orthogonal to the rod layers after impregnation with PCL and PLA by melt impregnation technique for sintered samples at 550 °C and 1000 °C.

Polymer impregnation of 45S5 scaffold changes the feature of stress-strain curves significantly. The linear elastic region is extended, but the slope of the curve remains unaltered since the stiff glass skeleton still controls the elastic strain of the material. After failure, which occurs at an increased stress in the impregnated scaffolds, the applied stress declines, but in the case of PCL infiltration the curve does not go to zero, and the material retains a significant load-bearing capacity even after large strains (> 20%). This indicates that the ductile PCL is able to hold the material together after the ceramic skeleton breaks. Regardless of the sintering temperature, it is clearly evident that both the compressive strength and the toughness, measured as the area under the curve, increase significantly upon the incorporation of polymer, even in the case of the degraded PLA (section 3.1.5.1).

To better analyze the strengthening effect of polymer infiltration, the evolution of the compressive strength versus sintering temperature is shown in Figure 3.28a for the bare robocast 45S5 scaffolds and for scaffolds impregnated with PCL or PLA together with previously reported values for cancellous bone [210]. It is evident, that the compressive strength increased steadily and strongly with sintering temperature for three groups. This highlights the importance of having a scaffold with strong, defect-free struts if mechanical resistance is a major concern for the intended application. Even when polymer infiltration is used for mechanical enhancement of the structure, maximization of the intrinsic resistance of the struts through an optimal sintering treatment should be sought. Nonetheless, infiltration of the ceramic structure with a polymer is a good alternative to an appropriate sintering treatment. For example, a 45S5 scaffold sintered at 550 ºC after full-impregnation, with either PCL or PLA, exhibits strength higher that the best attainable value in bare structures (i.e. after sintering at 1000 ºC).

The strengthening factor provided by each polymer, obtained by normalizing the corresponding results by the strength of the bare structures at each sintering temperature, are shown in Figure 3.28b versus in-rod porosity (calculated following the procedure described in Chapter 2). The strengthening of polymer-impregnated robocast scaffolds can occur by two different mechanism: stress shielding and defect healing [20]. The former, important where the infiltrating polymer has a high elastic modulus, consists in the continuous polymeric phase sustaining part of the applied load; the latter involves the sealing of pre-existing defects in the strut surfaces by the infiltrating polymer, which hinders the propagation of cracks from such flaws.

a)

b)
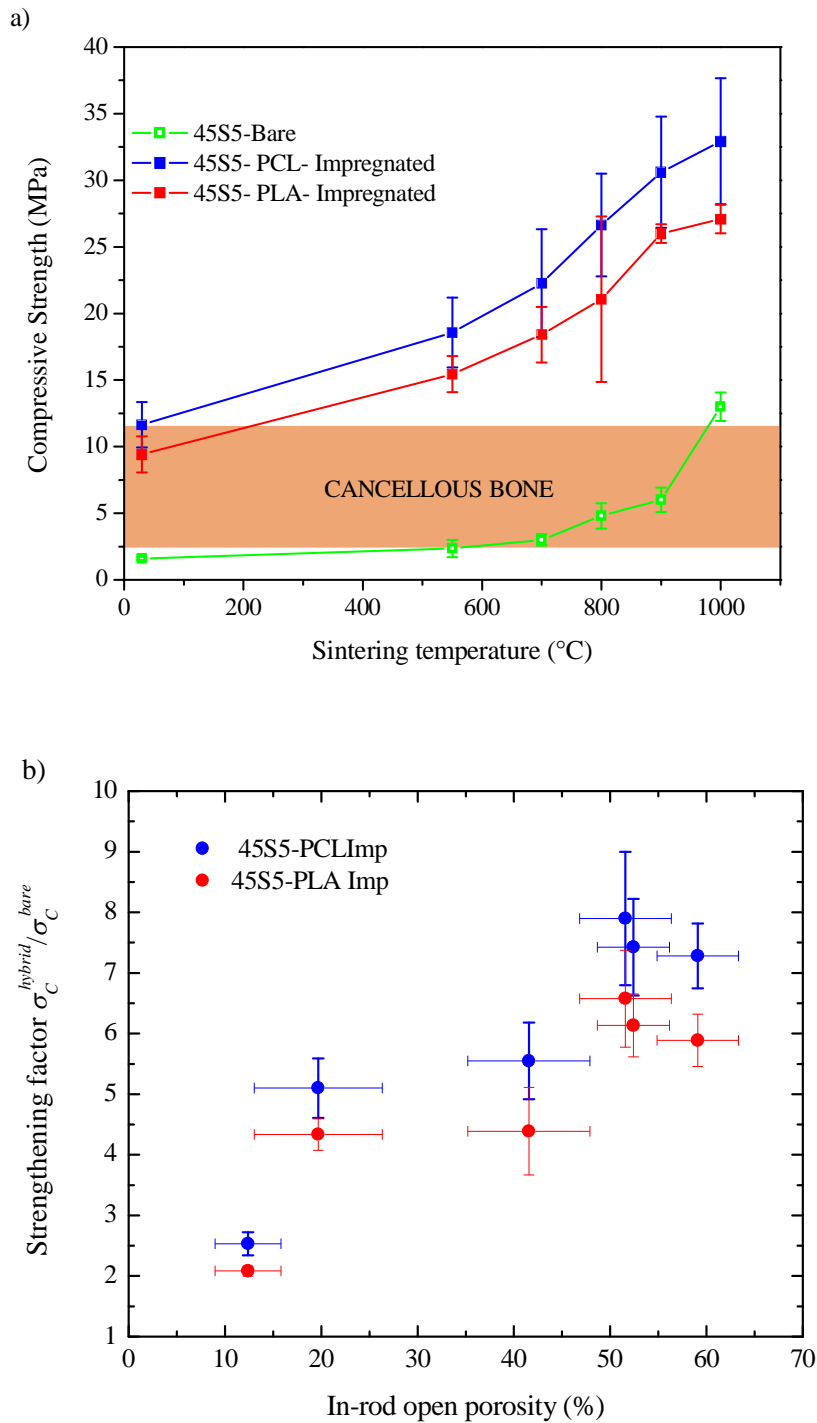
Figure 3.28. (a) The evolution of compressive strength versus sintering temperature for bare, PCL impregnated and PLA impregnated 45S5 scaffolds. (b) Strengthening factor for PCL impregnated and PLA impregnated 45S5 scaffolds as a function of the in-rod open porosity.

The stress-shielding effect is expected to decrease as the density of the bars (i.e. the sintering temperature) increases, since such increase will enhance the modulus mismatch between the ceramic skeleton and the polymer infiltrate. Nonetheless, since this effect is per se minor for compliant polymer infiltrates, the variability of the mismatch would be somewhat negligible and the stress-shielding effect independent of sintering temperature. So the increase of strengthening factor with the open porosity of the scaffold strut (Figure 3.28b) is due to defect healing. It is reasonable to assume that the actual dependence of the strengthening factor for healing is with the effective critical flaw size [262-263] rather than the in-rod open porosity, but since both will decrease during strut densification the results of Figure 3.28b are logical. In any case, it is worth highlighting yet again that even if the defect healing mechanism becomes less effective as the flaw population decreases, eliminating strut defects (by improving sintering /densification) is the best strategy for maximizing the strength even in hybrid ceramic/polymer structures (see Figure 3.28a).

Since defect healing should be similar for both polymers, it was expected that the stiffer PLA yields to higher strengthening than PCL, as in polymer impregnated ß-tricalcium phosphate robocast scaffolds [20]. However, in the case of 45S5 scaffolds, due to the degradation of the PLA properties in the presence of 45S5 bioglass (section 3.1.5.1), PCL impregnated structures are the strongest. Nonetheless, with the exception of green structures infiltrated with PLA, the strength of the hybrid materials are superior to values reported for cancellous bone although lower than the range 100-140 MPa frequently quoted for cortical bone [24].

Regarding toughening effect of polymer infiltration, Figure 3.29a shows the evolution with sintering temperature of the strain energy density, G_c, calculated from the area under experimental stress strain curves at 20 % strain. Values for human bone are also include for comparison [264]. Figure 3.29b shows the toughening factor provided by each polymer—obtained by normalizing the corresponding results by the strain energy density of the bare structures at each sintering temperature—versus the in-rod open porosity (calculated following the procedure described in Chapter 2). A significant improvement in the toughness ($G_{0.20}$) of the bioglass scaffolds is apparent upon infiltration with polymer especially with the ductile PCL. In fact, upon PCL infiltration the toughness of scaffolds sintered at temperature higher than 550 ºC reaches the lowest level of cortical bone values. The toughness of the impregnated structures seems to be fairly independent of the sintering temperature, with the exception of green

samples and those sintered at 550 ºC. This might indicate that it is the polymer in the macropores which determines the toughness of the structure, with the ceramic skeleton playing only a secondary role.
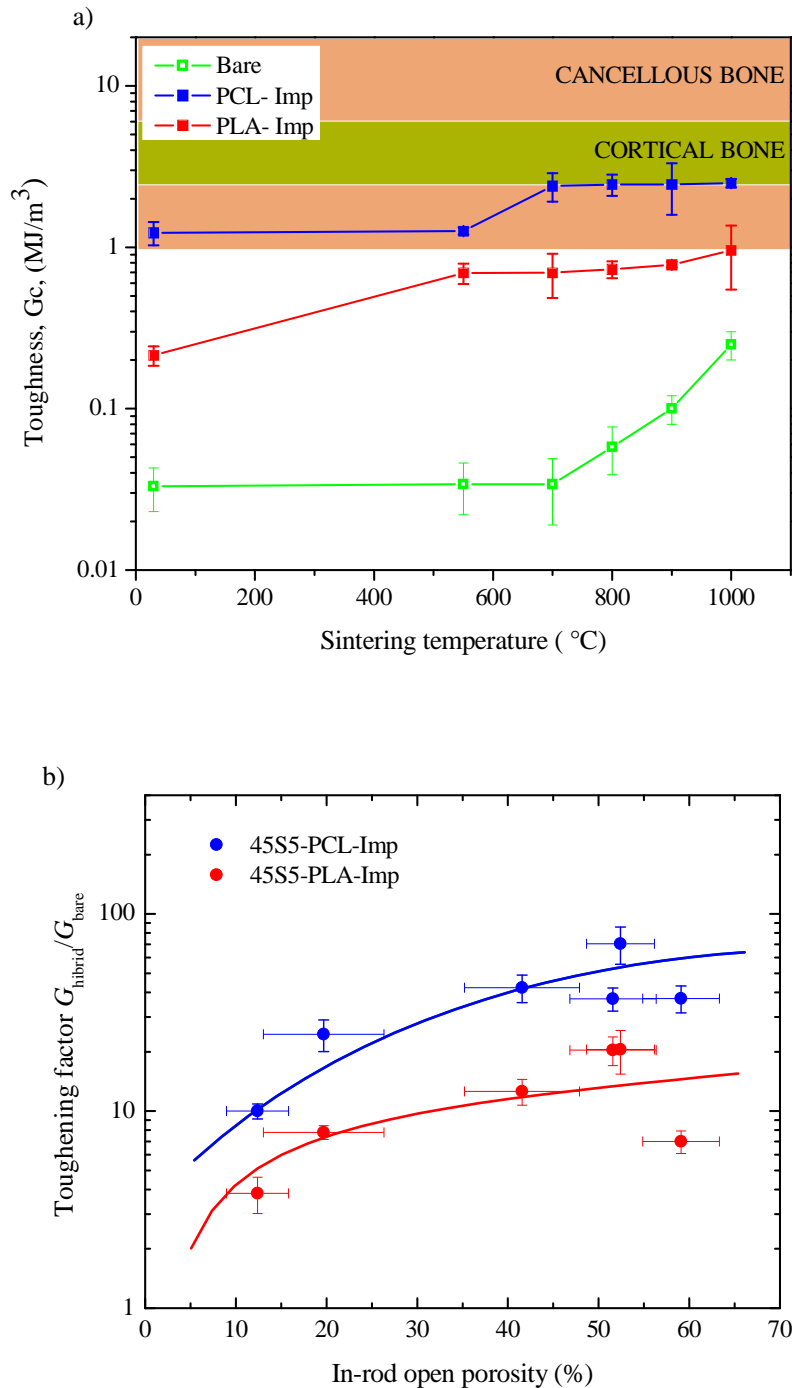
Figure 3.29. (a) Strain energy density, G_c, in compression for the indicated materials at the point of 20 % strain, $G_{0.2}$. (b) Toughening factor for fully-impregnated structures as a function of the in-rod open porosity. Error bars represent standard deviations.

The toughening obtained upon infiltration is produced as a consequence of the strengthening of the structure and, in the case of PLC, a crack bridging by polymeric fibers (see Figure 3.30). As shown in Figure 3.29b, the toughening factor decreases with the microporosity on the scaffold struts both as a consequence of the decreasing strengthening factor and the reduction in the number of polymer microfibrils bridging the crack tip as it propagates.
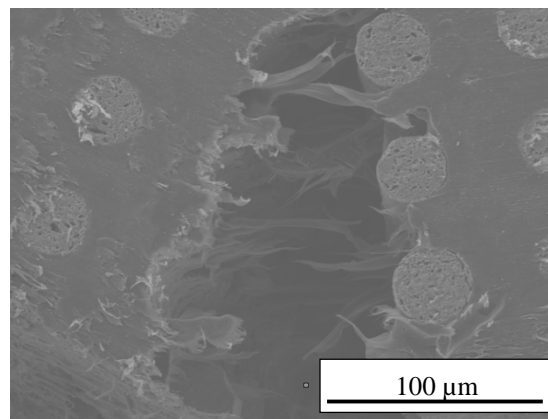
Figure 3.30. The crack bridging due to polymeric fibers in 45S5 scaffold, impregnated by PCL, during bending test.

The enhanced performance of PCL over PLA in terms of strain energy density in compression is related to its superior ductility and strength. It is interesting to point out that in polymer impregnated ß-tricalcium phosphate robocast scaffolds, where there is not PLA degradation during impregnation, PLA is more effective infiltrate than PCL for increasing the strain energy density, because its superior strength compensates its inferior ductility [265].

— *Bending tests*

The result of Young modulus obtained from four-point bending tests for bare and infiltrated scaffold are shown in Figure 3.31. For the scaffolds sintered at 1000 ºC, the stiffness of the structure is not significantly changed by polymer infiltration. This simply reflects the fact that the modulus of PCL and PLA are much lower than that of

the ceramic skeleton. In fact, for the highly porous structures sintered at 550 ℃ only the infiltration with the stiffer PLA produces a slight increase of the modulus of the structure, since the stiffness of the structure is not significantly ($P > 0.05$) changed by PCL impregnation.
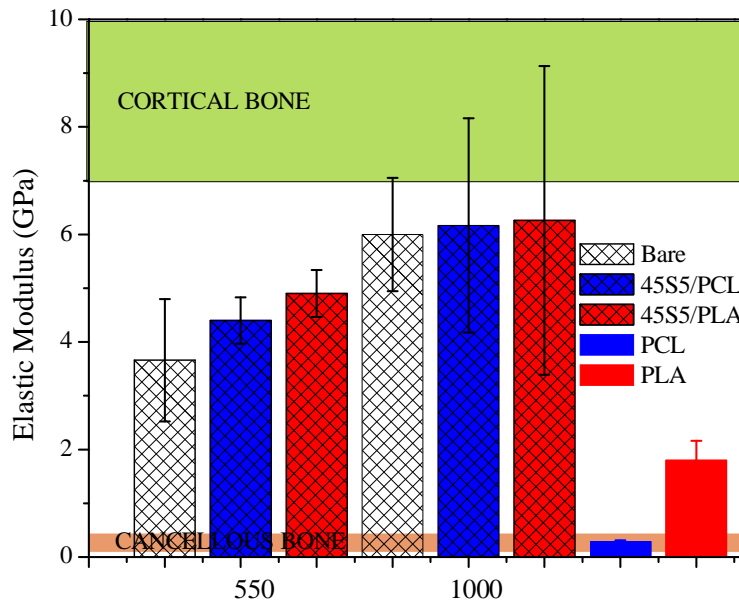
Figure 3.31. Elastic modulus, with standard deviations as error bars, for 45S5 bioglass scaffolds sintered at 550 ℃ y 1000 ℃ before and after impregnation with PCL or PLA. Typical values for human bone are shown as shaded band [22].

The representative force-displacement curves from 4-point bending tests of the bare and impregnated scaffolds are displayed in Figure 3.32. The loads in the curves have been normalized by the effective volume (i.e. that within the external contacts in the 4-point bending jig) of each sample. The bending curves of all presented materials show trends similar to those observed in compression (Figure 3.27).

A typical brittle, linear elastic behavior could be seen for bare scaffolds, and also for PLA impregnated scaffolds but in the case of PCL infiltrate the hybrid structures exhibited an extended load-bearing capacity and remained in one piece after the tests.
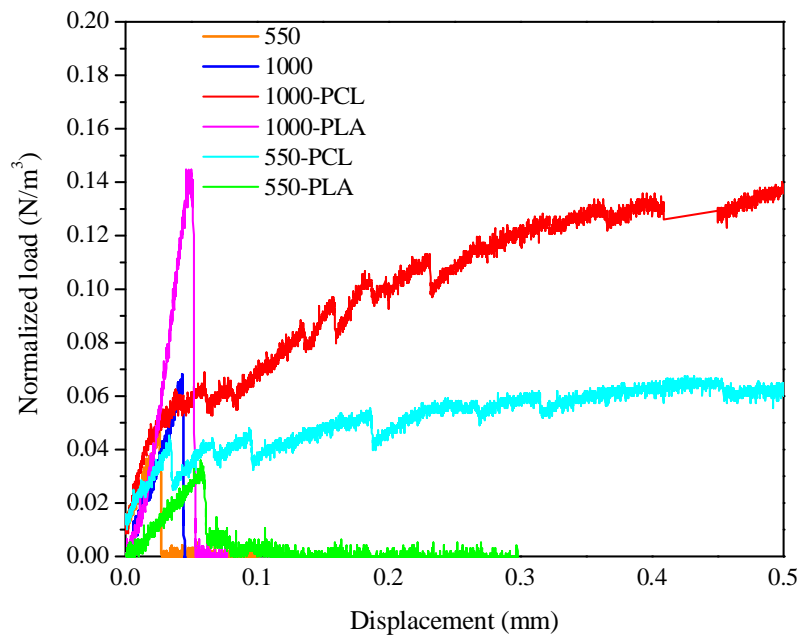
Figure 3.32. Typical bending load–displacement curves for the indicated materials. Loads have been normalized by the effective volume of each sample.

As shown in Figure 3.33, the flexural strength of the structure increases upon the incorporation of both PCL and PLA due to defect healing and stress shielding, and as in compression, the strengthening factor is higher in the amorphous samples (550 ºC) than in the glass-ceramic scaffolds (1000 ºC). Also, as in compression, the strengthening achieved after polymer infiltration is higher in the case of PCL because the chemical reaction observed to occur between molten PLA and 45S5 bioglass (section 3.1.5.1) prevented PLA-impregnated structures from exhibiting a superior mechanical enhancement.
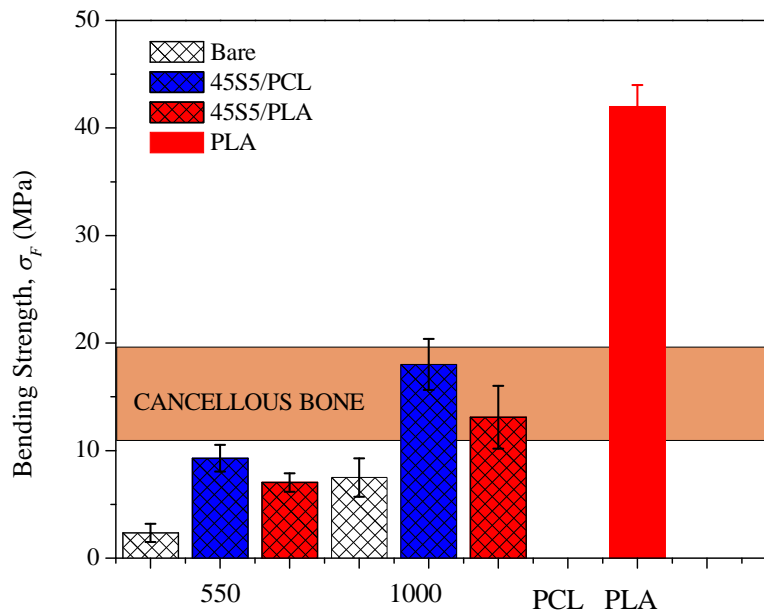
Figure 3.33. Flexural strength, with standard deviations as error bars, for 45S5 bioglass scaffolds sintered at 550 ºC y 1000 ºC before and after impregnation with PCL or PLA.

Figure 3.34 shows the fracture energy of bare and polymer-infiltrated 45S5 scaffolds as evaluated from the area under the force-stroke curves from four-point bending tests. Fracture energy in bending is significantly lower than the strain energy densities evaluated in compression for all analyzed structures, as expected for this most deleterious loading condition. Nevertheless, for both polymers, the fracture energy of impregnated scaffolds was higher than for the bare scaffolds regardless the sintering temperature. In the case of PCL-impregnated samples, they were not even completely broken after the test, and the plotted values were calculated at 0.5 mm of stroke.
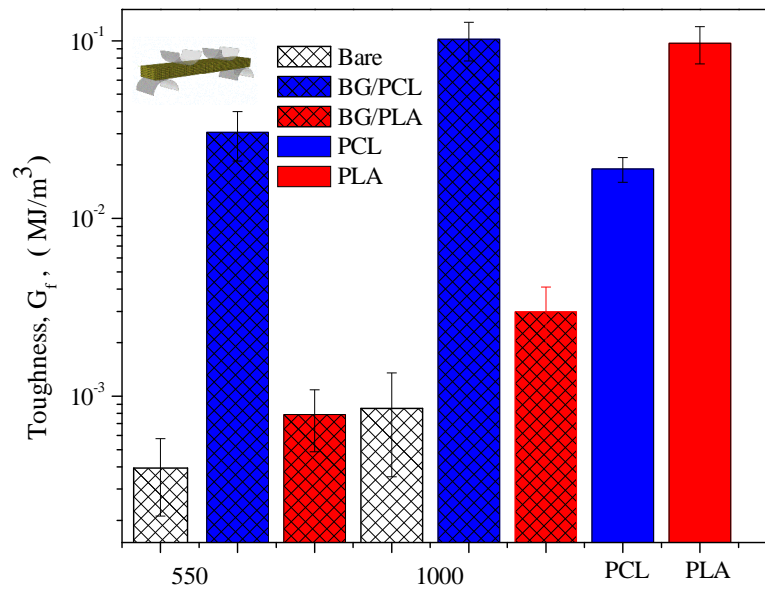
Figure 3.34. The strain energy, G_f, calculated from the area under the load- displacement curves from bending test at the point of 0.5mm of total deflection.

PCL impregnated scaffolds are significantly tougher due to the intrinsic greater ductility of PCL, which is able to provide some linkage between the crack walls, as shown in Figure 3.35b and e, while PLA impregnated scaffolds break in a somewhat brittle manner (Figure 3.35c and f) as bare scaffolds (Figure 3.35a and d). Therefore, the contribution of PLA to fracture energy is basically through the strengthening it provides, while the extraordinary toughening provided by PCL is provided both by the strengthening and by macro- and micro-fibrils (see Figure 3.35b and e as well as the insets) that bridge the crack opening.
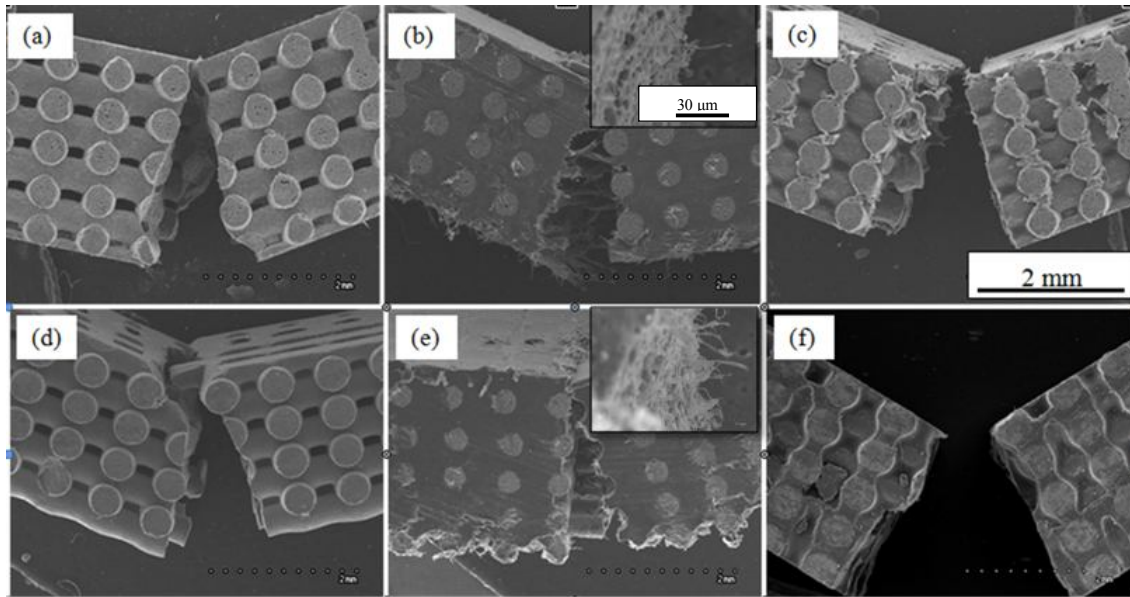
Figure 3.35. SEM micrographs of samples after bending tests: (a) crystalline bare scaffolds, (b) crystalline 45S5-PCL and (c) crystalline 45S5-PLA composties. (d) amorphous bare scaffolds, (e) amorphous 45S5-PCL and (f) amorphous 45S5-PLA composties.

From comparing Figure 3.35b and e it can be clearly perceived that there is a reduction in the number of polymer microfibrils with increasing sintering temperature (i.e. with decreasing microporosity). As discussed previously, this contributes to the decrease of the toughening factor in compression with decreasing microporosity. On the other hand, the comparison of Figure 3.35b and e reveals an unexpected effect: the number of fibers originating from the polymer in the macropores is significantly lower in the amorphous samples (Figure 3.27e) in comparison to crystalline ones (Figure 3.25b). Moreover, if one compares both figures with previous reports on other scaffold materials [21], the number of PCL fibers is lower in 45S5 bioglass scaffolds, even in those sintered at 1000 °C. This suggests that, although much milder in the case of PLA, some interaction between the 45S5 bioglass scaffold and PCL occurs during the melt impregnation process due to the relatively high temperatures involved which results in a degradation of the initial ductility of the polymer. Such embrittlement of PCL would be more dramatic for the amorphous structures (i.e. those sintered at 550 °C) as a consequence of their higher reactivity, and that would explain the differences observed between

Figure 3.35b and e. Therefore, care should be taken when selecting the processing conditions for the preparation of polymer–bioglass composites in order to avoid such deleterious interactions between the inorganic and organic materials. In this sense in situ polymerization processes might be considered an optimal alternative to melt impregnation [265].

All the results from mechanical characterization analyzed in the preceding paragraphs, both regarding compression and bending tests, are summarized in to facilitate access to the readership.

Table 3-2. Summary of mechanical characterization results.

Material	Compression Bending	E (GPa)	σ_0(MPa)	G (MJm^{-3})
45S5-550		-	2.4± 0.7	0.034 ± 0.012
45S5-550		3.7 ± 1.1	2.3 ± 0.8	0.0004 ± 0.0002
45s5-1000		-	13± 1	0.25 ± 0.05
45s5-1000		6 ± 1	7.5± 1.8	0.0008 ± 0.0005
45S5-550/PCL		-	18.6 ± 2.6	1.26 ± 0.06
45S5-550/PCL		4.4 ± 0.4	9.3 ± 1.2	0.03 ± 0.01
45S5-1000/PCL			33 ± 4.7	2.5 ± 0.15
45S5-1000/PCL		6.2 ± 2	18 ± 2.4	0.1 ± 0.02
45S5-550/PLA		-	15.5 ± 1.4	0.7 ± 0.1
45S5-550/PLA		4.9 ± 0.4	7 ± 0.9	0.007 ± 0.001
45S5-1000/PLA		-	27 ± 1	1 ± 0.4
45S5-1000/PLA		6.3 ± 2.9	13.5 ± 2.1	0.015 ± 0.008
PCL		-	17.4 ± 0.5	4.9 ± 0.4
PCL		0.3 ± 0.02	-	0.019 ± 0.003
PLA		-	74 ± 5	10.7 ± 0.4
PLA		1.8 ± 0.4	41 ± 2	0.10 ± 0.2

3.2 Fabrication of 13-93 bioactive glass scaffolds by robocasting

This section is discussing issues regarding fabrication of 13-93 bioglass scaffolds by robocasting. The strategy for making the ink was the same as the one used for robocasting of 45S5 ink.

3.2.1   Optimization of robocasting ink

Preparation of inks suitable for robocasting from bioactive glasses containing alkali ions such Na and Ca, as is the case with 13-93 and 45S5 is not simple. As the glass powder is immersed in deionized water for ink preparation, pH augments rapidly due to Na^+/H^+ ionic exchange [266][267][268], and the surface of the particles becomes negatively charged as a consequence of this ion exchange. Using anionic dispersants is quite impractical because of strong electrostatic repulsion forces, although there are some studies where Darvan or Easysperse dispersants were used for the stabilization of 13-93 bioactive glass suspensions [63][170]. Cationic dispersants, On the other hand, are not effective either because of their very low dissociation degree at the basic pH of these suspensions. In previous reports the fabrication of 13-93 scaffolds by robocasting was made either using complex ink formulations based on organic solvents and using a wide variety of polymeric additives [211] or water-based inks requiring a temperature-induced transformation of their rheological behavior to meet robocasting requirements [269][270].

As proved before (section 3.1), in the case of 45S5, we have been able to produce inks suitable for robocasting from 45S5 bioglass powders through a very simple recipe using small amounts (~ 1 vol.%) of carboxymethyl cellulose (CMC) as a single, multifunctional, acting as dispersant, thickener and coagulant, additive [244][271]. A similar approach was used for the fabrication of robocast 13-93 scaffolds.

The size and morphology of the used powder in ink preparation are critical [272][273] and usually a milling step is necessary prior to ink preparation. In this study, the effect of the milling milieu (water vs. ethanol) on the process ability of the 13-93 powder is analyzed. The particle size distribution of 13-93 bioactive glass particles after 3 hours (optimal time) of milling in ethanol and water is shown in Figure 3.36.
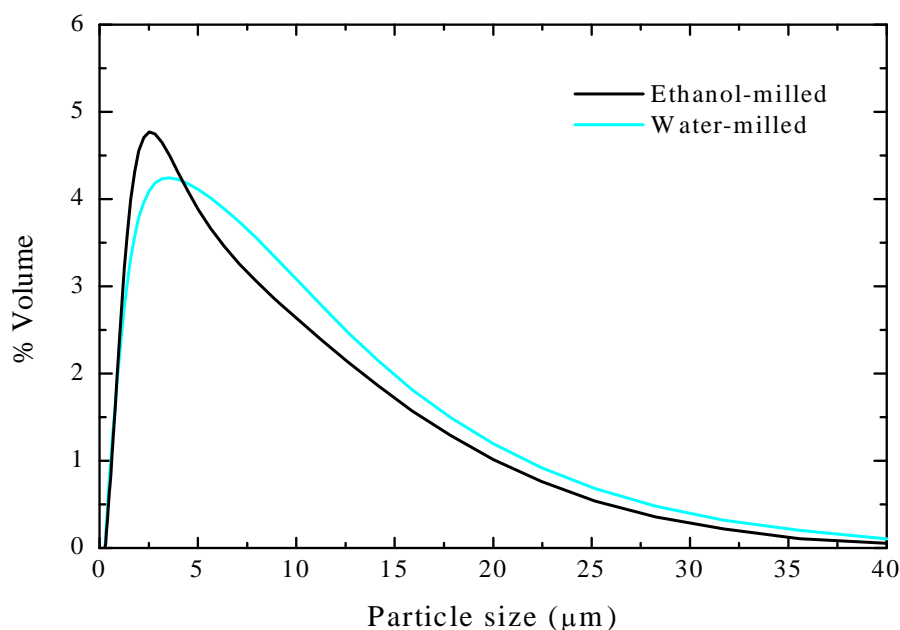
Figure 3.36. Particle size distribution of the 13-93 powder milled for 3h in ethanol or water, as indicated.

The ethanol-milled powder has a narrower distribution of sizes, with a median diameter (d_{50}) of 2.7 μm. The water-milled powder showed larger particle sizes ($d_{50} = 3.7$ μm), possibly indicating a stronger tendency of the 13-93 powder to agglomerate in this latter media since longer milling times did not provide any significant further refinement.

Both types of powders were appropriate for the preparation of inks suitable for robocasting using 1.5 wt.% carboxymethyl cellulose (CMC) as a single additive, although the performance of ethanol-milled powder in terms of process ability was superior, possibly due to the narrower, finer particle size distribution. In particular, air bubble removal was quite difficult in inks based on water-milled powder and their shape retention capacity upon deposition and drying was poorer as can be seen in Figure 3.37 showing that scaffold made of ethanol milled powder (on the right) have a better shape uniformity in comparison with that made of water milled powder (on the left).
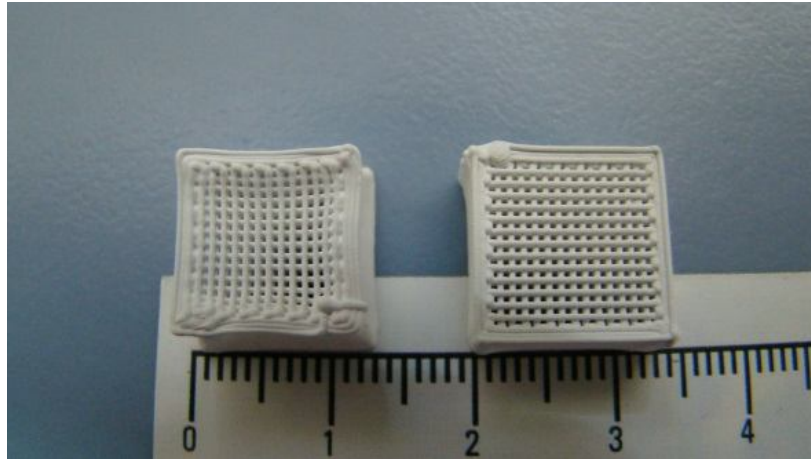
Figure 3.37. Optical images of green 13-93 scaffolds made of ethanol and water milled powder, after robocasting.

3.2.2   Sintering and microstructural characterization of 13-93 scaffolds

3.2.2.1   De-binding process

Thermogravimetric analysis (TGA, weight vs. temperature) of dried inks made of powder milled in ethanol and water showed (Figure 3.38) a weight loss of around 11 % and 9 %, respectively, which is significantly smaller than values (> 25 %) reported in previous works [211], because of the significantly lower concentration of polymeric species in the ink composition. With the exception of the magnitude of the weight loss, slightly higher for the ethanol-milled powder ink, the TGA curves showed similar trends (Figure 3.38).
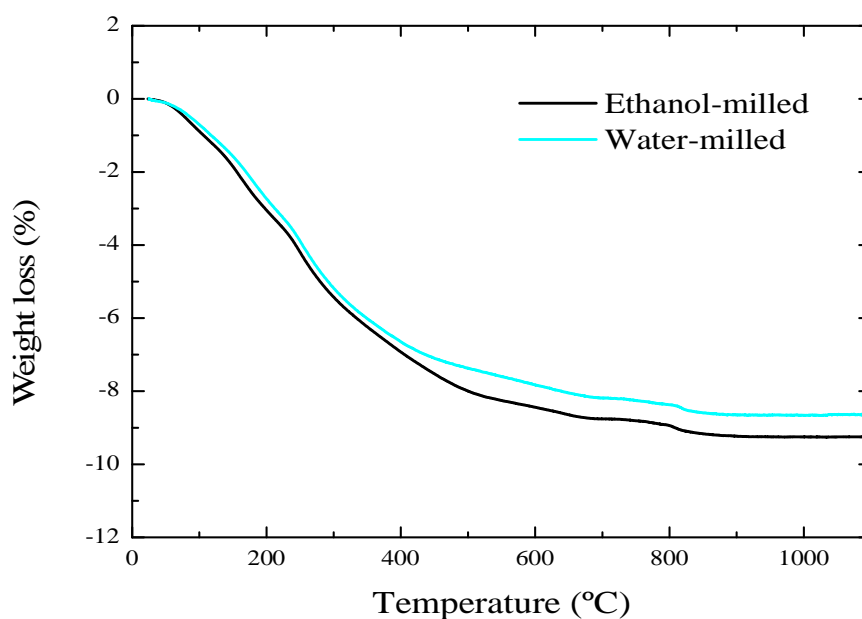
Figure 3.38. Thermogravimetric analysis (TGA) of as-dried robocasting inks made from water- and ethanol-milled powders, as indicated.

In both curves the largest weight loss occurs up to 450–500 ºC, which is attributed to the release of surface –OH groups and the removal of CMC. TGA/DTA tests performed on pure CMC (Figure 3.12), confirms that CMC is already decomposed at temperatures around 400 ºC.

Minor additional weight loss is observed starting around 700 ºC in both materials, if slightly delayed in the case of ethanol-milled inks. According to these TGA results, a debinding (CMC removal) treatment of the green constructs prepared by robocasting was carried out at a temperature of 400 °C for 1 hour, and a heating rate of 1 °C/min.

3.2.2.2   Sintering process

The differences between both types of initial powders are again evident upon analyzing their sintering behavior. Figure 3.39 shows the evolution of scaffolds' internal dimensions and macroscopic linear shrinkage with the sintering temperature (670 vs. 700 ºC) for samples made from both types of initial powders, with standard deviations as error bars. Above 700 °C, for both types of initial powders swelling and shape distortion of the scaffold was evident to the naked eye and therefore the samples were

not characterized. Internal dimensions data for as-dried green structures is also included in Figure 3.39 for comparison.
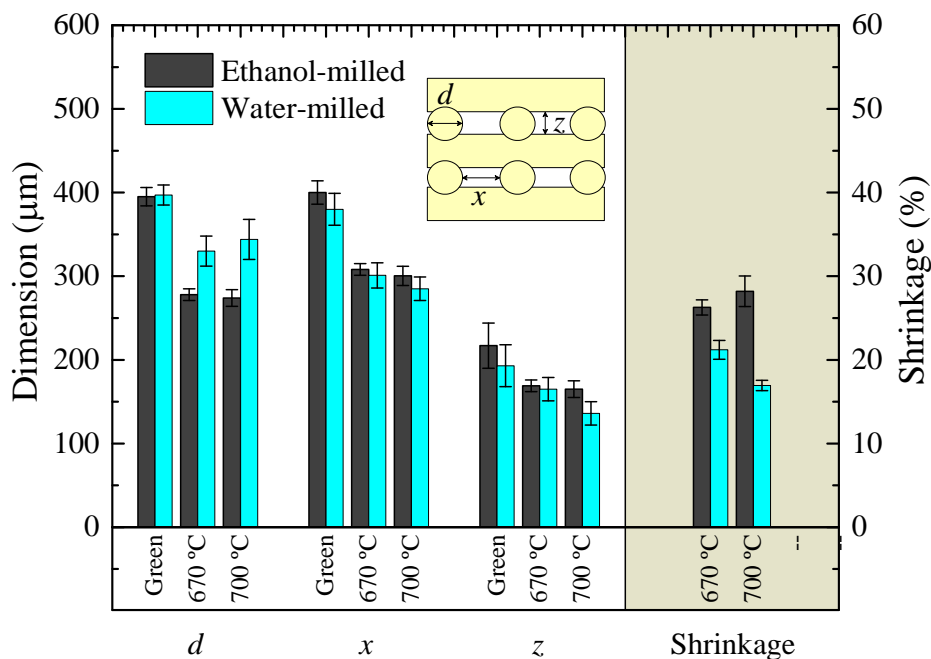
Figure 3.39. Internal dimensions and shrinkage in samples made from water- and ethanol-milled powder sintered at the indicated temperatures, with standard deviations as error bars. Internal dimensions for green samples are also included.

These green dimensions show a slight reduction in the in-plane (x) and, specially, out-of-plane (z) gaps between parallel rods (see inset diagram in Figure 3.39) for the water-milled samples compared to ethanol-milled samples, which is a consequence of the aforementioned poorer shape retention capacity of the water-milled inks. An important reduction was observed in all dimensions upon sintering. The structure shrinkage was essentially isotropic, and the scaffolds kept the designed parallelepipedical shape. However, shrinkage was larger (> 25%) and increased with sintering temperature for ethanol-milled samples, while in water-milled structures it was more moderate and decreasing with sintering temperature. This reduction in the shrinkage upon increasing the sintering temperature from 670 ℃ to 700 ℃ in water-milled structure is associated to a swelling of the structure rods (see rod diameter data in

Figure 3.39) due to internal bubble formation. This bubbling occurs also in ethanol-milled samples but only at higher sintering temperatures, where it is so important, for both types of materials, as to produce the aforementioned shape distortions in the samples.

This bubbling is also evident in Figure 3.40 which shows the relative porosity of scaffolds made from ethanol- and water-milled powders both green and after sintering at 670 °C and 700 °C. The over imposed patterned bars represent macroporosity estimations, with standard errors, from dimensional measurements (Figure 3.39) assuming a perfectly regular network of interpenetrating cylinders.
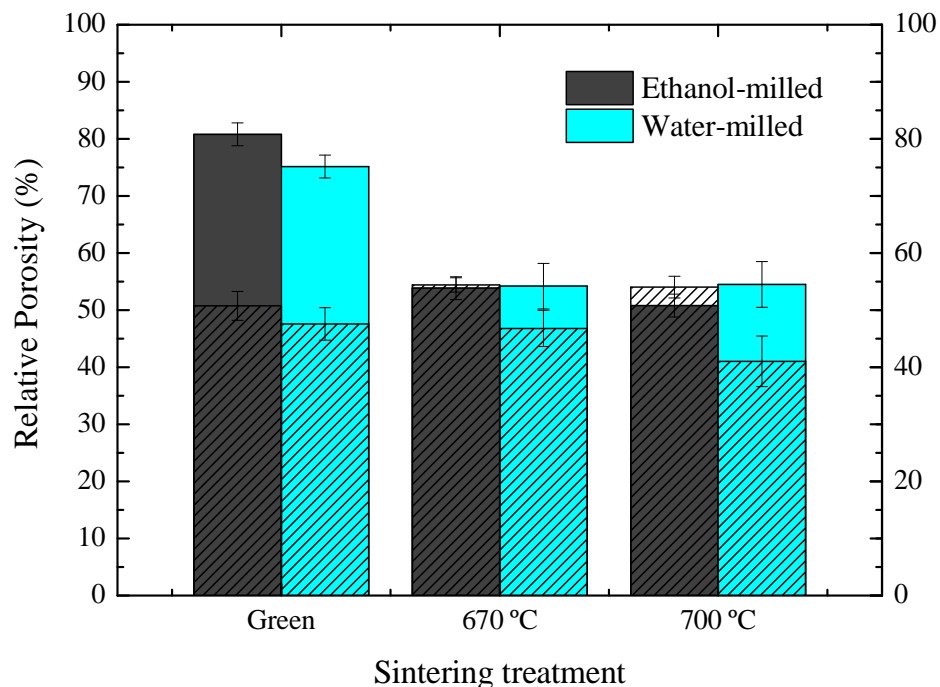
Figure 3.40. Relative total porosity for green and sintered samples made from water and ethanol milled powder, with standard deviations as error bars. Patterned bars indicate the relative macroporosity of each sample, with standard errors, as estimated from internal dimensions (Figure 3.39).

Samples made of ethanol-milled powder showed a bigger reduction of relative total porosity upon sintering in comparison with that of samples made of water-milled powder and their porosity was further reduced upon increasing the sintering temperature from 670 ℃ to 700 ℃. This reduction resulted from densification, close to full density, of the individual rods, since scaffold relative macroporosity remained virtually constant, as in 45S5 bioglass scaffolds fabricated by robocasting [271]. Macroporosity values from geometrical considerations are obviously slightly overestimated according to data in Figure 3.40, but this does not jeopardize the validity of this latter assertion. On the other hand, total porosity remained unchanged by the same increase in sintering temperature in water-milled structures due to internal bubbling, which increased microporosity within the rods at the expense of increasing rods' diameter and, thus, decreasing the pre-designed macroporosity. From the results in Figure 3.39 and Figure 3.40, it is evident that the optimal sintering temperature for ethanol-milled samples is 700 ℃ which yields virtually fully-dense 13-93 rods. However, 670℃ is the best sintering temperature for water-milled structures in order to minimize bubbling, although this temperature is insufficient to completely densify the glass rods.

3.2.2.3   Microstructural analysis

Figure 3.41 shows SEM micrographs of as-cut samples from both ethanol-milled and water-milled powders sintered at 700 ℃ and 670 ℃, respectively, which, according with previous section, are the optimal sintering condition for each type of powders. The differences in size and number of pores between both types of samples are evident, both at the surface (noticeably smoother in ethanol-milled samples) and at the transversal sections of the rods, and are in good agreement with the porosity results (Figure 3.40).
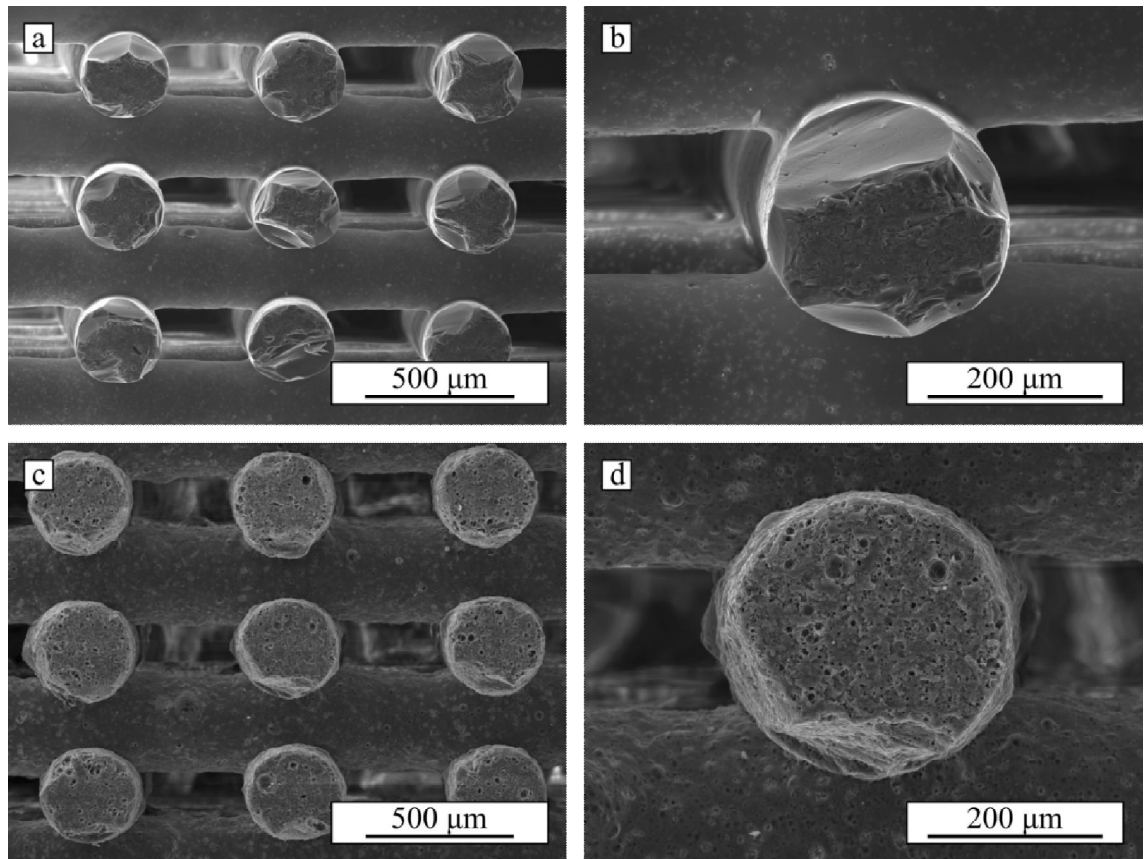
Figure 3.41 Microstructures of samples made from (a-b) ethanol-milled and (c-d) water-milled powder, sintered at 700 °C and 670 °C, respectively.

The pores formed, especially in water-milled structures, prove that the debinding process used in this study is imperfect. Bubbles could be reduced by decreasing the heating rate. As shown in Figure 3.42a and b, decreasing the heating rate from 1 to 0.2 ºC/min allows one to get almost bubble-free structures, especially from ethanol-milled starting powders.
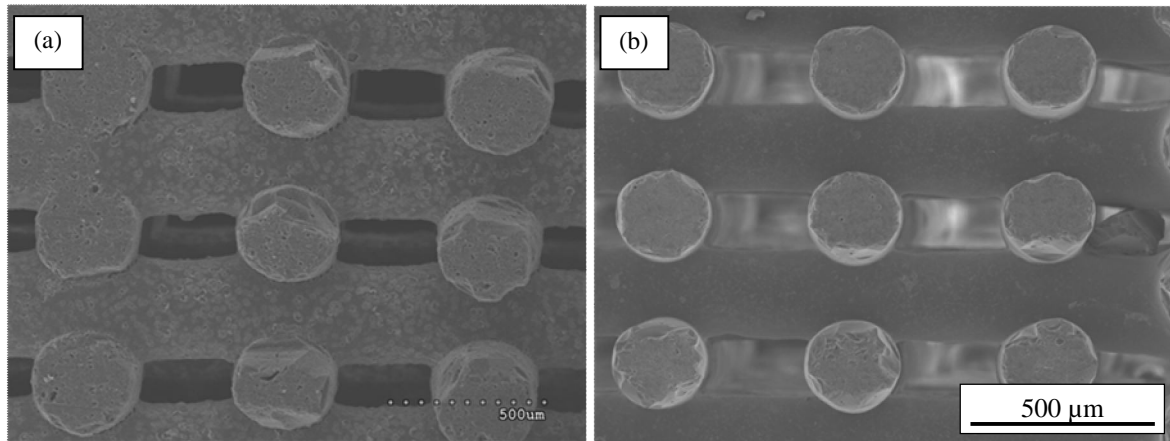
Figure 3.42 The microstructures of 13-93 bioglass scaffolds sintered with slower heating rate of 0.2 ºC/min made from (a) water-milled powder and (b), ethanol-milled sintered at 700 °C and 670 °C, respectively.

A more striking difference between water-milled and ethanol-milled samples can be appreciated in the optical images of 13-93 bioactive glass constructs shown in Figure 3.43.
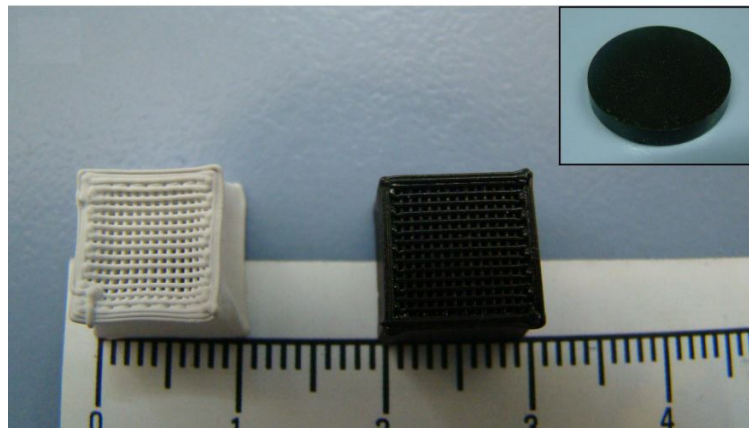
Figure 3.43. Optical images of (a) green and (b) optimally sintered 13-93 robocast scaffolds made from water-milled (on the left) and ethanol-milled powders (on the right). The inset in (b) corresponds to a 13-93 pellet made directly from compacted ethanol-milled powder after sintering at 700 ºC.

Sintered samples from water-milled powders (Figure 3.43, left sample) are all white, as are green robocast scaffolds (Figure 3.37), but samples made from ethanol-milled powder turn into a striking black color upon sintering (Figure 3.43, right sample). Specifically, the ethanol-milled samples turn black at temperatures between 500 ºC and sintering temperature (700 ºC), and the color remains even after a 1h heat-treatment at 900 ºC. The black color is attributed to some residual carbon from a species introduced during the milling process, as it was also found in pellets made of ethanol milled powder (without any CMC) fabricated by cold uniaxial pressing and sintered at 700°C (see inset in Figure 3.43). Also evident in these images is the fact that ethanol-milled samples are more regular than water-milled samples, which assess the greater quality in terms of shape retention of inks, made from ethanol-milled powders.

It is worth mentioning here some issues regarding interaction of bioglass powder and ethanol. During milling of 13-93 bioglass in the ethanol, ethyl groups of ethanol can undergo a reaction with SiOH groups of silica to form $SiOC_2H_5$ (silicon ethoxide) [274][275]. Silicon ethoxide could be converted to silicon dioxide (SiO_2) through a hydrolysis reaction as follow

$$Si(OC_2H_5)_4 + 2\ H_2O \rightarrow SiO_2 + 4\ C_2H_5OH \quad (\ 3.7)$$
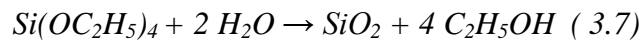
Silicon ethoxide is also stable up to temperatures around 700°C. Decomposition of silicon ethoxide (TEOS) at 680–720 °C could take place as follow

$$Si(OC_2H_5)_4 \rightarrow SiO_2 + 2\ H_2O + 4\ C_2H_4 \quad\quad (\ 3.8)$$
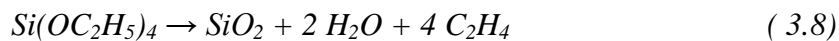
It is possible that some free carbon remains as a product of above mentioned equations. This free carbon phase can react consequently with Si- O bonds

$$C_{free} + \equiv Si\text{ - }O\text{ - }Si\equiv \rightarrow\ \equiv Si\text{ - }C\text{ - }O\text{ - }Si\equiv \quad\quad (3.9)$$
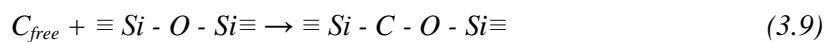
This reaction leads to the formation of new C-O and Si-C bonds [276-277]. The source of black color is the free carbon.

The increased presence of carbon in ethanol-milled samples was confirmed by X-Ray Photoelectron Spectroscopy (XPS). Figure 3.44 shows the XPS spectrum for as received 13-93 frits and sintered samples made from ethanol-milled and water-milled

powders, after ion-beam etching (100 s, 1000 V, 17 μA). The XPS results revealed that the concentration (at.%) of carbon in the sintered samples made from ethanol-milled powder are around 3 times that of the as-received powder and water-milled samples. The amount of carbon in the sintered samples made of water milled powder did not differ obviously from as received powder. The C(1s) XPS peak of the sintered samples made of ethanol milled powder suggested the presence of carbon atoms sharing bonds simultaneously with silicon and oxygen atoms forming $\equiv$ Si-O-C$\equiv$ units. This residual carbon is believed to be in solid solution within the 13-93 glass structure.
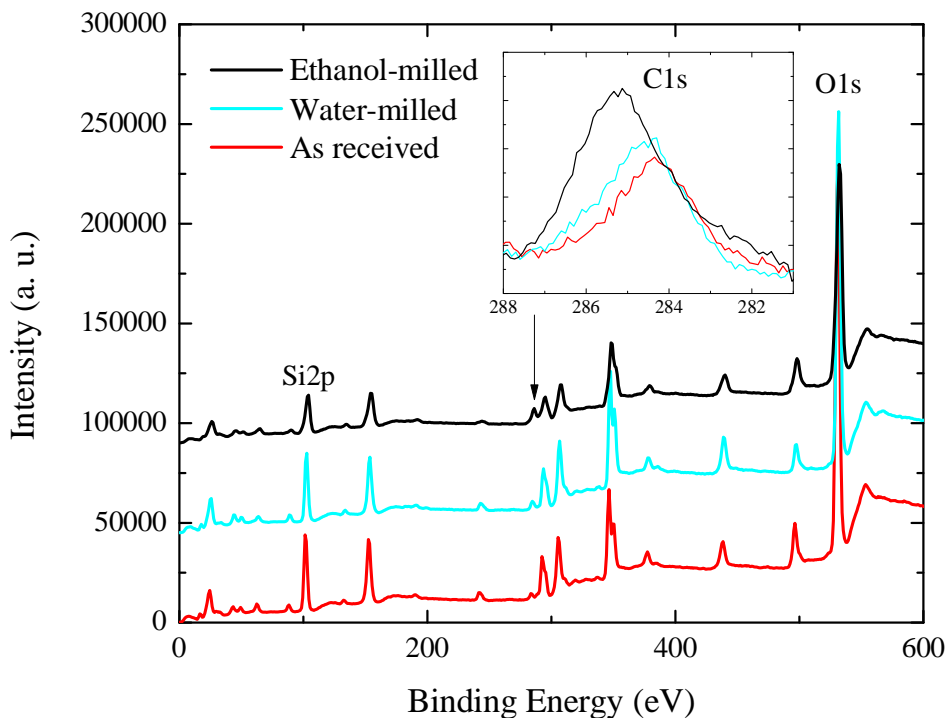
Figure 3.44. XPS spectra for as-received powders and water- or ethanol-milled samples sintered at 700 ºC. Inset shows a detail of C1s peak for all materials.

This hypothesis is consistent with the results from X-ray diffraction analysis, which are shown in Figure 3.45 for as-received 13-93 frits and sintered scaffolds made from both types of powders. As-received material showed the typical XRD pattern of an amorphous material with a broad band, centered around 30°-2θ, instead of diffraction peaks. The same is true also for all the sintered scaffolds, since no trace of the

wollastonite ($CaSiO_3$) phase into which 13-93 glass crystallizes was found at the selected sintering temperatures. The small peaks that appear in sintered samples are attributed to zirconia impurities from the YTZP milling balls and jar.
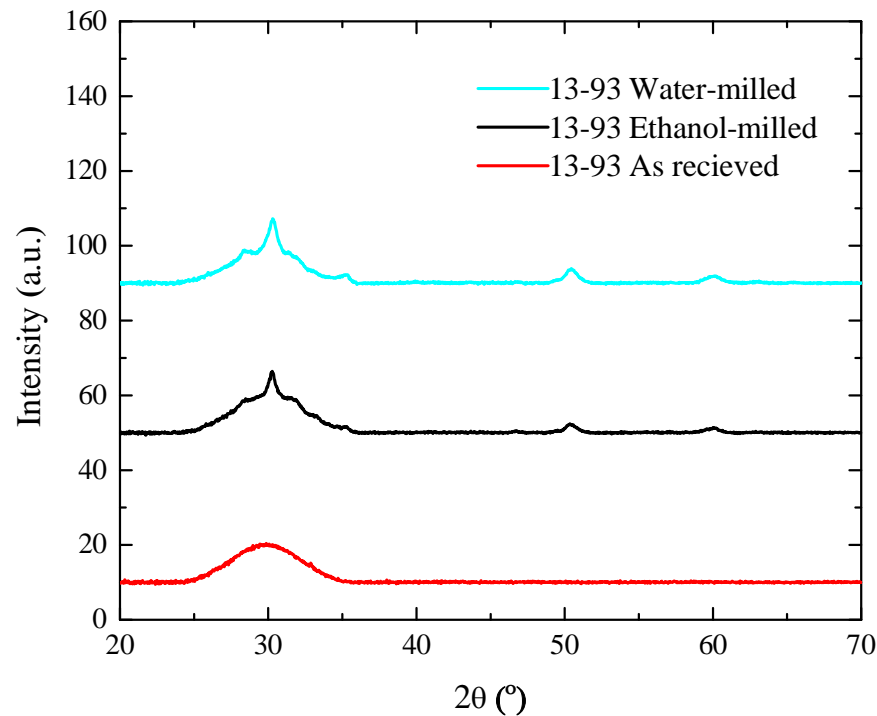
Figure 3.45. X-ray diffraction patterns of grinded samples of as received 13-93 bioactive glass frits and scaffolds made from ethanol- or water-milled 13-93 powders sintered at 700 ºC.

Both the black color in ethanol milled samples and the swelling and distortion of both types of samples around or above 700 °C indicate that some residues from sample preparation remain in the material after the de-binding treatment tested here. The existence of a residual species volatile around/above 700 ºC is in good agreement with TGA results (Figure 3.38), as is the fact that volatilization of such species seems to initiate at slightly lower temperature in water-milled samples. However, since volatilization of this species occurs so close to the optimal sintering temperature it is difficult to devise a simple debinding treatment capable of eliminating the residue without affecting the scaffold morphology. Even more challenging would be to eliminate the carbon responsible for blackening the ethanol-milled structures without

significantly altering the material since not even treatments at 900 ºC, well above the crystallization temperature (~700ºC) [49], were successful. Therefore, it was deemed essential to evaluate the effect of these persistent residues on the biological performance of the 13-93 bioactive glass scaffolds obtained by the proposed fabrication routes.

3.2.3 *In vitro* **bioactivity**

The change in the pH of the SBF solution as a function of immersion time in the solution of 13-93 glass scaffolds made from ethanol- and water-milled powders is shown in Figure 3.46 . The pH increase with immersion time results from the dissolution of the glass modifiers (Na^+ and K^+) and has been commonly observed for the bioactive glass reaction in SBF [120][278-279]. 13-93 bioglass scaffolds exhibit a slower pH change than 45S5 bioglass scaffolds (Figure 3.20b) due to the higher intrinsic degradation rate of 45S5 bioglass.
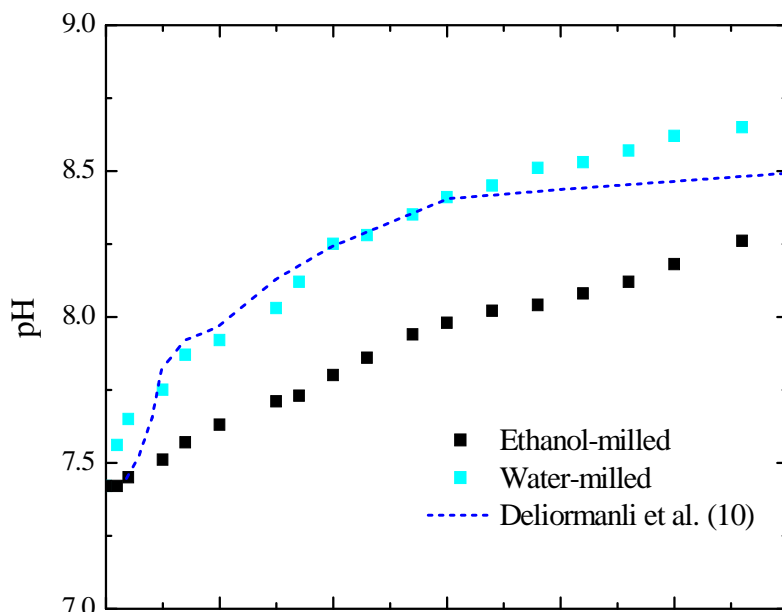
Figure 3.46. Plot of the variation of the pH of SBF solution as a function of immersion time for sintered scaffolds made from ethanol- and water-milled powder.

Water-milled powders exhibited pH change kinetics very similar to previously reported values by other authors (dashed line in Figure 3.46) [280], if the pH increase was somewhat faster initially, and eventually reached slightly higher values. There were more substantial differences in the behavior of scaffolds made of ethanol-milled powder, which exhibit significantly lower pH values over the whole degradation period analyzed. This is attributed to the dissolution of the acidic carbonaceous species introduced by milling. Indeed, as evidenced in. This slower pH change does not necessarily indicate slower degradation kinetics. Indeed, as evidenced in Figure 3.47, showing the weight loss, $\Delta W/W_0$, data as a function of immersion time in the SBF solution, the degradation kinetics of scaffolds made of ethanol-milled powder, followed closely that of 13-93 scaffolds fabricated from water-milled powders by other authors (dashed line) [280], although they were both significantly lower than the results obtained in this study for water-milled scaffolds.

In comparison with 45S5 bioglass scaffolds, the rate of weight loss of water-milled 13-93 bioglass scaffolds is considerably smaller than that of 45S5 bioglass scaffolds sintered at 1000ºC (Figure 3.20a), in spite of their similar level of microporosity (see Figure 3.15and Figure 3.40). As in the case of pH, this reflects that the chemical composition of 45S5 bioglass is more soluble in SBF, due to its higher alkali content.
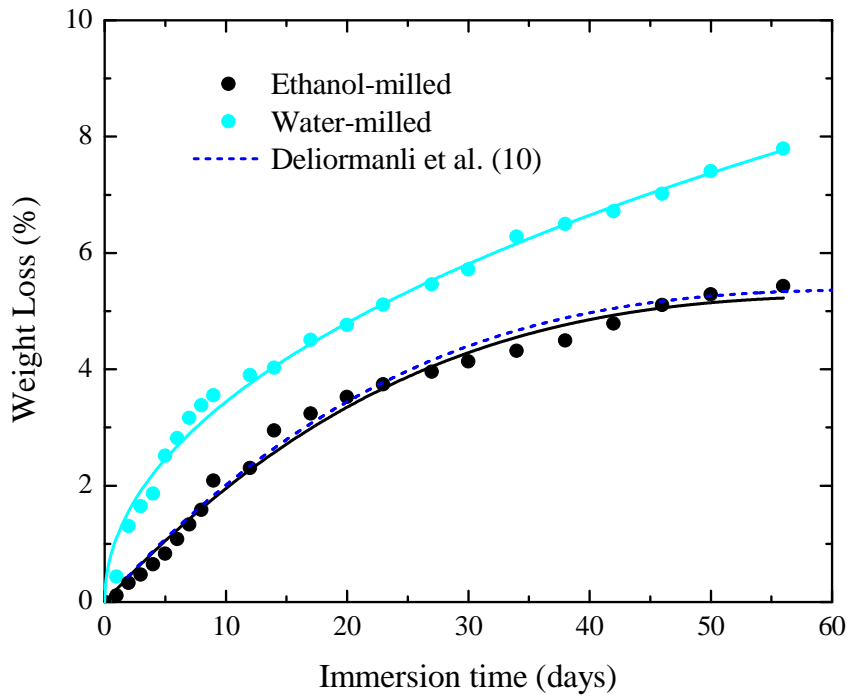
Figure 3.47. Plot of the variation of the weight loss of 13-93 scaffolds as a function of immersion time for sintered scaffolds made from ethanol- and water-milled powder.

Weight loss is associated to the dissolution of the glass in the solution and the HAp layer deposition, and therefore the $\Delta W/W_0$ data can be used to analyze the kinetics of the conversion reaction. In the case of the ethanol-milled scaffold fabricated here and water-milled scaffolds by other authors, $\Delta W/W_0$ data could be nicely fitted (solid black line) to a contracting volume model (CVM) function [281-284]:

$$\Delta W/W_0 = \Delta W_{max}/W_0[1-(1-kt)^3] \qquad (3.10)$$

where, the maximum weight loss $\Delta W_{max}/W_0$ and the kinetic constant k are adjustable parameters and t is the immersion time. CVM assumes that the reaction at the interface is rate controlling and that nucleation at the reaction interface is fast, so the reaction rate depends on the variation of geometry as the interface moves inward at a uniform rate. However, CVM could not provide a good fitting of the data corresponding to water-milled samples produced in this study. The degradation in this material was faster and data could only be fitted properly by a three-dimensional diffusion model (3DM) function [283-284]:

$$\Delta W/W_0 = \Delta W_{max}/W_0 \{1-[1-(kt)^{1/2}]^3\} \qquad\qquad (3.11)$$

3DM diffusion model assumes that volumetric diffusion to the reaction interface is what controls the degradation rate. Therefore, CVM seems to describe well the degradation kinetics of robocast scaffolds with smooth rod surfaces, regardless of the slight compositional differences that arise from the use of different milling media and processing route. Conversely, for scaffolds with greater in-rod microporosity and greater surface area, such as the water-milled structures fabricated in the current study, it seems that interfacial area reduction during degradation is no longer such a limiting factor and diffusion of the appropriate species through the rods volume receives the baton. The existence of microporosity seems to provide not only faster degradation kinetics but also a means for enhanced overall conversion factor of the bioactive glass to HA. Indeed, while dense-rod structures yield a total conversion, $\Delta W_{max}/W_0$, below 6 %, the estimated value for our microporous water-milled structures is around 35 % — maximum theoretical weight loss is 64.1% [284]. This could be attributed to the fact that in a pore-free material with a smooth surface it is easier to generate a HA layer capable of isolating the 13-93 bioglass from the SBF media and, thus, stopping the reaction.

In any case, the surface of scaffolds made from both ethanol- and water-milled 13-93 glass powder were fully covered by a HAp layer after immersion in an SBF for 7 days, as shown in the SEM micrographs of Figure 3.48, in good accordance with previous reports [285]. The treatment in the SBF produced a surface layer consisting of a porous network of nanometer-sized, needle-like HAp crystals as shown in the higher magnification inset images. The only observable difference between both types of materials is that the HAp excrescences are larger and more numerous in water-milled structures, as corresponds to its faster conversion kinetics.
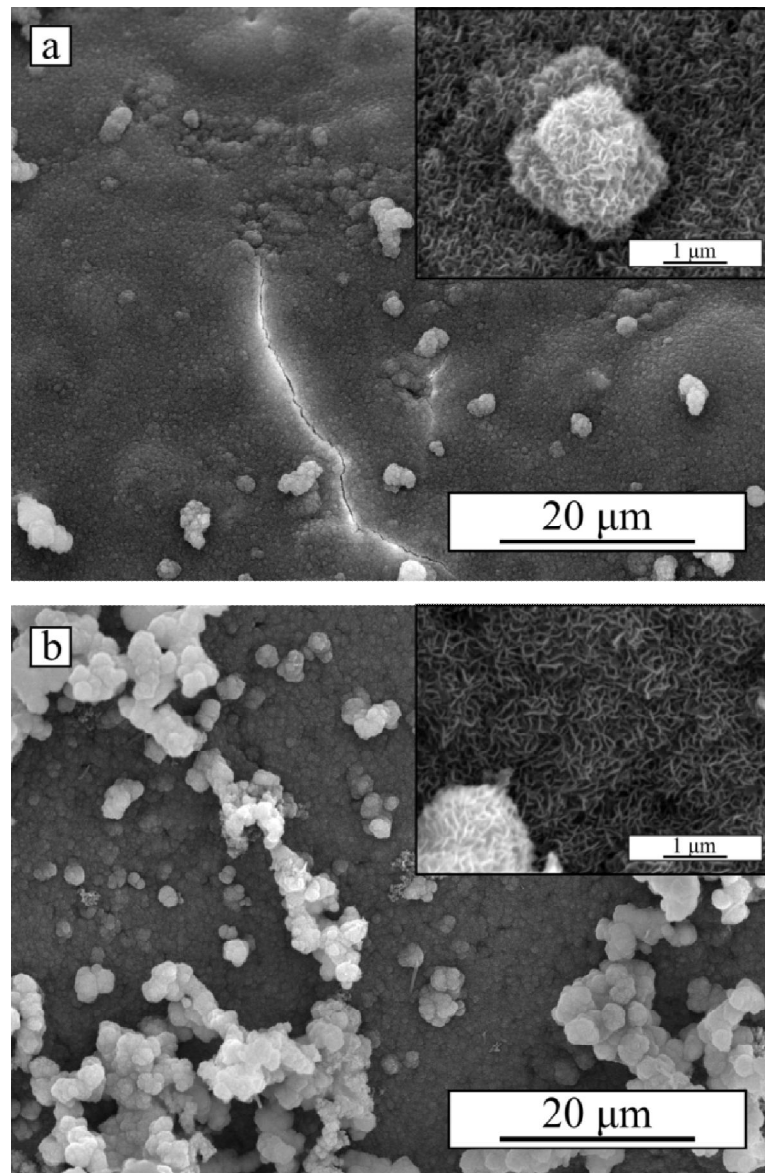
Figure 3.48. SEM micrographs of a rod-surface on a 13-93 glass scaffold made from (a) ethanol-milled and, (b) water-milled powders after immersion in SBF for 7 days. Insets show the same surfaces at higher magnification.

These results prove that the presence of microporosity within the rods of robocast scaffolds plays a major role in controlling the *in vitro* degradation of 13-93. The initially undesired presence of bubbles in water-milled samples has shown how the presence of such pores within the structure rods not only enhances the degradation rate but also the overall conversion factor of the 13-93 bioactive glass to HAp — from below 6%, for dense structures to around 35% for our microporous water-milled structures.

These effects are attributed to the inability of the forming HA layer to eventually passivate the surface of the water-milled 13-93 rods, as the internal microporosity continuously transforms into new paths for the media to reach unconverted material. These results suggest then a simple means for controlling the degradation behavior of bioactive robocast materials by tailoring their microposority, although further systematic studies are required to better quantify this effect both *in vitro*, and especially *in vivo*, where even dense 13-93 rods exhibit a much enhanced conversion to HAp [269].

According to our results the residual impurities introduced during the proposed fabrication route do not seem to affect the in-vitro bioactivity and degradation performance of 13-93 glass. This would not exclude, however, the presence of these species from affecting the capacity of the materials for interacting with cells. Figure 3.49 shows the results of cell cultures performed on 13-93 glass scaffold made from ethanol- and water-milled powders, compared to a control HA robocast scaffold of similar dimensions. The significant increase in the total amount of cells ($p < 0.05$) on the porous 13–93 glass scaffolds with increasing culture duration (Figure 3.49) demonstrates that cells can proliferate *in vitro* onto these structures, thereby excluding the possibility of cytotoxic effects associated to the leaching of impurities introduced during processing as the material degrades. At 16 days cells already thoroughly cover the surface of the rods in the 3D structure (see inset in Figure 3.49).
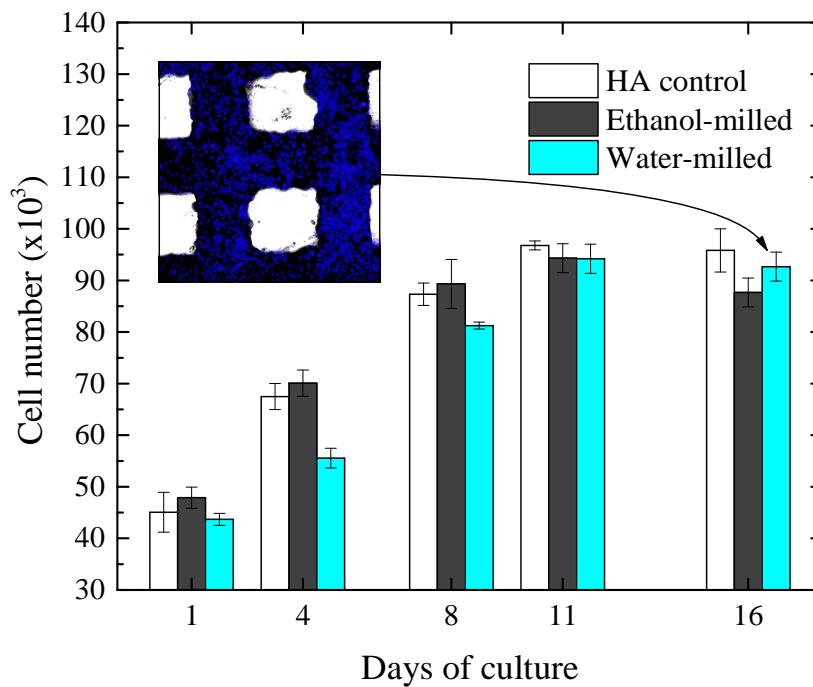
Figure 3.49. Quantitative measurement of cell number per scaffold in C2C12 cell cultures incubated for 1, 4, 8, 11 and 16 days on 13-93 glass scaffolds made from ethanol- and water-milled powders, and in control HA robocast scaffolds of similar dimensions. Result represent means values (n = 3) with standard deviations as error. Inset show a representative confocal image of a water-milled scaffold at 16 days.

Nonetheless, these results should be further confirmed by in vivo test in order to completely rule out any potential risks associated to the presence of the carbonaceous species in ethanol-milled 13-93 scaffolds.

3.2.4   Mechanical response before and after immersion in SBF

The fabricated scaffolds were tested in compression, with the applied load perpendicular to the plane of deposition of the constructs, before and after immersion in SBF. All samples showed an elastic response followed by failure in a brittle manner. The evolution of the compressive strengths of robocast scaffolds made from ethanol- and water-milled powders with immersion time in SBF is shown in Figure 3.50, with standard deviation as error bars. Despite the lower quality of the 13-93 scaffolds made from water-milled powder, compared to the virtually defect-free surfaces of ethanol-

milled structures (Figure 3.42), these constructs exhibit the highest initial compressive strength (114 ± 27 MPa vs. 80 ± 10 MPa), which is within the range of values (100–300 MPa) typically reported for human cortical bone [29,30][286-288]. The reason for these surprising results lies in the geometrical differences existing between both types of constructs. Particularly the larger diameter of the rods comprising the water-milled scaffolds explains why these constructs can sustain greater compressive stresses, despite the presence of larger defects in the material, which certainly reduce the intrinsic strength of the individual rods — 120 ± 20 MPa for water-milled vs. 280 ± 20 MPa for ethanol-milled samples, as determined from 3-point bending tests. Indeed, the compressive strength of open-cell foams, σ_C, can be roughly estimated by the following expression [289]:

$$\sigma_c \propto \sigma_s (d/x)^3 \qquad\qquad (3.12)$$

where, σ_s is the intrinsic strength of the struts, d is the strut diameter/thickness and x the size of the cell/separation between struts. Therefore, while the compressive strength varies linearly with the intrinsic strength of the struts/rods, it depends on the geometrical ratio d/x to the third power. This explains why small variations in the geometry of the scaffolds can yield substantially different strength values. This is the case not only of our two sets of results but also of other existing reports. Indeed, included in Figure 3.50 are results for 13-93 scaffolds by other authors showing vast discrepancies in the reported strength values for quite similar structures [211][269].
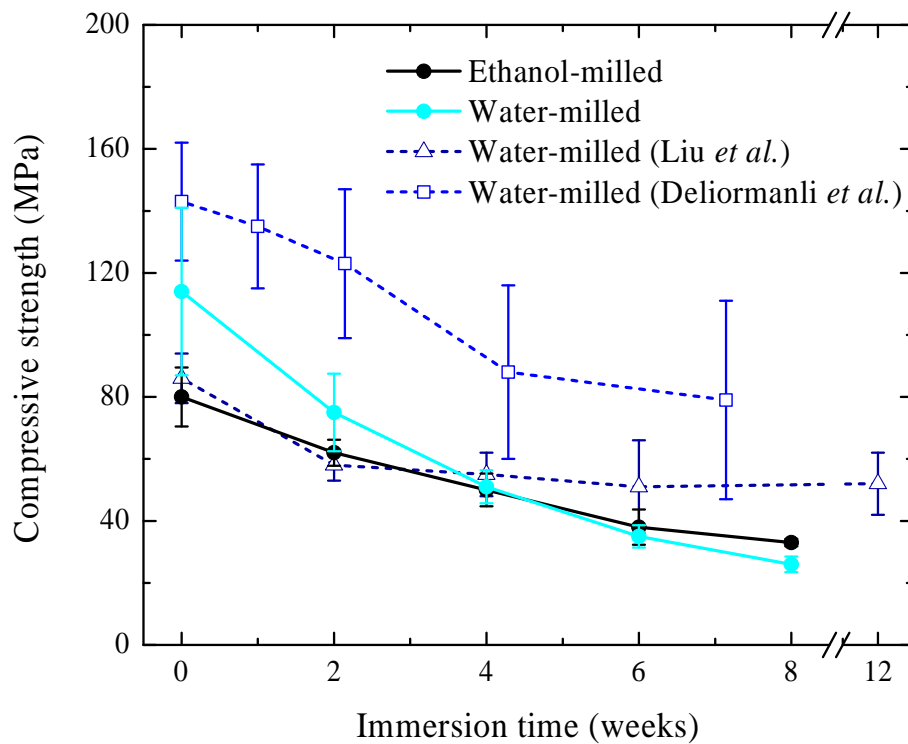
Figure 3.50. Evolution of the compressive strength of the 13-93 robocast scaffolds upon immersion in SBF, with standard deviation as error bars. Data from literature is included for comparison.

After immersion in SBF, the compressive strength of all 13-93 scaffolds decreased with immersion time, reflecting the degradation/conversion to HA of the material. Therefore, in good agreement with the results shown in Figure 3.47, the scaffolds made from water-milled powder showed a faster and greater decrease in strength when compared to the ethanol-milled scaffolds — down to 26 ± 2.5 MPa (77 % reduction) vs. 33 ± 1.2 MPa (58 %), after 8 weeks of immersion. The faster conversion of the scaffolds made of water-milled powder to a weak (porous) hydroxyapatite-like product resulted in a steeper and greater reduction in the strength. The strength reduction of 13-93 scaffolds, especially of ethanol-milled scaffolds, is slower than of 45S5 scaffolds, in good agreement with the higher degradation rate of 45S5 bioglass.

The reduction for water-milled samples seems to be far from complete after 8 week of immersion, while ethanol-milled sample's strength seems to be close to its final

asymptotic value. In any case, both groups of scaffolds exhibited compressive strengths higher than that of a human trabecular bone (1–10 MPa) [287] even after 8 weeks of immersion in SBF.

3.2.5   Polymer-impregnated 13-93 robocast scaffold

In this section, results related to the effect of PCL or PLA infiltration on the mechanical properties of 13-93 bioactive glass scaffolds fabricated by robocasting from ethanol-milled powder are shown. The mechanical enhancement achieved upon impregnation of 13-93 structures with nearly fully-dense struts reinforces the conclusions derived in section 3.1.5.3 regarding the role of strut microporosity in the strengthening and toughening mechanisms.

3.2.5.1   Microstructural characterization of polymer impregnated 13-93 scaffolds

Figure 3.51 shows SEM micrographs of representative as-cut specimens of the 13-93 robocast scaffolds fabricated from ethanol milled powders before (Figure 3.51 a) and after impregnation with PCL and PLA (Figure 3.51b and c, respectively).
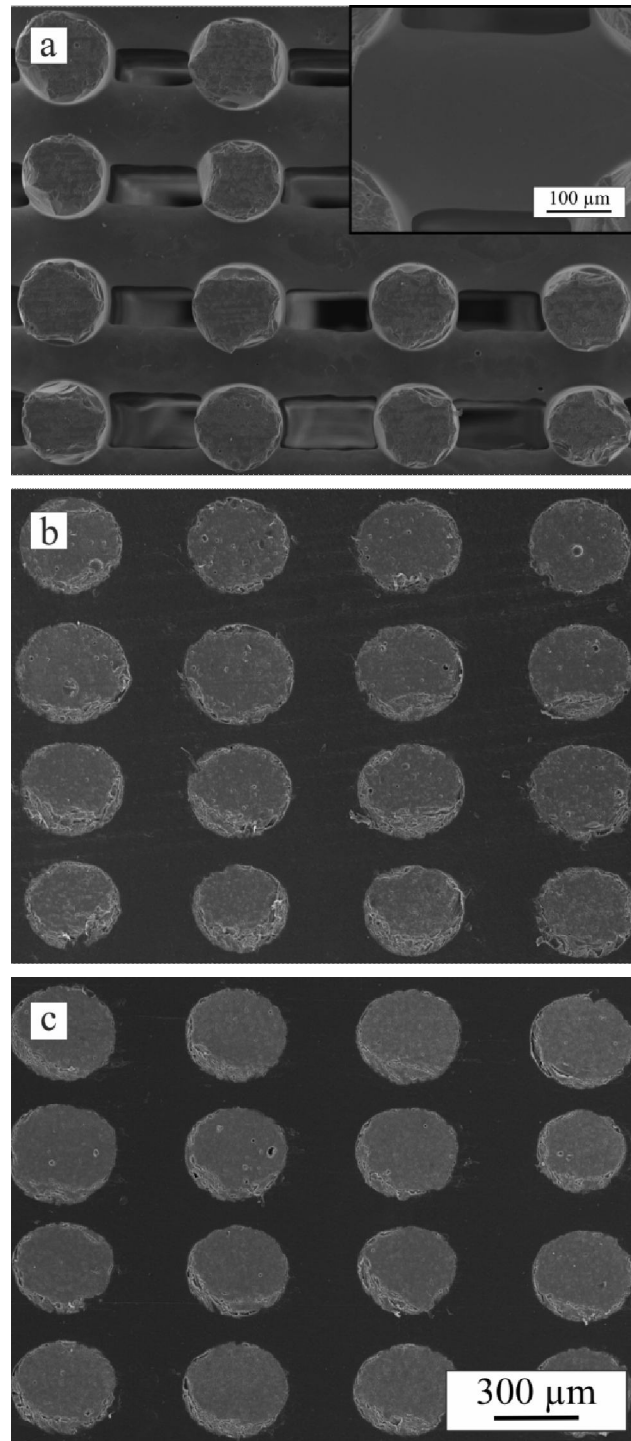
Figure 3.51. SEM micrographs of representative as-cut specimens of 13-93 robocast scaffolds: (a) bare, (b) PCL-impregnated and (c) PLA-impregnated structures.

13-93 bioactive glass scaffolds with average rod diameter of 274 ± 10 µm and in-plane and out-of-plane gaps between parallel rods of 300 ± 11 µm and 165 ± 10 µm, respectively, were obtained after sintering at 700 ºC, resulting in a relative porosity of

51 ± 2 % (Figure 3.40). The 13-93 bars exhibited a smooth, nearly defect-free surface and virtually no pores were visible in their transversal section (Figure 3.51 a). The images in Figure 3.51b and c confirmed that the selected infiltration conditions were appropriate to completely fill the robocast structure's macroporosities with PCL and PLA, respectively. The resulting co-continuous glass/polymer composites have then approximately a 50/50 vol. % composition. Unlike polymer impregnated 45S5 scaffolds (section 3.1.5.1 and 3.1.5.2), there is not any sign of polymer degradation in the presence of 13-93 bioglass at the impregnation temperature.

3.2.5.2   Mechanical characterization of polymer impregnated 13-93 scaffolds

— *Compression tests*

Figure 3.52 shows representative uniaxial compressive stress–strain curves for the three types of structures fabricated: bare 13-93 scaffolds, and 13-93/PCL and 13-93/PLA co-continuous composites. Typical curves for pure PCL and PLA polymers have been included also for comparison. As bare 45S5 scaffolds, uninfiltrated 13-93 scaffolds showed the typical brittle behavior of glasses with linear elastic response up to the point when the applied stress reached the compressive strength of the structure and catastrophic failure occurred, as evidenced by a drastic drop of the stress down to zero. Infiltration of the scaffolds with polymers does not change significantly the initial part of the stress-strain curves and the composites behave also linearly elastic until fracture of the ceramic skeleton occurs, but the presence of the polymer prevents then the catastrophic failure of the material, which retains a certain mechanical integrity. This is especially true in the case of PCL-impregnated structures where minor cracking events can occur before the maximum stress is reached and failure of the glass skeleton occurs, and which retain a remarkable load-bearing capacity afterwards—the stress remains with a roughly constant value not much lower (15-50 %) than the compressive strength of the material even after very large strains (> 30 %). Indeed, 13-93/PCL composite samples remained a single piece after the tests, like pure polymeric samples. On the other hand, samples infiltrated with PLA exhibited a higher compressive strength in comparison to bare and PCL-impregnated scaffolds, but a significantly lower residual load bearing capacity after failure (< 20 % of the maximum load), which continuously

declined to zero before 30 % strain was reached, and the sample was broken in pieces after the test.
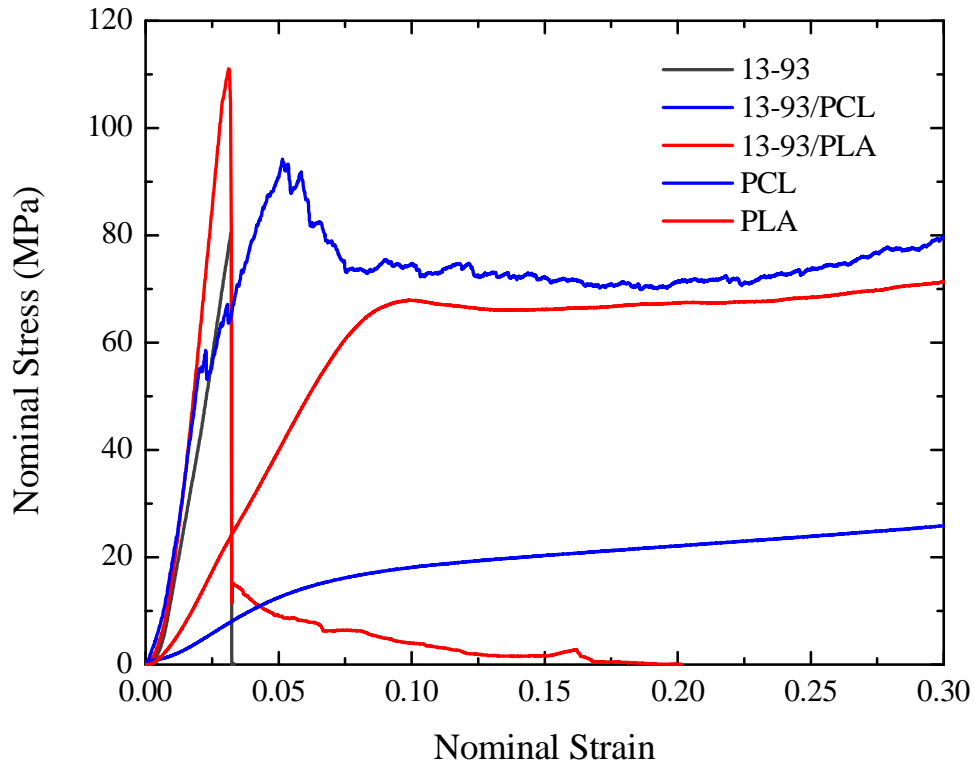
Figure 3.52. Representative uniaxial compressive stress–strain curves for: bare 13-93 scaffolds, 13 93/PCL and 13-93/PLA co-continuous composites, and pure PCL and PLA polymers.

To better analyze the strengthening effect, Figure 3.53 shows the Weibull plots of the compressive strength data obtained for all studied materials. This plot shows the failure probability as a function of applied compressive stress. Each point corresponds to a single test and the straight lines are best fits to data using the Weibull probability function.
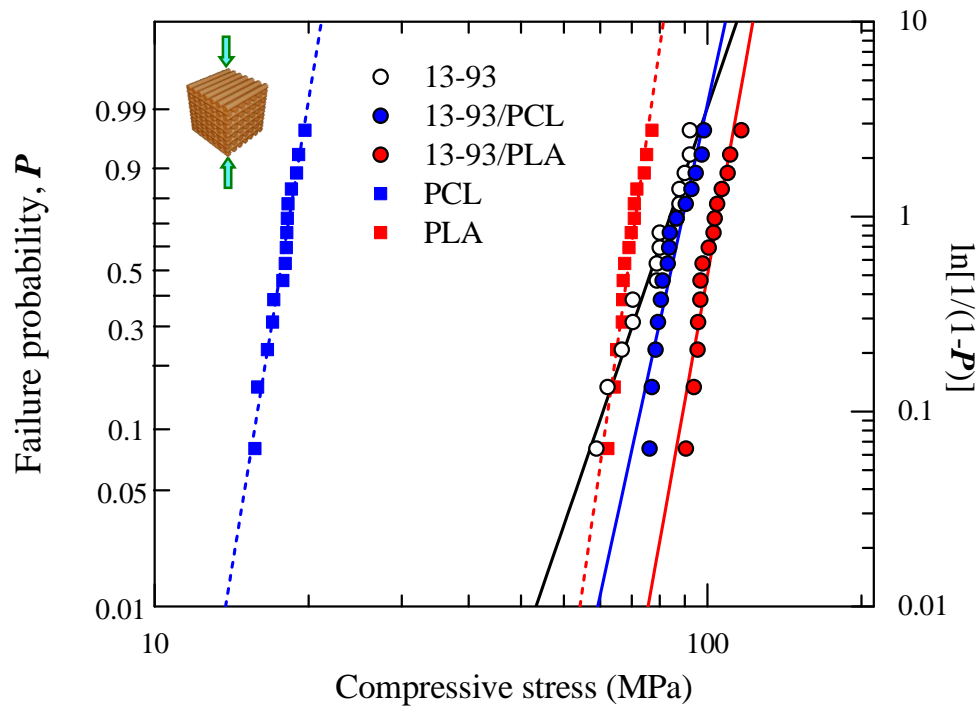
Figure 3.53. Weibull plot of the compressive strength data for indicated materials. Strength values for PCL correspond to yield stress. Straight lines are best fits to data using the Weibull probability function.

The fitting parameters of these regressions are summarized in Figure 3.54, with standard errors, together with typical values for human bone as shaded bands [290-291]. According to Figure 3.54 a, the central value of the distribution, i.e. the compressive strength of the scaffold, barely increased ($\sim 5\%$, significant at $p < 0.1$) after PCL impregnation but was improved by 21 % in 13-93/PLA composites, reaching the lower end of cortical bone strength range. In all cases composite strengths were also significantly superior to those of the bare polymers (5 times larger in the case of PCL and 40 % greater for PLA). As aforementioned (section 3.1.5.3), two different strengthening mechanisms occur upon polymer infiltration: stress shielding and defect healing [20][221][265]. The results of this study demonstrate, however, that the effectiveness of both mechanisms is highly reduced when the ceramic frame is dense as is the case of 13-93 scaffolds. Indeed, the strengthening achieved in this study upon

polymer impregnation are substantially lower than those obtained in 45S5 scaffolds, especially those sintered at higher temperature, (Figure 3.28) and tricalcium phosphate (TCP) structures with microporous rods [20-21]. The reason for this result is double. On the one hand, the high mismatch between the elastic properties of the dense ceramic bars and the polymer infiltrate is too high for the latter to sustain a significant part of the applied load. And on the other, when the rod microporosity, and thereby the precursor flaw population in the scaffold surface, is reduced, the effect of the infiltrating polymer when sealing those defects on the strength becomes less dramatic.

The reliability of the 13-93 structure, evaluated by the Weibull modulus (Figure 3.54 b), significantly improved in the impregnated structures by more than 50% in the case of PCL and nearly 100% for PLA, although in neither case the value reached the levels of the pure polymers. In any case, reliability of all tested materials was equal or superior to a previously reported value for human cortical bone under tensile fatigue ($m = 8$) [292].

Figure 3.54. Weibull best fitting parameters to data in Figure 3.55, with standard errors: (a) central values, σ_0, and (b) Weibull modulus, m. Strength value for PCL corresponds to yield stress. Typical values for human bone are shown as shaded bands[264][293].

In order to quantify the toughening effect of polymer infiltration, Figure 3.55 shows the strain energy density at 30% strain, G_c, calculated from the area under experimental stress strain curves such as the ones presented in Figure 3.52 for all five analyzed materials, as indicated, with standard deviation as error bars. Values for human bone [264][293] are also included as shaded bands for comparison.

A significant improvement in the strain energy density of the 13-93 bioglass scaffolds is apparent upon impregnation with polymers, especially with PCL. According to these data, toughening factors are 2.5 and 13.5 for PLA and PCL infiltrates, respectively. Indeed, 13-93/PCL composites exhibit, in compression, superior toughness to either PCL or PLA pure polymers and, like them and cancellous bone, will survive even larger strains (as schematically indicated by the upward-extending graded bands in Figure 3.55). Nevertheless, 13-93/PLA composite compression toughness, while substantially inferior than that of the pure polymers (or 13-93/PCL), is still significantly superior to that of the bare scaffolds, and comparable to cortical bone values.
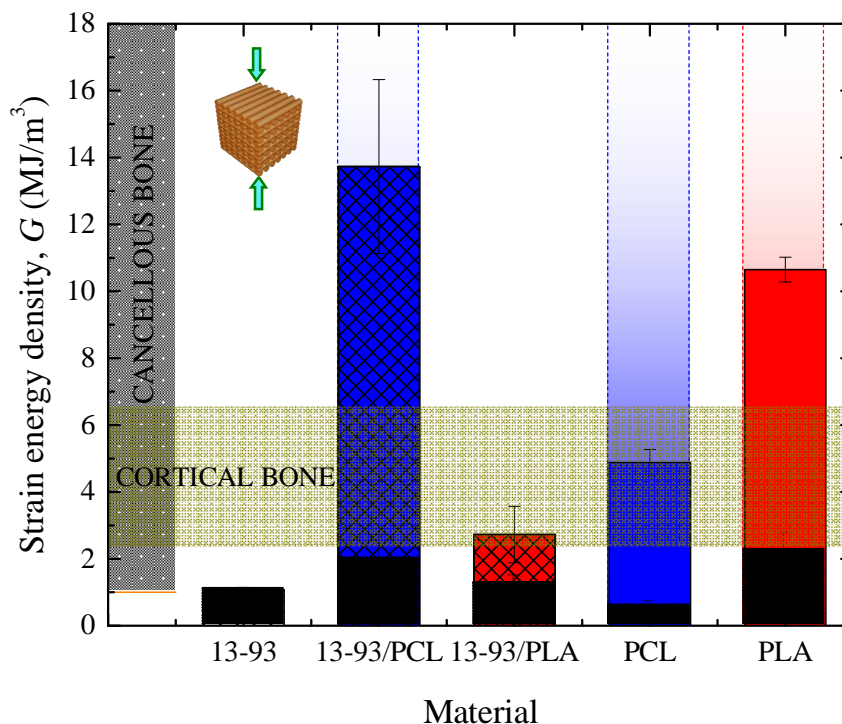
Figure 3.55. Strain energy density in compression for the indicated materials at 30 % strain with standard deviation as error bars. Values for human bone [264][293] are included as shaded bands for comparison.

Nonetheless, as the strengthening effect, the toughening effect of polymer impregnation is reduced in pristine glass robocast structures compared to 45S5 scaffolds, especially those sintered at higher temperature, (Figure 3.29) and microporous TCP scaffolds [21][265]. This is both due to the reduced strengthening achieved (see Figure 3.54a) and the absence of polymer microfibrils generating from the polymer inside micropores which enhance union between the organic and inorganic phases and is responsible for a crack microbridging toughening mechanism [21].

— *Bending tests*

Regarding the results of the four-point bending tests, Figure 3.56 shows the Young's modulus, with standard deviations as error bars, for all analyzed materials as evaluated from their elastic deflections with the aid of a suitable extensometer. The elastic modulus of porous 13-93 scaffolds did not increase significantly upon infiltration with either polymer, even the stiffer PLA. However, the converse is obviously true: hybridization of the polymers with the ceramic skeleton improved their moduli by at least one order of magnitude (by 10 and ~ 60 times for PLA and PCL, respectively), from values more typical of human cancellous bone (0.05-0.5 GPa) to well within cortical bone range (7-30 GPa), shown as shaded bands in Figure 3.56 [290].
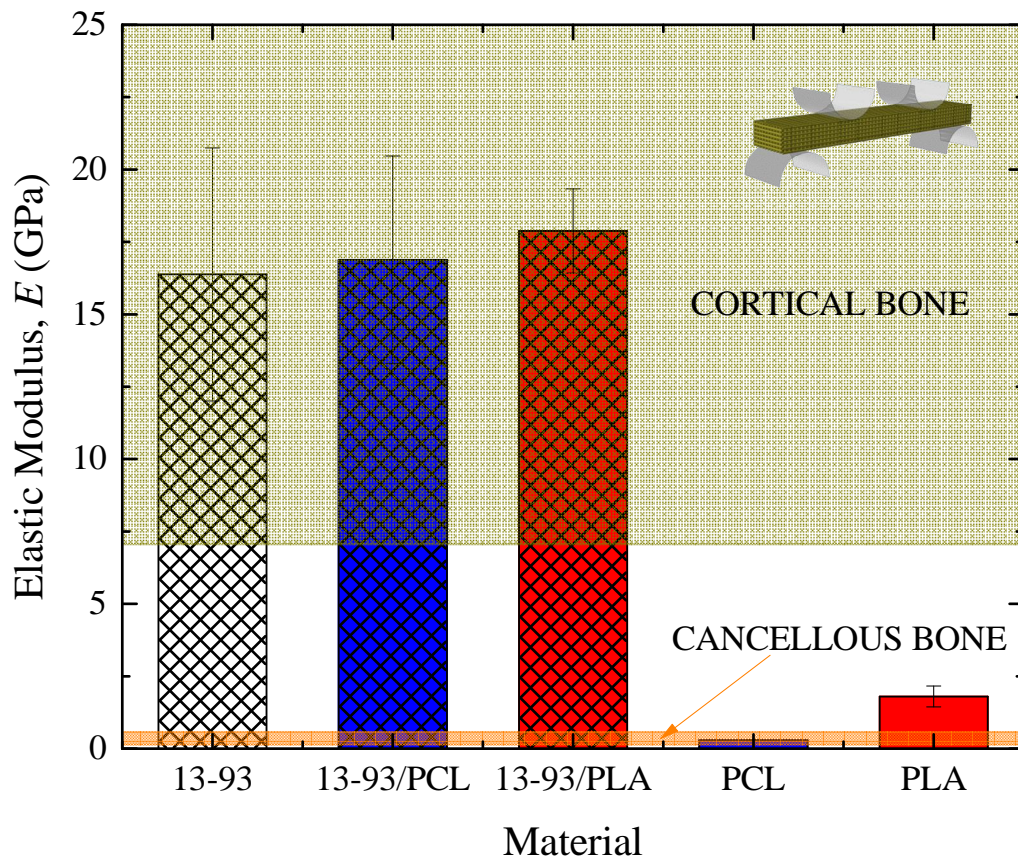
Figure 3.56. Elastic modulus, with standard deviations as error bars, for the indicated materials. Typical values for human bone are shown as shaded bands [294].

The results of Figure 3.56 prove that the elastic behavior of ceramic-polymer co-continuous composites obtained by impregnation of robocast scaffolds is controlled basically by the deformation of the ceramic—in this case 13-93 bioglass—skeleton. Indeed the bending modulus of the 13-93 robocast structures is not significantly changed with polymer addition because the modulus mismatch between the dense glass rods and the organic infiltrate is too large (even in the case of the stiffer PLA). However, this might not be completely true in robocast structures with a high degree of internal rod microporosity, since this microporosity can severely reduce the modulus of the ceramic bars to values closer to polymer range, and the effect of the infiltrate in sustaining the applied stress might become important, especially in scaffolds that also have a large percentage of pre-designed macroporosity.

Typical bending load–deflection curves for bare and infiltrated scaffolds are shown in Figure 3.57, together with the results for the bulk polymers for comparison. The loads in the curves have been normalized by the effective volume (i.e. that within the external contacts in the 4-point bending jig) of each sample. The bending curves of all 13-93-based materials show trends similar to those observed in compression (cf. Figure 3.52).
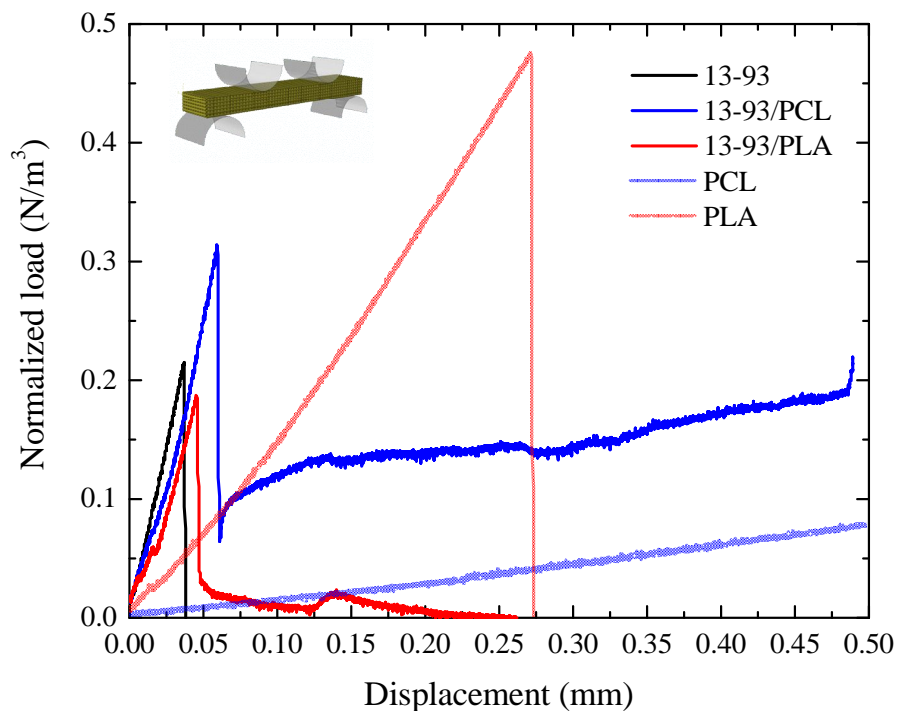
Figure 3.57. Typical bending load–deflection curves for the indicated materials. Loads have been normalized by the effective volume of each sample.

A typical brittle, linear elastic behavior could be seen for bare scaffolds, and also for pure PLA, although with significant differences in modulus and fracture energy. Pure PCL specimens exhibited a totally elastic response under the selected conditions and, therefore, were not broken during the tests. As in compression, the presence of the polymer in the composites prevents catastrophic failure after fracture of the ceramic skeleton occurs and the curves for infiltrated samples do not fall to zero after such cracking events indicating some residual mechanical integrity of the samples. As in

compression, 13-93/PLA samples were finally broken at larger deflections but 13-93/PCL samples exhibited an extended load-bearing capacity and remained in one piece after the tests.

This is clearly evidenced in the SEM *post-mortem* micrographs in Figure 3.58. The fracture is brittle for bare scaffolds (Figure 3.58 a) and 13-93/PLA composties (Figure 3.58 c) with no evidence of bridging filaments in the latter. Conversely, in 13-93/PCL samples (Figure 3.58 b), large stretched PCL macrofibrils bridged the crack walls together, being able to hold the sample together long after the glass skeleton failed, even after very large strains.
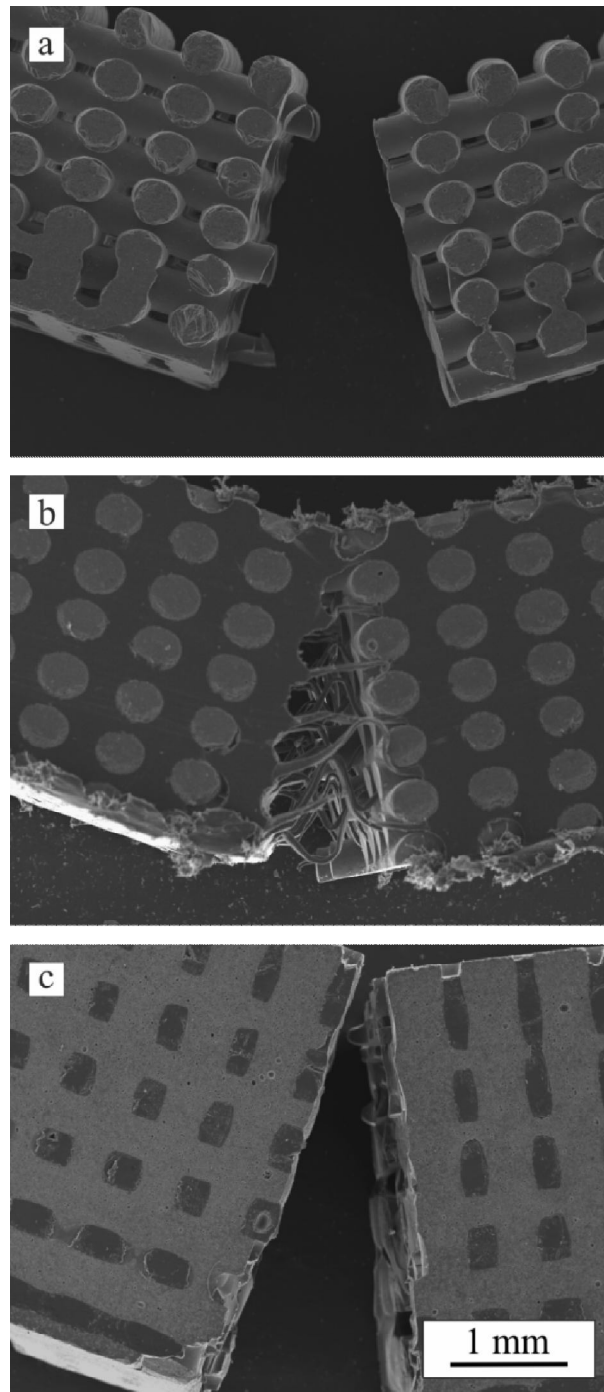
Figure 3.58. SEM micrographs of samples after bending tests: (a) bare scaffolds, (b) 13-93/PCL and (c) 13-93/PLA composties.

The distinct fracture behavior of both composites is clearly reflected in their fracture energy (strain energy density) as calculated from the curves in Figure 3.57. Figure 3.59, shows the magnitude of the total fracture energy (maximum values), G_f, with standard deviations as error bars. Since 13-93/PCL and pure PLC samples did not break during

the tests, the indicated value was calculated at 0.5 mm total deflection ($G_{0.5}$) and a graded color band was extended upwards to indicate that the actual fracture energy would be greater. This clearly evidences that, as in compression (Figure 3.55), the toughening obtained upon PCL infiltration is much higher than that obtained with PLA, due to intrinsic greater ductility of PCL, which is able to provide some linkage between the crack walls (Figure 3.58 b). The 13-93/PLA composite's fracture energy in bending, while doubling the value of the bare structure, is still an order of magnitude inferior to that of pure PLA. Besides, unlike in compression (Figure 3.55), the fracture energy of the materials that break during the bending tests (even pure PLA) falls far short of bone values, and only the materials including PCL might have comparable behavior due to their ability to survive larger strains.
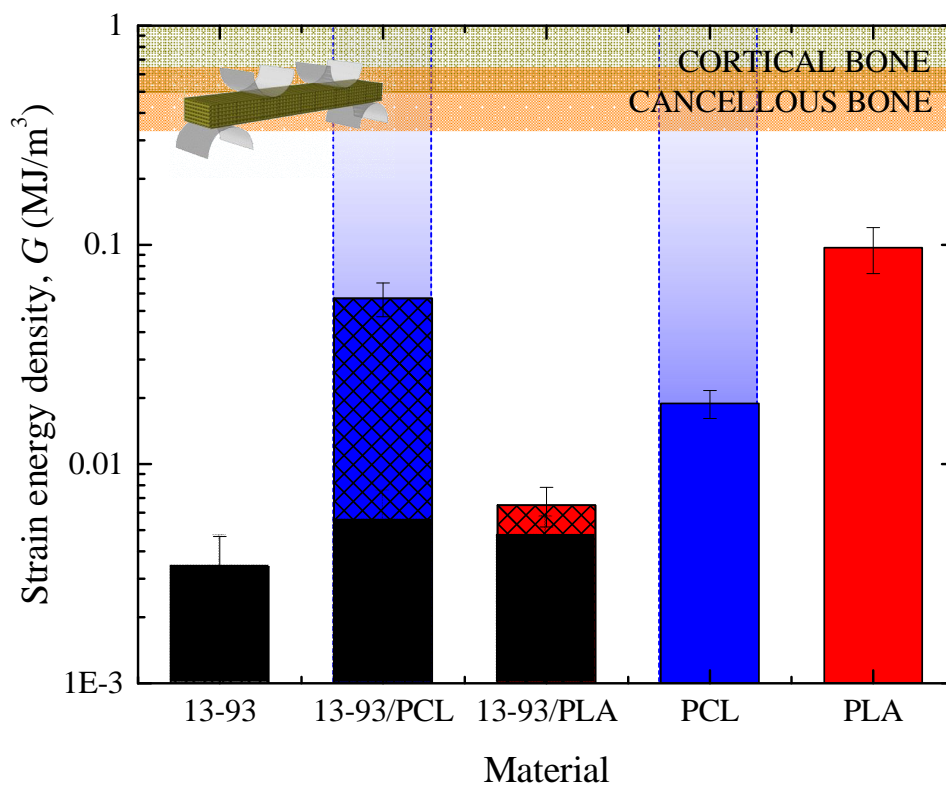
Figure 3.59. total fracture energy, with standard deviations as error bars, for the indicated materials in bending. Since 13-93/PCL and pure PLC samples did not break during the tests, strain energy density at 0.5 mm deflection ($G_{0.5}$) is indicated, with a graded color band extending upwards to indicate that the actual fracture energy would be greater.

Concerning the strengthening associated to polymer infiltration, Figure 3.60 shows the Weibull plots corresponding to strength data gathered in the bending tests. Since PCL response was completely elastic no strength values were measured for this material. As in compression, polymer infiltration enhanced strength and reliability of the bare 13-93 structures.
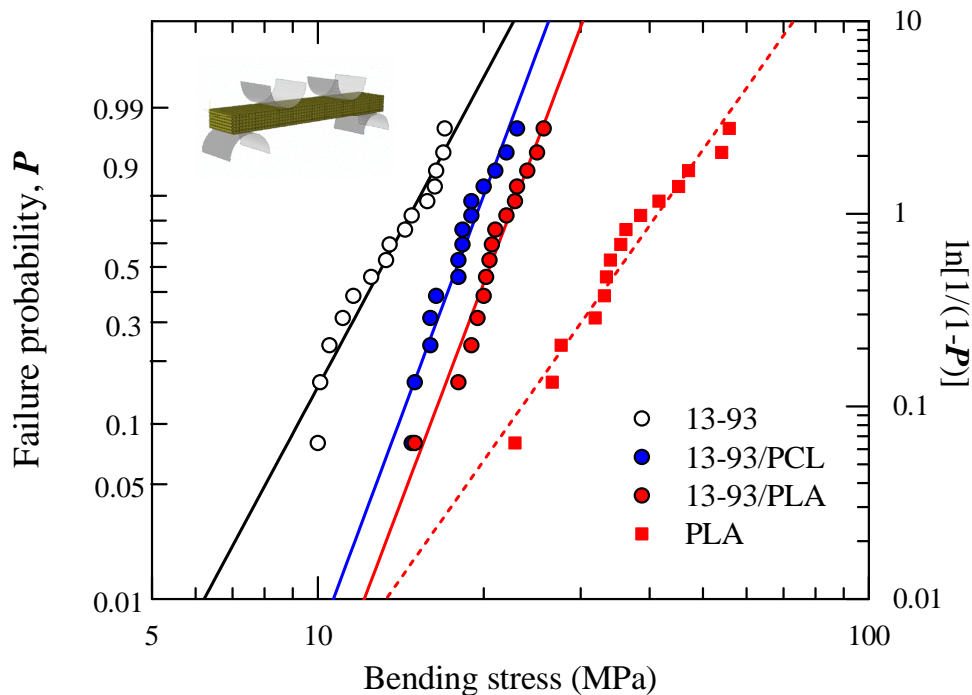
Figure 3.60. Weibull plots of the bending strength data for the indicated materials. PCL exhibited elastic response and no strength values could be measured.

This can be more clearly appreciated in Figure 3.61, were the central value and the Weibull modulus obtained from the data in Figure 3.60 are summarized, with standard errors. As in compression, the strengthening effect of polymer impregnation on the full-dense 13-93 glassy rods is significantly lower than those reported in structures with higher degree of micropososrosity [21]. Under this most deleterious loading mode, the strengthening (Figure 3.61 a) associated to polymer infiltration is more noticeable (~ 33 % and 47 % increase, respectively for PCL and PLA infiltrates) than in compression. In spite of that, the bending strengths of 13-93-based materials remained far from reaching cortical bone strength range. And unlike in compression, the bending

strengths of the composite were significantly inferior to those of the bare PLA (by around a factor of 2). Nonetheless, the reliability (i.e. Weibull modulus, Figure 3.61 b) of the co-continuous composites was significantly improved over both the bare structure and pure PLA (by ~ 45 % and ~ 87 %, respectively, nearly reaching the reported value for human cortical bone under tensile fatigue (m = 8) [23][292].
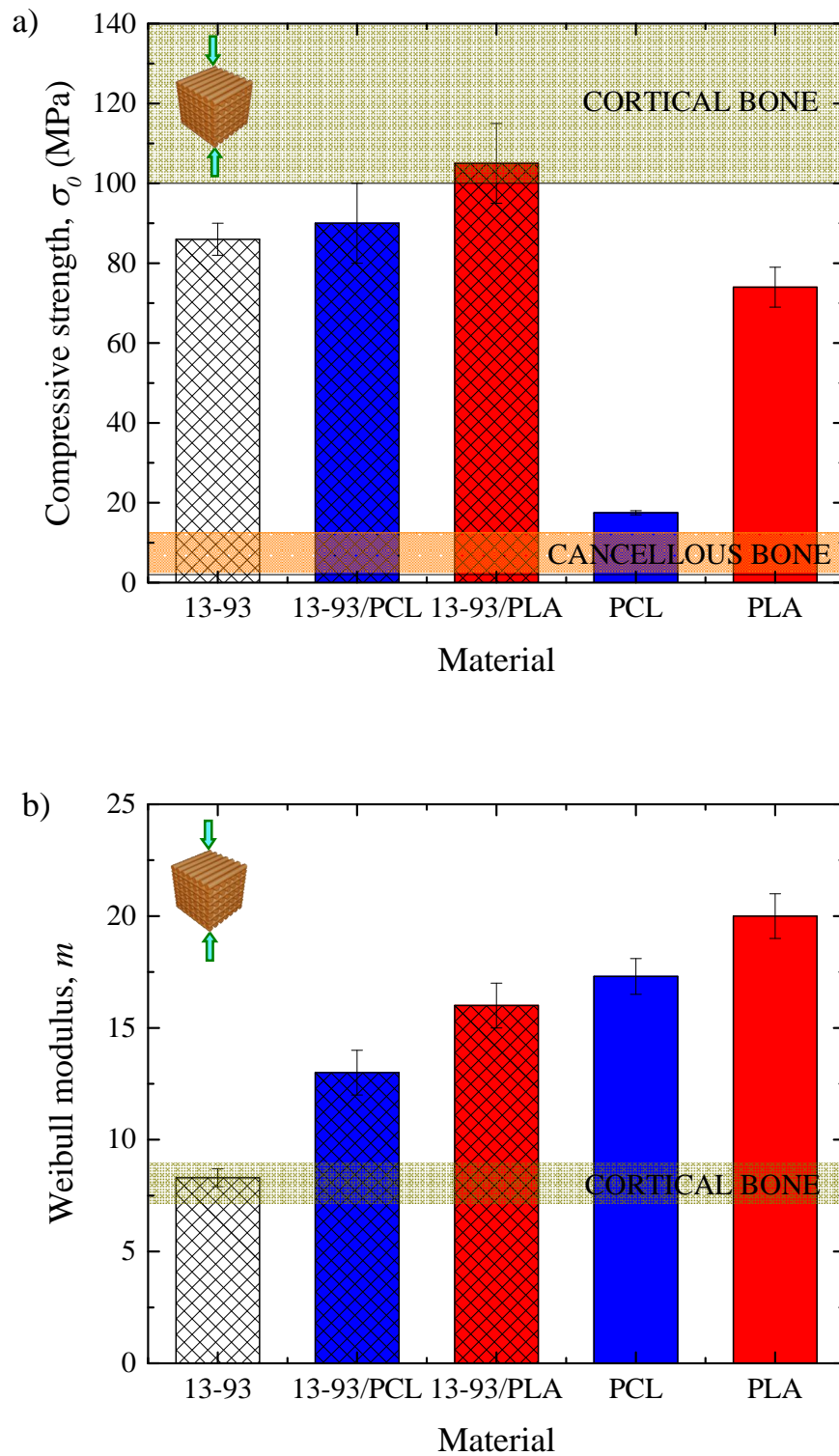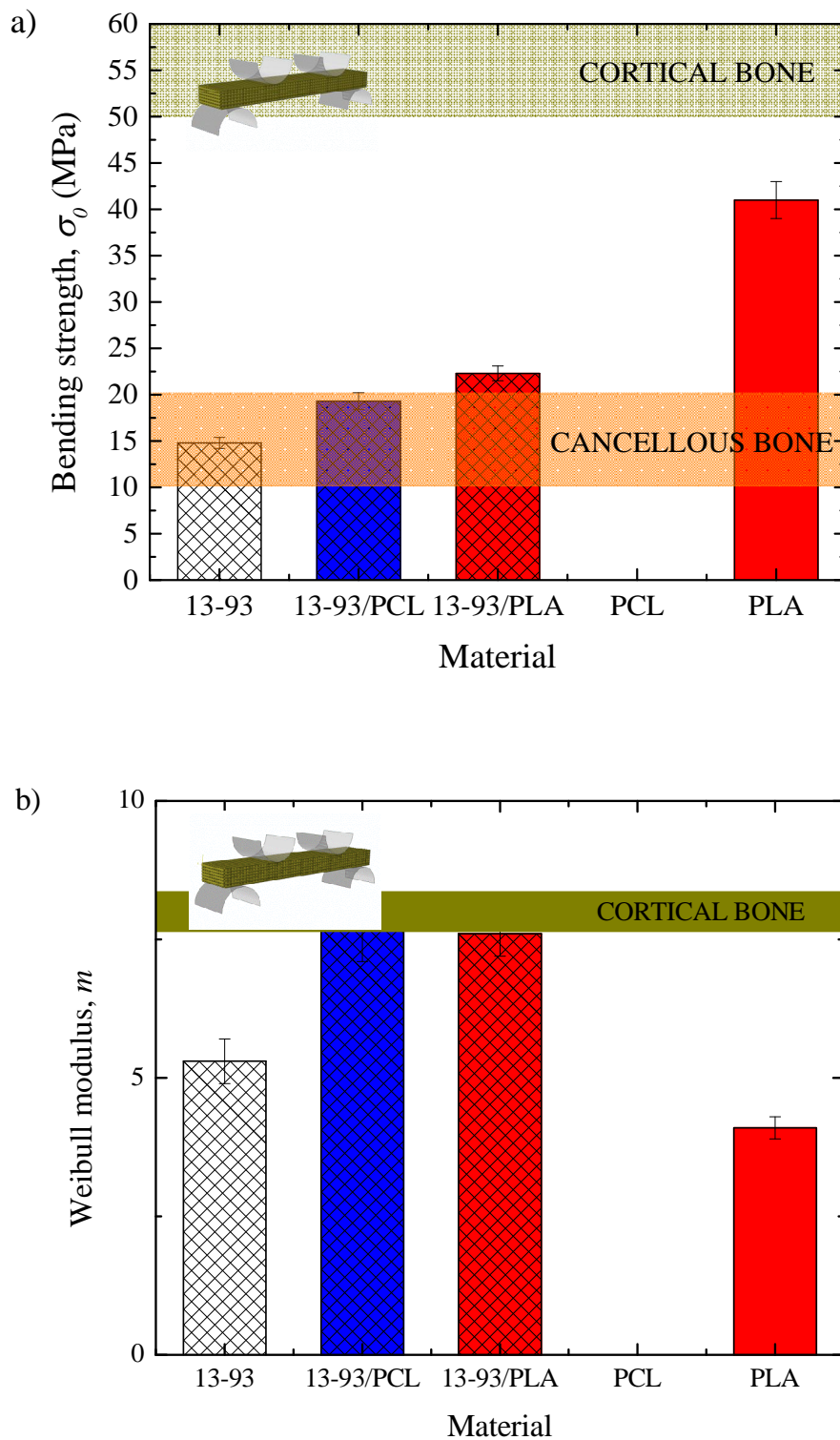
Figure 3.61. Weibull best fitting parameters to data in Figure 3.60, with standard errors: (a) central values, σ_0, and (b) Weibull modulus, m. PCL exhibited elastic response and no strength values could be measured. Typical values for human bone are shown as shaded bands [290][291].

All the results from mechanical characterization analyzed in the preceding paragraphs, both regarding compression and bending tests, are summarized in Table 3-3 to facilitate access to the readership.

Table 3-3. Summary of mechanical characterization results.

Material	Compression / Bending	E (GPa)	σ_0(MPa)	m	$G_{0.3}$ (MJm^{-3})
13-93	Compression	-	86 ± 4	8.3 ± 0.4	1.08 ± 0.02
	Bending	16 ± 4	15 ± 1	5.3 ± 0.4	0.003 ± 0.001
13-93/PCL	Compression	-	90 ± 10	13 ± 1	14 ± 3
	Bending	17 ± 4	20 ± 2	7.7 ± 0.6	0.06 ± 0.01
13-93/PLA	Compression	-	105 ± 10	16 ± 1	2.7 ± 0.8
	Bending	18 ± 1	22 ± 2	7.6 ± 0.4	0.007 ± 0.001
PCL	Compression	-	17.4 ± 0.5	17.3 ± 0.8	4.9 ± 0.4
	Bending	0.29 ± 0.02	-	-	0.019 ± 0.003
PLA	Compression	-	74 ± 5	20 ± 1	10.7 ± 0.4
	Bending	1.8 ± 0.4	41 ± 2	4.1 ± 0.2	0.10 ± 0.2

3.3   Implications

To conclude this chapter, in this section the preceding results and their implications are analyzed with a dual perspective. First, as pertaining to specific systems (13-93 and 45S5 scaffolds and derived composites) for bone replacement and regeneration applications and, second, with a broader perspective, regarding microstructure-mechanical properties relationship of porous ceramic structures and co-continuous ceramic/polymer composites in general, this may be of interest to other engineering applications.

3.3.1 Implications for bone replacement applications

As already mentioned, the challenge in the development of materials for bone replacement and regeneration lies in obtaining osteoconductive materials with mechanical performance close to that of natural bone tissue. This study has explored several paths leading towards this long sought after goal.

First, this work demonstrates how producing more regular struts and reducing the scaffold's struts microdefects lead to significant improvements in the strength of bioglass-derived—and, by extension, any bioceramic—scaffolds. Indeed, as shown in Figure 3.62, structures with uniform strut dimensions such as those created by robocasting exhibit significantly superior (note logarithmic scale) strength compared to scaffolds fabricated by conventional means with the same porosity (dashed lines are extrapolation of experimental results from the literature [62-63] according to Gibson and Ashby model [289].

The enhancement produced by improving densification and, thus, reducing flaw population in the scaffold's struts is also apparent in the 45S5 bioglass data in Figure 3.62. As the microdefect decreases in number and size, the density increases, and the strength of the 45S5 bioglass-derived scaffolds gets progressively closer to bone values, as predicted by Keller's model [294]. And the nearly defect-free ethanol-milled 13-93 bioglass structures lie well above bone values even when fabricated by conventional means. Please, remember that the data for water-milled 13-93 scaffolds are not directly comparable to the rest of robocast scaffolds since its level of macroporosity is lower (Figure 3.40), and that can have a dramatic effect in strength (see Section 3.2.4). Which points out to an additional route to further enhance the strength of robocast scaffolds: by reducing the level of pre-designed macroporosity (e.g. by reducing rod separation within each layer) it should be possible to notably strengthen the scaffold, although at the cost of reducing its capacity to promote tissue ingrowth.
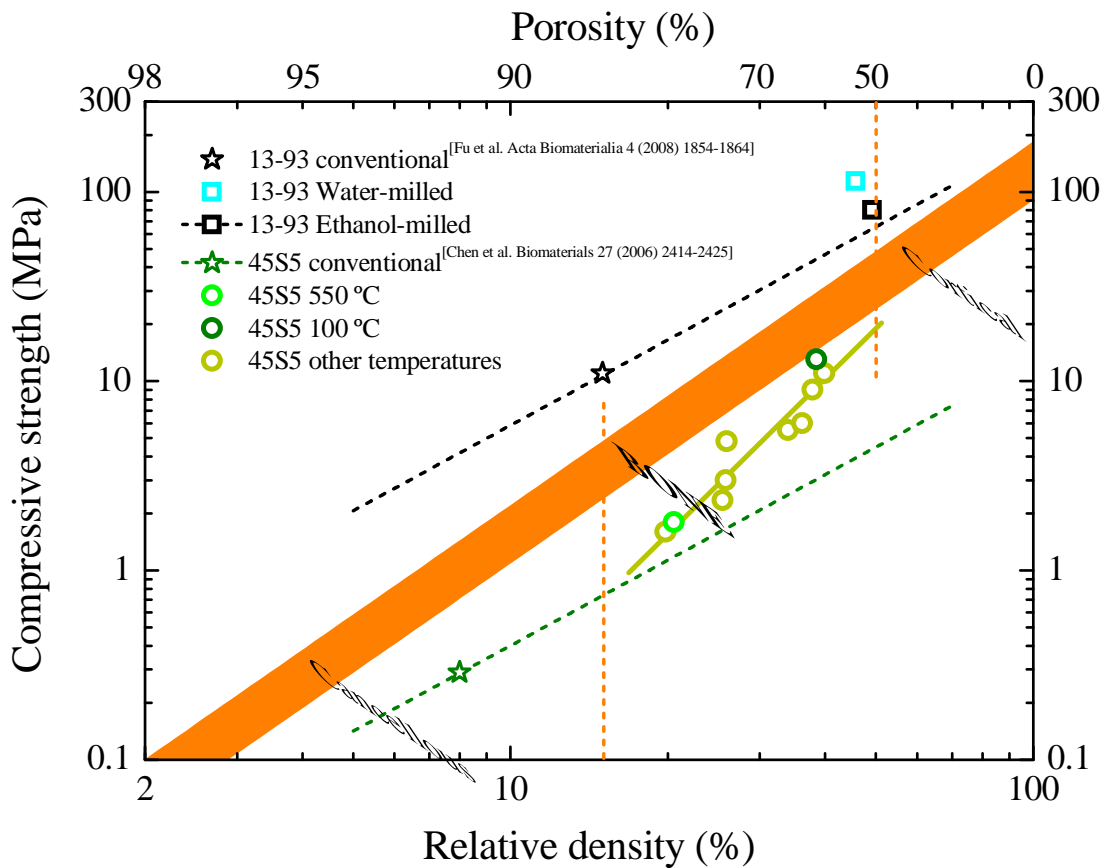
Figure 3.62. Summary of compressive strength results as a function of relative density for all bare bioglass-derived scaffolds. Data for conventional 45S5 [62] and 13-93 [63] scaffolds and bone properties [294] are included for comparison

Consequently, by optimizing the pore architecture and densification of scaffolds struts it seem feasible to produce bioceramic scaffolds with bone-like strengths. But obviously, strength is not the only critical mechanical parameter: modulus and, especially, toughness should also be taken into account. As can be appreciated in the Ashby diagrams of Figure 3.63, even the best bare bioglass-derived scaffolds are quite far from completely mimicking natural bone mechanical performance.
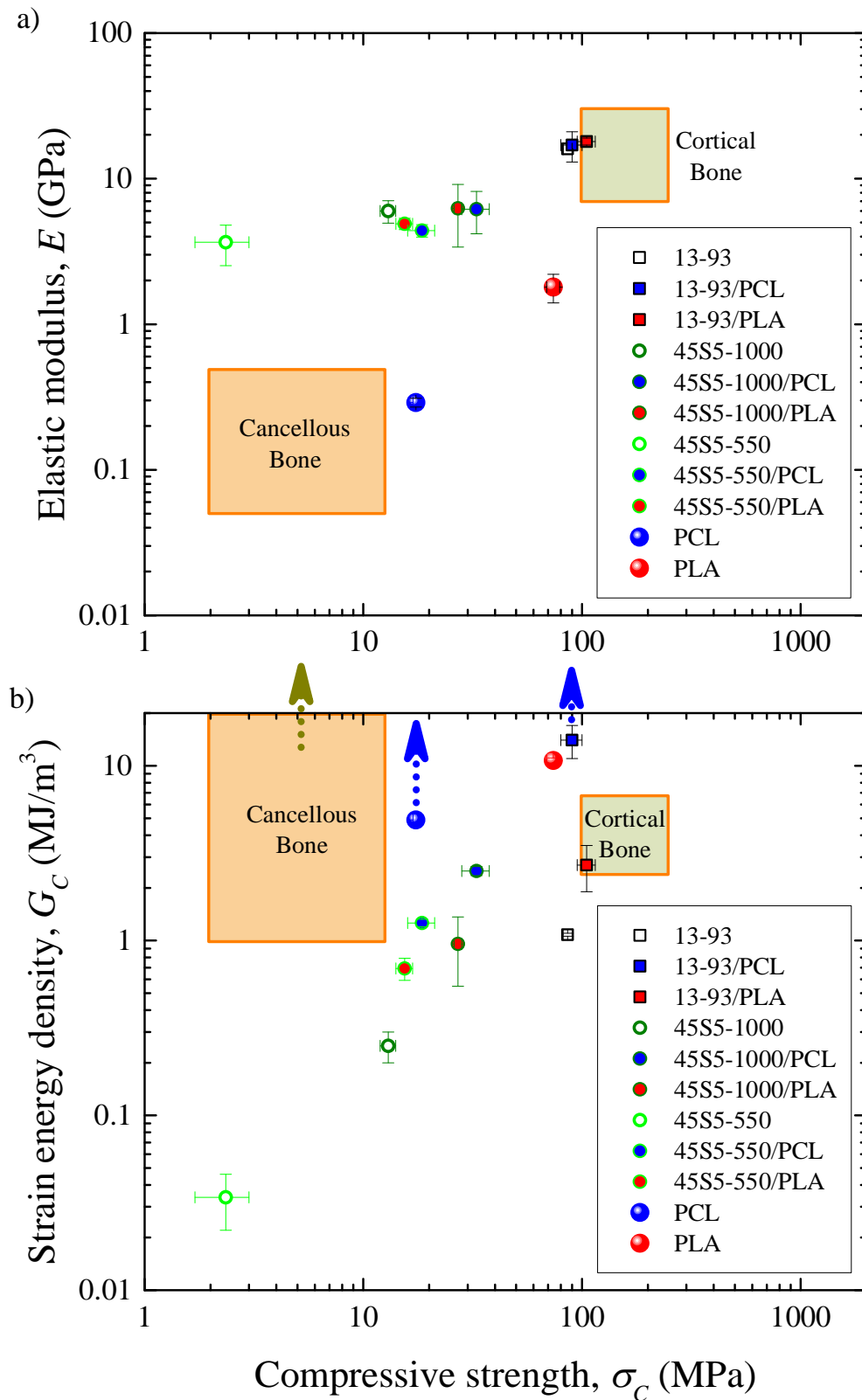
Figure 3.63. Plot of (a) elastic modulus, E, and (b) strain energy density, GC, versus comppressive strength, σC, for the materials evaluated in this study. Results are compared to bone properties [294].

Regarding modulus, the analyzed bare bioglass-derived scaffolds, with over 50% porosity in all cases, exhibited elastic moduli closer to cortical than to cancellous bone, with the fully-dense 13-93 scaffold well within the cortical bone range (Figure 3.63a)—so this latter material exhibits a combination of strength and modulus quite similar to cortical bone. This implies, however, that the pure bioceramic scaffolds will have a hard time mimicking the mechanical performance of cancellous bone. Indeed, while an increase in porosity will provide a reduced modulus, porosity affects more dramatically the strength (compare values corresponding to 45S5 bioglass-derived scaffolds sintered at 550 and 1000 °C). This might not be however a big hurdle in practice since their stiffness is not higher than those of cortical bone, and these materials, unlike bioinert metals, will degrade with time upon implantation.

Indeed, the greatest problem of these pure bioceramic structures lies in their brittleness. As can be seen in Figure 3.63b, even for the strongest 13-93 bioglass scaffolds, the strain energy density in compression barely reaches the lower limit of cancellous bone values, and less than half of the lowermost values for cortical bone. The lack of any type of ductility in these materials makes it difficult to overcome this limitation by simply modifying the scaffold's architecture. Fortunately, it is possible to substantially improve the toughness of these structures by impregnating them with biodegradable polymers. In particular, PLA infiltration of 13-93 bioglass scaffolds yields a material that closely matches the performance of cortical bone in compression in terms of the three mechanical properties analyzed: stiffness, strength and toughness. And when the more ductile PCL is used instead, the toughness of the structure is substantially improved over cortical bone values without significantly reducing the performance in terms of modulus or strength. Therefore, 13-93/PLA and, especially, 13-93/PCL bioglass composites seem optimal candidates for replacing cortical bone load-bearing function in compression.

Unfortunately, this exceptional match of mechanical properties is not reproduced when a more deleterious damage mode like bending is considered. As shown in Figure 3.64, under flexural stresses neither the strength nor the toughness of cortical bone could be matched by any of the analyzed materials, including the ceramic/polymer co-continuous composites. Although, again, the best overall performances were obtained by the combination of dense ceramic structure with a ductile polymer (i.e. for

13-93/PCL composites). This highlights the fact that mechanical testing should not be limited to compressive configurations when evaluating a material for bone replacement.
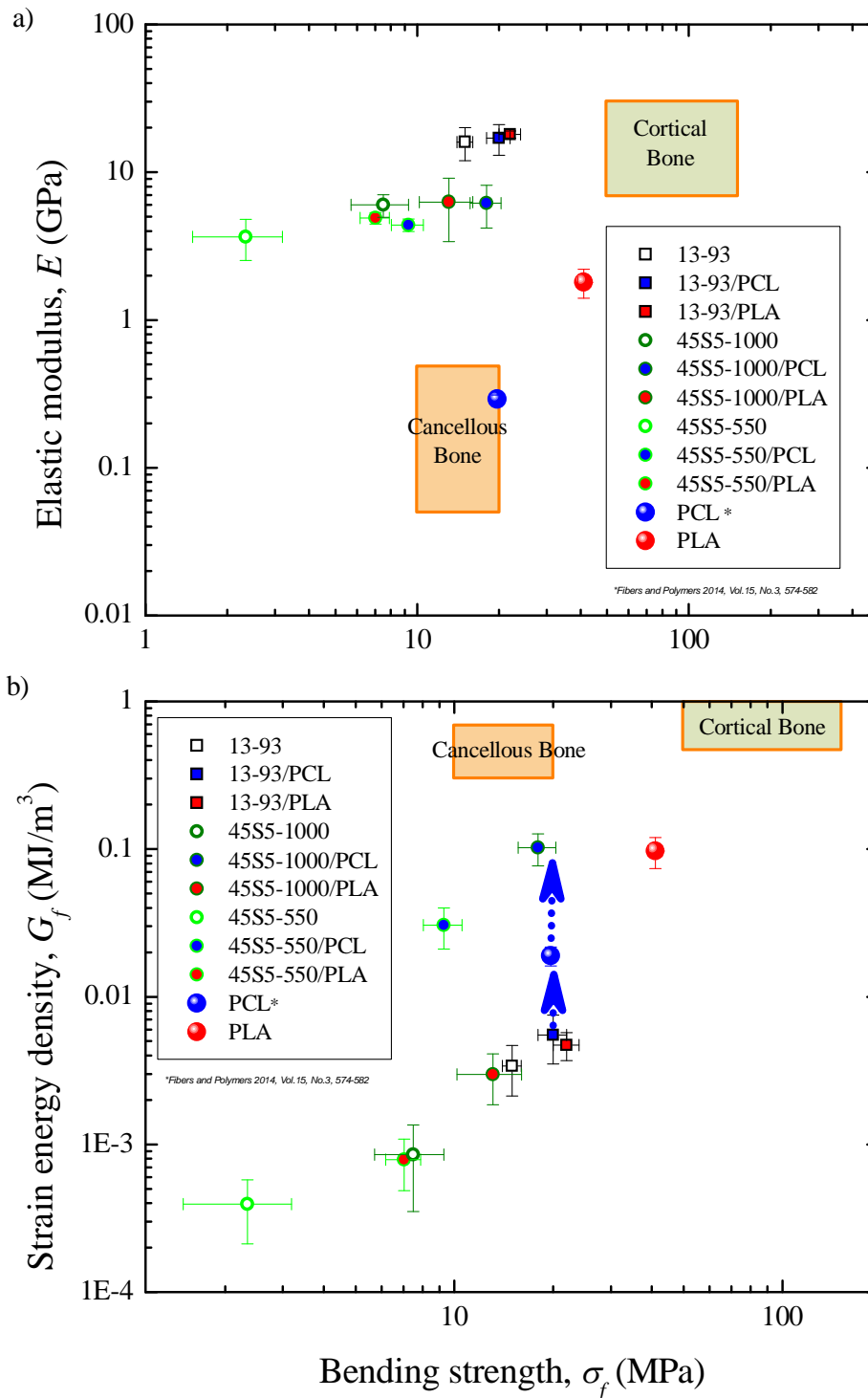
Figure 3.64. Plot of (a) elastic modulus, E, and (b) strain energy density, G_f, versus bending strength, σ_f, for the materials evaluated in this study. Results are compared to bone properties [294]. PCL bending strength was taken from literature [295].

This setback shouldn't diminish the major achievement of materials (13-93-based composites) whose combination of properties (stiffness, strength and toughness) under compression match and even surpass that of cortical bone. This has been achieved by mimicking the hybrid organic-inorganic composition of bone, if with a very different microarchitecture. What is really surprising is that such fine performance has been achieved by using a randomly chosen geometry for the initial robocast structures and off-the-shelf materials. This suggests that superior mechanical performances should be attainable in these hybrid structures through the optimization of the pore architecture of the initial robocast scaffold and a careful optimization of the individual materials. Hopefully, such enhancements will help bridging the gap still existing between the performances under bending stresses of the developed ceramic/polymer co-continuous composites and natural bone.

At this point, it is worth acknowledging, however, that these dense co-continuous materials have a limitation regarding their applicability as bone-regenerating materials: their lack of porosity impedes bone ingrowth, limiting tissue formation to the surface of the materials, at least initially. However, if the bioerosion rate of the polymer infiltrate was greater than that of the bioceramic skeleton (or viceversa), one would expect the generation of porosity in situ upon implantation, allowing bone in-growth at a later stage. This is an extreme that would be worth validating *in vivo* in the future. Such progressive *in situ* creation of porosity might allow materials to be developed that will remain strong enough to support loads until the regenerated bone can take over. Moreover, stress shielding of the surrounding tissue would not be an issue in this in situ pore generation scheme since, as the material is resorbed, more and more of the load will be transferred onto the surrounding bone, providing the proper loading environment required for bone regeneration. Obviously, determining the appropriate composition, microstructure, pore architecture and surface properties to ensure the maintenance of strength and stability throughout the whole regeneration process remains a scientific challenge.

It is worth highlighting too that all values reported in this work are dependent on the strain rate used in the tests, be them compressive or bending, as a consequence of the viscoelastic properties of the infiltrating polymers and the slow crack-growth phenomenon of the ceramics. This issue has been set aside here by setting a fixed crosshead speed for each type of test, so that a comparative study between the different

structures developed was possible. Nonetheless, natural bone mechanical properties are also strongly dependent on strain rate and a comparison of these effects would be a very interesting issue for future analysis.

3.3.2 Implications for other engineering applications

The main drawback of ceramic—the term ceramic is used here with its broadest meaning, to encompass crystalline materials, glasses and glass-ceramics— porous structures lies in their intrinsic brittleness and poor mechanical resistance associated to their porosity, which limits their use in structural applications. As previously discussed, the mechanical strength of porous structures can be enhanced by optimizing the macropore architecture and by improving the intrinsic properties of the ceramic rods. In fact, structures with more regular, thicker and defect-free struts are desirable when mechanical resistance is a major concern for the intended application. Besides, the addition of a polymer phase to the ceramic porous structure enhances not only its strength but also its toughness.

Regarding strength of hybrid structures, since it is virtually just the ceramic skeleton that sustains the elastic loads, and the structures remain largely elastic until failure occurs (Figure 3.52 and Figure *3.57*), it immediately follows that the onset of failure is also controlled by the ceramic frame. Thus, even when polymer infiltration is used to increase the strength of the ceramic structure, maximization of the intrinsic resistance of the struts should still be a main concern, since the final strength of the composite will depend on the initial strength, as shown in Figure 3.28. This is true despite the fact that the strengthening by defect healing mechanism upon polymer impregnation is higher for ceramic structures composed of strut with larger flaw populations—accordingly, the strengthening of 45S5 scaffolds sintered at 550 ºC is bigger than that of the same scaffolds sintered at 1000 ºC and even more than that of 13-93 scaffolds (see Figs. 3.30, 3.35, 3.56 and 3.63).

Nonetheless, even if the strengthening effect of polymer impregnation on structures with nearly full dense rods (as 13-93 scaffolds) is limited, polymer infiltration is still a suitable strategy to improve the mechanical performance of ceramic porous structures. Indeed, as shown in Figure 3.54 and 3.64, the reliability of the structure is greatly improved both in compression and bending. Moreover, the polymeric infiltrate might

enhance also the mechanical performance by protecting the ceramic surfaces from potentially damaging aerosols, and some of them even from exposure to environmental moisture, responsible for slow crack growth.

The strength improvement is also higher when the infiltrating polymer has a high modulus (see Figs. 3.30, 3.35, 3.56 and 3.63) because in this case a greater portion of the applied load is transferred to the polymer phase, i. e. the contribution of the stress shielding mechanism is more important. In this study, this is not true for the stiff PLA infiltrate on 45S5 bioglass-derived scaffolds, but only due to the degradation of the PLA properties in the presence of 45S5 at the selected impregnation temperature (section 3.1.5).

Additionally, the impregnation with polymer enhances dramatically the toughness and damage tolerance of the ceramic structure. Indeed, once the ceramic skeleton fails, the polymer infiltrate holds the composite together and prevent an immediate catastrophic failure of the whole part. In this regard, highly ductile polymers such as PCL are preferred as toughening agents over stronger but more brittle choices (like PLA) since they can provide significantly higher levels of load bearing capacity after the ceramic/glass fails, both in compression and bending, even after very large deformations (Figure 3.52 and Figure 3.57). Due to the extraordinary toughening provided by the polymer infiltrate, the hybrid material can support milling and drilling loads in order to modify their external shape, as shown in Figure 3.65. This could solve the difficulties of ceramic based additive manufacturing to produce actual net-shape parts, and opens the path for the fabrication of high-precision customized elements.
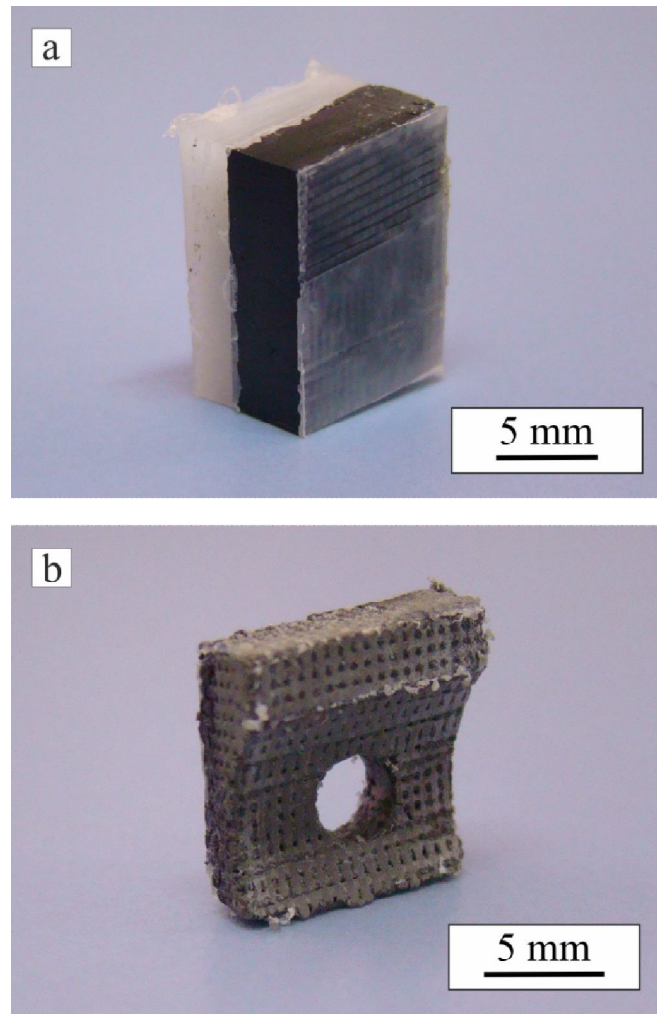
Figure 3.65. Optical images of 13-93/PCL composites: (a) as-cut block of the composite showing still the excess polymer from the infiltration procedure, and (b) part milled manually out of the block.

Besides the role of polymer impregnation in enhancing the mechanical performance of ceramic structures, it is also interesting to consider the reverse effect of the ceramic frame as a reinforcement of the polymeric phase. As evidenced in Figure 3.63 and Figure 3.64 the introduction of the ceramic frame notably increases the moduli of both analyzed polymers, in the case of the nearly porous-free 13-93 bioglass by one (in the case of PLA) or two (PCL) orders of magnitude. However, its aptitude as strengthening/toughening agent depends greatly on the selected polymer. For an already strong polymer, such as PLA, strengthening was achieved only in compression and upon the incorporation of a nearly porous-free frame (40% increase after the inclusion

of the 13-93 bioglass skeleton, Figure 3.63), while in bending the incorporation of the ceramic skeleton strongly reduces the strength of the bare polymer (Figure 3.64). And even in compression, the reported strength enhancement was only achieved at the expense of both reliability (Figure 3.54) and toughness (Figure 3.55). In contrast, the 13-93 bioglass skeleton proved an excellent reinforcement for a ductile polymer like PCL, greatly increasing both strength and strain energy densities in compression (Figure 3.63), without significantly degrading its strength and toughness in bending (Figure 3.64)—unlike 45S5 glass-derived frames which improved modulus and in some cases compressive strength but at the expense of toughness and bending strength. Thus, the 13-93/PCL composites exhibit significantly enhanced mechanical performance over both the bare PCL polymer and 13-93 bioglass scaffolds. Furthermore, unlike in aligned fiber-reinforced composites, the reinforcement achieved by the ceramic robocast skeleton is multidirectional, although obviously not isotropous, and the geometry of this supporting frame could be designed to provide maximal reinforcement against known loading conditions.

Again, it is worth mentioning that the reinforcement reported in this work was achieved using a simple geometry and infiltration method and therefore, the mechanical performance of the proposed co-continuous composites could be further enhanced by improving the geometrical design and, especially, the interfacial adhesion between the organic and inorganic phases. Impregnation methods such as in-situ polymerization [221][265] could be used to enhance interfacial adhesion through polymer grafting, and such interfacial strength improvements have already been shown to produce substantial improvements on the mechanical performance of co-continuous composites [296].

All in all, according to the preceding paragraphs, ceramic/polymer co-continuous composites have a great potential to find suitable niches of application as structural materials not only in the biomedical field but also in other engineering areas.

Chapter 4

Conclusions

Conclusions

The fabrication of 45S5 and 13-93 bioglass scaffolds by robocasting has been successfully achieved. This study included a comprehensive analysis of the rheological behavior of the ink used in robocasting, as well as the sintering and mechanical behavior of the robocast scaffolds. The bioactivity and the effect of immersion in simulated body fluid (SBF) on the mechanical behavior of the scaffolds was also investigated *in vitro* finally, the mechanical reinforcement of the developed scaffolds was attempted by infiltration of PCL and PLA biodegradable polymers into their open porosity by immersion in the polymer melt. A comparative analysis of the mechanical performance, both under uniaxial compression and, in some cases, bending stresses, of all the fabricated materials and natural bone was performed. Among the most relevant conclusions of this study, it is worth highlighting the following:

Regarding 45S5 bioglass ink preparation and robocasting

1- Robocasting technique provides a means to produce 45S5 bioglass-derived scaffolds with customized external geometry and internal pore architecture with compressive strengths that are far superior to any previously reported values. This is achieved through the use of carboxymethyl cellulose (CMC) as a single, multifunctional additive that allows one to prepare the concentrated suspensions required by robocasting, overcoming the inherent difficulties associated to the colloidal processing of 45S5 bioglass. The enhancement in mechanical performance associated to the novel pore architectures, with thicker struts and wider interconnections, produced by robocasting is enormous: more than one order of magnitude compared to existing scaffold strength data and well within, or even surpassing, cancellous bone strength range.

2- Robocasting allows one to produce, by sintering at sufficiently low temperature (550 ºC), fully amorphous robocast 45S5 bioglass scaffolds, which preserve intact all the outstanding bioactivity of 45S5 bioglass, with enough mechanical integrity for practical use. Therefore it could be said that robocasting, and perhaps also other solid freeform fabrication techniques, can overcome the main obstacle for the

successful application of 45S5 bioglass as a broad-use bone substitute material. The simplicity and versatility of the proposed robocasting process will greatly facilitate the development of patient-specific 45S5 bioglass scaffolds and significantly extend the current range of biomedical applications of this excellent bioactive material.

Regarding 13-93 bioglass ink preparation and robocasting

3- Three-dimensional scaffolds of silicate 13-93 glass with potential applications in bone regeneration can be fabricated also by robocasting using carboxymethyl cellulose (CMC) as a single, multifunctional additive to prepare the required concentrated suspension. 13-93 bioglass powder milled both in water and in ethanol can be used for this purpose with the latter media resulting in finer, narrower particle size distribution and better rheological control of the suspension.

4- The debinding process used in this work probed to be imperfect and resulted in bubble formation at temperatures close to the optimal sintering temperature (~700 °C), especially in water-milled structures, but further optimization of the process should enable the fabrication of bubble-free parts from either type of starting powders. On the other hand, ethanol-milled structures exhibited a striking black color after sintering resulting from the introduction of carbonaceous species in the glass during milling, which could not be removed even at temperatures well above that of crystallization. Fortunately, neither the impurities from the imperfect debinding nor the presence of the carbonaceous species in ethanol-milled samples hindered in any way the bioactivity and cell affinity of the material, according to *in vitro* tests, nor seemed to affect significantly the mechanical behavior of 13-93 bioglass robocast scaffolds, which remained comparable to previously reported data, with strength values (at porosities above 50%) close to those of cortical bone, depending on geometrical parameters.

Regarding in vitro study of 45S5 and 13-93 bioglass scaffolds in SBF

5- During immersion of 45S5 bioglass-derived scaffolds in SBF, the amorphous glass tends to leach more alkali to the solution, causing a larger weight loss and a higher increase of pH, due to the bigger amount of microporosity as well as bigger surface area, as compared to crystalline scaffolds. The existence of these two factors seems to provide not only faster degradation kinetics but also a means for enhanced overall conversion factor of the bioactive glass to HA. In both cases, the conversion of the material to a weak porous HA-like product resulted in a degradation of compressive strength, which in the case of crystalline scaffolds is accelerated by the formation of cracks in the HA layer.

6- The presence of microporosity within the rods of robocast scaffolds plays a major role in controlling the *in vitro* degradation and conversion to HA of 13-93 bioglass, which is nonetheless substantially slower than that of 45S5 composition. The initially undesired presence of bubbles in water-milled samples has shown how the presence of such pores within the structure rods not only enhances the degradation rate but also the overall maximum conversion factor— from below 6%, for dense structures to around 35% for our microporous water-milled structures. Obviously, this enhanced degradation rate translates into greater and faster reduction of mechanical strength, which was already intrinsically reduced by the presence of the microdefects. These results suggest that a simple means for controlling the degradation behavior of bioactive robocast materials is by tailoring their microporosity.

Regarding polymer melt impregnation

7- Melt impregnation method is a simple, cost-effective process for producing polymer/bioglass composites in a reliable way from commercial polymers. However, care should be taken when selecting the processing condition for the preparation of the composites in order to avoid deleterious interactions between the inorganic and organic materials, as the ones detected in this work between 45S5 bioglass and both PCL and, specially, PLA.

8- The results of this study confirm the positive effect of polymer impregnation on the mechanical properties of robocast ceramic or glass regardless of the type of loading

configuration (compression or bending). In fact, impregnation with a ductile polymer not only can alleviate the intrinsic brittleness of ceramics porous structures, but do so while enhancing the strength and reliability of the material.

9- This work's results prove also, for the first time, that existing micro-defects (microporosity) has a major role on the mechanical enhancement produce by polymer impregnation of robocast scaffolds. The strengthening produced by defect healing is greatly reduced as the pre-existing flaw population decreases. The same occurs with the toughening since fibrils generated from the polymer within the ceramic microporosity can significantly contribute to crack bridging.

10- Despite the diminishing effectiveness of the polymer infiltrate as a reinforcing agent as the microporosity is reduced, denser ceramic struts yield stronger and tougher hybrid structures after polymer infiltration. Consequently, optimization of the sintering conditions for the ceramic skeleton should still be a major concern for the maximization of the mechanical performance of ceramic/polymer co-continuous composites.

11- Highly ductile polymers such as PCL are preferred as toughening agents over stronger but more brittle choices (like PLA) since they can provide significantly higher levels of load bearing capacity after the ceramic/glass fails, both in compression and bending, even after very large deformations. Due to the extraordinary toughening provided by the polymer infiltrate, the 13-93/PCL hybrid materials produced in this work can support milling and drilling loads.

12- The mechanical properties of 13-93/PCL composites were significantly improved also over the bare polymer, which indicates that dense ceramic frames fabricated by robocasting could be successfully used as multidirectional mechanical reinforcements for ductile polymers, although not so much as reinforcement for strong and brittle polymers.

Regarding the comparison with natural bone properties

13- This work demonstrates that bare bioglass-derived scaffolds with uniform strut dimensions created by robocasting, when sintered to a good level of densification, can match or even surpass the compressive strength of natural bone with the same porosity. Elastic moduli similar to cortical bone are also easily attainable in

bioceramic structures, but their strain energy densities fall far short of the values for natural tissue.

14- On the contrary, co-continuous ceramic/polymer composites can match (as in the case of 13-93/PLA structures) or even surpass in some aspects (13-93/PCL) the performance of cortical bone in compression, in terms of the three mechanical properties analyzed here: stiffness, strength and toughness. Therefore, 13-93/PLA and, especially, 13-93/PCL bioglass composites seem optimal candidates for replacing cortical bone load-bearing function in compression.

15- Unfortunately, this exceptional match of mechanical properties is not reproduced in bending. Under flexural stresses neither the strength nor the toughness of cortical bone could be matched by any of the analyzed materials, including the ceramic/polymer co-continuous composites. This highlights the fact that mechanical testing should not be limited to compressive configurations when evaluating a material for bone replacement.

The results of this study provide valuable insight into the robocasting of bioglass-derived scaffolds and their mechanical and biological performance behavior, and into the mechanical behaviour of ceramic/polymer co-continuous composites with potential niches of application as structural materials not only in the biomedical field but also in other engineering areas.

En este trabajo se han fabricado andamiajes de los biovidrios 45S5 y 13-93 mediante moldeo robotizado. El estudio realizado ha incluido el análisis del comportamiento reológico de las tintas utilizadas en la técnica de moldeo robotizado, así como del proceso de sinterización y las propiedades mecánicas de los andamiajes. También, se ha investigado *in vitro* la bioactividad y el efecto de la inmersión en fluido corporal simulado (SBF) en el comportamiento mecánico de los andamiajes. Además, se ha conseguido mejorar las propiedades mecánicas de los andamiajes rellenado la porosidad abierta con polímeros biodegradables (PCL y PLA), mediante inmersión del andamiaje en el polímero fundido. Las propiedades mecánicas de los andamiajes obtenidas a partir de ensayos de compresión, y en algunos casos también de flexión, se han comparado con las propiedades mecánicas del hueso. Entre las conclusiones más relevantes que pueden derivarse de este estudio, cabe destacar:

En relación a la fabricación de andamiajes de biovidrio 45S5

1- La técnica de moldeo robotizado permite fabricar andamiajes derivados de biovidrio 45S5 con la forma exterior y la arquitectura de poros deseadas y con resistencia a compresión muy superior a cualquier valor publicado anteriormente. La utilización de carboximetilcelulosa como único aditivo ha permitido preparar suspensiones coloidales con la concentración adecuada para moldeo robotizado, superando las dificultades inherentes al procesado coloidal de biovidro 45S5. La mejora en las propiedades mecánicas asociada a la nueva arquitectura de poros obtenida mediante moldeo robotizado, con barras cerámicas más gruesas y con mayor grado de interconectividad, es enorme: en el caso de la resistencia a fractura se obtienen valores más de un orden de magnitud superior a los obtenidos hasta ahora y dentro, o incluso por encima, del rango de valores del hueso esponjoso.

2- El moldeo robotizado permite, mediante sinterización a temperaturas suficientemente bajas (550 °C), fabricar andamiajes de 45S5 amorfo—preservando así la bioactividad del biovidrio 45S5— con la integridad mecánica suficiente como para ser utilizado. Por tanto, el moldeo robtizado, y quizás también otras técnicas de conformado libre, permite superar el principal obstáculo para el uso de biovidrio 45S5 como sustituto óseo. La simplicidad y versatilidad del proceso de moldeo robotizado facilitarán permitirá fabricar andamiajes de 45S5 con la geometría

necesaria para adaptarse a la lesión de cada paciente y extender el ámbito actual de aplicación de este excelente material bioactivo.

En relación a la fabricación de andamiajes de biovidrio 13-93

3- La utilización de carboximetilcelulosa como único aditivo permite preparar suspensiones coloidales a partir de polvos de biovidrio 13-93 con la concentración necesaria para fabricar andamiajes mediante la técnica de moldeo robotizado. Para ello se pueden utilizar tanto polvos molidos en agua como en etanol. Los polvos molidos en etanol tienen una distribución de tamaños de partícula más fina y estrecha y permiten un mejor control de las propiedades reológicas de la suspensión.

4- El proceso utilizado en este trabajo para eliminar los componentes orgánicos de las tintas de 13-93 ha resultado inadecuado, ya que ha dado lugar a la formación de burbujas a temperaturas próximas a la temperatura óptima de sinterización, especialmente cuando se utilizan polvos molidos en agua. No obstante, la optimización del proceso podría permitir la fabricación de estructuras libres de burbujas a partir de los dos tipos de polvos. Por otra parte, tras la sinterización, las estructuras fabricadas a partir de polvos molidos en etanol exhiben un extraño color negro que resulta de la introducción durante el proceso de molienda de especies carbonosas, que no se eliminan ni a temperaturas superiores a la de cristalización. Afortunadamente, ni las impurezas que quedan en estructuras debido al inadecuado proceso de quemado ni las especies carbonosas en la muestras fabricadas a partir de polvos molidos en etanol dificultan la bioactividad o la adhesión celular, de acuerdo con los ensayos *in vitro*. Las impurezas, tampoco afectan a las propiedades mecánicas de los andamiajes de 13-93 que presentan valores similares a los de la literatura, con valores de resistencia a fractura (para porosidades superiores al 50 %) próximos a los valores del hueso cortical.

En relación a1 efecto de la inmersión de andamiajes de 45S5 y13-93 en SBF

5- Durante la inmersión de andamiajes de 45S5 sinterizados a 550 °C (amorfo) se produce una mayor pérdida de peso y aumento del pH que en el caso de andamiajes sinterizados a 1000 °C debido a la mayor disolución de especies alcalinas, como

consecuencia de la mayor microposidad y área superficial. Estos dos factores son también responsables de la mayor conversión de biovidrio a HA en las muestras sinterizadas a 550 ºC. En ambos materiales, la conversión a una capa porosa de HA da lugar a una degradación de la resistencia a compresión, que en el caso del andamiaje cristalino está acelerada por la formación de fisuras en la capa de HA.

6- La microporosidad de las barras que constituyen los andamiajes juega un papel muy importante en el control de la degradación in vitro y conversión a HA de los andamiajes de 13-93, que en todos los casos son considerablemente menor que en el caso de los andamiajes de 45S5. La presencia no deseada de burbujas en las muestras fabricadas a partir de polvos molidos en agua muestra que la presencia de tales poros en las barras de la estructura no solo aumenta la velocidad de degradación sino también el factor de conversión máximo—de menos del 6 % para muestras densas hasta alrededor del 35 % para las estructuras fabricadas en este trabajo a partir de polvos molidos en agua. Obviamente, esta mayor degradación velocidad de degradación se traduce en una mayor y más rápida disminución de la resistencia mecánica, que ya es más baja debido a la presencia de microdefectos. Estos resultados sugieren que una forma simple de controlar la degradación de andamiajes fabricados mediante moldeo robotizado es controlar su microporosidad.

En relación a1 efecto de la impregnación con polímeros

7- La impregnación mediante inmersión en el polímero fundido es un método simple, barato y efectivo para fabricar materiales compuestos polímero/biovidrio a partir de polímeros comerciales. Sin embargo, se debe de tener cuidado a la hora de seleccionar al seleccionar las condiciones del proceso de infiltración para evitar interacciones no deseadas entre las fases orgánicas e inorgánicas, como las que han tenido lugar al infiltrar 45S5 con PCL y, especialmente PLA.

8- Los resultados de este estudio confirman el efecto positivo de la impregnación con polímeros en las propiedades mecánicas de andamiajes derivados de biovidrio, independientemente del modo de carga (compresión o flexión). De hecho, la impregnación con un polímero dúctil no sólo reduce la fragilidad intrínseca de las estructuras cerámicas porosas sino que al mismo tiempo aumenta la resistencia a fractura y la fiabilidad del material.

9- Los resultados de este trabajo prueban, por primera vez, que la existencia de microporosidad en las barras juega un papel importante en el refuerzo mecánico que se obtiene mediante impregnación con polímeros de estructuras fabricadas mediante moldeo robotizado. El aumento de resistencia que se produce por curación de defectos disminuye considerablemente al disminuir la población de defectos precursores (microporos). Lo mismo ocurre con el aumento de tenacidad debido a que las fibras del polímero que está dentro de los microporos contribuye al mecanismo de refuerzo por puenteo de fisuras.

10- Aunque el poder reforzante del polímero disminuye al reducir la microporosidad, los materiales compuestos polímero/cerámico más resistentes y tenaces son aquellos en los que la estructura cerámica está constituido por barras densas. Por tanto, la optimización del proceso de sinterización del esqueleto cerámico es indispensable para maximizar la respuesta mecánica del material compuesto cerámicos/polímero.

11- Para aumentar la tenacidad son más efectivos los polímeros dúctiles como el PCL en lugar de los más resistentes y frágiles (como el PLA), puesto que proporcionan integridad mecánica tras la fractura del esqueleto cerámico, tanto en comprensión como en flexión, incluso tras grandes deformaciones. Debido al extraordinario aumento de tenacidad proporcionado por el polímero, el material híbrido 13-93/PCL puede ser mecanizado.

12- Las propiedades mecánicas del material híbrido 13-93/PCL son significativamente mejores que las del PCL, lo cual indica que esqueletos cerámicos constituidos por barras densas fabricados mediante moldeo robotizado pueden ser utilizados como refuerzos mecánicos multidireccionales de polímeros dúctiles, aunque no tanto de polímeros resistentes y frágiles.

En relación a la comparación con las propiedades del hueso

13- Los andamiajes derivados de biovidrio, constituidos por barras de dimensiones uniformes, fabricados mediante moldeo robotizado cuando se sinterizan de forma que se consigue un buen nivel de densificación exhiben valores de resistencia a compresión similares o incluso supriores a los del hueso con el mismo grado de porosidad. Valores de módulo elástico similares a los del hueso cortical también

pueden conseguirse en estructuras biocerámcias, pero con valores de tenacidad lejos de los valores correspondientes al tejido óseo.

14- Por el contrario, materiales híbridos cerámico/polímero pueden alcanzar (como en el caso de las estructuras 13-93/PLA) o incluso superar en algunos aspectos (13-93/PCL) las respuesta del hueso cortical bajo tensiones de compresión, en cuanto a rigidez, resistencia y tenacidad. Por tanto, el material compuesto 13-93/PLA y, especialmente, el 13-93/PCL son candidatos óptimos para reemplazar al hueso cortical en regiones sometidas a tensiones de compresión.

15- Desafortunadamente, estas excepcionales propiedades mecánicas no se reproducen en flexión. Bajo tensiones de flexión ni la resistencia ni la tenacidad del hueso cortical pueden ser alcanzadas por ninguno de los materiales fabricados en este estudio, ni siquiera las estructuras híbridas cerámico/polímero. Esto pone de manifiesto que la caracterización mecánica de materiales para sustitución ósea no pueden limitarse a ensayos de compresión.

Este trabajo proporciona información valiosa sobre al moldeo robotizado de andamiajes derivados de biovidrio y sus propiedades mecánicas y biológicas y sobre el comportamiento mecánico de materiales compuestos cerámico/polímero susceptibles de ser utilizados como materiales estructurales no solo en el campo biomédico sino también en otras áreas de la ingeniería.

References

[1]   TL, "Clinical Orthopaedics and Related Research," *The American Journal of the Medical Sciences*, vol. 254, no. 5. p. 766, 1967.

[2]   H. R. Piehler, "The future of medicine," *Biomaterials*, 2000.

[3]   C. J. Damien and J. R. Parsons, "Bone graft and bone graft substitutes: a review of current technology and applications.," *J. Appl. Biomater.*, vol. 2, no. 3, pp. 187–208, 1991.

[4]   P. N. De Aza, A. H. De Aza, P. Pena, and S. De Aza, "Bioactive glasses and glass-ceramics," *Boletin de la Sociedad Espanola de Ceramica y Vidrio*, vol. 46. pp. 45–55, 2007.

[5]   M. N. Rahaman, D. E. Day, B. S. Bal, Q. Fu, S. B. Jung, L. F. Bonewald, and A. P. Tomsia, "Bioactive glass in tissue engineering.," *Acta Biomater.*, vol. 7, no. 6, pp. 2355–73, Jun. 2011.

[6]   J. A. Roether, A. R. Boccaccini, L. L. Hench, V. Maquet, S. Gautier, and R. Jérôme, "Development and in vitro characterisation of novel bioresorbable and bioactive composite materials based on polylactide foams and Bioglass® for tissue engineering applications," *Biomaterials*, vol. 23, pp. 3871–3878, 2002.

[7]   L. L. Hench, R. J. Splinter, W. C. Allen, and T. K. Greenlee, "Bonding mechanisms at the interface of ceramic prosthetic materials," *J. Biomed. Mater. Res.*, vol. 5, no. 6, pp. 117–141, 1971.

[8]   L. L. Hench, "The story of Bioglass," in *Journal of Materials Science: Materials in Medicine*, 2006, vol. 17, pp. 967–978.

[9]   J. R. Jones, "Review of bioactive glass: From Hench to hybrids," *Acta Biomaterialia*, vol. 9. pp. 4457–4486, 2013.

[10]   I. D. Xynos, A. J. Edgar, L. D. K. Buttery, L. L. Hench, and J. M. Polak, "Gene-expression profiling of human osteoblasts following treatment with the ionic products of Bioglass® 45S5 dissolution," *J. Biomed. Mater. Res.*, vol. 55, no. 2, pp. 151–157, 2001.

[11] S. Hattar, A. Asselin, D. Greenspan, M. Oboeuf, A. Berdal, and J.-M. Sautier, "Potential of biomimetic surfaces to promote in vitro osteoblast-like cell differentiation.," *Biomaterials*, vol. 26, no. 8, pp. 839–48, Mar. 2005.

[12] G. C. Reilly, S. Radin, A. T. Chen, and P. Ducheyne, "Differential alkaline phosphatase responses of rat and human bone marrow derived mesenchymal stem cells to 45S5 bioactive glass," *Biomaterials*, vol. 28, no. 28, pp. 4091–4097, 2007.

[13] L. L. Hench and J. M. Polak, "Third-generation biomedical materials.," *Science*, vol. 295, pp. 1014–1017, 2002.

[14] A. R. Boccaccini, Q. Chen, L. Lefebvre, L. Gremillard, and J. Chevalier, "Sintering, crystallisation and biodegradation behaviour of Bioglass-derived glass-ceramics.," *Faraday Discuss.*, vol. 136, pp. 27–44; discussion 107–123, 2007.

[15] L. Lefebvre, J. Chevalier, L. Gremillard, R. Zenati, G. Thollet, D. Bernache-Assolant, and A. Govin, "Structural transformations of bioactive glass 45S5 with thermal treatments," *Acta Mater.*, vol. 55, pp. 3305–3313, 2007.

[16] O. Bretcanu, X. Chatzistavrou, K. Paraskevopoulos, R. Conradt, I. Thompson, and A. R. Boccaccini, "Sintering and crystallisation of 45S5 Bioglass powder," *J. Eur. Ceram. Soc.*, vol. 29, pp. 3299–3306, 2009.

[17] D. W. Hutmacher, "Scaffolds in tissue engineering bone and cartilage.," *Biomaterials*, vol. 21, pp. 2529–2543, 2000.

[18] E. Sachlos and J. T. Czernuszka, "Making tissue engineering scaffolds work. Review: the application of solid freeform fabrication technology to the production of tissue engineering scaffolds.," *Eur. Cell. Mater.*, vol. 5, pp. 29–39; discussion 39–40, 2003.

[19] T. S. Huang, M. N. Rahaman, N. D. Doiphode, M. C. Leu, B. S. Bal, D. E. Day, and X. Liu, "Porous and strong bioactive glass (13-93) scaffolds fabricated by freeze extrusion technique," *Mater. Sci. Eng. C*, vol. 31, pp. 1482–1489, 2011.

[20] F. J. Martínez-Vázquez, F. H. Perera, P. Miranda, A. Pajares, and F. Guiberteau, "Improving the compressive strength of bioceramic robocast scaffolds by polymer infiltration," *Acta Biomater.*, vol. 6, pp. 4361–4368, 2010.

[21] M.-V. J., A. Pajares, F. Guiberteau, and P. Miranda, "Effect of polymer infiltration on the flexural behavior of β-tricalcium phosphate robocast scaffolds," *Materials (Basel).*, vol. 7, pp. 4001–4018, 2014.

[22]   K. Chol, L. J. Kuhn, M. J. Ciarelli, and S. A. Goldstein, "The elastic moduli of human subchondral, trabecular, and cortical bone tissue and the size-dependency of cortical bone modulus," *J. Biomech.*, vol. 23, pp. 1103–1113, 1990.

[23]   S. Weiner and H. D. Wagner, "THE MATERIAL BONE: Structure-Mechanical Function Relations," *Annual Review of Materials Science*, vol. 28. pp. 271–298, 1998.

[24]   D. T. Reilly and A. H. Burstein, "The Mechanical Properties of Cortical Bone," *J. Bone Jt. Surg.*, vol. 56, pp. 1001–1022, 1974.

[25]   T. M. Keaveny, E. F. Morgan, and O. C. Yeh, "Bone mechanics," in *Standard Handbook of Biomedical Engineering and Design*, ,pp. 8.1–8.23, 2004.

[26]   K. Arvidson, B. M. Abdallah, L. A. Applegate, N. Baldini, E. Cenni, E. Gomez-Barrena, D. Granchi, M. Kassem, Y. T. Konttinen, K. Mustafa, D. P. Pioletti, T. Sillat, and A. Finne-Wistrand, "Bone regeneration and stem cells," *Journal of Cellular and Molecular Medicine*, vol. 15. pp. 718–746, 2011.

[27]   S. Ramakrishna, J. Mayer, E. Wintermantel, and K. W. Leong, "Biomedical applications of polymer-composite materials: A review," *Compos. Sci. Technol.*, vol. 61, pp. 1189–1224, 2001.

[28]   L.-C. Gerhardt and A. R. Boccaccini, "Bioactive Glass and Glass-Ceramic Scaffolds for Bone Tissue Engineering," *Materials*, vol. 3. pp. 3867–3910, 2010.

[29]   G. H. van Lenthe, M. M. M. Willems, N. Verdonschot, M. C. de Waal Malefijt, and R. Huiskes, "Stemmed femoral knee prostheses: effects of prosthetic design and fixation on bone loss.," *Acta Orthop. Scand.*, vol. 73, pp. 630–637, 2002.

[30]   G. H. Van Lenthe, M. C. de Waal Malefijt, and R. Huiskes, "Stress shielding after total knee replacement may cause bone resorption in the distal femur.," *J. Bone Joint Surg. Br.*, vol. 79, pp. 117–122, 1997.

[31]   R. Huiskes, H. Weinans, and B. van Rietbergen, "The relationship between stress shielding and bone resorption around total hip stems and the effects of flexible materials.," *Clin. Orthop. Relat. Res.*, pp. 124–134, 1992.

[32]   G. P. Kothiyal, A. Ananthanarayanan, and G. K. Dey, "Glass and glass-ceramics," in *Functional Materials*, 2012, pp. 323–386.

[33]   P. G. Debenedetti and F. H. Stillinger, "Supercooled liquids and the glass transition.," *Nature*, vol. 410, pp. 259–267, 2001.

[34] G. S. Henderson, G. Calas, and J. F. Stebbins, "The Structure of Silicate Glasses and Melts," *Elements*, vol. 2. pp. 269–273, 2006.

[35] J. F. Shackelford and R. H. Doremus, *Ceramic and glass materials: Structure, properties and processing*. 2008.

[36] T. Macfarlane, "Glass structures," *Structural Engineer*, vol. 85. pp. 41–44, 2007.

[37] H.-M. Kim, F. Miyaji, T. Kokubo, C. Ohtsuki, and T. Nakamura, "Bioactivity of Na2O-CaO-SiO2 Glasses," *J. Am. Ceram. Soc.*, vol. 78, pp. 2405–2411, 1995.

[38] L. L. Hench, "Sol-gel materials for bioceramic applications," *Current Opinion in Solid State and Materials Science*, vol. 2. pp. 604–610, 1997.

[39] L. L. Hench, J. M. Polak, I. D. Xynos, and L. D. K. Buttery, "Bioactive materials to control cell cycle," *Mater. Res. Innov.*, vol. 3, pp. 313–323, 2000.

[40] A. R. Boccaccini and J. J. Blaker, "Bioactive composite materials for tissue engineering scaffolds.," *Expert Rev. Med. Devices*, vol. 2, pp. 303–317, 2005.

[41] A. R. Boccaccini and J. J. Blaker, "Bioactive materials for tissue engineering scaffolds.," *Expert Rev. Med. Devices*, vol. 2, pp. 303–17, 2005.

[42] M. Hamadouche, A. Meunier, D. C. Greenspan, C. Blanchat, J. P. Zhong, G. P. La Torre, and L. Sedel, "Long-term in vivo bioactivity and degradability of bulk sol-gel bioactive glasses," *J. Biomed. Mater. Res.*, vol. 54, pp. 560–566, 2001.

[43] Z. Zhang, Y. Xiao, J. Voncken, Y. Yang, R. Boom, N. Wang, and Z. Zou, "Phase Equilibria in the Na2O-CaO-SiO2 system," *J. Am. Ceram. Soc.*, vol. 94, pp. 3088–3093, 2011.

[44] L. L. Hench, "Bioceramics," *J. Am. Ceram. Soc.*, vol. 81, pp. 1705–1728, 1998.

[45] O. Peitl, E. Dutra, and L. L. Hench, "Highly bioactive P 2 O 5 ± Na 2 O ± CaO ± SiO 2 glass-ceramics," *J. Non. Cryst. Solids*, vol. 292, pp. 115–126, 2001.

[46] T. Kokubo, "Bioactive glass ceramics: properties and applications.," *Biomaterials*, vol. 12, pp. 155–163, 1991.

[47] I. Lebecq, F. Désanglois, A. Leriche, and C. Follet-Houttemane, "Compositional dependence on the in vitro bioactivity of invert or conventional bioglasses in the Si-Ca-Na-P system," *J. Biomed. Mater. Res. - Part A*, vol. 83, pp. 156–168, 2007.

[48] H. Aguiar, J. Serra, P. González, and B. León, "Structural study of sol-gel silicate glasses by IR and Raman spectroscopies," *J. Non. Cryst. Solids*, vol. 355, pp. 475–480, 2009.

[49]   S. Fagerlund, J. Massera, M. Hupa, and L. Hupa, "T-T-T behaviour of bioactive glasses 1-98 and 13-93," *J. Eur. Ceram. Soc.*, vol. 32, pp. 2731–2738, 2012.

[50]   "EiC November 2006 - Feature - Glass bones." [Online]. Available: http://www.rsc.org/Education/EiC/issues/2006Nov/GlassBones.asp.   [Accessed: 08-Jun-2015].

[51]   A. Sola, D. Bellucci, V. Cannillo, and A. Cattini, "Bioactive glass coatings: a review," *Surface Engineering*, vol. 27. pp. 560–572, 2011.

[52]   Q. Z. Chen, K. Rezwan, V. Françon, D. Armitage, S. N. Nazhat, F. H. Jones, and A. R. Boccaccini, "Surface functionalization of Bioglass®-derived porous scaffolds," *Acta Biomater.*, vol. 3, pp. 551–562, 2007.

[53]   T. Kokubo, "Design of bioactive bone substitutes based on biomineralization process," in *Materials Science and Engineering C*, 2005, vol. 25, pp. 97–104.

[54]   O. P. Filho, G. P. Latorre, and L. L. Hench, "Effect of crystallization on apatite-layer formation of bioactive glass 45S5," *J. Biomed. Mater. Res.*, vol. 30, pp. 509–514, 1996.

[55]   M. Ogino, F. Ohuchi, and L. L. Hench, "Compositional dependence of the formation of calcium phosphate films on bioglass.," *J. Biomed. Mater. Res.*, vol. 14, pp. 55–64, 1980.

[56]   M. Bohner and J. Lemaitre, "Can bioactivity be tested in vitro with SBF solution?," *Biomaterials*, vol. 30, pp. 2175–2179, 2009.

[57]   S. Jalota, S. B. Bhaduri, and A. C. Tas, "Using a synthetic body fluid (SBF) solution of 27mM HCO3 - to make bone substitutes more osteointegrative," *Mater. Sci. Eng. C*, vol. 28, pp. 129–140, 2008.

[58]   C. Ohtsuki, H. Kushitani, T. Kokubo, S. Kotani, and T. Yamamuro, "Apatite formation on the surface of Ceravital-type glass-ceramic in the body.," *J. Biomed. Mater. Res.*, vol. 25, pp. 1363–1370, 1991.

[59]   A. Oyane, K. Onuma, A. Ito, H.-M. Kim, T. Kokubo, and T. Nakamura, "Formation and growth of clusters in conventional and new kinds of simulated body fluids.," *J. Biomed. Mater. Res. A*, vol. 64, pp. 339–348, 2003.

[60]   A. Oyane, H.-M. Kim, T. Furuya, T. Kokubo, T. Miyazaki, and T. Nakamura, "Preparation and assessment of revised simulated body fluids.," *J. Biomed. Mater. Res. A*, vol. 65, pp. 188–195, 2003.

[61] M. Plewinski, K. Schickle, M. Lindner, A. Kirsten, M. Weber, and H. Fischer, "The effect of crystallization of bioactive bioglass 45S5 on apatite formation and degradation," *Dent. Mater.*, vol. 29, pp. 1256–1264, 2013.

[62] Q. Z. Chen, I. D. Thompson, and A. R. Boccaccini, "45S5 Bioglass[®]-derived glass-ceramic scaffolds for bone tissue engineering," *Biomaterials*, vol. 27, pp. 2414–2425, 2006.

[63] Q. Fu, M. N. Rahaman, B. Sonny Bal, R. F. Brown, and D. E. Day, "Mechanical and in vitro performance of 13-93 bioactive glass scaffolds prepared by a polymer foam replication technique," *Acta Biomater.*, vol. 4, pp. 1854–1864, 2008.

[64] Q. Fu, M. N. Rahaman, B. S. Bal, W. Huang, and D. E. Day, "Preparation and bioactive characteristics of a porous 13-93 glass, and fabrication into the articulating surface of a proximal tibia," *J. Biomed. Mater. Res. - Part A*, vol. 82, pp. 222–229, 2007.

[65] C. Wu and J. Chang, "Mesoporous bioactive glasses: structure characteristics, drug/growth factor delivery and bone regeneration application," *Interface Focus*, vol. 2. pp. 292–306, 2012.

[66] R. Li, A. E. Clark, and L. L. Hench, "An investigation of bioactive glass powders by sol-gel processing.," *J. Appl. Biomater.*, vol. 2, pp. 231–239, 1991.

[67] P. Sepulveda, J. R. Jones, and L. L. Hench, "Synthesis of Sol-Gel Derived Bioactive Foams," *Key Engineering Materials*, vol. 218–220. pp. 287–290, 2002.

[68] M. M. Pereira, J. R. Jones, R. L. Orefice, and L. L. Hench, "Preparation of bioactive glass-polyvinyl alcohol hybrid foams by the sol-gel method," *J. Mater. Sci. Mater. Med.*, vol. 16, pp. 1045–1050, 2005.

[69] J. R. Jones and L. L. Hench, "Factors affecting the structure and properties of bioactive foam scaffolds for tissue engineering.," *J. Biomed. Mater. Res. B. Appl. Biomater.*, vol. 68, pp. 36–44, 2004.

[70] J. R. Jones, S. Ahir, and L. L. Hench, "Large-scale production of 3D bioactive glass macroporous scaffolds for tissue engineering," *J. Sol-Gel Sci. Technol.*, vol. 29, pp. 179–188, 2004.

[71] C. J. Brinker and G. W. Scherer, *Sol-gel science: the physics and chemistry of sol-gel processing*, vol. 8. 1990.

[72] M. Guglielmi, "Sol-gel science," *Materials Chemistry and Physics*, vol. 26. pp. 211–212, 1990.

[73] L. L. Hench, D. L. Wheeler, and D. C. Greenspan, "Molecular Control of Bioactivity in Sol-Gel Glasses," *J. Sol-Gel Sci. Technol.*, vol. 250, pp. 245–250, 1998.

[74] C. Liu, Z. Xia, and J. T. Czernuszka, "Design and Development of Three-Dimensional Scaffolds for Tissue Engineering," *Chem. Eng. Res. Des.*, vol. 85, pp. 1051–1064, 2007.

[75] D. W. Hutmacher, "Scaffold design and fabrication technologies for engineering tissues — state of the art and future perspectives," *Journal of Biomaterials Science, Polymer Edition*, vol. 12. pp. 107–124, 2001.

[76] H. P. Wiesmann, B. Lüttenberg, and U. Meyer, "Tissue Engineering of Bone," in *Handbook of Biomineralization: Biological Aspects and Structure Formation*, vol. 3, pp. 145–156, 2008.

[77] S. Pezzatini, R. Solito, L. Morbidelli, S. Lamponi, E. Boanini, A. Bigi, and M. Ziche, "The effect of hydroxyapatite nanocrystals on microvascular endothelial cell viability and functions," *J. Biomed. Mater. Res. - Part A*, vol. 76, pp. 656–663, 2006.

[78] K. Whang, K. E. Healy, D. R. Elenz, E. K. Nam, D. C. Tsai, C. H. Thomas, G. W. Nuber, F. H. Glorieux, R. Travers, and S. M. Sprague, "Engineering bone regeneration with bioabsorbable scaffolds with novel microarchitecture.," *Tissue Eng.*, vol. 5, pp. 35–51, 1999.

[79] S. J. Hollister, "Porous scaffold design for tissue engineering.," *Nat. Mater.*, vol. 4, pp. 518–524, 2005.

[80] A. L. DiRienzo, C. M. Yakacki, M. Frensemeier, A. S. Schneider, D. L. Safranski, A. J. Hoyt, and C. P. Frick, "Porous poly(para-phenylene) scaffolds for load-bearing orthopedic applications," *J. Mech. Behav. Biomed. Mater.*, vol. 30, pp. 347–357, 2014.

[81] M. C. Wake, C. W. Patrick, and A. G. Mikos, "Pore morphology effects on the fibrovascular tissue growth in porous polymer substrates," *Cell Transplant.*, vol. 3, pp. 339–343, 1994.

[82] S. Bose, M. Roy, and A. Bandyopadhyay, "Recent advances in bone tissue engineering scaffolds," *Trends in Biotechnology*, vol. 30. pp. 546–554, 2012.

[83] S. Lv, D. M. Dudek, Y. Cao, M. M. Balamurali, J. Gosline, and H. Li, "Designed biomaterials to mimic the mechanical properties of muscles.," *Nature*, vol. 465, pp. 69–73, 2010.

[84] J. Kundu, F. Pati, Y. Hun Jeong, and D. W. Cho, "Biomaterials for Biofabrication of 3D Tissue Scaffolds," in *Biofabrication: Micro- and Nano-fabrication, Printing, Patterning and Assemblies*, 2013, pp. 23–46.

[85] S. J. Hollister, "Scaffold engineering: a bridge to where?," *Biofabrication*, vol. 1, p. 012001, 2009.

[86] E. Di Maio, G. Mensitieri, S. Iannace, L. Nicolais, W. Li, and R. W. Flumerfelt, "Structure optimization of polycaprolactone foams by using mixtures of CO2 and N2 as blowing agents," *Polym. Eng. Sci.*, vol. 45, pp. 432–441, 2005.

[87] H. Haugen, V. Ried, M. Brunner, J. Will, and E. Wintermantel, "Water as foaming agent for open cell polyurethane structures," in *Journal of Materials Science: Materials in Medicine*, vol. 15, pp. 343–346, 2004.

[88] S. Siripurapu, Y. J. Gay, J. R. Royer, J. M. DeSimone, R. J. Spontak, and S. A. Khan, "Generation of microcellular foams of PVDF and its blends using supercritical carbon dioxide in a continuous process," *Polymer (Guildf).*, vol. 43, pp. 5511–5520, 2002.

[89] R. A. Quirk, R. M. France, K. M. Shakesheff, and S. M. Howdle, "Supercritical fluid technologies and tissue engineering scaffolds," *Current Opinion in Solid State and Materials Science*, vol. 8. pp. 313–321, 2004.

[90] R. A. Martin, S. Yue, J. V Hanna, P. D. Lee, R. J. Newport, M. E. Smith, and J. R. Jones, "Characterizing the hierarchical structures of bioactive sol-gel silicate glass and hybrid scaffolds for bone regeneration.," *Philos. Trans. A. Math. Phys. Eng. Sci.*, vol. 370, no. 1963, pp. 1422–43, Mar. 2012.

[91] P. Sepulveda and L. L. Hench, "Bioactive Hierarchical Structures for Genetic Control of Bone Morphogenesis," *Mater. Res.*, vol. 5, no. 3, pp. 243–246, Sep. 2002.

[92] J. R. Jones and L. L. Hench, "Effect of surfactant concentration and composition on the structure and properties of sol-gel-derived bioactive glass foam scaffolds for tissue engineering," *J. Mater. Sci.*, vol. 38, pp. 3783–3790, 2003.

[93] J. E. Gough, J. R. Jones, and L. L. Hench, "Osteoblast Nodule Formation and Mineralisation on Foamed 58S Bioactive Glass," *Key Engineering Materials*, vol. 254–256. pp. 985–988, 2004.

[94] J. R. Jones, L. M. Ehrenfried, and L. L. Hench, "Optimising bioactive glass scaffolds for bone tissue engineering," *Biomaterials*, vol. 27, pp. 964–973, 2006.

[95] A. Rainer, S. M. Giannitelli, F. Abbruzzese, E. Traversa, S. Licoccia, and M. Trombetta, "Fabrication of bioactive glass-ceramic foams mimicking human bone portions for regenerative medicine," *Acta Biomater.*, vol. 4, pp. 362–369, 2008.

[96] J. E. Gough, J. R. Jones, and L. L. Hench, "Nodule formation and mineralisation of human primary osteoblasts cultured on a porous bioactive glass scaffold," *Biomaterials*, vol. 25, pp. 2039–2046, 2004.

[97] M. J. Pikal, S. Shah, M. L. Roy, and R. Putman, "The secondary drying stage of freeze drying: Drying kinetics as a function of temperature and chamber pressure," *Int. J. Pharm.*, vol. 60, pp. 203–217, 1990.

[98] J. C. Bischof and X. He, "Thermal stability of proteins.," *Annals of the New York Academy of Sciences*, vol. 1066. pp. 12–33, 2005.

[99] K. Araki and J. W. Halloran, "New freeze-casting technique for ceramics with sublimable vehicles," *J. Am. Ceram. Soc.*, vol. 87, pp. 1859–1863, 2004.

[100] B. H. Yoon, Y. H. Koh, C. S. Park, and H. E. Kim, "Generation of large pore channels for bone tissue engineering using camphene-based freeze casting," *J. Am. Ceram. Soc.*, vol. 90, pp. 1744–1752, 2007.

[101] B.-H. Yoon, W.-Y. Choi, H.-E. Kim, J.-H. Kim, and Y.-H. Koh, "Aligned porous alumina ceramics with high compressive strengths for bone tissue engineering," *Scripta Materialia*, vol. 58. pp. 537–540, 2008.

[102] Y. M. Soon, K. H. Shin, Y. H. Koh, J. H. Lee, and H. E. Kim, "Compressive strength and processing of camphene-based freeze cast calcium phosphate scaffolds with aligned pores," *Mater. Lett.*, vol. 63, pp. 1548–1550, 2009.

[103] E. J. Lee, Y. H. Koh, B. H. Yoon, H. E. Kim, and H. W. Kim, "Highly porous hydroxyapatite bioceramics with interconnected pore channels using camphene-based freeze casting," *Mater. Lett.*, vol. 61, pp. 2270–2273, 2007.

[104] S. W. Yook, H. E. Kim, B. H. Yoon, Y. M. Soon, and Y. H. Koh, "Improvement of compressive strength of porous hydroxyapatite scaffolds by adding polystyrene to camphene-based slurries," *Mater. Lett.*, vol. 63, pp. 955–958, 2009.

[105] J. Han, C. Hong, X. Zhang, J. Du, and W. Zhang, "Highly porous ZrO2 ceramics fabricated by a camphene-based freeze-casting route: Microstructure and properties," *J. Eur. Ceram. Soc.*, vol. 30, pp. 53–60, 2010.

[106] A. Macchetta, I. G. Turner, and C. R. Bowen, "Fabrication of HA/TCP scaffolds with a graded and porous structure using a camphene-based freeze-casting method.," *Acta Biomater.*, vol. 5, no. 4, pp. 1319–27, 2009.

[107] S. Deville, E. Saiz, and A. P. Tomsia, "Freeze casting of hydroxyapatite scaffolds for bone tissue engineering," *Biomaterials*, vol. 27, pp. 5480–5489, 2006.

[108] Q. Fu, M. N. Rahaman, F. Dogan, and B. S. Bal, "Freeze-cast hydroxyapatite scaffolds for bone tissue engineering applications.," *Biomed. Mater.*, vol. 3, p. 025005, 2008.

[109] J. H. Song, Y. H. Koh, H. E. Kim, L. H. Li, and H. J. Bahn, "Fabrication of a porous bioactive glass-ceramic using room-temperature freeze casting," *J. Am. Ceram. Soc.*, vol. 89, pp. 2649–2653, 2006.

[110] X. Liu, M. N. Rahaman, and Q. Fu, "Oriented bioactive glass (13-93) scaffolds with controllable pore size by unidirectional freezing of camphene-based suspensions: Microstructure and mechanical response," *Acta Biomater.*, vol. 7, pp. 406–416, 2011.

[111] X. Liu, M. N. Rahaman, Q. Fu, and A. P. Tomsia, "Porous and strong bioactive glass (13-93) scaffolds prepared by unidirectional freezing of camphene-based suspensions," *Acta Biomater.*, vol. 8, pp. 415–423, 2012.

[112] "Method of making porous ceramic articles." 21-May-1963.

[113] D. Bellucci, A. Sola, V. Cannillo, "a-revised replication method for bioceramic scaffolds," *Bioceramics Development and Applications*., vol.1, pp. 1-8, 2011.

[114] H. R. Ramay and M. Zhang, "Preparation of porous hydroxyapatite scaffolds by combination of the gel-casting and polymer sponge methods," *Biomaterials*, vol. 24, pp. 3293–3302, 2003.

[115] E. Saiz, L. Gremillard, G. Menendez, P. Miranda, K. Gryn, and A. P. Tomsia, "Preparation of porous hydroxyapatite scaffolds," *Mater. Sci. Eng. C*, vol. 27, pp. 546–550, 2007.

[116] Y. Zhang and M. Zhang, "Three-dimensional macroporous calcium phosphate bioceramics with nested chitosan sponges for load-bearing bone implants," *J. Biomed. Mater. Res.*, vol. 61, pp. 1–8, 2002.

[117] K. K. Mallick, J. Winnett, W. Van Grunsven, J. Lapworth, and G. C. Reilly, "Three-dimensional porous bioscaffolds for bone tissue regeneration: Fabrication via adaptive foam reticulation and freeze casting techniques, characterization, and cell study," *J. Biomed. Mater. Res. - Part A*, vol. 100 A, pp. 2948–2959, 2012.

[118] Y. Li, M. N. Rahaman, Q. Fu, B. S. Bal, A. Yao, and D. E. Day, "Conversion of Bioactive Borosilicate Glass to Multilayered Hydroxyapatite in Dilute Phosphate Solution," *J. Am. Ceram. Soc.*, p. 070918221104004, Sep. 2007.

[119] H. Fu, Q. Fu, N. Zhou, W. Huang, M. N. Rahaman, D. Wang, and X. Liu, "In vitro evaluation of borate-based bioactive glass scaffolds prepared by a polymer foam replication method," *Mater. Sci. Eng. C*, vol. 29, pp. 2275–2281, 2009.

[120] Q. Fu, M. N. Rahaman, B. S. Bal, L. F. Bonewald, K. Kuroki, and R. F. Brown, "Silicate, borosilicate, and borate bioactive glass scaffolds with controllable degradation rate for bone tissue engineering applications. II. In vitro and in vivo biological evaluation," *J. Biomed. Mater. Res. - Part A*, vol. 95, pp. 172–179, 2010.

[121] C. Vitale-Brovarone, E. Verné, L. Robiglio, P. Appendino, F. Bassi, G. Martinasso, G. Muzio, and R. Canuto, "Development of glass-ceramic scaffolds for bone tissue engineering: Characterisation, proliferation of human osteoblasts and nodule formation," *Acta Biomater.*, vol. 3, pp. 199–208, 2007.

[122] Q. Z. Chen, A. Efthymiou, V. Salih, and A. R. Boccaccini, "Bioglass[®]-derived glass-ceramic scaffolds: Study of cell proliferation and scaffold degradation in vitro," *J. Biomed. Mater. Res. - Part A*, vol. 84, pp. 1049–1060, 2008.

[123] S. Yang, K.-F. Leong, Z. Du, and C.-K. Chua, "The design of scaffolds for use in tissue engineering. Part II. Rapid prototyping techniques.," *Tissue Eng.*, vol. 8, pp. 1–11, 2002.

[124] W.-Y. Yeong, C.-K. Chua, K.-F. Leong, and M. Chandrasekaran, "Rapid prototyping in tissue engineering: challenges and potential.," *Trends Biotechnol.*, vol. 22, pp. 643–652, 2004.

[125] R. Landers, A. Pfister, U. Hübner, H. John, R. Schmelzeisen, and R. Mülhaupt, "Fabrication of soft tissue engineering scaffolds by means of rapid prototyping techniques," *J. Mater. Sci.*, vol. 37, pp. 3107–3116, 2002.

[126] P. A. Webb, "A review of rapid prototyping (RP) techniques in the medical and biomedical sector.," *J. Med. Eng. Technol.*, vol. 24, no. 4, pp. 149–53, 2000 .

[127] D. W. Hutmacher, M. Sittinger, and M. V. Risbud, "Scaffold-based tissue engineering: Rationale for computer-aided design and solid free-form fabrication systems," *Trends in Biotechnology*, vol. 22. pp. 354–362, 2004.

[128] M. N. Cooke, J. P. Fisher, D. Dean, C. Rimnac, and A. G. Mikos, "Use of stereolithography to manufacture critical-sized 3D biodegradable scaffolds for bone ingrowth.," *J. Biomed. Mater. Res. B. Appl. Biomater.*, vol. 64, pp. 65–69, 2003.

[129] K. W. Lee, S. Wang, B. C. Fox, E. L. Ritman, M. J. Yaszemski, and L. Lu, "Poly(propylene fumarate) bone tissue engineering scaffold fabrication using stereolithography: Effects of resin formulations and laser parameters," *Biomacromolecules*, vol. 8, pp. 1077–1084, 2007.

[130] F. P. W. Melchels, J. Feijen, and D. W. Grijpma, "A review on stereolithography and its applications in biomedical engineering," *Biomaterials*, vol. 31. pp. 6121–6130, 2010.

[131] R. Sodian, M. Loebe, A. Hein, D. P. Martin, S. P. Hoerstrup, E. V Potapov, H. Hausmann, T. Lueth, and R. Hetzer, "Application of stereolithography for scaffold fabrication for tissue engineered heart valves.," *ASAIO J.*, vol. 48, no. 1, pp. 12–6, 2002.

[132] A. Naumann, J. Aigner, R. Staudenmaier, M. Seemann, R. Bruening, K. H. Englmeier, G. Kadegge, A. Pavesio, E. Kastenbauer, and A. Berghaus, "Clinical aspects and strategy for biomaterial engineering of an auricle based on three-dimensional stereolithography.," *Eur. Arch. Otorhinolaryngol.*, vol. 260, no. 10, pp. 568–75, Nov. 2003.

[133] R. Sodian, P. Fu, C. Lueders, D. Szymanski, C. Pritsche, M. Gutberlet, S. P. Hoerstrup, H. Hausmann, T. Lueth, and R. Hetzer, "Tissue engineering of vascular conduits: Fabrication of custom-made scaffolds using rapid prototyping techniques," *Thorac. Cardiovasc. Surg.*, vol. 53, pp. 144–149, 2005.

[134] T. Matsuda, M. Mizutani, and S. C. Arnold, "Molecular design of photocurable liquid biodegradable copolymers. 1. Synthesis and photocuring characteristics," *Macromolecules*, vol. 33, pp. 795–800, 2000.

[135] M. Mizutani and T. Matsuda, "Liquid acrylate-endcapped biodegradable poly(caprolactone-co-trimethylene carbonate). I. Preparation and visible light-

induced photocuring characteristics," *J. Biomed. Mater. Res.*, vol. 62, pp. 387–394, 2002.

[136] V. K. Popov, A. V. Evseev, A. L. Ivanov, V. V. Roginski, A. I. Volozhin, and S. M. Howdle, "Laser stereolithography and supercritical fluid processing for custom-designed implant fabrication," *J. Mater. Sci. Mater. Med.*, vol. 15, pp. 123–128, 2004.

[137] P. Tesavibul, R. Felzmann, S. Gruber, R. Liska, I. Thompson, A. R. Boccaccini, and J. Stampfl, "Processing of 45S5 Bioglass® by lithography-based additive manufacturing," *Mater. Lett.*, vol. 74, pp. 81–84, 2012.

[138] P. P. Kruth, "Material Incress Manufacturing by Rapid Prototyping Techniques," *CIRP Ann. - Manuf. Technol.*, vol. 40, pp. 603–614, 1991.

[139] J.-P. Kruth, B. Van der Schueren, J. E. Bonse, and B. Morren, "Basic Powder Metallurgical Aspects in Selective Metal Powder Sintering," *CIRP Annals - Manufacturing Technology*, vol. 45. pp. 183–186, 1996.

[140] J. P. Kruth, X. Wang, T. Laoui, and L. Froyen, "Lasers and materials in selective laser sintering," *Assembly Automation*, vol. 23. pp. 357–371, 2003.

[141] Y. Chivel and I. Smurov, "On-line temperature monitoring in selective laser sintering/melting," in *Physics Procedia*, vol. 5, pp. 515–521, 2010.

[142] S. Kumar, "Selective laser sintering: A qualitative and objective approach," *JOM*, vol. 55. pp. 43–47, 2003.

[143] J. P. Kruth, G. Levy, F. Klocke, and T. H. C. Childs, "Consolidation phenomena in laser and powder-bed based layered manufacturing," *CIRP Ann. - Manuf. Technol.*, vol. 56, pp. 730–759, 2007.

[144] T. Kraft and H. Riedel, "Numerical simulation of solid state sintering; model and application," *J. Eur. Ceram. Soc.*, vol. 24, pp. 345–361, 2004.

[145] J. Kruth, G. Levy, R. Schindel, T. Craeghs, and E. Yasa, "Consolidation of Polymer Powders by Selective Laser Sintering," *Int. Conf. Polym. Mould. Innov.*, pp. 15–30, 2008.

[146] B. Qian and Z. Shen, "Laser sintering of ceramics," *J. Asian Ceram. Soc.*, vol. 1, pp. 315–321, 2013.

[147] C. K. Chua, K. F. Leong, K. H. Tan, F. E. Wiria, and C. M. Cheah, "Development of tissue scaffolds using selective laser sintering of polyvinyl

alcohol/hydroxyapatite biocomposite for craniofacial and joint defects," *J. Mater. Sci. Mater. Med.*, vol. 15, pp. 1113–1121, 2004.

[148] C. Shuai, Z. Mao, H. Lu, Y. Nie, H. Hu, and S. Peng, "Fabrication of porous polyvinyl alcohol scaffold for bone tissue engineering via selective laser sintering.," *Biofabrication*, vol. 5, p. 015014, 2013.

[149] K. H. Tan, C. K. Chua, K. F. Leong, C. M. Cheah, W. S. Gui, W. S. Tan, and F. E. Wiria, "Selective laser sintering of biocompatible polymers for applications in tissue engineering.," *Biomed. Mater. Eng.*, vol. 15, pp. 113–124, 2005.

[150] S. Das, S. J. Hollister, C. Flanagan, A. Adewunmi, K. Bark, C. Chen, K. Ramaswamy, D. Rose, and E. Widjaja, "Freeform fabrication of Nylon-6 tissue engineering scaffolds," *Rapid Prototyp. J.*, vol. 9, pp. 43–49, 2003.

[151] K. H. Tan, C. K. Chua, K. F. Leong, C. M. Cheah, P. Cheang, M. S. Abu Bakar, and S. W. Cha, "Scaffold development using selective laser sintering of polyetheretherketone-hydroxyapatite biocomposite blends," *Biomaterials*, vol. 24, pp. 3115–3123, 2003.

[152] M. C. Azevedo, R. L. Reis, M. B. Claase, D. W. Grijpma, and J. Feijen, "Development and properties of polycaprolactone/hydroxyapatite composite biomaterials," in *Journal of Materials Science: Materials in Medicine*, vol. 14, pp. 103–107, 2003.

[153] F. E. Wiria, K. F. Leong, C. K. Chua, and Y. Liu, "Poly-epsilon-caprolactone/hydroxyapatite for tissue engineering scaffold fabrication via selective laser sintering.," *Acta Biomater.*, vol. 3, pp. 1–12, 2007.

[154] C. K. Chua, K. F. Leong, K. H. Tan, F. E. Wiria, and C. M. Cheah, "Development of tissue scaffolds using selective laser sintering of polyvinyl alcohol/hydroxyapatite biocomposite for craniofacial and joint defects.," *J. Mater. Sci. Mater. Med.*, vol. 15, no. 10, pp. 1113–21, 2004.

[155] T. Hungría, J. Galy, and A. Castro, "Spark plasma sintering as a useful technique to the nanostructuration of piezo-ferroelectric materials," *Advanced Engineering Materials*, vol. 11. pp. 615–631, 2009.

[156] C. Shuai, P. Feng, L. Zhang, C. Gao, H. Hu, S. Peng, and A. Min, "Correlation between properties and microstructure of laser sintered porous β-tricalcium phosphate bone scaffolds," *Sci. Technol. Adv. Mater.*, vol. 14, no. 5, p. 055002, Oct. 2013.

[157] R. D. Goodridge, C. Ohtsuki, M. Kamitakahara, D. J. Wood, and K. W. Dalgarno, "Fabrication of Bioactive Glass-Ceramics by Selective Laser Sintering," in *Key Engineering Materials*, vol. 309–311, pp. 289–292, 2006.

[158] K. Xiao, K. W. Dalgarno, D. J. Wood, R. D. Goodridge, and C. Ohtsuki, "Indirect selective laser sintering of apatite-wollostonite glass-ceramic.," *Proc. Inst. Mech. Eng. H.*, vol. 222, pp. 1107–1114, 2008.

[159] K. C. R. Kolan, M. C. Leu, G. E. Hilmas, and M. Velez, "Effect of material, process parameters, and simulated body fluids on mechanical properties of 13-93 bioactive glass porous constructs made by selective laser sintering," *J. Mech. Behav. Biomed. Mater.*, vol. 13, pp. 14–24, 2012.

[160] K. C. R. Kolan, M. C. Leu, G. E. Hilmas, R. F. Brown, and M. Velez, "Fabrication of 13-93 bioactive glass scaffolds for bone tissue engineering using indirect selective laser sintering.," *Biofabrication*, vol. 3, p. 025004, 2011.

[161] J. Liu, H. Hu, P. Li, C. Shuai, and S. Peng, "Fabrication and Characterization of Porous 45S5 Glass Scaffolds via Direct Selective Laser Sintering," *Mater. Manuf. Process.*, vol. 28, no. 6, p. 130219154812009, 2013.

[162] J. A. Lewis, "Direct ink writing of 3D functional materials," *Adv. Funct. Mater.*, vol. 16, pp. 2193–2204, 2006.

[163] G. M. Gratson, M. Xu, and J. A. Lewis, "Microperiodic structures: direct writing of three-dimensional webs.," *Nature*, vol. 428, p. 386, 2004.

[164] D. Therriault, S. R. White, and J. A. Lewis, "Chaotic mixing in three-dimensional microvascular networks fabricated by direct-write assembly.," *Nat. Mater.*, vol. 2, pp. 265–271, 2003.

[165] J. Nosek, M. Sulc, L. Burianova, C. Soyer, E. Cattan, and D. Remiens, "Non-linear piezoelectric properties of the thin Pb(ZrxTi1-x)O3 (PZT) films deposited on the Si-substrate," *J. Eur. Ceram. Soc.*, vol. 25, pp. 2257–2261, 2005.

[166] J. E. Smay, J. Cesarano, B. A. Tuttle, and J. A. Lewis, "Piezoelectric properties of 3-X periodic Pb(ZrxTi1-x)O-3-polymer composites," *J. Appl. Phys.*, vol. 92, pp. 6119–6127, 2002.

[167] S. L. Morissette, J. A. Lewis, P. G. Clem, J. Cerano, and D. B. Dimos, "Direct-Write Fabrication of Pb(Nb,Zr,Ti)O3 Devices: Influence of Paste Rheology on Print Morphology and Component Properties," *J. Am. Ceram. Soc.*, vol. 84, pp. 2462–2468, 2001.

[168] A. Bandyopadhyay, R. K. Panda, V. F. Janas, M. K. Agarwala, R. van Weeren, S. C. Danforth, and A. Safari, "Processing of piezocomposites by fused deposition technique," *ISAF '96. Proc. Tenth IEEE Int. Symp. Appl. Ferroelectr.*, vol. 2, 1996.

[169] M. Allahverdi, S. C. Danforth, M. Jafari, and A. Safari, "Processing of advanced electroceramic components by fused deposition technique," *J. Eur. Ceram. Soc.*, vol. 21, pp. 1485–1490, 2001.

[170] T. S. Huang, M. N. Rahaman, N. D. Doiphode, M. C. Leu, B. S. Bal, D. E. Day, and X. Liu, "Freeze extrusion fabrication of 13-93 bioactive glass scaffolds for repair and regeneration of load-bearing bones," in *Ceramic Transactions*, 2011, vol. 228, pp. 45–55.

[171] X. Zhao, J. R. G. Evans, M. J. Edirisinghe, and J. H. Song, "Ink-jet printing of ceramic pillar arrays," *J. Mater. Sci.*, vol. 37, pp. 1987–1992, 2002.

[172] S. Gamerith, A. Klug, H. Scheiber, U. Scherf, E. Moderegger, and E. J. W. List, "Direct ink-jet printing of Ag-Cu nanoparticle and Ag-precursor based electrodes for OFET applications," *Adv. Funct. Mater.*, vol. 17, pp. 3111–3118, 2007.

[173] V. Chovancova, A. Pekarovicova, and P. D. I. Fleming, "Hot Melt Inks for 3D Printing," in *IS&T Digital Fabrication Conference Proceedings*, 2005, pp. 143–147.

[174] X. Lu, Y. Lee, S. Yang, Y. Hao, J. R. G. Evans, and C. G. Parini, "Solvent-based paste extrusion solid freeforming," *J. Eur. Ceram. Soc.*, vol. 30, pp. 1–10, 2010.

[175] J. E. Smay, J. Cesarano, and J. A. Lewis, "Colloidal inks for directed assembly of 3-D periodic structures," *Langmuir*, vol. 18, pp. 5429–5437, 2002.

[176] J. E. Smay, G. M. Gratson, R. F. Shepherd, J. Cesarano, and J. A. Lewis, "Directed colloidal assembly of 3D periodic structures," *Adv. Mater.*, vol. 14, pp. 1279–1283, 2002.

[177] J. J. Guo and J. Lewis, "Aggregation effects on the compressive flow properties and drying behavior of colloidal silica suspensions," *J. Am. Ceram. Soc.*, vol. 82, pp. 2345–2358, 1999.

[178] J. N. Israelachvili, *Intermolecular and Surface Forces*. 2011.

[179] G. Fritz, V. Schädler, N. Willenbacher, and N. J. Wagner, "Electrosteric stabilization of colloidal dispersions," *Langmuir*, vol. 18, pp. 6381–6390, 2002.

[180] E. B. Zhulina, O. V Borisov, and V. A. Priamitsyn, "Theory of steric stabilization of colloid dispersions by grafted polymers," *J. Colloid Interface Sci.*, vol. 137, no. 2, pp. 495–511, 1990.

[181] D. V. Boger, "An Introduction to Rheology," *Journal of Non-Newtonian Fluid Mechanics*, vol. 32. pp. 331–333, 1989.

[182] M. S. Romero-Cano, A. Martín-Rodríguez, and F. J. De las Nieves, "Electrosteric stabilization of polymer colloids with different functionality," *Langmuir*, vol. 17, pp. 3505–3511, 2001.

[183] Q. Fu, E. Saiz, and A. P. Tomsia, "Bioinspired strong and highly porous glass scaffolds," *Adv. Funct. Mater.*, vol. 21, pp. 1058–1063, 2011.

[184] J. N. Stuecker, J. Cesarano, and D. A. Hirschfeld, "Control of the viscous behavior of highly concentrated mullite suspensions for robocasting," *J. Mater. Process. Technol.*, vol. 142, pp. 318–325, 2003.

[185] Q. Li and J. A. Lewis, "Nanoparticle Inks for Directed Assembly of Three-Dimensional Periodic Structures," *Adv. Mater.*, vol. 15, pp. 1639–1643, 2003.

[186] A. Şakar-Deliormanli, E. Çelik, and M. Polat, "Rheological behavior of PMN gels for solid freeform fabrication," *Colloids Surfaces A Physicochem. Eng. Asp.*, vol. 324, pp. 159–166, 2008.

[187] I. M. Krieger, "A Mechanism for Non-Newtonian Flow in Suspensions of Rigid Spheres," *Journal of Rheology*, vol. 3. p. 137, 1959.

[188] J. A. Lewis, J. E. Smay, J. Stuecker, and J. Cesarano, "Direct ink writing of three-dimensional ceramic structures," *J. Am. Ceram. Soc.*, vol. 89, pp. 3599–3609, 2006.

[189] Z. D. Jastrzebski, "Entrance Effects and Wall Effects in an Extrusion Rheometer during Flow of Concentrated Suspensions," *Ind. Eng. Chem. Fundam.*, vol. 6, no. 3, pp. 445–454, Aug. 1967.

[190] R. Buscall, "The rheology of concentrated dispersions of weakly attracting colloidal particles with and without wall slip," *Journal of Rheology*, vol. 37. p. 621, 1993.

[191] J. Cesarano, "A Review of Robocasting Technology," *MRS Proceedings*, vol. 542. 1998.

[192] K. V. Wong and A. Hernandez, "A Review of Additive Manufacturing," *ISRN Mechanical Engineering*, vol. 2012. pp. 1–10, 2012.

[193] M. Vaezi, H. Seitz, and S. Yang, "A review on 3D micro-additive manufacturing technologies," *International Journal of Advanced Manufacturing Technology*, vol. 67. pp. 1721–1754, 2013.

[194] I. E. Pinwill, M. J. Edirisinghe, and M. J. Bevis, "Development of temperature-heating rate diagrams for the pyrolytic removal of binder used for powder injection moulding," *J. Mater. Sci.*, vol. 27, pp. 4381–4388, 1992.

[195] K. S. Hwang and T. H. Tsou, "Thermal debinding of powder injection molded parts: Observations and mechanisms," *Metall. Trans. A*, vol. 23, pp. 2775–2782, 1992.

[196] S. J. Lombardo and Z. C. Feng, "Determination of the Minimum Time for Binder Removal and Optimum Geometry for Three-Dimensional Porous Green Bodies," *J. Am. Ceram. Soc.*, vol. 86, pp. 2087–2092, 2003.

[197] Z. Lei, Z. Ke-Chao, L. Zhi-you, and Z. Xiao-yong, "Degradation and the kinetics of binder removal," *Met. Powder Rep.*, vol. 61, pp. 28–33, 2006.

[198] K. Krishnamurthy and S. J. Lombardo, "Development of a heating schedule for rapid thermal debinding of green multilayer ceramic capacitors," *J. Ceram. Process. Res.*, vol. 11, pp. 405–410, 2010.

[199] N. D. Doiphode, T. Huang, M. C. Leu, M. N. Rahaman, and D. E. Day, "Freeze extrusion fabrication of 13-93 bioactive glass scaffolds for bone repair.," *J. Mater. Sci. Mater. Med.*, vol. 22, no. 3, pp. 515–23, 2011.

[200] N. H. Loh, S. B. Tor, B. Y. Tay, Y. Murakoshi, and R. Maeda, "Fabrication of micro gear by micro powder injection molding," *Microsyst. Technol.*, vol. 14, no. 1, pp. 43–50, 2007.

[201] L. Lefebvre, L. Gremillard, J. Chevalier, R. Zenati, and D. Bernache-Assolant, "Sintering behaviour of 45S5 bioactive glass," *Acta Biomater.*, vol. 4, pp. 1894–1903, 2008.

[202] X. Chatzistavrou, T. Zorba, E. Kontonasaki, K. Chrissafis, P. Koidis, and K. M. Paraskevopoulos, "Following bioactive glass behavior beyond melting temperature by thermal and optical methods," *Phys. status solidi*, vol. 201, no. 5, pp. 944–951, Apr. 2004.

[203] X. Chatzistavrou, T. Zorba, K. Chrissafis, G. Kaimakamis, E. Kontonasaki, P. Koidis, and K. M. Paraskevopoulos, "Influence of particle size on the crystallization process and the bioactive behavior of a bioactive glass system," *J. Therm. Anal. Calorim.*, vol. 85, no. 2, pp. 253–259, Jul. 2006.

[204] M. O. Prado and E. D. Zanotto, "Glass sintering with concurrent crystallization," *Comptes Rendus Chimie*, vol. 5. pp. 773–786, 2002.

[205] D. C. Clupper and L. L. Hench, "Crystallization kinetics of tape cast bioactive glass 45S5," *J. Non. Cryst. Solids*, vol. 318, pp. 43–48, 2003.

[206] F. S. and H. L., "Crystallization of 45S5 during Isothermal Heat Treatment," *Mater. Ceram. /Ceramic Mater.*, vol. 62, no. 3, pp. 349–354, 2010.

[207] Q. Chen and A. R. Boccaccini, "Coupling Mechanical Competence and Bioresorbability in Bioglass®-Derived Tissue Engineering Scaffolds," *Adv. Eng. Mater.*, vol. 8, no. 4, pp. 285–289, Apr. 2006.

[208] Q. Z. Chen, J. L. Xu, L. G. Yu, X. Y. Fang, and K. A. Khor, "Spark plasma sintering of sol-gel derived 45S5 Bioglass®-ceramics: Mechanical properties and biocompatibility evaluation," *Mater. Sci. Eng. C-Materials Biol. Appl.*, vol. 32, pp. 494–502, 2012.

[209] B. van Rietbergen, S. Majumdar, W. Pistoia, D. C. Newitt, M. Kothari, A. Laib, and P. Rüegsegger, "Assessment of cancellous bone mechanical properties from micro-FE models based on micro-CT, pQCT and MR images.," *Technol. Health Care*, vol. 6, pp. 413–420, 1998.

[210] E. B. W. Giesen, M. Ding, M. Dalstra, and T. M. G. J. Van Eijden, "Mechanical properties of cancellous bone in the human mandibular condyle are anisotropic," *J. Biomech.*, vol. 34, pp. 799–803, 2001.

[211] A. M. Deliormanli and M. N. Rahaman, "Direct-write assembly of silicate and borate bioactive glass scaffolds for bone repair," *J. Eur. Ceram. Soc.*, vol. 32, pp. 3637–3646, 2012.

[212] D. Mohamad Yunos, O. Bretcanu, and A. R. Boccaccini, "Polymer-bioceramic composites for tissue engineering scaffolds," in *Journal of Materials Science*, 2008, vol. 43, pp. 4433–4442.

[213] J. J. Blaker, V. Maquet, R. Jérôme, A. R. Boccaccini, and S. N. Nazhat, "Mechanical properties of highly porous PDLLA/Bioglass® composite foams as scaffolds for bone tissue engineering," *Acta Biomater.*, vol. 1, pp. 643–652, 2005.

[214] J. A. Roether, J. E. Gough, A. R. Boccaccini, L. L. Hench, V. Maquet, and R. Jérôme, "Novel bioresorbable and bioactive composites based on bioactive glass and polylactide foams for bone tissue engineering," in *Journal of Materials Science: Materials in Medicine*, 2002, vol. 13, pp. 1207–1214.

[215] J. Hum, K. W. Luczynski, P. Nooeaid, P. Newby, O. Lahayne, C. Hellmich, and A. R. Boccaccini, "Stiffness improvement of 45S5 bioglass®-based scaffolds through natural and synthetic biopolymer coatings: An ultrasonic study," *Strain*, vol. 49, pp. 431–439, 2013.

[216] I. Wu and J. Elisseeff, *Natural and Synthetic Biomedical Polymers*. 2014.

[217] R. S. R. Murthy, "Biodegradable polymers," in *Biodegradable polymers*, 1997, pp. 27–51.

[218] N. Angelova and D. Hunkeler, "Rationalizing the design of polymeric biomaterials," *Trends in Biotechnology*, vol. 17. pp. 409–421, 1999.

[219] W. Xue, A. Bandyopadhyay, and S. Bose, "Polycaprolactone coated porous tricalcium phosphate scaffolds for controlled release of protein for tissue engineering," *J. Biomed. Mater. Res. - Part B Appl. Biomater.*, vol. 91, pp. 831–838, 2009.

[220] K. O. Siegenthaler, A. Kuenkel, G. Skupin, and M. Yamamoto, *Synthetic Biodegradable Polymers*, vol. 245. 2012.

[221] F. J. Martínez-Vázquez, P. Miranda, F. Guiberteau, and A. Pajares, "Reinforcing bioceramic scaffolds with in situ synthesized ε-polycaprolactone coatings," *J. Biomed. Mater. Res. - Part A*, vol. 101, pp. 3551–3559, 2013.

[222] X. Miao, W. K. Lim, X. Huang, and Y. Chen, "Preparation and characterization of interpenetrating phased TCP/HA/PLGA composites," *Mater. Lett.*, vol. 59, pp. 4000–4005, 2005.

[223] S. S. Henriksen, M. Ding, M. V. Juhl, N. Theilgaard, and S. Overgaard, "Mechanical strength of ceramic scaffolds reinforced with biopolymers is comparable to that of human bone," *J. Mater. Sci. Mater. Med.*, vol. 22, pp. 1111–1118, 2011.

[224] M. Peroglio, L. Gremillard, C. Gauthier, L. Chazeau, S. Verrier, M. Alini, and J. Chevalier, "Mechanical properties and cytocompatibility of poly(ε-caprolactone)-infiltrated biphasic calcium phosphate scaffolds with bimodal pore distribution.," *Acta Biomater.*, vol. 6, no. 11, pp. 4369–79, Nov. 2010.

[225] S. Sharifi, Y. Shafieyan, H. Mirzadeh, S. Bagheri-Khoulenjani, S. M. Rabiee, M. Imani, M. Atai, M. A. Shokrgozar, and A. Hatampoor, "Hydroxyapatite scaffolds infiltrated with thermally crosslinked polycaprolactone fumarate and polycaprolactone itaconate," *J. Biomed. Mater. Res. - Part A*, vol. 98 A, pp. 257–267, 2011.

[226] S. Eqtesadi, A. Motalleh, A. Pajares, and P. Miranda, "Effect of milling media on processing and performance of 13-93 bioactive glass scaffolds fabricated by robocasting," *Ceram. Int.*, vol. In press, Sep. 2014.

[227] M. Instruments, "Zeta potential: An Introduction in 30 minutes," *Zetasizer Nano Serles Tech. Note. MRK654-01*, vol. 2, pp. 1–6, 2011.

[228] W. Weibull, "A statistical distribution function of wide applicability," *J. Appl. Mech.*, vol. 18, pp. 293–297, 1951.

[229] T. Kokubo, H. Kushitani, S. Sakka, T. Kitsugi, and T. Yamamuro, "Solutions able to reproduce in vivo surface-structure changes in bioactive glass-ceramic A-W3," *J. Biomed. Mater. Res.*, vol. 24, pp. 721–734, 1990.

[230] P. P. Lopes, B. J. M. Leite Ferreira, N. A. F. Almeida, T. E. Silva, M. C. Fredel, M. H. F. V. Fernandes, and R. N. Correia, "In vitro bioactivity of PMMA-based composite in simulated plasma with albumin," *Matéria (Rio Janeiro)*, vol. 12, no. 1, pp. 128–133, 2007.

[231] M. Cerruti, D. Greenspan, and K. Powers, "Effect of pH and ionic strength on the reactivity of Bioglass$^{®}$ 45S5," *Biomaterials*, vol. 26, pp. 1665–1674, 2005.

[232] R. K. Iler, *The chemistry of silica: solubility, polymerization, colloid and surface properties, and biochemistry*. 1979.

[233] J. Sun and L. Gao, "Dispersing SiC powder and improving its rheological behaviour," *J. Eur. Ceram. Soc.*, vol. 21, pp. 2447–2451, 2001.

[234] K. S. Soppimath, T. M. Aminabhavi, A. R. Kulkarni, and W. E. Rudzinski, "Biodegradable polymeric nanoparticles as drug delivery devices.," *J. Control. Release*, vol. 70, pp. 1–20, 2001.

[235] D. L. Jiang, "Gelcasting of Carbide Ceramics," *Key Engineering Materials*, vol. 403. pp. 163–164, 2009.

[236] M. Nardin, E. Papirer, and J. Schultz, "An electrokinetic study of the interactions between glass fibers and aqueous solutions of calcium," *Journal of Colloid and Interface Science*, vol. 88. pp. 204–213, 1982.

[237] P. Somasundaran and G. . Agar, "The zero point of charge of calcite," *Journal of Colloid and Interface Science*, vol. 24. pp. 433–440, 1967.

[238] E. J. W. VERWEY, "Theory of the stability of lyophobic colloids.," *J. Phys. Colloid Chem.*, vol. 51, pp. 631–636, 1947.

[239] G. Girod, J. . Lamarche, and A. Foissy, "Adsorption of partially hydrolyzed polyacrylamides on titanium dioxide," *J. Colloid Interface Sci.*, vol. 121, no. 1, pp. 265–272, 1988.

[240] C. E. Giacomelli, M. J. Avena, and C. P. De Pauli, "Aspartic acid adsorption onto TiO2 particles surface. Experimental data and model calculations," *Langmuir*, vol. 11, no. 9, pp. 3483–3490, 1995.

[241] C. W. Hoogendam, A. de Keizer, M. A. Cohen Stuart, and B. H. Bijsterbosh, "Adsorption mechanisms of carboxymethyl cellulose on mineral surfaces," *Langmuir*, vol. 14, pp. 3825–3839, 1998.

[242] F. H. Chowdhury and S. M. Neale, "Acid behavior of carboxylic derivatives of cellulose. Part I. Carboxymethylcellulose," *J. Polym. Sci. Part A Gen. Pap.*, vol. 1, no. 9, pp. 2881–2891, 1963.

[243] J. A. Lewis and G. M. Gratson, "Direct writing in three dimensions," *Materials Today*, vol. 7. pp. 32–39, 2004.

[244] S. Eqtesadi, A. Motealleh, P. Miranda, A. Lemos, A. Rebelo, and J. M. F. Ferreira, "A simple recipe for direct writing complex 45S5 Bioglass[®] 3D scaffolds," *Mater. Lett.*, vol. 93, pp. 68–71, 2013.

[245] A. El-Ghannam, E. Hamazawy, and A. Yehia, "Effect of thermal treatment on bioactive glass microstructure, corrosion behavior, zeta potential, and protein adsorption.," *J. Biomed. Mater. Res.*, vol. 55, pp. 387–395, 2001.

[246] M. Erol, S. Küçükbayrak, and A. Ersoy-Meriçboyu, "Influence of particle size on the crystallization kinetics of glasses produced from waste materials," *J. Non. Cryst. Solids*, vol. 357, pp. 211–219, 2011.

[247] R. Xin, Q. Zhang, and J. Gao, "Identification of the wollastonite phase in sintered 45S5 bioglass and its effect on in vitro bioactivity," *J. Non. Cryst. Solids*, vol. 356, no. 23–24, pp. 1180–1184, 2010.

[248] O. Guillon, S. Cao, J. Chang, L. Wondraczek, and A. R. Boccaccini, "Effect of uniaxial load on the sintering behaviour of 45S5 Bioglass[®] powder compacts," *J. Eur. Ceram. Soc.*, vol. 31, pp. 999–1007, 2011.

[249] P. Miranda, A. Pajares, E. Saiz, A. P. Tomsia, and F. Guiberteau, "Fracture modes under uniaxial compression in hydroxyapatite scaffolds fabricated by robocasting," *J. Biomed. Mater. Res. - Part A*, vol. 83, pp. 646–655, 2007.

[250] P. Miranda, A. Pajares, and F. Guiberteau, "Finite element modeling as a tool for predicting the fracture behavior of robocast scaffolds," *Acta Biomater.*, vol. 4, pp. 1715–1724, 2008.

[251] L. J. Gibson, "Cellular Solids," *MRS Bulletin*, vol. 28. pp. 270–274, 2003.

[252] J. R. Jones, J. R. Jones, L. M. Ehrenfried, L. M. Ehrenfried, L. L. Hench, and L. L. Hench, "Optimising bioactive glass scaffolds for bone tissue engineering.," *Biomaterials*, vol. 27, no. 7, pp. 964–73, 2006.

[253] Q. Chen, D. Mohn, and W. J. Stark, "Optimization of Bioglass® scaffold fabrication process," *J. Am. Ceram. Soc.*, vol. 94, pp. 4184–4190, 2011.

[254] D. Meng, S. N. Rath, N. Mordan, V. Salih, U. Kneser, and A. R. Boccaccini, "In vitro evaluation of 45S5 Bioglass®-derived glass-ceramic scaffolds coated with carbon nanotubes," *J. Biomed. Mater. Res. - Part A*, vol. 99 A, pp. 435–444, 2011.

[255] J. R. Jones, L. M. Ehrenfried, and L. L. Hench, "Optimising bioactive glass scaffolds for bone tissue engineering.," *Biomaterials*, vol. 27, pp. 964–73, 2006.

[256] A. Abarrategi, C. Moreno-Vicente, F. J. Martínez-Vázquez, A. Civantos, V. Ramos, J. V. Sanz-Casado, R. Martínez-Corriá, F. H. Perera, F. Mulero, P. Miranda, and J. L. López-Lacomba, "Biological properties of solid free form designed ceramic scaffolds with bmp-2: In vitro and in vivo evaluation," *PLoS One*, vol. 7, 2012.

[257] S. K. Lan Levengood, S. J. Polak, M. B. Wheeler, A. J. Maki, S. G. Clark, R. D. Jamison, and A. J. Wagoner Johnson, "Multiscale osteointegration as a new paradigm for the design of calcium phosphate scaffolds for bone regeneration.," *Biomaterials*, vol. 31, no. 13, pp. 3552–63, 2010.

[258] a Abarrategi, M. E. Fernandez-Valle, T. Desmet, D. Castejón, a Civantos, C. Moreno-Vicente, V. Ramos, J. V Sanz-Casado, F. J. Martínez-Vázquez, P. Dubruel, P. Miranda, and J. L. López-Lacomba, "Label-free magnetic resonance imaging to locate live cells in three-dimensional porous scaffolds.," *J. R. Soc. Interface*, vol. 9, pp. 2321–31, 2012.

[259] L. L. Hench and J. Wilson, "Surface-active biomaterials.," *Science*, vol. 226, pp. 630–636, 1984.

[260] W. Huang, D. E. Day, K. Kittiratanapiboon, and M. N. Rahaman, "Kinetics and mechanisms of the conversion of silicate (45S5), borate, and borosilicate glasses

to hydroxyapatite in dilute phosphate solutions.," *J. Mater. Sci. Mater. Med.*, vol. 17, no. 7, pp. 583–96, Jul. 2006.

[261] S. Kashyap, K. Griep, and J. A. Nychka, "Crystallization kinetics, mineralization and crack propagation in partially crystallized bioactive glass 45S5," *Mater. Sci. Eng. C*, vol. 31, pp. 762–769, 2011.

[262] P. Miranda, A. Pajares, F. Guiberteau, F. L. Cumbrera, and B. R. Lawn, "Role of flaw statistics in contact fracture of brittle coatings," *Acta Mater.*, vol. 49, no. 18, pp. 3719–3726, 2001.

[263] H.-W. Kim, Y. Deng, P. Miranda, A. Pajares, D. K. Kim, H.-E. Kim, and B. R. Lawn, "Effect of Flaw State on the Strength of Brittle Coatings on Soft Substrates," *J. Am. Ceram. Soc.*, vol. 84, no. 10, pp. 2377–2384, 2004.

[264] T. M. Keaveny and W. C. Hayes, "Mechanical Properties of Cortical and Trabecular Bone," in *Bone*, pp. 285–344, 1993.

[265] F. J. Martínez-Vázquez, F. H. Perera, I. Van Der Meulen, A. Heise, A. Pajares, and P. Miranda, "Impregnation of β-tricalcium phosphate robocast scaffolds by in situ polymerization," *J. Biomed. Mater. Res. - Part A*, vol. 101, pp. 3086–3096, 2013.

[266] T. R. Zeitler and A. N. Cormack, "Interaction of water with bioactive glass surfaces," *J. Cryst. Growth*, vol. 294, pp. 96–102, 2006.

[267] E. Verné, C. Vitale-Brovarone, E. Bui, C. L. Bianchi, and A. R. Boccaccini, "Surface functionalization of bioactive glasses," *J. Biomed. Mater. Res. - Part A*, vol. 90, pp. 981–992, 2009.

[268] A. Tilocca and A. N. Cormack, "Exploring the surface of bioactive glasses: Water adsorption and reactivity," *J. Phys. Chem. C*, vol. 112, pp. 11936–11945, 2008.

[269] X. Liu, M. N. Rahaman, G. E. Hilmas, and B. S. Bal, "Mechanical properties of bioactive glass (13-93) scaffolds fabricated by robotic deposition for structural bone repair," *Acta Biomater.*, vol. 9, pp. 7025–7034, 2013.

[270] X. Liu, M. N. Rahaman, Y. Liu, B. S. Bal, and L. F. Bonewald, "Enhanced bone regeneration in rat calvarial defects implanted with surface-modified and BMP-loaded bioactive glass (13-93) scaffolds," *Acta Biomater.*, vol. 9, pp. 7506–7517, 2013.

[271] S. Eqtesadi, A. Motealleh, P. Miranda, A. Pajares, A. Lemos, and J. M. F. Ferreira, "Robocasting of 45S5 bioactive glass scaffolds for bone tissue engineering," *J. Eur. Ceram. Soc.*, vol. 34, pp. 107–118, 2014.

[272] P. Miranda, E. Saiz, K. Gryn, and A. P. Tomsia, "Sintering and robocasting of tricalcium phosphate scaffolds for orthopaedic applications," *Acta Biomater.*, vol. 2, pp. 457–466, 2006.

[273] S. Michna, W. Wu, and J. A. Lewis, "Concentrated hydroxyapatite inks for direct-write assembly of 3-D periodic scaffolds," *Biomaterials*, vol. 26, pp. 5632–5639, 2005.

[274] M. D. Driessen and V. H. Grassian, "Adsorption and reaction of ethyl fragments on reduced and oxidized silica-supported copper particles," *Langmuir*, vol. 14, pp. 1411–1418, 1998.

[275] Q. Wang, C. G. Pantano, and J. F. Annett, "Ab initio Calculation on Atomic Structure and Charge Transfer of Silicon Oxycarbide (SiOxCy) at the SiC/SiO₂ Interface," *Phys. status solidi*, vol. 216, no. 2, pp. 909–916, Dec. 1999.

[276] G. D. Sorarù, G. D'Andrea, and A. Glisenti, "XPS characterization of gel-derived silicon oxycarbide glasses," *Materials Letters*, vol. 27. pp. 1–5, 1996.

[277] R. G. Azrak and C. L. Angell, "Study of alcohol-silica surface reactions via infrared spectroscopy," *J. Phys. Chem.*, vol. 77, no. 26, pp. 3048–3052, Dec. 1973.

[278] J. Ning, A. Yao, D. Wang, W. Huang, H. Fu, X. Liu, X. Jiang, and X. Zhang, "Synthesis and in vitro bioactivity of a borate-based bioglass," *Mater. Lett.*, vol. 61, pp. 5223–5226, 2007.

[279] A. Saboori, M. Rabiee, F. Moztarzadeh, M. Sheikhi, M. Tahriri, and M. Karimi, "Synthesis, characterization and in vitro bioactivity of sol-gel-derived SiO2-CaO-P2O5-MgO bioglass," *Mater. Sci. Eng. C*, vol. 29, pp. 335–340, 2009.

[280] A. M. Deliormanlı and M. N. Rahaman, "Direct-write assembly of silicate and borate bioactive glass scaffolds for bone repair," *J. Eur. Ceram. Soc.*, vol. 32, no. 14, pp. 3637–3646, 2012.

[281] K. M. El Badry, F. A. Moustafa, M. A. Azooz, and F. H. El Batal, "Corrosion behaviour of some selected bioglasses by different aqueous solutions," *Glas. Technol.*, vol. 43, pp. 162–170, 2002.

[282] Y. Zhang, Y. Cai, Q. Wang, Y. Zhao, F. Monchau, A. Lefevre, and H. F. Hildebrand, "Biodegradation of synthetic bioglasses with different crystallinity in vitro," *Sheng Wu Yi Xue Gong Cheng Xue Za Zhi*, vol. 22, pp. 990–994, 2005.

[283] A. Khawam and D. R. Flanagan, "Solid-state kinetic models: Basics and mathematical fundamentals," *J. Phys. Chem. B*, vol. 110, pp. 17315–17328, 2006.

[284] Q. Fu, M. N. Rahaman, H. Fu, and X. Liu, "Silicate, borosilicate, and borate bioactive glass scaffolds with controllable degradation rate for bone tissue engineering applications. I. Preparation and in vitro degradation," *J. Biomed. Mater. Res. - Part A*, vol. 95, pp. 164–171, 2010.

[285] B. Lei, X. Chen, Y. Wang, N. Zhao, G. Miao, Z. Li, and C. Lin, "Fabrication of porous bioactive glass particles by one step sintering," *Mater. Lett.*, vol. 64, pp. 2293–2295, 2010.

[286] J. Y. Rho, L. Kuhn-Spearing, and P. Zioupos, "Mechanical properties and the hierarchical structure of bone," *Med. Eng. Phys.*, vol. 20, pp. 92–102, 1998.

[287] D. R. Carter and W. C. Hayes, "Bone compressive strength: the influence of density and strain rate.," *Science*, vol. 194, pp. 1174–1176, 1976.

[288] D. R. Carter and W. C. Hayes, "The compressive behavior of bone as a two-phase porous structure.," *J. Bone Joint Surg. Am.*, vol. 59, pp. 954–962, 1977.

[289] A. M. Gibson LJ, "Cellular Solids Structure and Properties | Materials science | Cambridge University Press," *Cambridge University Press*, 1997. [Online]. Available: http://www.cambridge.org/us/academic/subjects/engineering/materials-science/cellular-solids-structure-and-properties-2nd-edition. [Accessed: 28-Oct-2014].

[290] M. J. Lever, *Biomaterials, Artificial Organs and Tissue Engineering*. 2005.

[291] D. Taylor and J. H. Kuiper, "The prediction of stress fractures using a 'stressed volume' concept.," *J. Orthop. Res.*, vol. 19, no. 5, pp. 919–26, Sep. 2001.

[292] D. Taylor and J. H. Kuiper, "The prediction of stress fractures using a 'stressed volume' concept," *J. Orthop. Res.*, vol. 19, pp. 919–926, 2001.

[293] D. R. Carter, G. H. Schwab, and D. M. Spengler, "Tensile fracture of cancellous bone.," *Acta Orthop. Scand.*, vol. 51, pp. 733–741, 1980.

[294] T. S. Keller, Z. Mao, and D. M. Spengler, "Young's modulus, bending strength, and tissue physical properties of human compact bone.," *J. Orthop. Res.*, vol. 8, no. 4, pp. 592–603, 1990.

[295] F. Croisier, A. S. Duwez, C. Jérôme, A. F. Léonard, K. O. Van Der Werf, P. J. Dijkstra, and M. L. Bennink, "Mechanical testing of electrospun PCL fibers," *Acta Biomater.*, vol. 8, no. 1, pp. 218–224, 2012.

[296] E. Munch, M. E. Launey, D. H. Alsem, E. Saiz, A. P. Tomsia, and R. O. Ritchie, "Tough, bio-inspired hybrid materials.," *Science*, vol. 322, pp. 1516–1520, 2008.